# CONTROL OF SOLAR PV SYSTEM BASED MICROGRID FOR ENHANCED PERFORMANCE

**Thesis submitted to**

**DELHI TECHNOLOGICAL UNIVERSITY**

**FOR**

**THE AWARD OF THE DEGREE OF**
**DOCTOR OF PHILOSOPHY**

by

**PALLAVI VERMA**
**(2K16/Ph.D./EE/22)**

Under the Supervision of

**Prof. Rachana Garg and Prof. Priya Mahajan**
**Department of Electrical Engineering**
**Delhi Technological University**
**Delhi-110042**


**DEPARTMENT OF ELECTRICAL ENGINEERING**
**DELHI TECHNOLOGICAL UNIVERSITY**
**DELHI-110042**

**OCTOBER 2021**

# DECLARATION

This is to certify that the thesis titled **"Control of solar PV system based microgrid for enhanced performance"** was carried out by Ms. Pallavi Verma under the supervision of Prof. Rachana Garg and Prof. Priya Mahajan, Delhi Technological University, Delhi, India.

The interpretations put forth are based on my reading and understanding of the original texts and they are not published anywhere in the form of books, monographs or articles. The other books, articles and websites, which I have referred are acknowledged at the respective place in the text.

For the present thesis, which I am submitting to the university, no degree or diploma has been conferred on me before, either in this or in any other university.

Date: 06/10/2021
Place: New Delhi

Ms. Pallavi Verma
2K16/Ph.D./EE/22
Department of Electrical Engineering
Delhi Technological University
Shahbad Daulatpur, Delhi-110042, India

# CERTIFICATE

This is to certify that the thesis titled **"Control of solar PV system based microgrid for enhanced performance"** submitted for the award of the Doctor of Philosophy is original to the best of our knowledge. The work was carried out by Ms. Pallavi Verma under our guidance and has not been submitted in parts or full to this or any other University for the award of any degree or diploma. All the assistance and help received during the course of study have been duly acknowledged.

Prof. Rachana Garg
Department of Electrical Engineering
Delhi Technological University
Shahbad Daulatpur, Delhi-110042, India

Prof. Priya Mahajan
Department of Electrical Engineering
Delhi Technological University
Shahbad Daulatpur, Delhi-110042, India

# ACKNOWLEDGEMENT

Writing this thesis has been fascinating and extremely rewarding. First of all, I am thankful to God, who has blessed me strength and support throughout my life and always provides me with a path to acquire knowledge and learning.

I would like to express my sincere gratitude to my supervisors, Prof. Rachana Garg and Prof. Priya Mahajan, for all their help, guidance, valuable suggestions, explanation, advices and above all, their support for carrying out this thesis work. Throughout my thesis-writing period, they were highly supportive and encouraging.

I would like to express my deepest thanks to Prof. Madhusudan Singh, DRC Chairman and Prof. Uma Nangia, HOD, Electrical Engineering, Delhi Technological University (formerly Delhi College of Engineering) for their immense support and valuable guidance during the entire work of this thesis.

I extend my gratitude to Prof. Yogesh Singh (Vice Chancellor) for his co-operation and support for providing a supportive environment to complete my research at Delhi Technological University. My sincere thanks and deep gratitude are to Prof. Pramod Kumar and all SRC members for their valuable guidance and consistent support during my research work.

Sincere thanks to Delhi Technological University authorities for providing me necessary facilities for the smooth completion of my work. I would like to give special thanks Mr. Mukesh Kumar of Project and Research Lab, Mr. Vickey of UEE Lab and Mr. T.P.S. Rana of Machines Lab, DTU Delhi for providing me with the facilities and assistance during this work. I would like to thank the office staff of EED, Central Library and Central Computer Centre for their valuable co-operation and support.

I would like to thank all my seniors, Dr. Nikita Gupta, Dr. Shikha Gupta to motivate and guide me in the starting of my research work. I would like to use this opportunity to thank my fellow researchers and juniors, Dr. Rupam Singh, Mr. Hemant Saxena, Mr. Suryakant Shukla, Mr. Avdhesh Kumar for their co-operation and informal support

in pursuing this research work.

I am extremely grateful to my parents, Mr. R.K. Verma, Late Mrs. Usha Verma, my in-laws, Mr. Mathew Raju, Mrs. Jessy Raju, for their dreams, blessings and constant encouragement. Their trust in my capabilities had been a key factor in all my achievements. I find myself at a loss of words to express my gratitude to my husband, Mr. Roby Mathew Raju who spent sleepless nights with me during my research work and motivated me to make me believe in myself. He has been always there with his critical review of my work and suggestions. I am indebted to my son Ved for his tremendous support, unfailing faith and patience throughout my study period.

I am thankful to those who have directly or indirectly helped me to finish my dissertation study. It is not possible to mention all of them; nonetheless, I wish to acknowledge their contribution to this work.

**Pallavi Verma**

**(2k16/Ph.D./EE/22)**

# ABSTRACT

With the depletion of non-renewable resources and growing public awareness about the advantages of green energy, alternative renewable sources are evolving as a significant source of energy since past few years. Furthermore, the electrical grid is on the verge of a paradigm shift, from centralized power generation, transmission, and huge power grids towards distributed generation (DG). DG fundamentally uses small-scale generators like photovoltaic (PV) panels, wind turbine, fuel cells, small and micro hydropower, diesel generator set, etc., and is limited to small distribution networks to produce power close to the end users. Renewable energy sources (RES) are essential components of DG because they are more environment friendly than conventional power generators and once established maintenance cost is also low. One of the most popular renewable energy source is solar energy because it is abundant, accessible and can be easily converted into electricity. The electricity produced from SPV system can be utilized by the local loads within the microgrid or it can be integrated with conventional grid.

Microgrid (MG), which is a cluster of distributed generation, renewable sources, and local loads connected to the utility grid provides solution to manage local generations and loads as a single grid level entity. It has the potential to maximize overall system efficiency, power quality, and energy surety for critical loads. A microgrid can operate either in stand-alone mode or grid connected mode. Due to abundant availability of solar energy, an SPV based microgrid is widely used around the world. Due to intermittent nature of solar energy, stand-alone SPV based microgrid needs an energy storage system also, whereas in grid connected system, the microgrid is connected to conventional grid which takes care of the solar intermittency by having bi-directional flow of power. Depending on the technical specifications, grid-connected solar PV-based microgrid can be single-stage or double-stage. In single stage configuration, PV array is directly connected to a DC/AC converter whereas in double-stage configuration, DC/DC converter is coupled in between the solar PV array and PV inverter and provides the desired fixed DC voltage to the inverter.

The present work aims at modelling, design, development and control of a solar PV

based microgrid for enhanced performance. Also, the characterization studies of the developed system have been carried out. Modeling of the system is required in order to predict its behaviour under both steady and dynamic states. Characterization studies such as sensitivity and reliability analysis are used to evaluate the performance of the system. Sensitivity analysis is the performance evaluation technique for evaluating the change in the system's performance with respect to the change in its parameters. The sensitivity functions for solar cell and boost converter with respect to influential parameters have been developed using first derivative of Taylor's series. Reliability analysis for electrical and electronic components of the system have been performed using pareto analysis and reliability model of the PV based microgrid has been developed using reliability block diagram for different PV array configurations. The Fault tree analysis (FTA) model of the system has been developed to find the cause of failure and to step the events leading to failure serially. Further, Markov's model has been used to develop the reliability functions of individual components and hence, the reliability of complete grid connected PV system has been calculated.

Solar PV system gives maximum power under uniform shading. But many a times PV panels are non-uniformly irradiated and this condition is known as called partial shading condition (PSC). PSC occur due to shadow of big trees, nearby buildings and dense clouds etc. PSC in PV system is an inevasible situation and exhibits multiple peaks, consisting of a single global maximum power point and many local maximum power points, in its power-voltage curve. PSC makes tracking of global maximum power point more difficult and also reduces the efficiency of the system. The conventional MPPT control algorithms work well under uniform shading condition but under partial shading scenario, they may not be able to track global peak out of multiple peaks. Therefore, an efficient controller is required to overcome the raised issue. Further, various PV array configurations such as series, series-parallel, total cross tied, bridge linked etc. may be used to improve the system efficiency. In the present work, novel maximum power point control algorithms viz. an asymmetrical fuzzy logic control (AFLC) and asymmetrical interval type-2 FLC (AIT-2 FLC) are developed for stand-alone PV system under partial shading condition. The developed algorithms are tested for different PV array configurations.

In stand-alone PV system, the power supplied to the load depends upon the available solar energy. The output of SPV is intermittent in nature as it depends on the environmental conditions. This intermittency problem can be addressed by adding an energy storage system along with PV system. Battery is the most commonly used energy storage device and is very pivotal in maintaining continuity of power to the load. But when two or more energy sources are connected, then control of dc link voltage at common coupling point (CCP) is an area of concern. Therefore, in a SPV system with BESS a controller is required which can maintain constant DC link voltage irrespective of system transients. The PI controller is commonly used controller for controlling dc-link voltage, but it cannot regulate DC-link voltage under dynamic operating conditions and have overshoots and long settling time in its response. Suitable intelligent controllers are designed to replace the conventional PI controller, as they provide a better transient response. In order to overcome the drawbacks of the conventional PI control algorithm, nonlinear autoregressive moving average-L2 (NARMA-L2) control algorithm is proposed and developed for the stand-alone PV system with BESS. The proposed control scheme maintains the voltage across DC-link under change in irradiation and load condition.

In a grid connected SPV based microgrid, the output of boost converter i.e., DC link is connected to voltage source inverter which is connected to grid at the point of common coupling (PCC). Voltage source inverter converts the generated DC power from PV system to AC of required voltage and frequency, as well as maintains the balance of power between the SPV system, load, and grid. The inverter is regulated by the interfacing controllers for effective operation and grid synchronization. The interfacing controllers are used to control the output of PV inverter for its efficient utilization and for improving power quality at PCC by providing reactive power compensation, harmonics compensation and load balancing. Conventional control algorithm like synchronous reference frame theory (SRFT) uses proportional integral (PI) controller for DC-link voltage regulation. These controllers are not best suited for SPV based microgrid as the overshoots and long settling time in their response are inevitable. In order to overcome this, novel smooth Least Mean Square (SLMS), improved zero attracting LMS (IZALMS) and reweighted $L_0$ norm variable step size continuous mixed p-norm ($RL_0$-VSSCMPN) based adaptive interfacing control algorithms are proposed

and developed for the PV based microgrid. The efficacy of the proposed control algorithms has been tested on hardware prototype developed in the laboratory using MicroLab box (dSPACE 1202). The developed prototype system acts as distribution static compensator (DSTATCOM) and consists of inverter that is tied in parallel to the grid at the point of common coupling. FLUKE power analyzer has been used to measure the response of the system.

The research work presented in the thesis is expected to provide good exposure to design, development and control of the solar PV based microgrid.

# CONTENTS


| | | |
|---|---|---|
| COVER PAGE | | i |
| DECLARATION | | ii |
| CERTIFICATE | | iii |
| ACKNOWLEDGEMENT | | iv |
| ABSTRACT | | vi |
| TABLE OF CONTENTS | | x |
| LIST OF FIGURES | | xvi |
| LIST OF TABLES | | xxiii |
| LIST OF ABBREVIATIONS | | xxiv |
| LIST OF SYMBOLS | | xxvi |
| **CHAPTER-1** | **INTRODUCTION** | **1-9** |
| 1.1 | Introduction | 1 |
| 1.2 | Solar PV based microgrid | 2 |
| | 1.2.1 Stand-alone SPV microgrid | 2 |
| | 1.2.2 Grid connected SPV based microgrid | 3 |
| 1.3 | Characterization studies of solar PV based microgrid | 4 |
| | 1.3.1 Sensitivity Analysis | 4 |
| | 1.3.2 Reliability Analysis | 5 |
| 1.4 | Maximum Power Point Tracking Control Algorithm Under PSC | 5 |
| 1.5 | DC Link Voltage Regulation of Stand-Alone PV System with BESS | 6 |
| 1.6 | PV inverter control algorithm for grid tied solar PV system | 6 |
| 1.7 | Motivation and Research Objectives | 6 |
| 1.8 | Problem Identification | 7 |
| 1.9 | Organization of Thesis | 8 |
| 1.10 | Concluding Remarks | 9 |
| **CHAPTER-2** | **LITERATURE REVIEW** | **10-18** |
| 2.1 | Introduction | 10 |

2.2 Solar PV based microgrid 10
2.2.1 Modelling and Design of Grid-tied SPV based Microgrid 11
2.3 Sensitivity and reliability studies of grid-tied SPV based microgrid 11
2.3.1 Sensitivity Analysis 11
2.3.2 Reliability Analysis 12
2.4 MPPT control algorithm under partial shading condition 13
2.5 DC Link Voltage Control of Stand-Alone PV System with BESS 15
2.6 PV inverter control algorithm for grid-tied PV based microgrid 16
2.7 Identified research areas 18
2.8 Concluding Remarks 18

**CHAPTER-3 MODELLING AND DESIGN OF SOLAR PV BASED MICROGRID AND ITS CHARACTERIZATION STUDIES 19-47**

3.1 Introduction 19
3.2 Design and modelling of stand-alone Solar PV system 20
3.2.1 PV array 20
3.2.1.1 PV Array Configuration 22
3.2.2 Design of boost converter 24
3.2.3 Maximum Power Point Tracking 24
3.2.3.1 Perturb and Observe (P&O) Algorithm 25
3.2.3.2 Incremental Conductance (INC) Algorithm 26
3.2.4 Design of Inverter 28
3.3 Design and modelling of Grid tied Solar PV system 28
3.3.1 PV array 29
3.3.2 Design of boost converter 29
3.3.3 DC Link Voltage 29
3.3.4 DC Link Capacitor 29
3.3.5 Interfacing Inductors 30
3.3.6 Design of Inverter 30
3.4 Characterization studies of solar PV based microgrid 30
3.4.1 Sensitivity Analysis 30

3.4.2 Numerical results and Analysis 32
3.4.3 Reliability analysis 34
3.4.3.1 Component Reliability 34
3.4.3.2 Reliability calculation of different PV array configuration 36
3.4.3.3 Reliability of SPV based microgrid 39
3.4.3.4 Numerical results and Analysis 41
3.4.3.5 Fault Tree Analysis Model 42
3.4.3.6 Markov Reliability Model 43
3.5 Concluding Remarks 47

**CHAPTER-4 MPPT CONTROL ALGORITHMS FOR SOLAR PV SYSTEM UNDER PARTIAL SHADING CONDITION 48-72**

4.1 Introduction 48
4.2 MPPT control algorithms for partial shading condition 48
4.2.1 Adaptive control algorithm 50
4.2.2.1 Adaptive neuro fuzzy inference system control algorithm 50
4.2.2 Intelligent control algorithm 52
4.2.2.1 Proposed Asymmetrical FLC algorithm 52
4.2.2.2 Proposed Asymmetrical Interval Type-2 (AIT-2 FLC) FLC algorithm 56
4.3 Results and Discussions 58
4.3.1 Performance evaluation of ANFIS based MPPT control algorithm under PSC 59
4.3.1.1 Under steady state condition 59
4.3.1.2 Under dynamic change in irradiation level 61
4.3.2 Performance evaluation of proposed asymmetrical fuzzy logic control algorithm under PSC 62
4.3.2.1 Under steady state conditions 62
4.3.2.2 Under dynamic change in irradiation level 64
4.3.3 Performance evaluation of proposed asymmetrical interval 65

type-2 fuzzy logic control algorithm under PSC
4.3.3.1 Under steady state conditions 65
4.3.3.2 Under dynamic change in irradiation level 66
4.4 Concluding Remarks 71

**CHAPTER-5 DC LINK VOLTAGE CONTROL OF STAND-ALONE PV SYSTEM WITH BATTERY ENERGY STORAGE SYSTEM 73-90**

5.1 Introduction 73
5.2 Design and modelling of stand-alone PV system with BESS 73
5.2.1 Modelling of Battery 73
5.2.2 Bidirectional dc-dc converter 75
5.3 Control Algorithm for DC Link Voltage Control of Stand-Alone PV System with BESS 77
5.3.1 Proportional Integral algorithm 77
5.3.2 Nonlinear Autoregressive Moving Average algorithm 78
5.3.3 Nonlinear Autoregressive Moving Average-L2 algorithm 79
5.4 Results and Discussions 80
5.4.1 Proportional Integral control algorithm 80
5.4.1.1 System performance with linear load 80
5.4.1.2 System performance with non-linear load 82
5.4.2 Nonlinear Autoregressive Moving Average-L2 control algorithm 84
5.4.2.1 System performance with linear load 84
5.4.2.2 System performance with non-linear load 86
5.4.3 Comparison of proposed NARMA-L2 algorithm with PI controller 88
5.5 Concluding Remarks 90

**CHAPTER-6 PV INVERTER CONTROL ALGORITHM FOR GRID-TIED SOLAR PV BASED MICROGRID 91-132**

6.1 Introduction 91

6.2 System Description 91
6.3 PV inverter control algorithms 92
6.3.1 Synchronous reference frame theory-based conventional control algorithm 93
6.3.2 Unit Template based convention control algorithm 94
6.3.3 Least Mean Square (LMS) based Adaptive Control Algorithm 95
6.3.4 Proposed smooth LMS based adaptive control algorithm 98
6.3.5 Proposed improved zero attracting LMS based control algorithm 99
6.3.6 Proposed reweighted $L_0$ norm variable step size continuous mixed p-norm algorithm 101
6.4 Results and Discussions (MATLAB/Simulink) 103
6.4.1 Smooth LMS Control Algorithm 103
6.4.1.1 System performance with linear load under load variation and irradiation variation 103
6.4.1.2 System performance with non-linear load 105
6.4.2 Improved Zero Attracting LMS Control Algorithm 108
6.4.2.1 System performance with linear load under load variation and irradiation variation 108
6.4.2.2 System performance with non-linear load 109
6.4.3 $RL_0$-VSSCMPN Control Algorithm 112
6.4.3.1 System performance with linear load under load variation and irradiation variation 112
6.4.3.2 System performance with non-linear load 113
6.4.4 Comparison of Proposed Control Algorithms with Other Control Algorithms 116
6.4.4.1 Total Harmonics Distortion (THD) 116
6.4.4.2 Weight convergence and dc-offset rejection capability 118
6.5 Hardware Implementation and Parameter selection 119
6.5.1 Choice of DC-link voltage 119
6.5.2 Sizing of DC-Link capacitor 120

6.5.3 Interfacing Inductors 120
6.6 Results and Discussions (Experimental Realization) 120
6.6.1 Smooth LMS Control Algorithm 120
6.6.1.1 System performance with linear load under load variation 120
6.6.1.2 System performance with non-linear load 121
6.6.2 Improved Zero Attracting LMS Control Algorithm 123
6.6.2.1 System performance with linear load under load variation 123
6.6.2.2 System performance with non-linear load 123
6.6.3 $RL_0$-VSSCMPN Control Algorithm 126
6.6.3.1 System performance with linear load under load variation 126
6.6.3.2 System performance with non-linear load 128
6.6.4 Comparison of Proposed Control Algorithms with Other Control Algorithms 130
6.6.4.1 Total Harmonics Distortion 130
6.6.4.2 Weight convergence 131
6.7 Concluding Remarks 131

**CHAPTER-7 CONCLUSIONS AND SCOPE FOR FURTHER WORK 133-136**

7.1 Introduction 133
7.2 Main Conclusions 134
7.3 Suggestions for Further Work 136

**REFERENCES 138-152**
**APPENDICES 153-158**
**LIST OF PUBLICATIONS 159-160**

# LIST OF FIGURES


| Figure | Description | Page No. |
|---|---|---|
| 1.1 | Pie Chart of renewable energy source wise power (GW) installed capacity in India as on 31-07-2021 | 1 |
| 1.2 | Block Diagram of stand-alone PV system with BESS | 2 |
| 1.3 | Block diagram of two-stage three-phase grid-tied PV based microgrid | 3 |
| 3.1 | Schematic Diagram of stand-alone PV system | 20 |
| 3.2 | Formation of PV array from PV cell | 20 |
| 3.3 | Equivalent circuit of single diode PV cell | 21 |
| 3.4 | Current vs Voltage and Power vs Voltage curve of Solar PV system | 22 |
| 3.5 | Schematic diagram of various PV array configuration | 23 |
| 3.6 | Equivalent circuit of Boost Converter | 24 |
| 3.7 | Flowchart for Perturb and Observe MPPT algorithm | 25 |
| 3.8 | Block Diagram of the P&O algorithm | 26 |
| 3.9 | Flowchart for INC MPPT algorithm | 27 |
| 3.10 | Block diagram of the INC algorithm | 27 |
| 3.11 | Equivalent circuit of three-phase voltage source inverter | 28 |
| 3.12 | Schematic Diagram of SPV system connected to Grid | 28 |
| 3.13 | Sensitivity graphs for (a) Photoncurrent and (b) Boost converter output voltage. | 33 |
| 3.14 | Pareto Analysis of (a) Electronic components and (b) Electrical Components | 36 |
| 3.15 | Reliability calculation of (a) Series PV array configuration and (b) Parallel PV array configuration | 37 |
| 3.16 | Reliability calculation of Series-Parallel PV array configuration | 37 |
| 3.17 | Reliability calculation of Total Cross Tied PV array configuration | 38 |
| 3.18 | Reliability calculation of Bridge linked PV array configuration | 38 |
| 3.19 | Reliability calculation of Honey comb PV array configuration | 39 |

| | | |
|---|---|---|
| 3.20 | Reliability block diagram of stand-alone PV based microgrid | 39 |
| 3.21 | Reliability block diagram of stand-alone PV based microgrid with BESS | 40 |
| 3.22 | Reliability block diagram of grid interfaced SPV based microgrid with BESS | 40 |
| 3.23 | 3-D Reliability curve of grid interfaced PV based microgrid with BESS considering stress factor. | 41 |
| 3.24 | FTA model of grid interfaced PV based microgrid with BESS | 42 |
| 3.25 | Markov state transition diagram of (a) PV array (b) Boost Converter (c) PV inverter (d) Battery | 44 |
| 3.26 | Markov state transition diagram of (a) Grid interfaced PV based microgrid with BESS (b) Grid interfaced PV based microgrid with BESS considering repair rate | 46 |
| 4.1 | Simulated Power vs. Voltage curve under partial shading condition | 49 |
| 4.2 | (a) Training error v/s Epoch waveform for ANFIS (b) Training Data and FIS output v/s index waveform. | 50 |
| 4.3 | 3-D surface view representation between two inputs (irradiation and temperature) and one output (Power) generated by ANFIS | 51 |
| 4.4 | Structure of ANFIS | 52 |
| 4.5 | Membership functions for input variable ‘Error’, ‘Error Change’ and Output variable ‘Duty Ratio’ for Asymmetrical FLC | 54 |
| 4.6 | 3-D surface view representation between two inputs (error and change in error) and output (duty ratio) generated by AFLC for the proposed PV system | 55 |
| 4.7 | Block diagram of asymmetrical FLC based control algorithm for MPPT | 55 |
| 4.8 | (a) Type-1 FLC and (b) Blurring of type-1 membership function | 56 |
| 4.9 | Membership functions of (a) Error (E) (b) Change in Error (ΔE) | 57 |
| 4.10 | Block Diagram of Interval type-2 fuzzy logic based MPPT algorithm under PSC | 58 |
| 4.11 | Various shading scenarios under STC and PSC | 58 |
| 4.12 | Schematic Diagram of various PV array configurations | 59 |

| | | |
|---|---|---|
| 4.13 | Dynamic change in insolation level for EN 50530 standard MPPT efficiency test | 59 |
| 4.14 | Power vs. Time plot for ANFIS MPPT technique with different PV array arrangements under STC (case 1) | 60 |
| 4.15 | Power vs. Time plot for ANFIS MPPT technique with different PV array arrangements under Left corner shading (case 2) | 60 |
| 4.16 | Power vs. Time plot for ANFIS MPPT technique with different PV array arrangements under Top shading (case 3) | 61 |
| 4.17 | Power vs. Time plot for ANFIS MPPT technique with different PV array arrangements under Patch Shading (case 4) | 61 |
| 4.18 | Power vs. Time plot for ANFIS MPPT technique with different PV array arrangements under dynamic change in irradiation level | 62 |
| 4.19 | Power vs. Time plot for AFLC MPPT technique with different PV array arrangements under STC (case 1) | 62 |
| 4.20 | Power vs. Time plot for AFLC MPPT technique with different PV array arrangements under Left corner shading (case 2) | 63 |
| 4.21 | Power vs. Time plot for AFLC MPPT technique with different PV array arrangements under Top shading (case 3) | 63 |
| 4.22 | Power vs. Time plot for AFLC MPPT technique with different PV array arrangements under Patch Shading (case 4) | 64 |
| 4.23 | Power vs. Time plot for Asymmetrical FLC MPPT technique with different PV array arrangements under dynamic change in irradiation level | 64 |
| 4.24 | Power vs. Time plot for IT-2 FLC MPPT technique with different PV array arrangements under STC (case 1) | 65 |
| 4.25 | Power vs. Time plot for IT-2 FLC MPPT technique with different PV array arrangements under Left corner shading (case 2) | 65 |
| 4.26 | Power vs. Time plot for IT-2 FLC MPPT technique with different PV array arrangements under Top shading (case 3) | 66 |
| 4.27 | Power vs. Time plot for IT-2 FLC MPPT technique with different PV array arrangements under Patch Shading (case 4) | 66 |
| 4.28 | Power vs. Time plot for Asymmetrical interval type-2 FLC MPPT | 68 |

| | | |
|---|---|---|
| | technique with different PV array arrangements under dynamic change in irradiation level | |
| 5.1 | Schematic Diagram for DC link voltage control of stand-alone PV system with BESS | 74 |
| 5.2 | Equivalent circuit diagram of battery | 74 |
| 5.3 | Discharge characteristics of the battery | 75 |
| 5.4 | Bidirectional converter in buck-boost mode | 76 |
| 5.5 | Block diagram for controlling dc link voltage of stand-alone PV system with BESS using PI controller | 78 |
| 5.6 | Block diagram for controlling dc link voltage of stand-alone PV system with BESS using NARMA-L2 controller | 79 |
| 5.7 | Performance under variable irradiation condition with PI controller | 80 |
| 5.8 | Performance under variable load conditions with PI controller | 81 |
| 5.9 | Performance under variable irradiation condition with PI controller | 82 |
| 5.10 | Performance under variable load condition with PI controller | 83 |
| 5.11 | Performance under variable irradiation condition with NARMA-L2 Controller | 84 |
| 5.12 | Performance under variable load conditions with NARMA-L2 Controller | 85 |
| 5.13 | Performance under variable irradiation condition with NARMA-L2 Controller | 86 |
| 5.14 | Performance under variable load condition with NARMA-L2 controller | 87 |
| 5.15 | DC bus voltage ($V_{dc}$) comparison of NARMA-L2 with PI control algorithm (a) Irradiation Variation (b) Load Variation | 88 |
| 6.1 | Schematic Diagram of Grid interfaced SPV system | 92 |
| 6.2 | Block diagram of control scheme for SRF theory based conventional control algorithm | 93 |
| 6.3 | Block diagram of control scheme for Unit template based conventional control algorithm | 95 |
| 6.4 | Block Diagram of LMS based adaptive control algorithm | 96 |
| 6.5 | Block Diagram of Smooth LMS Control Algorithm | 98 |

| | | |
|---|---|---|
| 6.6 | Block Diagram of improved zero attracting control algorithm | 100 |
| 6.7 | Block Diagram of Reweighted $L_0$ VSS-CMPN control algorithm | 102 |
| 6.8 | System performance with linear load under load variation and irradiation variation (a) waveform of solar irradiation ($I_{rr}$), output power of SPV system ($P_{PV}$), Three phase waveform of grid voltage ($V_g$), load current ($I_L$), source current (Is) and grid current ($I_g$), and voltage at DC bus ($V_{dc}$) (b) Active and reactive power of grid, load and source | 104 |
| 6.9 | System performance with non-linear load under load/irradiation variation) (a) Three phase waveform of grid voltage ($V_g$), load current ($I_L$), source current ($I_s$) and grid current ($I_g$), and voltage at DC bus ($V_{dc}$) (b) Active power of load, source and grid | 105 |
| 6.10 | System performance with unbalanced non-linear load | 106 |
| 6.11 | System performance with non-linear load under unbalanced grid | 107 |
| 6.12 | System performance with non-linear load under grid voltage swell and sag | 107 |
| 6.13 | System performance with linear load under load variation and irradiation variation (a) waveform of solar irradiation ($I_{rr}$), output power of SPV system ($P_{PV}$), Three phase waveform of grid voltage ($V_g$), load current ($I_L$), source current ($I_s$) and grid current ($I_g$), and voltage at DC bus ($V_{dc}$) (b) Active and reactive power of load, source and grid. | 108 |
| 6.14 | System performance with non-linear load under load/irradiation variation) (a) Three phase waveform of grid voltage ($V_g$), load current ($I_L$), source current ($I_s$) and grid current ($I_g$), and voltage at DC bus (b) Active power of load, source and grid. | 110 |
| 6.15 | System performance with unbalanced non-linear load | 111 |
| 6.16 | System performance with non-linear load under unbalanced grid | 111 |
| 6.17 | System performance with non-linear load under grid voltage swell and sag | 112 |
| 6.18 | System performance with linear load under load variation and irradiation variation (a) waveform of solar irradiation ($I_{rr}$), output | 113 |

| | | |
|---|---|---|
| | power of SPV system ($P_{PV}$), Three phase waveform of grid voltage ($V_g$), load current ($I_L$), source current ($I_s$) and grid current ($I_g$), and voltage at DC bus ($V_{dc}$) (b) Active and reactive power of load, source and grid. | |
| 6.19 | System performance with non-linear load under load/irradiation variation) (a) Three phase waveform of grid voltage ($V_g$), load current ($I_L$), source current ($I_s$) and grid current ($I_g$), and voltage at DC bus (b) Active power of load, source and grid | 114 |
| 6.20 | System performance with unbalanced non-linear load | 115 |
| 6.21 | System performance with non-linear load under unbalanced grid | 115 |
| 6.22 | System performance with non-linear load under grid voltage swell and sag | 116 |
| 6.23 | Comparison of proposed control schemes with other control algorithms in terms of THD | 117 |
| 6.24 | Comparison of proposed $RL_0$-VSSCMPN control scheme with LMS, Smooth LMS and IZALMS | 118 |
| 6.25 | Hardware setup | 119 |
| 6.26 | System performance with (a) Steady linear load (b) variable linear load condition | 121 |
| 6.27 | Grid Power (a) Before Compensation and (b)After Compensation (c) increased load | 121 |
| 6.28 | System performance with non-linear load | 122 |
| 6.29 | System performance with variable non-linear load condition | 122 |
| 6.30 | System performance with unbalanced grid voltage condition | 123 |
| 6.31 | System performance with voltage sag and swell in grid voltage | 123 |
| 6.32 | System performance with (a) Steady linear load (b) variable linear load condition | 124 |
| 6.33 | Grid Power (a) Before Compensation and (b)After Compensation (c) increased load | 124 |
| 6.34 | System performance with non-linear load | 124 |
| 6.35 | System performance with variable non-linear load condition | 124 |
| 6.36 | System performance with unbalanced grid voltage condition | 126 |

| | | |
|---|---|---|
| 6.37 | System performance with voltage sag and swell in grid voltage | 126 |
| 6.38 | System performance with linear load | 127 |
| 6.39 | (a) System performance with varying linear load and Grid Power (b) Before Compensation and (c) After Compensation (d) increased load | 127 |
| 6.40 | System performance with non-linear load | 128 |
| 6.41 | System performance with varying non- linear load | 129 |
| 6.42 | System performance with unbalanced grid voltages | 129 |
| 6.43 | System performance with grid voltage sag and voltage swell | 130 |
| 6.44 | THD analysis under non-linear load: (a) Load Current (b) Grid Current (Smooth LMS) (c) Grid Current (IZALMS) (d) Grid Current ($RL_0$-VSSCMPN) | 130 |
| 6.45 | Smooth LMS, IZALMS and RL0-VSSCMPN comparison with LMS control algorithm in terms of weight convergence | 131 |

# LIST OF TABLES


| Table | Description | Page No. |
|---|---|---|
| 3.1 | Operation of the P&O Algorithm | 26 |
| 3.2 | Sensitivity function and its values of solar cell and boost converter | 32 |
| 3.3 | Failure rate and MTBF of Electronics components | 35 |
| 3.4 | Failure rate and MTBF of Electrical components | 35 |
| 3.5 | Reliability of different PV array configuration | 39 |
| 3.6 | Reliability of stand-alone and PV based microgrid with BESS | 41 |
| 4.1 | Fuzzy rule base for computing output variable 'Duty ratio' | 54 |
| 4.2 | Fuzzy rule base for computing output variable 'Duty ratio' | 57 |
| 4.3 | GMPP (W) tracking by various MPPT techniques under study with different PV array arrangements | 67 |
| 4.4 | Dynamic response of various MPPT techniques | 68 |
| 4.5 | Shading loss (W) in various MPPT techniques under study with different PV array arrangements | 69 |
| 4.6 | Mismatch losses (%) in various MPPT techniques under study with different PV array arrangements | 70 |
| 4.7 | Fill Factor in various MPPT techniques under study with different PV array arrangements | 70 |
| 4.8 | Efficiency (%) of various MPPT techniques under study with different PV array arrangements | 71 |
| 5.1 | (a) Comparison of dc link voltage of NARMA-L2 control algorithm with PI controller with irradiation variation (b) Comparison of dc-link voltage of NARMA-L2 control algorithm with PI controller with load variation | 89 |
| 6.1 | THD of proposed control algorithms and all other control algorithms | 118 |

# LIST OF ABBREVIATIONS

| | |
|---|---|
| AFLC | Asymmetrical FLC |
| ANFIS | Adaptive Neuro-Fuzzy Inference System |
| BESS | Battery Energy Storage System |
| BL | Bridge Linked |
| CCP | Common Coupling Point |
| DG | Distributed Generation |
| DSO | Digital Storage Oscilloscope |
| DSTATCOM | Distribution Static Compensator |
| FLC | Fuzzy Logic Controller |
| FTA | Fault Tree Analysis |
| GMPP | Global Maximum Power Point |
| HC | Honey Comb |
| HCC | Hysteresis Current Control |
| IGBT | Insulated-Gate Bipolar Transistor |
| INC | Incremental Conductance |
| IT-2 | Interval Type-2 FLC |
| IZALMS | Improved Zero Attracting LMS |
| LMF | Least Mean Fourth |
| LMPP | Local Maximum Power Point |
| LMS | Least Mean Square |
| MOSFET | Metal–Oxide–Semiconductor Field-Effect Transistor |
| MPP | Maximum Power Point |
| MPPT | Maximum Power Point Tracking |
| MTBF | Mean Time Between Failure |
| MTTR | Mean Time To Repair |
| NARMA-L2 | Nonlinear Autoregressive Moving Average-L2 |
| P&O | Perturb And observe |
| PCC | Point Of Common Coupling |
| PFC | Power Factor Correction |

| | |
|---|---|
| PI | Proportional Integral |
| PLL | Phase-Locked Loop |
| PQ | Power Quality |
| PSC | Partial Shading Condition |
| PWM | Pulse Width Modulation |
| RBD | Reliability Block Diagram |
| RES | Renewable Energy Sources |
| $RL_0$-VSSCMPN | Reweighted $L_0$ Norm Variable Step Size Continuous Mixed P-Norm |
| RMS | Root Mean Square |
| SLMS | Smooth Least Mean Square |
| SoC | State Of Charge |
| SP | Series-Parallel |
| SPV | Solar Photo Voltaic |
| SPVGS | Solar Photovoltaic Generating System |
| SRFT | Synchronous Reference Frame |
| STC | Standard Test Condition |
| TCT | Total Cross Tied |
| THD | Total Harmonic Distortion |
| UPF | Unity Power Factor |
| USC | Uniform Shading Condition |
| VSI | Voltage Source Inverter |

# LIST OF SYMBOLS

| | |
|---|---|
| $\hat{S}_n^F$ | Normalized Sensitivity of function 'F' with respect to 'n' |
| $J_{o_{Pi}}^F$ | Jacobian matrix |
| $I_{o/p(PVCell)}$ | Output current of the PV cell |
| $I_{cs}$ | Photon current |
| $I_d$ | Diode current |
| $I_{sh}$ | Reverse saturation current |
| $I_o$ | Diode saturation current of a PV cell |
| $q$ | Elementary charge ($1.602*10^{-19}$ C) |
| $A$ | Ideal factor of the PV cell |
| $k$ | Boltzmann constant ($1.38*10^{-23}$ J) |
| $T$, $T_{ref}$ | Actual and reference operating temperature |
| $s$, $p$ | Number of cells in series and parallel |
| $H$, $H_{ref}$ | Solar insolation and reference solar insolation ($1000W/m^2$) |
| $R_s$ , $R_{sh}$ | Series resistance and shunt resistance (Ω) of solar cell |
| $V_{o/p}$ | Output voltage of PV array |
| $I_{scc}$ | Short circuit current of PV cell |
| $V_{oc}$ | Open circuit voltage of PV cell |
| $L$ | Inductance of boost converter |
| $C$ | Capacitance of boost converter |
| $\alpha$ | Duty ratio |
| $V_{i/p}$ | Input voltage of boost converter, |
| $V_o$ | Output voltage of boost converter |
| $\Delta I$ | Output ripple current of boost converter |
| $f_{sw}$ | Switching frequency of boost converter |
| $\Delta V$ | Peak ripple voltage of boost converter |
| $V_{dc}$ | DC link voltage |
| $V_{LL}$ | RMS value of three phase ac side voltage |
| $m$ | Modulation index |

| | |
|---|---|
| $C_{dc}$ | DC-link capacitor |
| $I_M$ | PV array current at maximum power |
| $\omega$ | Grid frequency |
| $V_{dcripple}$ | Ripple in dc link voltage |
| $L_f$ | Interfacing inductors |
| $\Delta i$ | Current ripple taken as 10 % of inverter current |
| $h$ | Overload factor |
| $\lambda$ | Failure rate |
| $\lambda_p$ | Actual failure rate |
| $\lambda_b$ | Manufacturer failure rate |
| $\mu_i$ | Product of all stress factors of electronics components |
| $R_i$ | Reliability |
| $\lambda_{sys}$ | Failure rate of a system |
| $\lambda_{inco}$ | Failure rate of individual component |
| $R_{series}$ | Reliability with components connected in series |
| $R_{parallel}$ | Reliability with components connected in parallel |
| $S_{ij}$ | Transition probability |
| Q | Transition probability matrix |
| $\overrightarrow{S}$ | Probability vector |
| $\upsilon$ | Repair rate |
| $P_{o/p}$ | Output power of the PV system |
| $I_{o/p}$ | Output current of the PV system |
| $E_r$ | Error obtained from sensed voltage and current of PV array |
| $\Delta E_r$ | Change in error obtained from sensed voltage and current of PV array |
| $z_o$ | Defuzzifier |
| $x$ | Aggregate output of fuzzy controller |
| $\mu x_i$ | Activation degree on rule 'i' of fuzzy controller |
| $x_i$ | Center of the Max-Min composition of the output membership functions of fuzzy controller |
| $\tilde{A}$ | AIT-2 FLC set |

| | |
|---|---|
| $P_{MP,\ shadinglosses}$ | PV power loss due to shading |
| $P_{mml}$ | Mismatch loss in PV array |
| $P_{mpi}$ | PV array individual maximum power |
| $P_{GMPP}$ | PV array global maximum power |
| $\eta_{MPPT}$ | MPPT tracking efficiency |
| $V_{bat}$ | Actual voltage of the battery |
| $E_{con}$ | Controlled battery voltage |
| $R_b$ | Battery internal resistance |
| $i$ | Battery current |
| $Q_{bat}$ | Battery capacity |
| K | Polarization constant |
| $K_P, K_i$ | Coefficients for the proportional, integral terms respectively |
| $Y_{(k)}$, $U_{(k)}$ | Input and output of the system for NARMA-L2 controller |
| d | Relative degree for NARMA-L2 controller |
| $f$ and $g$ | Two sub-functions for NARMA-L2 controller |
| $i_{loss}$ | Loss component of PV inverter |
| $v_e$ | Voltage error signal |
| $i_d^*$ | Reference active component of supply current |
| $i_d$ | Fundamental DC current component of load current |
| $V_t$ | Peak value of per phase PCC voltage |
| $U_{aa}$, $U_{ab}$, $U_{ac}$, $U_{\text{ra}}$, $U_{\text{rb}}$, $U_{\text{rc}}$ | In-phase unit template, reactive unit templates |
| $i_{ga}^*$, $i_{gb}^*$, $i_{gc}^*$ | Instantaneous values of reference grid currents |
| $V_a$, $V_b$, $V_c$ | Sensed grid voltages |
| $i_{la}$, $i_{lb}$, $i_{lc}$ | Load current |
| $\varrho$ | Step size for LMS algorithm |
| $w(i)$ | Weight component at $i^{th}$ instant of LMS algorithm |
| $e(i)$ | Estimated error signal of LMS algorithm |
| $\psi_1$ and $\psi_2$ | Decaying sequence of Smooth LMS algorithm |
| $G$ | Smoothing gradient of Smooth LMS algorithm |

| | |
|---|---|
| $\varrho_v$ | Variable step size for IZALMS algorithm |
| $Q$ | Zero-attractor controller which decide the strength of attraction |
| $sgn(w(i))$ | Sgn function |
| $C_{RL_0}$ | Cost function with reweighted $L_0$ norm function |
| $\lambda_i$ | Probability density-like weighting function of $RL_0$-VSSCMPN |
| $\gamma$ | Regularization parameter of $RL_0$-VSSCMPN |
| $\|.\|_0$ | $L_0$ norm of $RL_0$-VSSCMPN |
| $f_\beta$ | Threshold parameter of $RL_0$-VSSCMPN |
| $\lambda_i$ | Variable step size of $RL_0$-VSSCMPN |
| $ln$ | Natural logarithm value of $RL_0$-VSSCMPN |
| $I_{rr}$ | Solar irradiation |
| $P_{PV}$ | Output power of SPV system |
| $V_g$ | Grid voltage |
| $I_L$ | Load current |
| $I_s$ | Source i.e., inverter current |
| $I_g$ | Grid current |
| $P_L$, $P_s$, $P_g$ | Active power of load, source and grid |
| $Q_L$, $Q_s$, $Q_g$ | Reactive power of load, source and grid |

# CHAPTER-I

# INTRODUCTION

## INTRODUCTION

Electrical energy is the most convenient form of energy and in modern times it is unthinkable to imagine life without electricity. As the daily needs are increasing, so is the need of electrical energy. In recent years, the increased concern for environment and the adverse impact due to burning of conventional fossil fuels has led to the utilization of renewable resources, along with existing system, to fulfill the energy demand. Renewable energy sources (RES) such as solar, wind, geothermal, tidal, hydrogen energy etc. can be used for the generation of electrical energy [1]–[6].

In standalone mode, renewable energy is an appropriate, scalable and viable solution for providing power to un-electrified or power deficient villages and hamlets. Renewable energy sources are gradually evolving as a sustainable and economical solution to meet the electricity demand. Figure 1.1 shows the source wise renewable energy installed capacity in India as on 31-07-2021 and estimated renewable energy potential from commercially exploitable sources viz. Solar power 44 GW, wind – 39.5 GW; small hydro – 4.8 GW; bioenergy–10.6 GW. One of the most popular renewable energy sources is solar energy because of technological advancements, abundant availability and satisfactory performance.

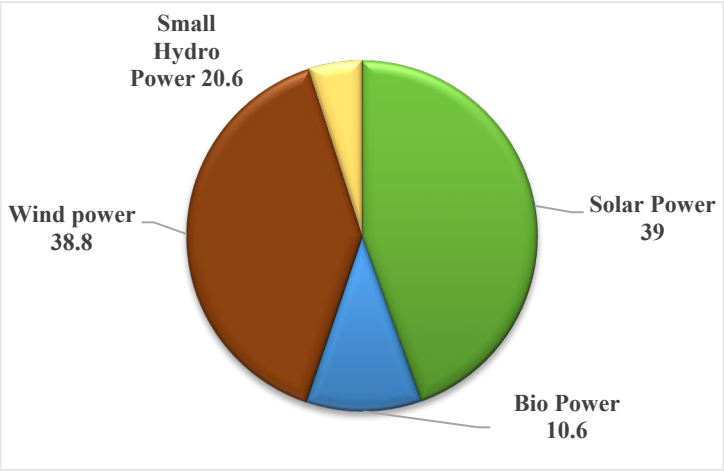


**Fig.1.1. Pie Chart of renewable energy source wise power (GW) installed capacity in India as on 31-07-2021**

Solar energy is converted into electrical energy using Solar photovoltaic (SPV) cell. SPV is a transducer which can convert photon energy into electrical energy based on principle of photovoltaic effect. The electricity produced from SPV system can be used by local loads or can

be integrated with conventional grid. Microgrid articulates the idea of integration of RESs to harness their potential as a solution to meet continuously increasing energy needs. Microgrid can be operated in autonomous and/or grid-connected mode. The microgrid has many benefits such as higher reliability, stability, efficiency and reduced transmission losses as the generators are in close proximity to the load.

## 1.2 SOLAR PV BASED MICROGRID

SPV based microgrid can be made to operate either as stand-alone microgrid or grid tied microgrid.

### 1.2.1. Stand-alone SPV based microgrid

Stand-alone SPV based microgrid is independent of the utility grid and operates autonomously as a self-sustained unit. In stand-alone PV system, the power supplied to the load depends upon the available solar energy. The output of SPV is intermittent in nature as it depends on the environmental conditions [7]–[10]. To maintain the continuity of supply to the load, an energy storage system along with PV system needs to be added. Battery is most commonly used storage device and can maintain continuity of power to the load.

Block diagram of stand-alone PV system with BESS is shown in figure 1.2. The system comprises of PV array, battery energy storage system with charge controller, dc-dc converter, inverter and load.

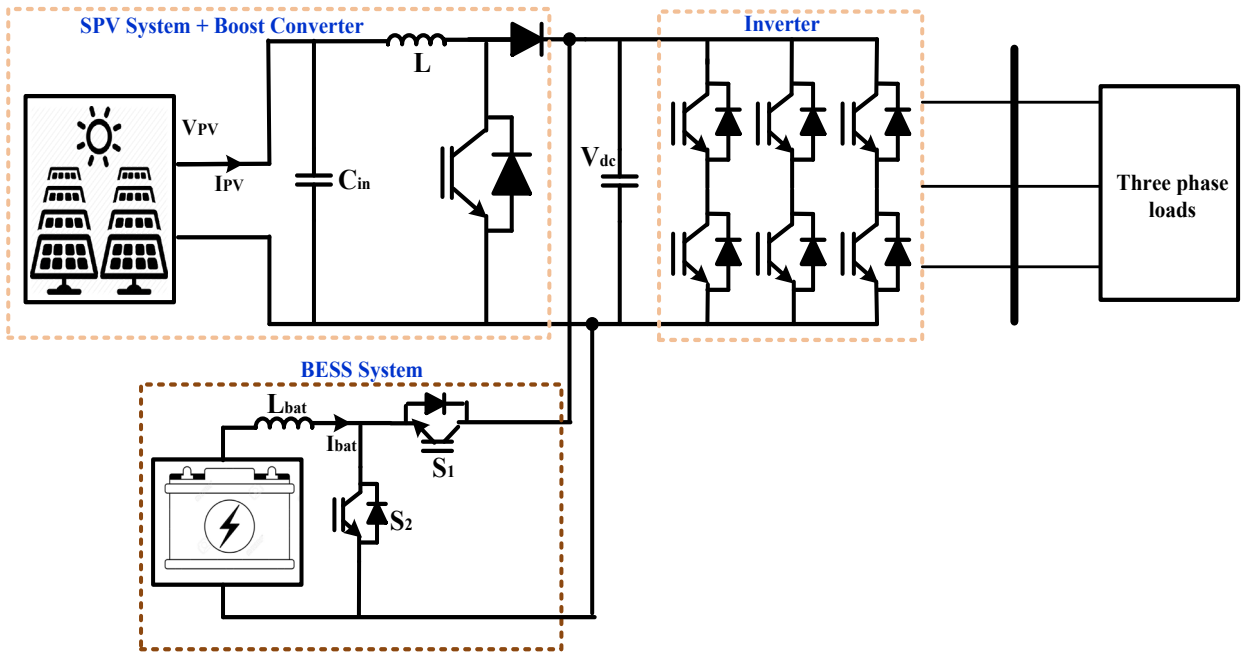


**Fig. 1.2. Block Diagram of stand-alone PV system with BESS**

### 1.2.2. Grid connected SPV based microgrid

Grid tied or grid-connected SPV based microgrid is a system that facilitates the bidirectional power flow. It consists of solar PV, dc-dc converter, voltage source inverter, interfacing inductors, loads. If the load demand is less than the output of SPV, the excess power from SPV is fed to the grid and when the load demand exceeds than the SPV power generation, the remaining load power is supplied by the grid. The inverter is one of the most important components in SPV based microgrid. A PV inverter is used to convert generated dc voltage to ac voltage. Grid tied SPV based microgrid can also be configured as single stage or two stage. Both single-stage or two stage configurations can be used to generate single phase or three phase supply. Three phase grid tied SPV based microgrid can be connected as three phase three wire or three phase four wire system.

A two-stage grid-tied PV based microgrid has PV array integrated to three phase grid as shown in figure 1.3.

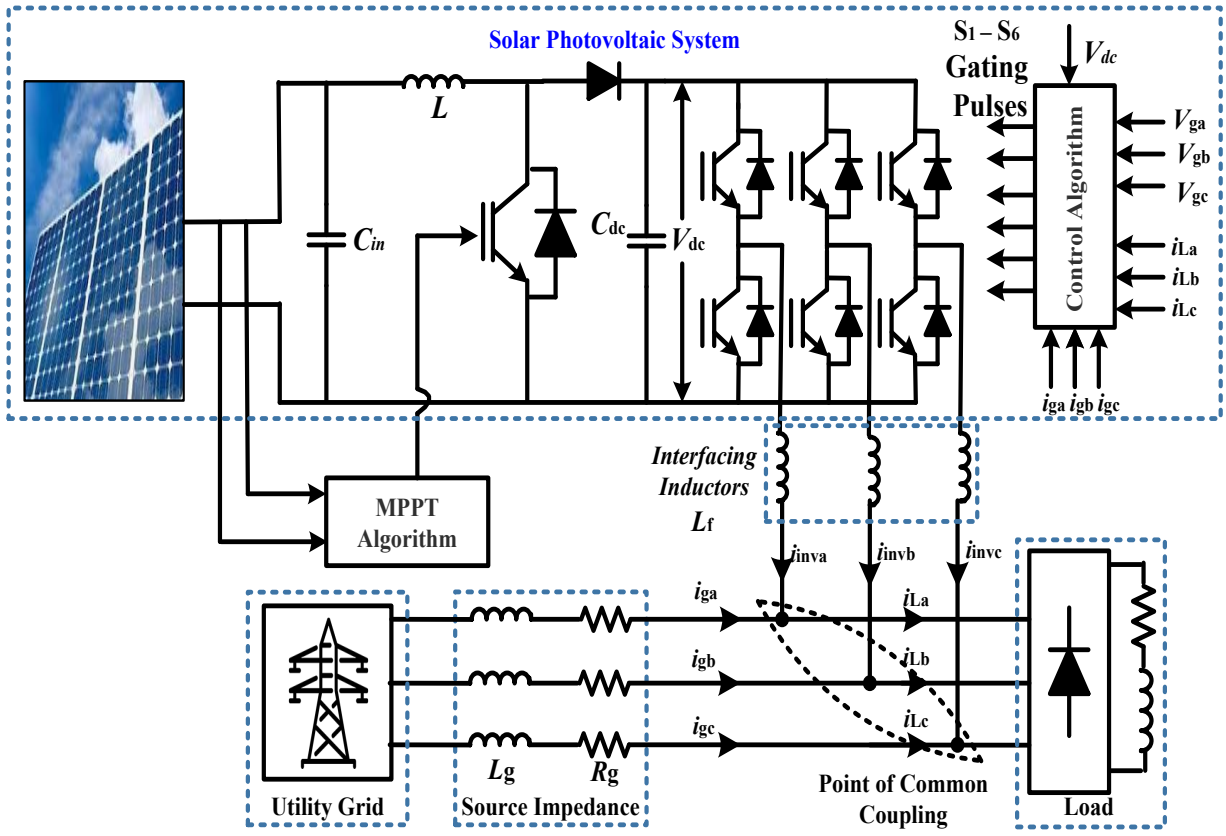


**Fig. 1.3. Block diagram of two-stage three-phase grid-tied PV based microgrid**

The basic unit of PV array is PV cell which is an active transducer that converts energy from sunlight (photons) into electricity (current). PV cells are connected in series and / or parallel to

form PV modules which can be further connected in series or parallel to make PV array of desired output voltage and current. The system consists of two stage conversions: firstly, variable dc from PV array is converted into fixed dc of required magnitude by boost converter and then grid connected PV inverter is used to convert this dc voltage into ac voltage of desired magnitude and frequency for supplying ac load.

A two-stage grid-tied PV based microgrid basically requires two control algorithms: (a) algorithm for Maximum Power Point Tracking (MPPT), and (b) algorithm for controlling the grid-interfacing inverter. MPPT is required to track peak power of a solar photovoltaic energy conversion system. Voltage source inverter converts dc voltage into ac voltage of desired magnitude and frequency to be utilised by the ac loads. In a grid tied PV system, the output of VSI can be synchronized with the conventional ac grid using synchronization algorithms and thus avoiding instabilities and system failures. Voltage source inverter control schemes are required to improve power quality, reduce harmonics, provide active filtering, control reactive power flow etc.

## 1.3 CHARACTERIZATION STUDIES OF SPV BASED MICROGRID

For efficient and reliable performance of grid interfaced SPV based microgrid, sensitivity and reliability analysis need to be performed at the design stage.

### 1.3.1. Sensitivity Analysis

Sensitivity analysis is the performance evaluation technique for evaluating the change in the system's performance with respect to the change in its parameters.

The majority of investigators utilize only a few of the methods for sensitivity analysis including partial differentiation, partial correlation, and regression techniques. Partial differentiation gives the normalized sensitivity of a quantity i.e. the percentage change in the value of the quantity for one per cent change in the value of the parameter of interest. The normalized sensitivity of a function, F with respect to parameter, n can be evaluated by equation (1.1):

$$\hat{S}_n^F = \frac{\frac{\partial F}{F}}{\frac{\partial n}{n}} = \left(\frac{n}{F}\right)\left(\frac{\partial F}{\partial N}\right) \tag{1.1}$$

If number of parameters change at the same time, the sensitivity of the function is calculated by Jacobian matrix as shown in equation (1.2):

$$J_{o_{ni}}^{F} = \begin{bmatrix} \frac{\partial F1}{\partial n1} & \frac{\partial F1}{\partial n2} \cdots & \frac{\partial F1}{\partial nN} \\ \vdots & \ddots & \vdots \\ \frac{\partial FA}{\partial n1} & \frac{\partial FA}{\partial n2} & \frac{\partial FA}{\partial nN} \end{bmatrix} \quad (1.2)$$

The PV output power is mostly influenced by the changing weather condition, which can be depicted as non-linearity in P-V curve. Also, the output of a converter depends upon its designed parameters. Thus, the sensitivity analysis of solar cell parameters needs to be performed with respect to insolation and temperature. Further the sensitivity of boost converter output voltage can be determined with respect to inductance value, capacitance value and duty ratio.

### 1.3.2. Reliability Analysis

According to the Institute of Electrical and Electronic Engineers (IEEE), "Reliability is the ability of a system or component to perform its required functions under stated conditions for a specified period of time". Reliability can be defined as the probability of system's availability. Availability can further be defined as a ratio of the expected value [E] of the uptime of a system to the aggregate of the expected values of up and down time, or

$$A = \frac{E[uptime]}{E[uptime]+E[downtime]} \quad (1.3)$$

Downtime can also be termed as Mean Time to Repair (MTTR). Reliability can be computed as, $Reliability = e^{-\lambda t}$, where λ is the failure rate and can be calculated as $(MTBF)^{-1}$. Reliability analysis can be performed using reliability block diagram, fault tree analysis, markov model etc.

## 1.4. MPPT CONTROL ALGORITHM UNDER PARTIAL SHADING CONDITION

Solar PV system gives maximum power under standard test condition or uniform shading but many times PV panels are non-uniformly irradiated i.e. are partially shaded. The shading on solar PV array can be caused due to shadow of nearby big building, trees, dense clouds, dust and panel aging or cracking. PSC in PV system is an inevasible situation and exhibits multiple peaks consisting of a single global maximum power point and many local maximum power points in its power-voltage curve. The presence of multiple peaks makes tracking of maximum power point more difficult and demands an efficient controller to track the global peak of the P-V curve. Along with implementing MPPT controller, to minimise the adverse effect of partial shading on PV system, different PV array arrangements like series-parallel (SP), honey comb (HC), total cross tied (TCT) etc may be used.

## 1.5. DC LINK VOLTAGE REGULATION OF STAND-ALONE PV SYSTEM WITH BATTERY ENERGY STORAGE SYSTEM (BESS)

In stand-alone PV system, the power supplied to the load depends upon the available solar energy. The output of SPV is intermittent in nature which depends on the environmental conditions. This intermittency problem can be addressed by using battery energy storage system (BESS) along with PV system. But when two or more energy sources are connected, then control of dc link voltage at common coupling point (CCP) is an area of concern. Also, any change in the PV output or change in load will affect the dc link voltage. Inverter output depends upon dc link voltage and hence any variation in dc link voltage is undesirable for reliable operation of microgrid and the transients in dc link voltage needs to be damped out. The conventional PI controllers cannot do the needful efficiently as they suffer from overshoot/undershoots and have long settling time. Hence, to regulate DC link voltage of stand-alone PV system with BESS, an efficient controller is needed.

## 1.6. PV INVERTER CONTROL ALGORITHM FOR GRID TIED SOLAR PV SYSTEM

The SPV system along with boost converter is connected to voltage source inverter (VSI) which is connected to grid at the point of common coupling (PCC). PV inverter control algorithm is used to convert generated DC power into AC of required voltage and frequency for grid synchronization and also provides load compensation by regulating the DC link voltage using a voltage controller. The main objective of grid integration of SPV system is to meet the load demand and surplus/deficit power to be supplied/taken to/from the grid. Presence of non-linear loads and power electronics-based devices in SPV system deteriorates the power quality at point of common coupling. In order to mitigate the power quality issues effectively and to comply with the required IEEE standards, an efficient control for optimal operation of VSI is required. The interfacing control algorithms are used to control the output of VSI for its efficient utilization and for improving power quality at PCC by providing reactive power compensation, harmonics compensation and load balancing.

## 1.7. MOTIVATION AND RESEARCH OBJECTIVES

In recent time, SPV based microgrid has received widespread acceptance as, it is a green source with less harmful effect on environment. Further, the price of PV module is reducing day by day making the energy production more economical. As per the operating conditions, SPV based

microgrid can be used either in stand-alone or in grid tied manner. All these advantages of PV based microgrid motivated and led to the following research objectives:

1. Development of reliability and sensitivity model of the PV based microgrid.

2. Development of control algorithms for tracking of Global Maximum Power Point (GMPP) under partial shading condition.

3. DC link voltage control of stand-alone PV system with battery energy storage system for improved performance.

4. Design and development of inverter control algorithms for enhanced performance of the system.

## 1.8. PROBLEM IDENTIFICATION

For meeting the defined objectives, the following problems are identified:

1. The mathematical model of SPV based microgrid and its components viz. PV cell, dc-dc converter, PV inverter, DC link capacitor and interfacing inductors need to be developed and the simulation studies needs to be carried out.

2. To investigate the model's validity for variations in the parameters of interest, sensitivity analysis needs to be carried out. For this, the sensitivity functions for solar cell and boost converter with respect to influential parameters for different PV array configurations are required to be developed. Also, reliability analysis of solar PV based microgrid needs to be performed at the design stage itself using reliability block diagram, markov's model, fault tree analysis etc.

3. Different MPPT algorithms are used to track the maximum power of PV array but conventional MPPT algorithms shows best performance under uniform insolation. Under PSC's, the Power vs Voltage (P-V) plot of SPV system consists of multiple local maxima power point and one global maxima power point. The solar PV system under partial shading scenarios requires the synthesis of modified controller which is able to discriminate between local and global peak point. Along with implementing modified MPPT controller, to minimize the adverse effect of partial shading on PV system, different PV array arrangements like series-parallel (SP), honey comb (HC), total cross tied (TCT) etc. may be used.

4. In stand-alone PV system, the power supplied to the load depends upon the available solar energy. The output of SPV is intermittent in nature. This intermittency problem can be addressed

by adding an energy storage system along with PV system. Battery is most commonly used storage device and it is very pivotal in maintaining continuity of power to the load. But when two or more energy sources are connected at generating point, then the dc link voltage control is the area of concern. Therefore, a controller which can maintain constant dc link voltage during the system transients (occurs due to abrupt change of load demand or any sudden change in generation capacity) needs to developed and implemented.

5. The grid tied solar PV system needs power electronics-based devices to integrate SPV based microgrid to utility grid. Because of extensive usage of these power electronics-based devices as well as non-linear load, the power quality (PQ) at the point of common coupling is affected So, PV inverter control algorithms to overcome the power quality issues are required to be developed.

## 1.9. ORGANIZATION OF THESIS

Chapter-I presents the introduction, motivation, objectives and problem identification of the research work carried out. The organization of the thesis is also given in this chapter.

Chapter-II includes the literature review of SPV based microgrid and its associated areas. Literature review related to sensitivity and reliability assessment of grid interfaced PV based microgrid for different PV array configurations, control algorithms for MPPT under PSC's, DC link voltage regulation of stand-alone PV system with BESS and grid-interfacing PV inverter have been presented.

Chapter-III discusses the design and modelling of solar PV based microgrid and its characterization studies viz. sensitivity and reliability studies. Sensitivity functions for solar cell and boost converter with respect to influential parameters have been developed. Reliability analysis of solar PV based microgrid by different reliability assessment methods viz. reliability block diagram, markov reliability model and fault tree analysis has been performed.

Chapter-IV proposes MPPT control algorithms under PSCs for stand-alone PV system. The PSC causes the power loss of PV array which can be reduced by using intelligent controllers along with different PV array arrangement schemes viz. series, series-parallel, total cross tied. The intelligent modified controller identifies the global maximum power point out of many local maximum power points in PV array characteristics. In this work, novel intelligent MPPT algorithms viz. asymmetrical FLC and asymmetrical interval type-2 FLC have been developed.

Chapter-V presents the dc link voltage regulation of stand-alone PV system with battery energy storage system. The proposed NARMA-L2 control scheme, maintains the voltage across dc-link under varying input i.e. varying atmospheric condition as well as varying output i.e. varying load condition. The performance of the proposed control scheme is investigated using MATLAB Simulink toolbox.

Chapter-VI presents the least mean square (LMS) based adaptive interfacing algorithms viz. Smooth LMS, improved zero attracting LMS and $RL_0$-VSSCMPN for inverter control in a two-stage three phase grid-tied PV system. Mitigation of power quality problems is a crucial issue for the utility side as well as customer end. The proposed algorithms, along with compensating the load harmonics, reduces voltage fluctuation at PCC and supplies the reactive power demand of the local load. The algorithm has been tested under steady state and transient conditions for both input variation as well as load variation under power factor correction (PFC) mode of operation. The efficacy of the proposed PV inverter control algorithms has been tested using MATLAB /Simulink toolbox. Further, a hardware prototype, acting as DSTATCOM, has been developed for evaluating the performance of the developed algorithms.

Chapter-VII summarizes and highlights the main conclusions of the proposed work. The scope for further work in this area is also enlisted at the end of this chapter.

At the end of the thesis, the list of references and appendices are provided.

## 1.10. CONCLUDING REMARKS

This chapter delivers a summary of the research work carried out and embedded in this dissertation. The motivation and the objectives of the research work are presented and the research problems have been identified. The overview of the research work carried out is presented chapter wise.

# CHAPTER-II

# LITERATURE REVIEW

## INTRODUCTION

The chapter-I, defines the objectives, motivation and identification of the research problems. To gain the right perspective of research problems, a literature review has been carried out in the related areas of the research work. This chapter presents the brief review on the (i) Solar PV based microgrid, (ii) Modelling of solar PV system, (iii) Sensitivity and reliability characterization studies of solar PV system, (iv) Maximum power point tracking algorithm of solar PV system under partial shading condition, (v) DC link voltage regulation of stand-alone PV system with battery energy storage system (vi) PV inverter control algorithm for grid tied to solar PV system. In the subsequent sections each topic is briefly discussed and reviewed without trying to be exhaustive. The references cited in this chapter are also representative rather than exhaustive.

## 2.2. SOLAR PV BASED MICROGRID

With the demand for energy constantly increasing alternative sources of generation such as wind, hydro, solar, fuel cell etc. are becoming more popular. Among other sources, solar photovoltaic (SPV) system has emerged as one of the best solutions as it free, low maintenance cost, reduced cost etc. Microgrid has a limited electricity consumer network with a local source of supply that is normally connected to a centralised national grid but can also run independently. It basically consists of distributed generations, linear/non-linear loads and storage devices that can run in a regulated, organised manner when connected to the grid or working in isolation. Grid connected to microgrids not only ensures the continous supply to customers but also increases the reliability of the system. The DGs generally are close to customer and requires power electronic devices for interfacing to grid. Synchronisation of solar PV system to the grid introduces many challenges viz. efficiency, reliability, power quality, etc. Appropriately designed power electronics and controls ensure that the microgrid meets the challenges of its customers as well as the utility [2].

The modelling of the complete system, along with control strategies, is therefore essential to predict the behaviour of the system in a steady state as well as in dynamic state before making an investment [3-5].

### 2.2.1. Modelling and Design of Grid-tied SPV based Microgrid

Grid-tied SPV based microgrid consists of PV array, dc-dc converter, dc-ac converter, interfacing inductors, linear/non-linear loads and grid. The primary unit of PV generation system is PV cell. Series/parallel connection of PV cell makes PV modules and further series-parallel arrangement of PV module makes PV array. Output parameters of a PV array depend upon the meteorological parameters like solar irradiance and temperature. The non-linear I-V and P-V characteristics of PV array depends upon the changes of irradiation and temperature. The variable dc output from PV array is given to dc-dc converter (boost) to make the fixed dc. As most of the loads are ac, so dc output is converted into ac using inverter. The inverter output can be single phase or three phase but for connecting PV system to grid, three phase is needed.

## 2.3. Sensitivity And Reliability Studies of Grid-Tied PV Based Microgrid

Characterization studies viz. sensitivity and reliability studies are important aspects of system modelling [9-14] as deviation between design and actual operation can have significant effects on systems performance.

### 2.3.1. Sensitivity analysis

Sensitivity analysis helps in reducing the parametric uncertainty and improves system accuracy. It provides a powerful method for validating a system by studying a change in the system response with a 1 % change in any of its parameters. Many remarkable contributions by Emilio, QU Li-nan, Xue-Gui Zhu, M. A. Azghandi, Ruifeng [11]–[15] have been made in the field of sensitivity. C. Rodriguez et al. [16] have presented mathematical modeling of grid connected PV system for stability studies. By performing eigen value and vector analysis, dynamic orbits are shown which may help in seeing problem that may arise due to disturbances. MATLAB/Simulations results show the instances where voltage of PV panel collapses, working near to the maximum power point.

Diego Oliva et al. [17] have proposed artificial bee colony algorithm to estimate the unknown parameters of PV cell for sensitivity analysis. Artificial bee colony algorithm was found to be most effective in identifying parameters of solar cell models when compared with other algorithms. P. P. Dash et al. [18] performed sensitivity analysis of current source inverter-based grid tied SPV system. The model parameters for the equivalent circuit of PV cell were derived. The uncertainties related to PV array, controller and grid are considered. Sensitivity analysis of system considering different parametric variation was examined by the location of eigenmode.

Yaosuo Xue et al. [19] conducted sensitivity analysis and voltage stability of grid connected PV system. The authors studied the impact of disturbing parameters viz. temperature, irradiation, load change on static and transient behavior of the system. Lei Guo et al. [20] presented cat swarm optimization algorithm for parameter identification and sensitivity analysis of solar cell single and double diode model. The presented results show that with proposed algorithm higher accuracy of estimated parameters, and calculated I–V characteristic of PV system is in good agreement with experimental I–V data. L. Shu et al. [21] presented track sensitivity analysis method for analyzing the parameters of inverter and filter, which influence the PV system. Studies showed that parameters of the outer voltage loop control and filter parameter have higher sensitivity than other inverter control parameters on the active and reactive power.

H. Andrei et al. [22] discussed that the PV cell parameters are dependent on irradiation and temperature. LabVIEW and Matlab software are used to compute the measured and theoretical parameters of the PV cell model. T.F. Elshatter et al. [23] have introduced sensitivity analysis of the unknown parameters of PV model with respect to suggested fuzzy model parameters. FRM of the PV modules is affected by environmental parametric change. J. Chureemart et al. [24] performed sensitivity analysis and its application in improvising power system. The sensitivity method needs much less computational work of computing optimal power flow for several different systems, since only one optimal power flow computation is needed.

### 2.3.2. Reliability Analysis

Reliability is the probability of the system performing satisfactorily over given period of time under stated conditions. Researchers have suggested several methods to improve the reliability of a system or component, for reducing cost and failure time, etc. [25]–[30]. Hua Lu [31] presented power electronic module design reliability. It highlights the need for a probabilistic approach to the estimation of reliability, including the effects of variations in design.

M. Aten et al.[32], shows the reliability anticipation for different topologies of converter drive suitable for aerospace applications. While the matrix converter has a higher number of semiconductor switches, it is subjected to a lower voltage stress, which lowers its failure rate. Carlos Olalla et al. [33] presented effect of distributed power electronics on the lifetime and reliability of PV systems. It was shown how module or submodule-level converters can alleviate variations in cell degradation over time. Shaoyong Yang et al. [34] conducted questionnaire for the requirements of industrial equipment's and reliability expectation of converters. It was concluded from survey that the most fragile components in converters are the power

semiconductor devices and capacitors. Freddy Chan et al. [35] calculated reliability of the power stages in three grid tied PV system. The reliability parameters like failure rate etc. was calculated by MIL-HDBK 217. A comparison has been drawn among different topologies to find the component with highest failure rate. M. Reni Sagayaraj et al. [36] developed markov model to evaluate the reliability of series and parallel configuration network. Also, fault tree analysis was presented to study the sequence of occurrence of events. Freddy Chan et al. [37] had carried out studies for improvement of reliability for different design of inverter. If a set of design parameters has been chosen, the reliability can be further enhanced by carefully adjusting the stress factors. F. Obeidat et al. [38] discussed the reliability of PV(250W) microinverter. The failure rate and mean time between failure for gate drive, voltage and current sensor, power supply has been calculated using MIL-HANDBOOK method. Variation in the failure rate of different configurations of microinverter was observed for over a wide variation of temperature stress factor and voltage ratio stress factor.

Researchers also evaluated and illustrated through experiments that the improvement of even a single component of PV system could improve the overall reliability. Elio Chiodo et al. [39] discussed few reliability structure adopted to include redundancy in industrial systems. It was shown that FR of redundant reliability system is not constant even though the FR of related component was fixed. E.E. Kostandyan et al. [40] estimated reliability considering uncertainties for high power IGBTs in 2.3 MW wind turbine system. Reliability level were calculated by first order reliability method considering uncertainties.

### 2.4. MPPT Control Algorithm Under Partial Shading Condition

Maximum Power Point Tracking algorithm is used for extracting maximum available power from PV module. The voltage at which PV module can produce maximum power is called maximum power point (or peak power voltage) [41]–[46]. MPPT is a commonly discussed subject from the evolution of the PV generation system. Several MPPTs were discussed in various literature [46]–[57] on the basis of simplicity, faster convergence speed, cost etc. Review of the different MPPT algorithm presented between 1968-2015 was given by T. Eshram et al. [58] and S. Lyden et al. [59].

M. A. Elgendy et al.[54] presented incremental conductance MPPT for PV array connected to resistive load. The MPPT was tested at different weather conditions. The MPPT shows faster response to temperature and irradiation transients. S. Singh et al. [42] presented an intelligent MPPT control for solar panel. Perturb and observation and fuzzy logic control was compared for

different conditions. The FLC performance was better with less oscillations. T.K. Soon et al. [60] introduces fast converging MPPT under varying irradiation and load resistance for PV system. In the presented work, the relationship between the load line and the I–V curve is used with trigonometry rule to obtain the fast response. Results. It is found that the proposed algorithm was 4times faster than I&C MPPT as results are verified through both simulation and hardware. Chun-Liang Liu et al. [43] proposed asymmetrical fuzzy logic control based MPPT for PV system. To achieve higher accuracy the asymmetrical membership functions of FLC were selected. When compared with symmetrical FLC, the proposed algorithm was improved 42.8% in terms of transient time and 0.06% in terms of tracking accuracy. K. Sundareswaran et al. [61] developed hybrid MPPT for PV system under non-uniform irradiation. Genetic algorithm and P&O were combined to ensure the MPP tracking. Both simulation and experimental results verify the accuracy of the proposed algorithm. P. Mohanty et al. [62] compares the performance of different MPPT algorithm. MATLAB/Simulink model was developed to test the performance of MPPT under consideration for variable environmental condition. But under non-uniform shading conditions, known as partial shading condition, the system performance is affected considerably and is caused due to shadow of dense clouds, shadow of big trees, nearby tall tower/building etc. This causes difference in current-voltage and complex power-voltage curve exhibiting multiple peak with one global peak point having maximum power and many local peaks resulting in power loss and reduced efficiency [63]–[67]. Although the conventional techniques were easy to understand and implement but the main drawback of these algorithms were that they may not be able to trace global peak out of multiple peaks caused due to partial shading and also show ripple. Advancement in control strategy leads to the better tracking of GMPP[61], [64], [68]–[72]. Many MPPT techniques based on intelligent, adaptive, genetic algorithms were introduced in recent research work. J. Shi et al. [73] proposes dual search algorithm in which firstly a dormant particle swarm optimization searches the global peak point of the P-V curve and then using INC algorithm maximum power from peak is tracked. Performance of the proposed algorithm has been validated through both simulation and hardware results. M. Seyedmahmoudian et al. [74] employed hybrid differential evolution and PSO to obtain maximum power from PV array during PSC's. S.E. Boukebbous et al. [75] studied behaviour of PV panels under uniform and non-uniform irradiation condition. From obtained MATLAB/Simulink results it can be concluded that during PSC the tracking of peak power can only be obtained by efficient controller. Along with implementing modified MPPT controller, to improve the performance of PV system under partial shading, different PV array arrangements like series-parallel (SP), total cross tied (TCT), honey comb (HC) etc may be used.

A. A. Elserougi et al. [76] presented the enhanced power from PV array under PSC using switched PV approach. To evaluate switched PV approach, a numerical comparison among proposed and other conventional scheme has been established for the same condition. Validity of the proposed scheme has been established through both simulation and hardware results. O. Bingöl et al. [77] analysed and compared different PV array configuration under PSC. Total cross tied PV array configuration shows the best performance among different configurations of PV array in terms of shading loss, mismatch loss, and fill factor. F. Belhachat et al. [78] used a 6 X 4 PV array size for various shading scenarios. From conducted studies it has been that TCT PV configuration shows the best performance. Similarly, various other researchers worked in this area [79]–[81], [48], [51], [70], [72], [82]–[84].

## 2.5. DC Link Voltage Control of Stand-Alone PV System with Battery Energy Storage System

For stand-alone PV system, solar power is the only energy source. The intermittency problem in stand-alone PV system can be addressed by adding any storage system with PV system. Battery is most commonly used storage device and it is very pivotal in maintaining power balancing between supply and demand [7], [9], [85]–[88]. The major concern is to maintain the DC link voltage. Many authors worked in the area to control the voltage across DC bus [89]–[93].

S. Barcellona et al. in [94] presented control strategies for photovoltaic and battery system. Control scheme can charge/discharge the battery pack accordingly to the difference between the power generated by the PV system and the one absorbed by the loads. S. Jha et al. in [95] gives modified enhanced phase locked loop control scheme for PV-battery stand-alone system. For continuous supply to load, a diesel generator is used at low solar irradiation and battery condition. Simulation studies and hardware realization of the proposed control scheme was done to establish the efficacy of control operation. Author's in [96] developed hybrid energy source with common dc link connected to grid. Adaptive Neurofuzzy inference system (ANFIS) was used as MPP tracker. Battery state of charge was governed using bidirectional controller. MATLAB/Simulink software is used to model the utility grid linked hybrid system and efficacy of the control algorithm was tested under various input/output conditions. In [90], authors presented single stage grid tied to solar and battery system. The proposed system minimises the losses by removing boost converter and power flow was made flexible by using battery. The obtained test results were studied on both fixed and variable power mode. In [97] authors gives real-time implementation of SPV and battery energy storage (BES) to control DC connection

voltage and mitigate reactive power thereby delivering active power to local loads in grid-connected service. Fitting Toolbox in MATLAB/Simulink was used to regulate dc voltage. Variation in input and output was given to verify the efficacy of the controller. A. Karni et al. in [98] gives the energy balance control algorithm for DC bus regulation of grid-battery PV system. Using proposed control algorithm, system gives good performance in terms of accuracy, speed, overshoot as can be seen from simulation results. Battery can also be used with other renewable energy sources to continuously supply the load demand and lessens the burden of the conventional grid. This type of system is known as hybrid energy storage system. Many research articles were presented in this area that was reported in [91], [99]–[101].

In [102] authors gives the findings of a wind/PV/BESS integrated system simulations study to enhance the smoothing efficiency of wind and PV power generation. An energy smoothing control scheme fuzzy logic - based and wavelet based is proposed for reducing output power fluctuations in wind/PV/BESS hybrid power generation systems. A. Mohammadzadeh et al. in [103] presented a novel design fuzzy control method of power management in a PV-battery hybrid system is presented. The adaptive interval type-2 fuzzy neural networks estimate the uncertainties online. In contrast to other well-known control techniques, the applied control technique results in good performance in the presence of time-varying radiation, temperature shifts, and output load variance.

### 2.6. PV Inverter Control Algorithm for Grid-Tied PV Based Microgrid

Grid interfaced PV system is used for feeding PV power into the grid. Grid interfaced PV system acts as DSTATCOM to work upon power quality issues like load reactive power compensation, load unbalance compensation, load harmonic compensation [48], [51], [70], [72], [82]–[84], [104]–[108]. The grid connected PV systems can either be a single stage configuration or a two-stage configuration. In single stage configuration, PV array is interfaced directly to the dc-link of VSI [108]–[110]. L.B.G. Campanhol et al. [111] presented dual compensating and feedforward control loop for single stage three phase grid interfaced PV system. A.A. Hassan et al. [112] presented modeling and simulation of single phase grid interfaced PV system. The THD has found to be well within the IEEE standard. Singh et al. [113] have proposed a single stage configuration with ILST control of VSI, the VSI transfer the extracted PV energy to three-phase grid and simultaneously helps in enhancing power quality.

In two-stage configuration the PV array is interfaced to dc-link of VSI by a dc-dc converter [114]. Also, the efficiency of the grid interface inverter depends mainly on the generation of the reference or the compensation signal [105]. Substantial literature is available on control

algorithms for double stage three phase grid tied PV system. Some conventional time domain control algorithms are synchronous reference frame (SRF) theory, power balance theory, instantaneous reactive power theory, conductance fryze, etc [115]–[119]. The controllers based on intelligent techniques such as neural network, fuzzy logic and adaptive neural-fuzzy network have been presented in the literature [105], [118], [120], [121]. Various authors have proposed in the literature that the parameters of conventional controller such as proportional integral (PI) vary according to variation in system parameters and require exact mathematical model of the system. However, intelligent controllers such as fuzzy, adaptive neuro-fuzzy etc. are robust and exhibit better transient and steady state response than conventional PI controller [122], [123]. N. Gupta et al. [124] presented asymmetrical fuzzy logic controller for solar tied to grid. The fuzzy membership functions were fine-tuned at center while they may be coarse tuned away from center, depending on the error to maintain power quality under linear/nonlinear loads.

Adaptive control algorithms such as [125]–[129] are implemented for PV inverter control and are also used to regulate the output of the system using the basics of the LMS (least mean square) and the LMF (least mean fourth) techniques. Better performance under steady state condition can be attained using LMS while LMF has faster convergence rate. Adaptive control techniques provide a systematic approach for automatic adjustment of controllers in real time in order to achieve desired performance [116], [125], [127], [130], [131]. This area is developed in terms of adaptive filtering, control algorithms and analysis. Adaptive control can provide automatic tuning in closed loop for the developed controller parameters [1], [122], [123], [132]–[134].

Arya et al. [135] have developed leaky least mean square based control algorithm for control of three phase DSTATCOM, with improved dynamic response and fast convergence. Various other adaptive filtering techniques based on Wiener filter, fixed step LMS and variable step size LMS have been presented for numerous applications of noise reduction in signal processing and harmonic detection in shunt active power filter [136]–[140]. Singh et al. [133] have presented an implementation of adaptive filter for three phase DSTATCOM for harmonics elimination, reactive power compensation and load balancing.

M. Mangaraj et al. in [141] presented sparse least mean square for controlling the DSTATCOM. It is observed that the sparse LMS algorithm has better DC link response, reduced harmonic in source current, balanced 3-phase voltages etc. S. Pradhan et al. [142] have developed modified VSS-LMS (variable step size LMS) algorithm for control and synchronisation of 1-phase voltage source inverter. Its performance has been compared on both simulation and hardware for different input output conditions. A. Arora et al. [143] have implemented functional link artificial

neural network (FLANN) for shunt compensation. The developed algorithm performs satisfactorily under steady state and transient response as well as it has fast convergence.

## 2.7. IDENTIFIED RESEARCH GAPS

Though a lot of research work has been carried out in the field of solar PV based microgrid, still some of the issues remain unresolved. Based on the aforementioned extensive literature survey, following research gaps were identified:

i. There are uncertainties in system which has not been taken care of at design stage. Further, different PV array arrangements are not considered for sensitivity and reliability studies.
ii. MPPT control algorithms developed till now can be improved further for tracking global peak point efficiently under partial shading condition.
iii. In a standalone PV system, battery is used as alternate energy source for continuous supply of power to load. DC link voltage control in stand-alone PV system with BESS is area of concern.
iv. PV inverter control algorithms developed till now have scope for improvements in terms of convergence rate, dc offset rejection capability, working under unbalanced grid etc.

## 2.8. CONCLUDING REMARKS

In this chapter, the literature review on solar PV based microgrid and allied zones have been carried out. Researchers' contribution in the area of design and modelling of SPV connected to utility grid with their control algorithms has been presented. A survey of the sensitivity and reliability analysis of PV system and relevant areas has been brought out. Work in the area of dc-link voltage control for PV system with battery storage are presented. Review of the work of various researchers in the area of control PV inverter for SPV tied to grid is presented. Based on the literature studied, the research gaps in the solar PV based microgrid are identified.

# CHAPTER-III

# MODELLING AND DESIGN OF SOLAR PV BASED MICROGRID AND ITS CHARACTERIZATION STUDIES

## INTRODUCTION

Renewable energy source based microgrids are gaining importance due to the exhaustion of fossil fuels and increase in greenhouse gases. Solar PV based microgrid is one of the most suitable RES based microgrid, especially in remote areas where electricity from the central grid is not available and alternative sources of electricity such as diesel are expensive. This chapter contributes toward the modelling and design of solar PV based microgrid and its characterization studies. The simulation model of the Solar PV based microgrid is developed in MATLAB environment using SIMULINK and Sim Power System tool boxes. The characterization studies are performed to get a clear insight about the performance of the system at the design stage itself.

Characterization studies viz. sensitivity analysis and reliability analysis are carried out to validate the design of the developed system. Sensitivity analysis is used to study the validity of parametric variance, while reliability analysis is used to study risk management. Different PV array configurations have been considered for developing sensitivity and reliability functions. The sensitivity functions for solar cell and boost converter with respect to influential parameters have been developed by first derivative of Taylor's series. Also, reliability analysis for electrical and electronic components of the system have been performed using pareto analysis and reliability model of the PV based microgrid has been developed using reliability block diagram for different PV array configuration. The Fault tree analysis (FTA) model of the system has been established to find the cause of failure and steps the events serially. Further, Markov's model has been used to develop the reliability functions of individual component and hence from it the reliability model of the complete grid connected PV system has been developed.

A SPV based microgrid can be configured as:

- Stand-alone SPV based microgrid
- Grid connected SPV based microgrid

---

This chapter is based on the papers - (i) "Sensitivity Analysis of solar PV system for different PV array configurations" accepted in Springer CCIS proceedings, of 16th ICInPro 2021. (ii) "Reliability assessment of Grid interfaced PV based Microgrid for different PV array configurations" accepted in International Journal of Information Technology (Springer).

The mathematical modelling and parameter selection of both stand-alone PV system as well as grid connected systems have been presented in the subsequent sections.

## 3.2 DESIGN AND MODELLING OF STAND-ALONE SOLAR PV SYSTEM

The stand-alone SPV system as shown in figure 3.1 comprises of main components viz. PV array, boost converter, MPPT controller for maximum power point tracking, voltage source inverter and load. The output of SPV system is converted into regulated dc output using dc-dc (boost) converter and further the output of dc-dc (boost) converter is converted into ac voltage using three phase inverter for utilisation by ac loads.

The mathematical modelling and design of stand-alone PV system is presented below. SimPower/Simulink software is used for the simulation studies.

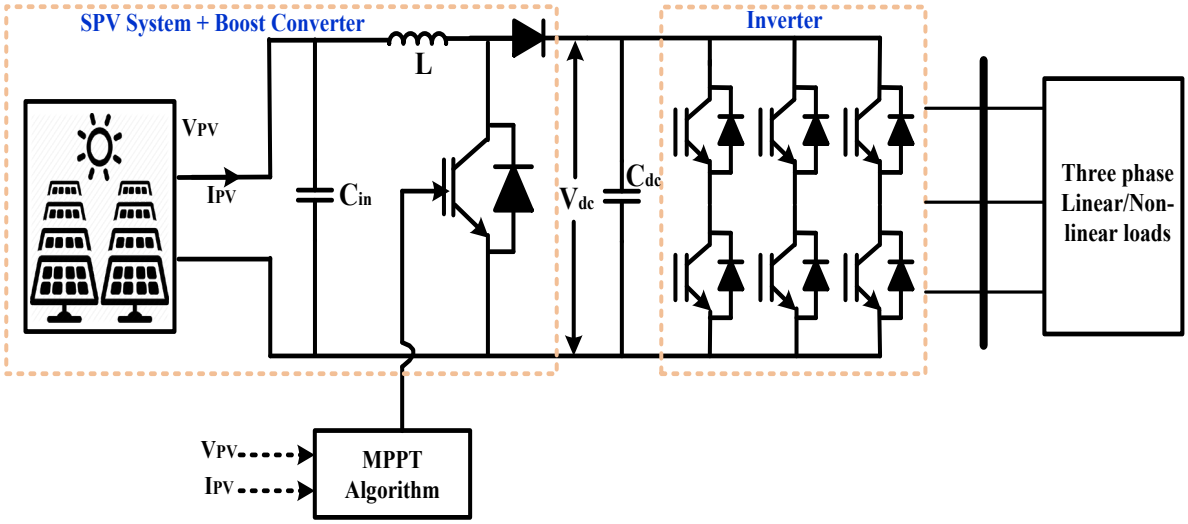


**Fig. 3.1. Schematic Diagram of stand-alone PV system**

### 3.2.1. PV Array

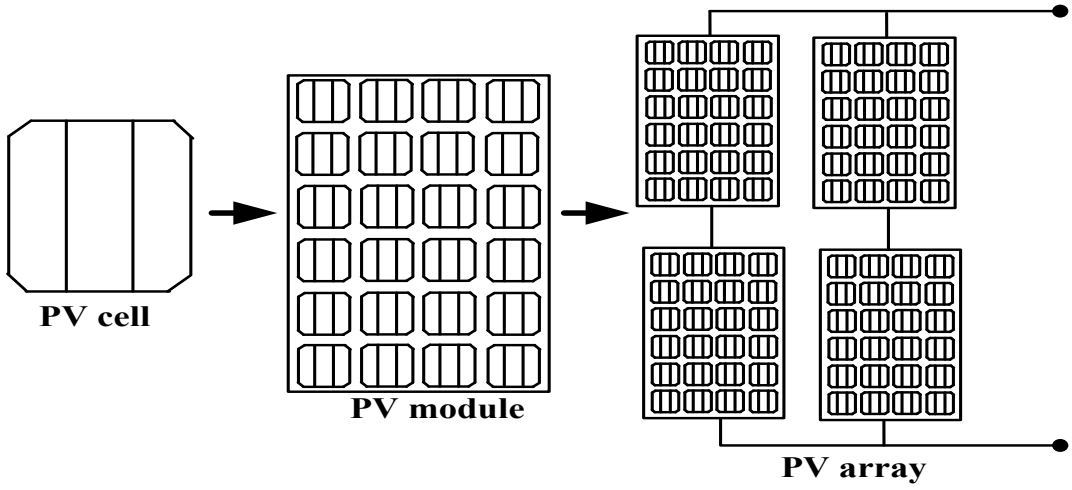


**Fig. 3.2. Formation of PV array from PV cell**

The basic unit of PV array is PV cell which is an active transducer that converts energy from sunlight (photons) into electricity (current). PV cells are connected in series and / or parallel to form PV modules which can be further connected in series or parallel to make PV array of desired output voltage and current as shown in figure 3.2.

The ideal single diode model of solar cell comprises of light generated current source with a single anti-parallel diode. Figure 3.3 presents the ideal and practical equivalent circuit of single diode model used in the proposed system. $R_s$ and $R_{sh}$ represent series and shunt resistance of the solar cell.

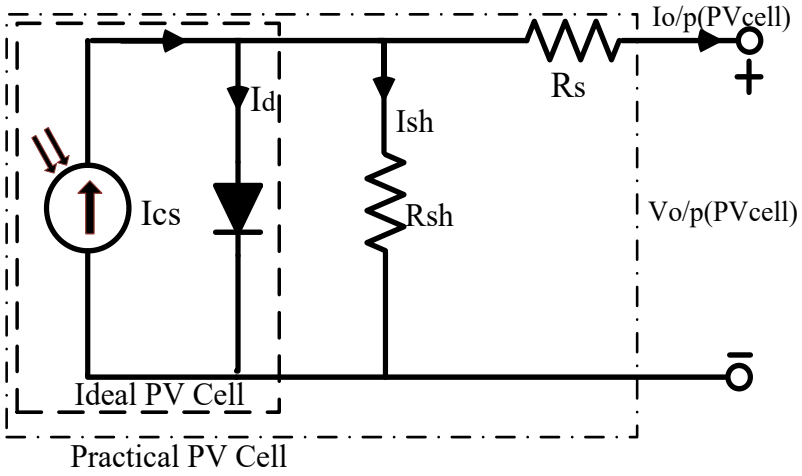


**Fig. 3.3 Equivalent circuit of single diode PV cell**

The output current for the PV cell $I_{o/p}$ (PV cell) can be expressed using Kirchhoff's law as given in equation (3.1) [144]:

$$I_{o/p(PVCell)} = I_{cs} - I_d - I_{sh} \tag{3.1}$$

where, $I_{cs}$ is the photon current, $I_d$ is the diode current and $I_{sh}$ is the reverse saturation current

$$I_{o/p(PVcell)} = I_{cs} - I_o * \left[exp\left(\frac{q\left(V_{o/p} + I_{o/p} * R_s\right)}{AkT}\right) - 1\right] - \frac{V_{o/p} + I_{o/p} R_s}{R_{sh}} \tag{3.2}$$

The output current for the PV array $I_{o/p}$ is given as shown in equation (3.3):

$$I_{o/p} = p.I_{phc} - p.I_o * \left[exp\left(\frac{q\left(V_{o/p} + I_{o/p} * R_s\,(s/p)\right)}{sAkT}\right) - 1\right] - \frac{V_{o/p} + I_{o/p} R_s\,(s/p)}{R_{sh}(s/p)} \tag{3.3}$$

The photon current ($I_{cs}$), short circuit current of cell ($I_{scc}$) and open circuit voltage ($V_{oc}$) are given by equations (3.4) to (3.6):

$$I_{cs} = I_{scc}\,\frac{H}{H_{ref}}\left(1 + k\left(T - T_{ref}\right)\right) \tag{3.4}$$

$$I_{SCC} = \left(\frac{I_{cs}}{1+\frac{R_S}{R_{sh}}}\right) \quad (3.5)$$

$$V_{OC} = \frac{N_S\, A\, k\, T}{q} ln\left(\frac{I_{cs}}{I_o} + 1\right) \quad (3.6)$$

where, q is the elementary charge ($1.602*10^{-19}$ C), $V_{o/p}$ is the output voltage of a PV array, A is the ideal factor of the cell and is dependent on PV technology, $R_s$ is the series resistance (Ω) and $R_{sh}$ is the shunt resistance (Ω) of solar cell, k is the Boltzmann constant ($1.38*10^{-23}$ J), T and $T_{ref}$ is the actual and reference operating temperature, s and p are the number of cells in series and parallel, H and $H_{ref}$ is the solar insolation and reference solar insolation ($1000W/m^2$), $I_o$ is the diode saturation current.

PV modules are electrically wired together in series or parallel configuration to form PV array of desired rating. The I-V and P-V characteristics of PV array depends upon the intensity of insolation and temperature. Figure 3.4 shows the influence of insolation and temperature on I-V and P-V curve of 1.28 kW PV array having 70.8 V maximum voltage and 18.08 A maximum current (Appendix B (a)). It can be seen that, with change in temperature, voltage changes appreciably while change in insolation causes appreciable change in current.

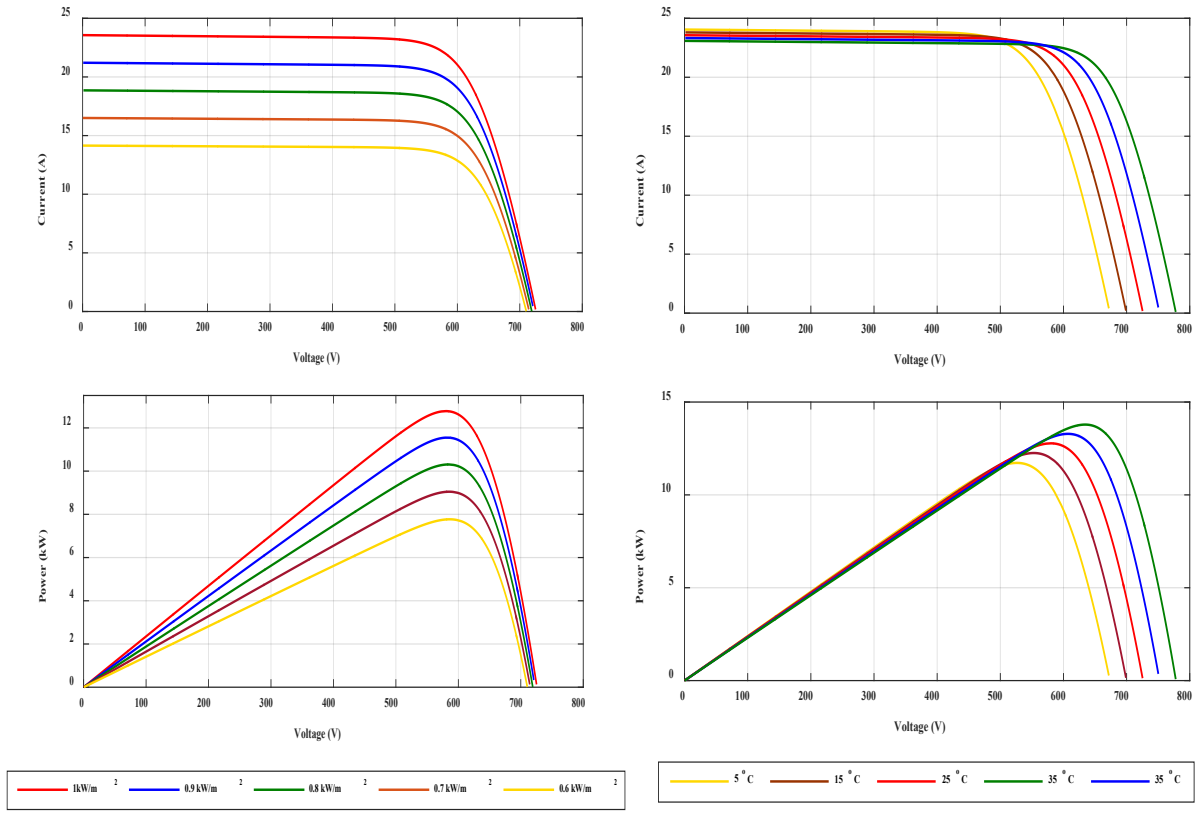


**(a)** **(b)**

**Fig. 3.4. Current vs Voltage and Power vs Voltage curve of proposed SPV system at a) Variable insolation b) Variable temperature**

### 3.2.1.1. PV Array Configuration

The performance of PV array depends upon the way different modules are connected. Various PV array configuration are series (S), parallel (P) series-parallel (SP), total cross tied (TCT) bridge linked (BL), honey comb (HC) as shown in figure 3.5. Generally, series-parallel PV array configuration is used but other configurations can also be implemented to enhance the performance of the system.

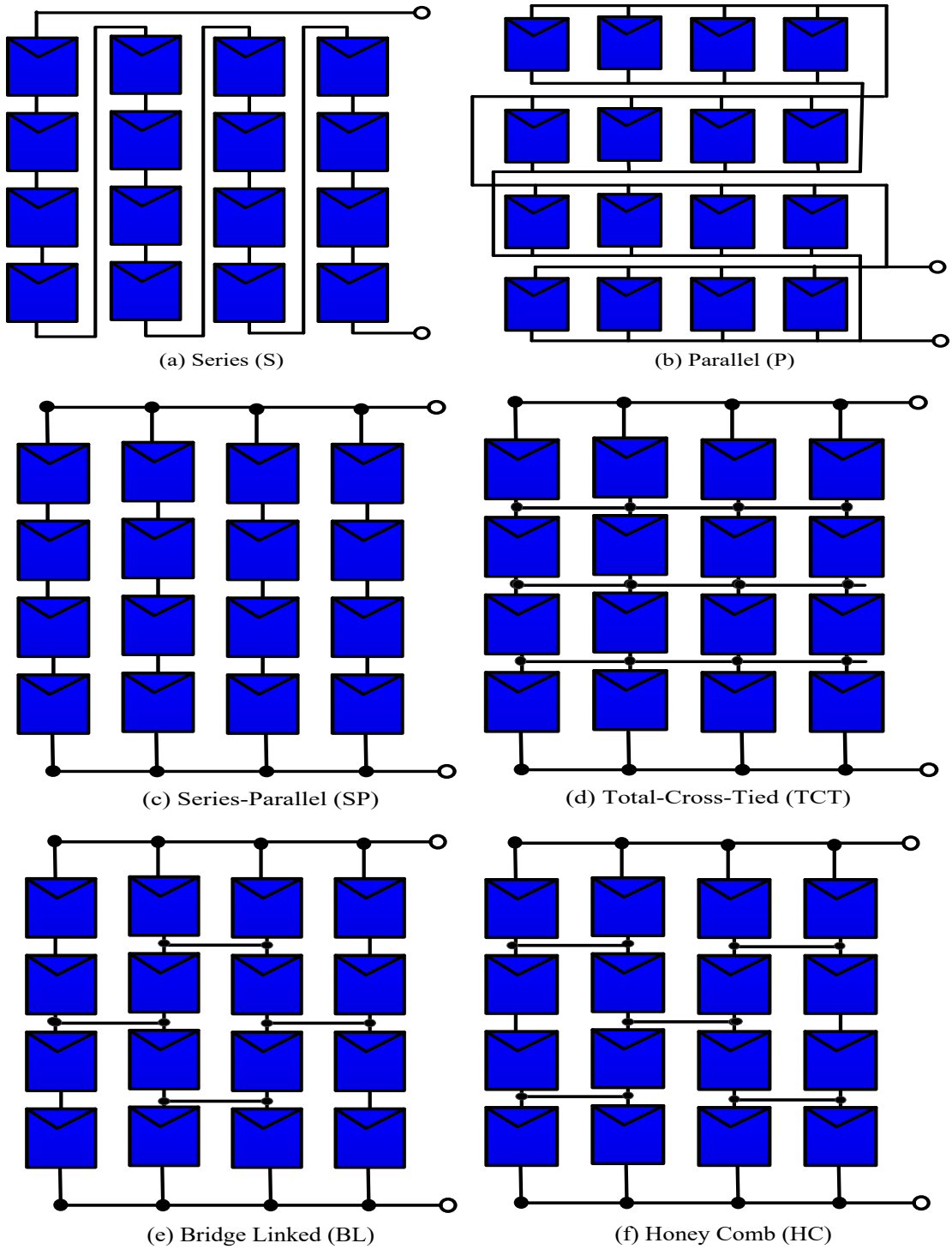


**Fig. 3.5. Schematic diagram of various PV array configuration**

### 3.2.2. Design of Boost Converter

The output of PV array is not constant but depends upon the atmospheric conditions. A dc-dc converter is used to regulate the output of PV array. Converters are basically of three types: buck converter, boost converter and buck-boost converter. In the present work, dc-dc boost converter is used. The equivalent circuit of boost converter is shown in figure 3.6.

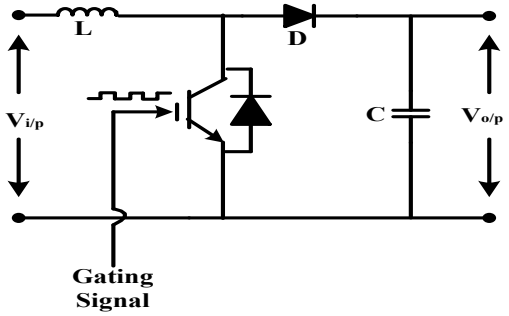


**Fig. 3.6. Equivalent circuit of Boost Converter**

The main components of boost converter along with IGBT switch are the series inductor and shunt capacitor. The values of inductance, capacitance and duty ratio can be obtained from equations (3.7) to (3.9).

$$L = \frac{V_{i/p} * (V_o - V_{i/p})}{(\Delta I f_{sw} V_{o/p})} \tag{3.7}$$

$$\alpha = 1 - \left(\frac{V_{i/p}}{V_o}\right) \tag{3.8}$$

$$C = \frac{I_a (V_o - V_{i/p})}{(\Delta V V_o f_{sw})} \tag{3.9}$$

Where, $V_{i/p}$ is the input voltage of the boost converter, $V_o$ is the output voltage of the boost converter, α is the duty ratio, ΔI is the output ripple current and it is considered as 10% of the input current, $f_{sw}$ is the switching frequency, ΔV is the peak ripple voltage and it is considered as 3% of the output voltage. For the proposed system (Appendix B (a)), the value of the inductor is calculated as 1.1mH and capacitor as 500μF. The reference duty ratio of the converter is obtained using the MPPT algorithm. Switching frequency of 10 kHz is used to generate gating signal for the IGBT switch of boost converter.

### 3.2.3. Maximum Power Point Tracking

Maximum power generated by PV system varies due to ambiguous weather conditions, as can be seen from figure 3.4. MPPT is used for extracting maximum available power from PV module.

The voltage at which PV module can produce maximum power is called maximum power point (or peak power voltage) [145]–[148]. For tracking MPP, several conventional algorithms viz. perturb and observe (P&O), incremental conductance (INC), fractional short circuit current, fractional open circuit voltage etc. can be used. In the proposed work, P&O and INC algorithms are used to track maximum power and are explained below:

### 3.2.3.1. Perturb and Observe (P&O) Algorithm

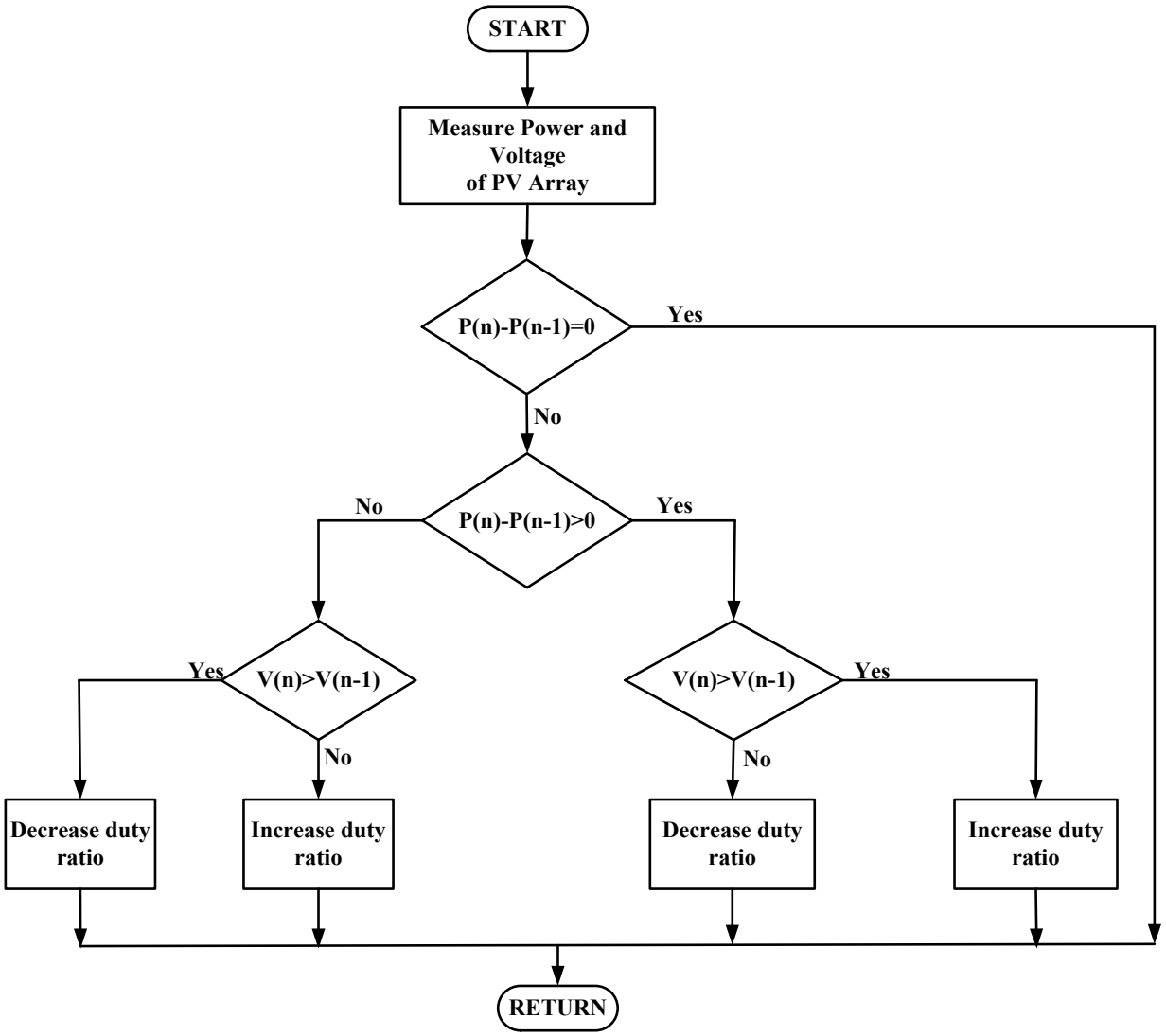


**Fig. 3.7. Flowchart for Perturb and Observe MPPT algorithm**

Perturb and observe operates by periodically perturbing (i.e. incrementing or decrementing) the duty cycle and comparing the PV output power with that of the previous perturbation. It measures the derivative of power ΔP and the derivative of voltage ΔV to determine the movement of the operating point. If the perturbation leads to an increase (or decrease) in array power, the subsequent perturbation is made in the same (or opposite) direction as seen from flowchart in

figure 3.7. Figure 3.8 shows the block diagram of a P&O algorithm for solar PV system. Table 3.1 shows the operation of P&O algorithm.

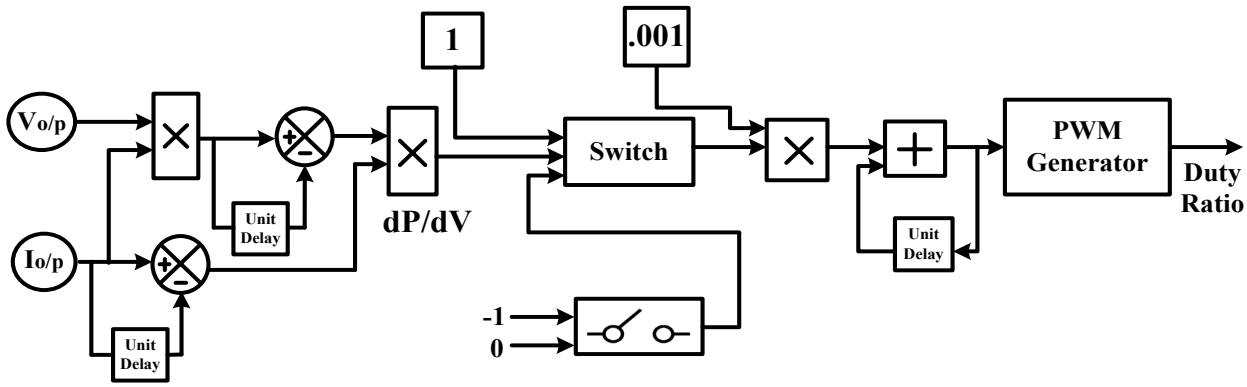


**Fig. 3.8. Block Diagram of the P&O algorithm**

**Table 3.1. Operation of the P&O Algorithm**

| S. No. | $\Delta P_{pv}$ | $\Delta V_{pv}$ | $V_{pv}$(ref.) | Duty Ratio |
|---|---|---|---|---|
| 1. | >0 | >0 | + | − |
| 2. | >0 | <0 | − | + |
| 3. | <0 | >0 | − | + |
| 4. | <0 | <0 | + | − |

### 3.2.3.2. Incremental Conductance (INC) Algorithm

The INC algorithm detects the MPP by comparing $\frac{\Delta I}{\Delta V}$ against $-I/V$ till the incremental conductance is equal to the source conductance. At the MPP, $\frac{\Delta I}{\Delta V} = -\frac{I}{V}$, no control action is needed and the algorithm will update the stored parameters at the end of the cycle. In order to detect any changes in weather conditions, the algorithm detects whether a control action took place when the array was operating at the previous cycle MPP ($\Delta V$=0).

$$\frac{\Delta I}{\Delta V} = -\frac{I}{V} \text{ At MPP}$$

$$\frac{\Delta I}{\Delta V} > -\frac{I}{V} \text{ Left of MPP} \qquad (3.10)$$

$$\frac{\Delta I}{\Delta V} < -\frac{I}{V} \text{ Right of MPP}$$

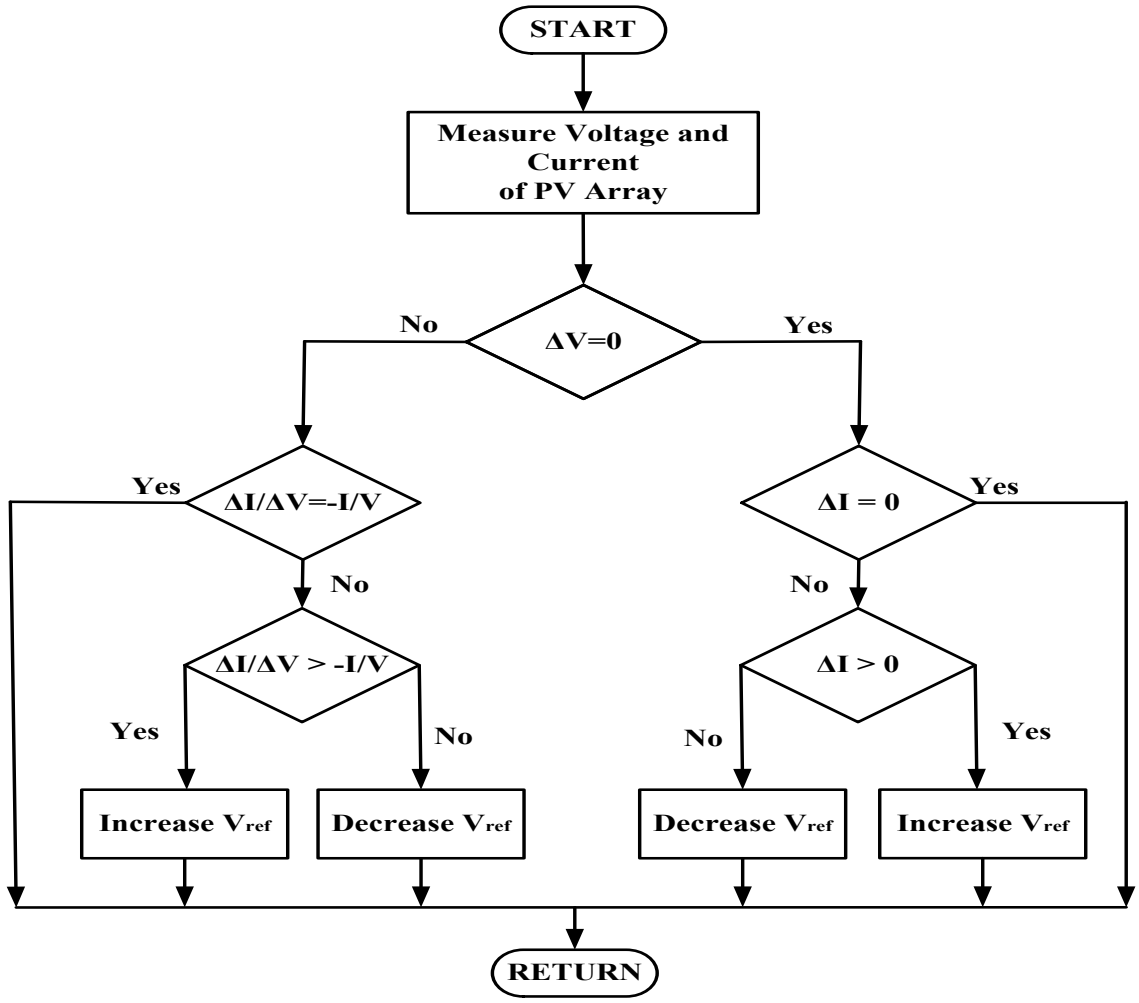


**Fig. 3.9. Flowchart for INC MPPT algorithm**

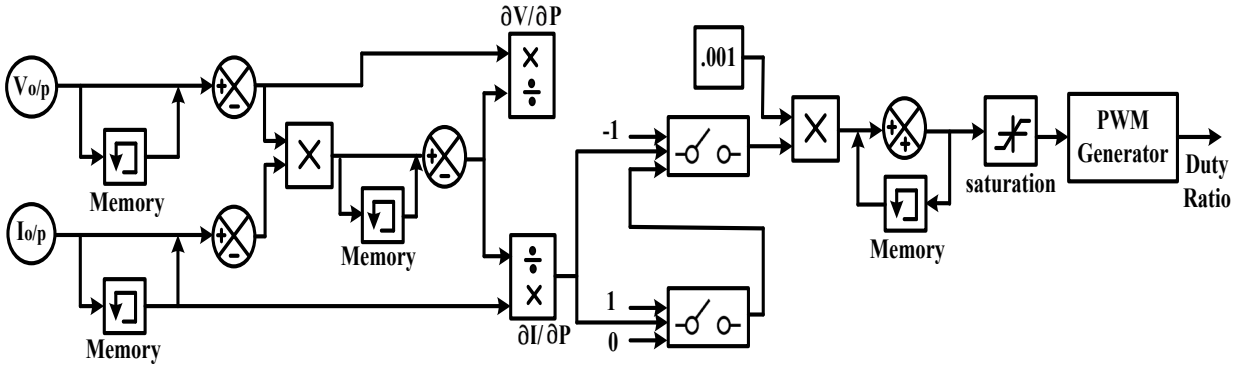


**Fig. 3.10. Block diagram of the INC algorithm**

The flow chart of realizing INC algorithm is given in figure 3.9. The flow chart gives insight steps to realize INC MPPT algorithm for controlling the switching action of boost converter to achieve MPP operation. Figure 3.10 shows the block diagram of INC algorithm for the solar PV system.

### 3.2.4. Design of Inverter

The output of dc-dc converter is converted into ac voltage using three phase inverter. A three phase two level VSI having 6 IGBT switches is used as shown in figure 3.11. Each IGBT switch shall be capable of blocking complete dc link voltage and the voltage rating of IGBT switches should be selected accordingly. The current rating of each switch depends on the current that will flow through the switch. This current is due to the PV array current, and harmonic compensating current.

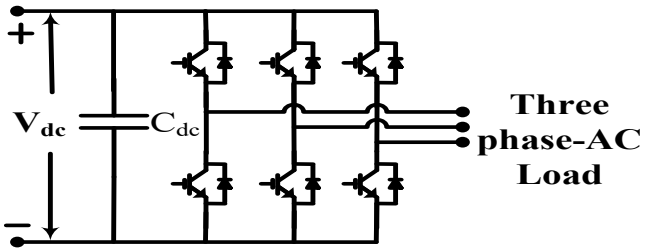


**Fig. 3.11. Equivalent circuit of three-phase voltage source inverter**

## 3.3. DESIGN AND MODELLING OF GRID TIED SOLAR PV SYSTEM

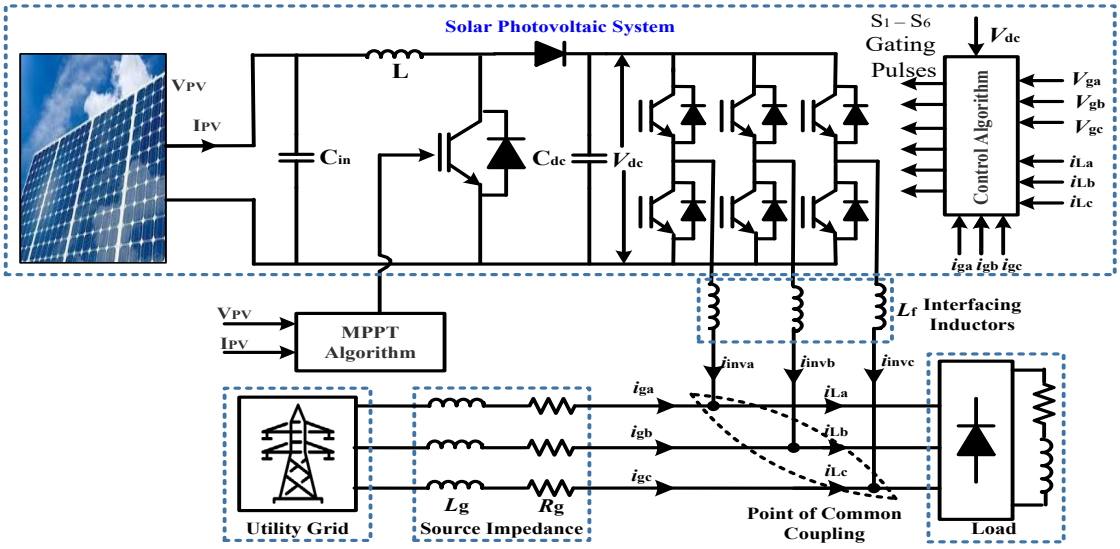


**Fig. 3.12. Schematic Diagram of SPV system connected to Grid**

This section deals with the modelling and design of a grid tied solar PV system. The schematic diagram of double stage grid tied solar PV system consisting of a PV array of 11.78 kW capacity integrated to three phase grid at 415 V, 50 Hz is shown in figure 3.12. is given. The system consists of two stage conversions: firstly, variable dc from PV array is converted into fixed dc of required magnitude by boost converter and then grid connected PV inverter is used to convert this dc voltage into ac voltage of desired magnitude and frequency for supplying ac load. MATLAB SimPower/Simulink software is used for the simulation studies.

### 3.3.1. PV array

An inbuilt PV module of MATLAB/Simulink has been used to make PV array of desired rating and specification. In the present work, Sun modules are used. The specifications of the same are given in appendix A. The PV array of 11.78 kW is formed with 3 strings having 20 PV modules connected in series in each string. (Appendix B (b)).

### 3.3.2. Design of Boost Converter

For the proposed system, the value of the inductor and capacitor is calculated as 5mH and 2.2 μF respectively, from the equations (3.7) to (3.9). The reference duty ratio of the converter is obtained using the MPPT algorithm. Switching frequency of 10 kHz is used to generate gating signal for the IGBT switch of boost converter.

### 3.3.3. DC Link Voltage

The value of DC link voltage ($V_{dc}$) must be greater than twice the peak value of supply line to line voltage. For a three-phase system, it can be calculated by equation (3.11) as given below:

$$V_{dc} = \frac{2.\sqrt{2}.V_{LL}}{\sqrt{3}m} \tag{3.11}$$

Where, $V_{LL}$ is the RMS value of three phase ac side voltage, taken as 415V, $m$ is the modulation index and is taken as 0.9. The calculated value of DC link voltage is 753 V while the selected value is 800V.

### 3.3.4. DC Link Capacitor

The dc-link capacitor value should be large enough to address system dynamics; thus, its size is determined by the instantaneous energy available to the VSI during transients. The dc-link voltage should be kept constant despite variation in load and generation. The value of dc link capacitor can be calculated by equation (3.12):

$$C_{dc} = \frac{I_M}{2.\omega.V_{dcripple}} \tag{3.12}$$

where $I_M$ is PV array current at maximum power, $\omega$ is grid frequency, $V_{dcripple}$ is ripple in dc link voltage (2% of $V_{dc}$). For the proposed system, the calculated value of $C_{dc}$ is 2.2 μF. The selected value of capacitor is 3 μF.

### 3.3.5. Interfacing Inductors

Interfacing inductors, $L_f$ are used at the ac side of PV inverter, which couple the inverter to the grid. The inductors are used to minimise the ripple in output current of inverter. The interfacing inductors are designed using equation (3.13),

$$L_f = \frac{\sqrt{3}mV_{dc}}{12hf_{sw}\Delta i} \tag{3.13}$$

where $\Delta i$ is the current ripple taken as 10 % of inverter current, $f_{sw}$ is the switching frequency taken as 10 kHz in the present work and $h$ is the overload factor taken as 1.2. The value of interfacing inductor is calculated to be 5mH for the proposed system.

### 3.3.6. Design of Inverter

A three phase two level VSI having 6 IGBT switches is used as shown in figure 3.11. Each IGBT switch shall be capable of blocking complete dc link voltage and the voltage rating of IGBT switches should be selected accordingly. The current rating of each switch depends on the current that will flow through the switch. This current is due to the PV array current, and harmonic compensating current. In the proposed design $V_{dc}$ is equal to 800V therefore with safety factor of 1.5, voltage rating of IGBT should be 1200 V.

## 3.4. CHARACTERIZATION STUDIES OF SOLAR PV BASED MICROGRID

For efficient and reliable performance of PV based microgrid, sensitivity and reliability analysis need to be performed at the design stage. Sensitivity analysis is performed to determine the change in the behaviour of a system due to change in influential parameter while reliability is the system's ability to perform without fail under the stated period of time.

### 3.4.1. Sensitivity Analysis

Sensitivity analysis is the performance evaluation technique for evaluating the change in the system's performance with respect to the change in its parameters. Normalised sensitivity is the percentage variation in the value of the system for 1% variation in the value of the influential parameter. The normalized sensitivity of a function, F with respect to parameter 'n' can be evaluated by using equation (3.14):

$$\hat{S}_n^F = \frac{\frac{\partial F}{F}}{\frac{\partial n}{n}} = \left(\frac{n}{F}\right)\left(\frac{\partial F}{\partial N}\right) \tag{3.14}$$

If number of parameters change at the same time, the sensitivity is calculated by Jacobian matrix as given in equation (3.15):

$$J_{o_{ni}}^{F} = \begin{bmatrix} \frac{\partial F1}{\partial n1} & \frac{\partial F1}{\partial n2} \cdots & \frac{\partial F1}{\partial nN} \\ \vdots & \ddots & \vdots \\ \frac{\partial FA}{\partial n1} & \frac{\partial FA}{\partial n2} & \frac{\partial FA}{\partial nN} \end{bmatrix} \tag{3.15}$$

In the present work, the sensitivity analysis of solar cell parameters viz. photon current, short circuit current and open circuit voltage ($I_{CS}$, $I_{SCC}$, $V_{OC}$) is performed with respect to insolation and temperature (H, T). Further, sensitivity of boost converter output voltage has been determined with respect to inductance value, capacitance value and duty ratio.

Sensitivity functions of $I_{CS}$, $I_{SCC}$, $V_{OC}$ with respect to H, T are given by equation (3.16) to (3.21):

$$\hat{S}_{H}^{I_{CS}} = \frac{H}{I_{CS}} * \left( [1 + (T - T_{ref}) * K_i] * \frac{I_{scc}}{H_{ref}} \right) \tag{3.16}$$

$$\hat{S}_{T}^{I_{CS}} = \frac{T}{I_{CS}} \left( \frac{I_{scc} * K_i * H}{H_{ref}} \right) \tag{3.17}$$

$$\hat{S}_{H}^{I_{SCC}} = \frac{H}{I_{SCC}} \left( \frac{1}{1 + \frac{R_S}{R_{sh}}} * \frac{\partial I_{cs}}{\partial H} \right) \tag{3.18}$$

$$\hat{S}_{T}^{I_{SCC}} = \frac{T}{I_{SCC}} * \left( \frac{1}{1 + \frac{R_S}{R_{sh}}} * \frac{\partial I_{cs}}{\partial T} \right) \tag{3.19}$$

$$\hat{S}_{H}^{V_{OC}} = \frac{H}{V_{OC}} * \left( \frac{N_s \, A \, k \, T_{ac}}{q \, (I_{cs} + I_o)} * \frac{\partial I_{cs}}{\partial H} \right) \tag{3.20}$$

$$\hat{S}_{T}^{V_{OC}} = \frac{T}{V_{OC}} * \left[ - \left( \frac{N_s}{q} E_g - V_{oc} + \frac{N_s \, A \, k \, T_{ac}}{q} \left( 3 + \frac{\gamma}{2} \right) \right) \right] \tag{3.21}$$

Sensitivity Function of Boost Converter output voltage with respect to capacitance value (C), duty ratio (α) and inductance value (L) are given by equation (3.22) to (3.24):

$$\hat{S}_{C}^{V_{O/P}} = \frac{C}{V_{O/P}} \left( \frac{\Delta V \, f_{sw} \, V_{i/P} \, I_a}{(I_a - C \, \Delta V \, f_{sw})^2} \right) \tag{3.22}$$

$$\hat{S}_{\alpha}^{V_{O/P}} = \frac{\alpha}{V_{O/P}} \left( \frac{V_{i/p}}{(1-\alpha)^2} \right) \tag{3.23}$$

$$\hat{S}_{L}^{V_{O/P}} = \frac{L}{V_{O/P}} \left( \frac{\Delta I f_{sw} V_{i/p}^2}{(V_{i/P} - L \, \Delta I \, f_{sw})^2} \right) \tag{3.24}$$

### 3.4.2. Numerical results and Analysis

**Table 3.2. Sensitivity function and its values of solar cell and boost converter**

| Sensitivity Function | | PV Array Configuration | Partial Differentiation | Difference Equation |
|---|---|---|---|---|
| Solar Cell parameters | $\hat{S}_H^{I_{CS}}$ | S | 1.000 | 0.999 |
| | | P/SP/TCT/BL/HC | 1.000 | 0.999 |
| | $\hat{S}_T^{I_{CS}}$ | S | 0.097 | 0.098 |
| | | P/SP/TCT/BL/HC | 0.097 | 0.098 |
| | $\hat{S}_H^{I_{SCC}}$ | S | 0.998 | 0.998 |
| | | P/SP/TCT/BL/HC | 0.997 | 0.997 |
| | $\hat{S}_T^{I_{SCC}}$ | S | 0.096 | 0.096 |
| | | P/SP/TCT/BL/HC | 0.096 | 0.096 |
| | $\hat{S}_H^{V_{OC}}$ | S | 0.0040 | 0.0040 |
| | | P/SP/TCT/BL/HC | 0.0041 | 0.0041 |
| | $\hat{S}_T^{V_{OC}}$ | S | -1.05 | -0.99 |
| | | P/SP/TCT/BL/HC | -1.04 | -0.99 |
| Boost converter parameters | $\hat{S}_C^{V_{O/P}}$ | S | 0.57 | 0.56 |
| | | P/SP/TCT/BL/HC | 0.55 | 0.55 |
| | $\hat{S}_\alpha^{V_{O/P}}$ | S | 0.965 | 0.965 |
| | | P/SP/TCT/BL/HC | 0.964 | 0.964 |
| | $\hat{S}_L^{V_{O/P}}$ | S | 0.95 | 0.96 |
| | | P/SP/TCT/BL/HC | 0.94 | 0.95 |

Corresponding normalized sensitivity values calculated using data in appendix C are shown in table 3.2. The sensitivity values have been calculated for different PV array configuration. Further, to validate the results of sensitivity analysis, the sensitivity values obtained from sensitivity functions are compared with the results obtained from difference equations by changing values of parameters of interest by 1%. The two results conform.

It can be observed from table 3.2 that all the PV array configurations are equally sensitive to the parameters of interest. The effect of insolation on the $V_{oc}$ is least for all configuration while $I_{cs}$ is most sensitive with respect to insolation. Also, it can be seen that open circuit voltage is negatively affected by temperature which is also validated from figure 3.4. The $V_{oc}$ decreases with increase in temperature and increases with increase in insolation level.

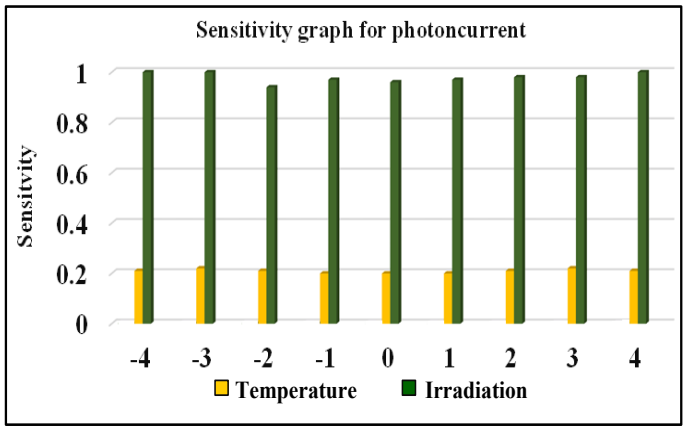


(a)

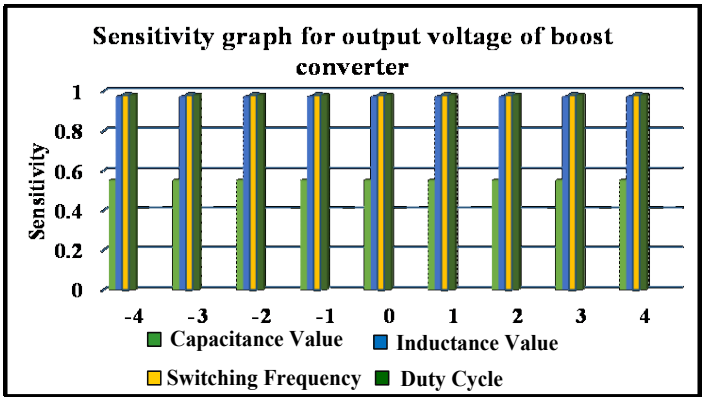


(b)

**Fig. 3.13. Sensitivity graphs for (a) Photoncurrent and (b) Boost converter output voltage**

Sensitivity graphs for photoncurrent with respect to temperature and irradiation, and boost converter output voltage with respect to capacitance value, inductance value, switching frequency and duty cycle has been obtained from the developed sensitivity functions. Fig. 3.13

(a) and (b) shows the calculated sensitivity values by changing each design variable from −4% to +4% in steps of 1%.

### 3.4.3. Reliability Analysis

According to Institute of Electrical and Electronic Engineers (IEEE), "Reliability is the ability of a system or component to perform its required functions under stated conditions for a specified period of time". Reliability model of the PV based microgrid has been developed using reliability block diagram considering different PV array configurations. The Fault tree analysis (FTA) model of the system has been developed. Further, Markov's model has been developed of individual components and from it the reliability model of the complete grid connected PV system has been developed.

#### 3.4.3.1 Component Reliability

Reliability of any system depends upon the probability of its components functioning satisfactorily over the specified interval of time. As the actual working condition of components are different than the conditions at which they are tested, to compute the reliability of components, actual failure rate ($\lambda_p$) needs to be calculated. Failure rate ($\lambda$) can be defined as the anticipated number of times that an item fails in a specified period of time. Actual failure rate can be calculated by multiplying manufacturer failure rate ($\lambda_b$) values, listed in MIL-HDBK 217, with its stress factors is given by equation (3.25):

$$\lambda_p = \lambda_b(\prod_{i=1}^{n} \mu_i) \tag{3.25}$$

where, $\mu_i$ is the product of all stress factors of electronics components in the system. The various stress factors considered are reverse voltage index failure of diode ($\mu_s$), device power rating ($\mu_a$), capacitance value ($\mu_c$), temperature ($\mu_t$), component's quality ($\mu_q$), operational environment ($\mu_e$), capacitor voltage index factor ($\mu_v$), power factor ($\mu_p$) and power stress factor ($\mu_{ps}$).

The mean time between failure (MTBF) can be expressed in relation to failure rate as given by equation (3.26):

$$MTBF = \lambda_p^{-1} \tag{3.26}$$

Then reliability can be computed from equation (3.27),

$$Reliability, R_i = e^{-\lambda_p t} \tag{3.27}$$

Table 3.3. and 3.4. tabulates the failure rate, in per million hours and MTBF, in hours, of the various electronics and electrical components respectively [29,30,112].

**Table 3.3. Failure rate and MTBF of Electronics components**

| Electronic Devices | Manufacture Failure Rate | Stress Factors | | | | | | | | | Actual Failure Rate | MTBF |
|---|---|---|---|---|---|---|---|---|---|---|---|---|
| | $\lambda_b$ | $\mu_s$ | $\mu_{ps}$ | $\mu_a$ | $\mu_c$ | $\mu_q$ | $\mu_e$ | $\mu_v$ | $\mu_p$ | $\mu_t$ | $\lambda_p$ | $\lambda_p^{-1}$ |
| **Inductor** | $3.24*10^{-5}$ | | | | | 20 | 1 | | | $\exp\left(-\frac{0.11}{8.617*10^{-5}}\left[\frac{1}{T_j+273}-\frac{1}{298}\right]\right) = 2.36$ Where, $T_j$=Junction Temperature | 0.00152 | $6.578\times 10^8$ |
| **Resistor** | 0.0037 | | 2.3 | | | 10 | 1 | | 1 | $\exp\left(-\frac{0.08}{8.617*10^{-5}}\left[\frac{1}{T+273}-\frac{1}{298}\right]\right) = 10.58$ Where, T= Temperature | 0.9003 | $1.109\times 10^6$ |
| **Switch** | 0.012 | | | 10 | | 8 | 1 | | | $\exp\left(-1925\left[\frac{1}{T_j+273}-\frac{1}{298}\right]\right) = 3.63$ | 3.48 | $2.87\times 10^5$ |
| **Diode** | 0.03 | $V_s^{2.43} = 0.29$ | | | | 8 | 1 | | | $\exp\left(-3091\left[\frac{1}{T_j+273}-\frac{1}{298}\right]\right) = 8.004$ | 0.271 | $3.690\times 10^6$ |
| **Capacitor** | $7*10^{-4}$ | | | | $C^{0.23} = 1.3$ | 10 | 1 | 5.21 | | $\exp\left(-\frac{0.35}{8.617*10^{-5}}\left[\frac{1}{T+273}-\frac{1}{298}\right]\right) = 15.33$ | 0.1245 | $8.032\times 10^6$ |

**Table 3.4. Failure rate and MTBF of Electrical components**

| Component | Failure Rate | MTBF |
|---|---|---|
| PV Module | 0.0152 | $6.578\times10^7$ |
| Inverter | 21.2 | $4.7169\times10^4$ |
| Battery Energy Storage System | 10.958 | $9.125\times10^4$ |
| Charge Controller | 5.479 | $1.8251\times10^5$ |
| Load | 10 | $1\times10^5$ |

Pareto analysis of the electronic and electrical components is shown in figure 3.14 (a) and (b). From table 3.3, 3.4 and figure 3.14 (a) and (b), it can be concluded that switch and inverter have the highest failure rate amongst electronics and electrical components respectively.

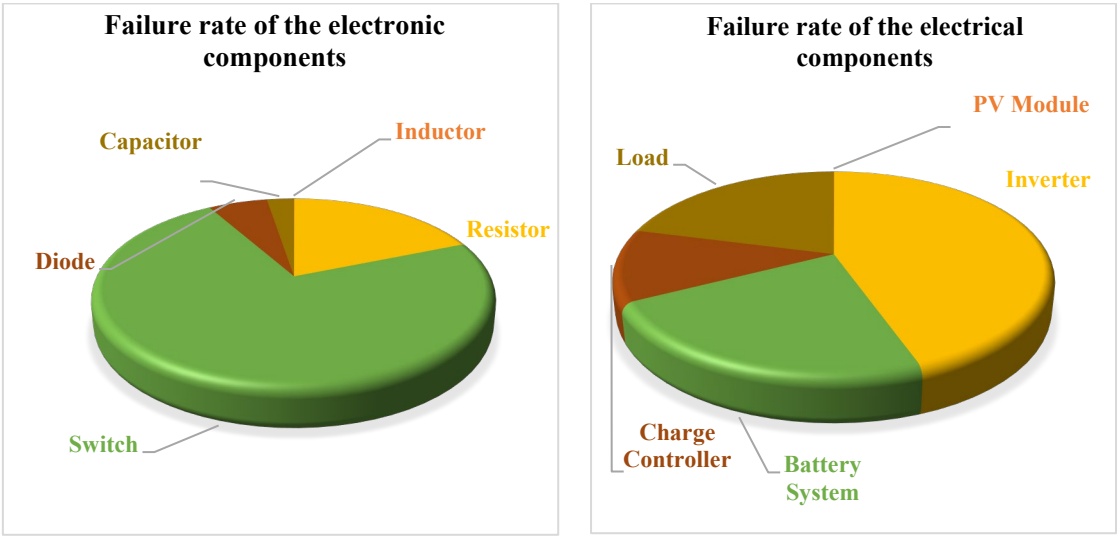


**Fig. 3.14. Pareto Analysis of (a) Electronic components and (b) Electrical Components**

Failure rate of a system, $\lambda_{sys}$, can be calculated by the summation of failure rate of all the individual components ($\lambda_{inco}$).

$$\lambda_{sys} = \sum \lambda_{inco} \tag{3.28}$$

The reliability of individual components can be calculated as given by equation (3.29):

$$Reliability = e^{-\lambda_{inco} t} \tag{3.29}$$

Reliability of the system with components connected in series is given by equation (3.30):

$$R_{series} = \prod_{i=1}^{n} R_i \tag{3.30}$$

and the reliability of the system with components connected in parallel is given by equation (3.31):

$$R_{parallel} = 1 - \prod_{i=1}^{n} (1 - R_i) \tag{3.31}$$

**3.4.3.2. Reliability calculation of different PV array configuration** - The reliability of different PV array configurations has been calculated as below.

Case 1 (Series $R_S$): For series configuration of PV array, all PV modules are connected in series as shown in figure 3.15 (a) and the reliability $R_s$ can be calculated by using equation (3.30).

Case 2 (Parallel $R_p$): For parallel PV array configuration, all PV modules are connected in parallel with each other as shown in figure 3.15 (b) and the reliability $R_p$ has been calculated using equation (3.31).

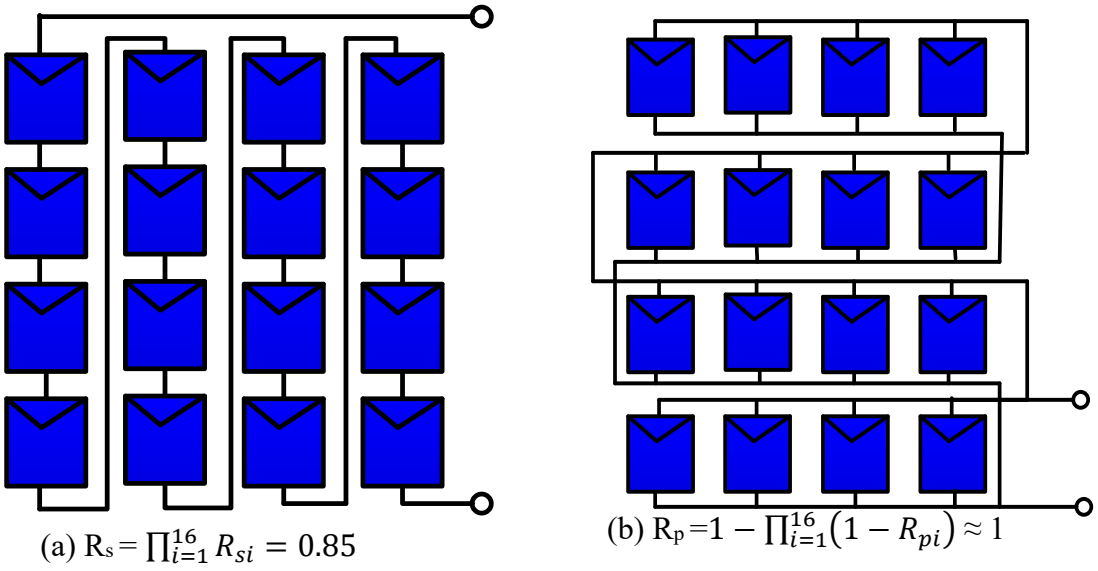


**Fig. 3.15. Reliability calculation of (a) Series PV array configuration and (b) Parallel PV array configuration**

Case 3 (Series-Parallel $R_{SP}$): The PV string (each column) in array configuration is connected in series as shown in figure 3.16. So firstly, the reliability of each string of PV array, $R_{PVst}$, is calculated and finally, the reliability of series-parallel combination, $R_{SP}$, of PV array has been calculated.

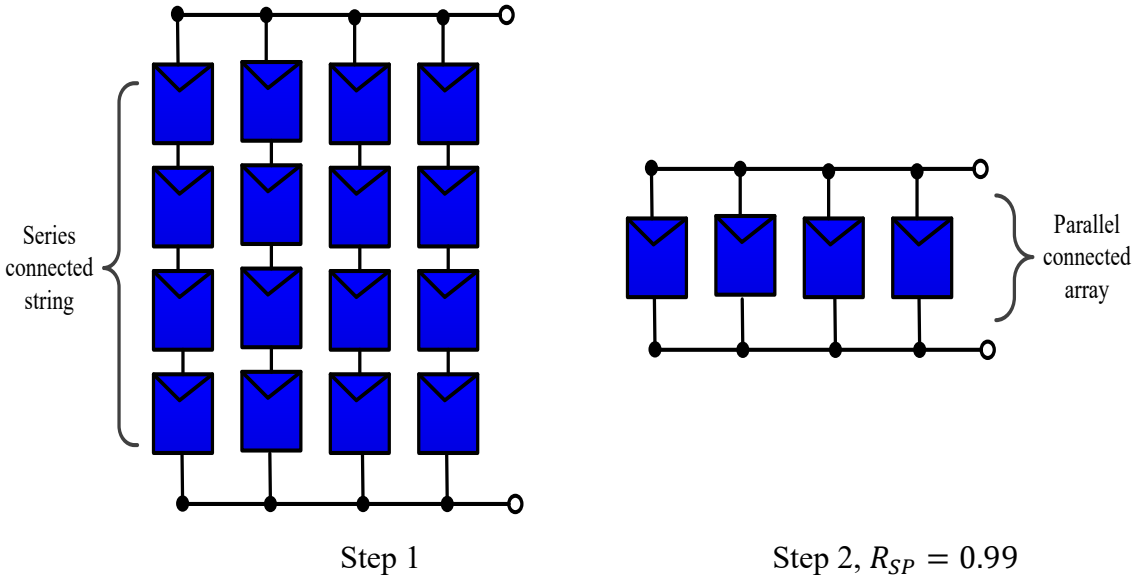


**Fig. 3.16. Reliability calculation of Series-Parallel PV array configuration**

Case 4 (Total Cross Tied): In total cross tied PV array configuration as shown in figure in 3.17, each row is connected in parallel and further, the PV array is reduced to series connection, $R_{pst}$.

Finally, the reliability of TCT configuration, $R_{TCT}$, of PV array has been calculated. The reliability of total cross tied PV array configuration is 0.96.

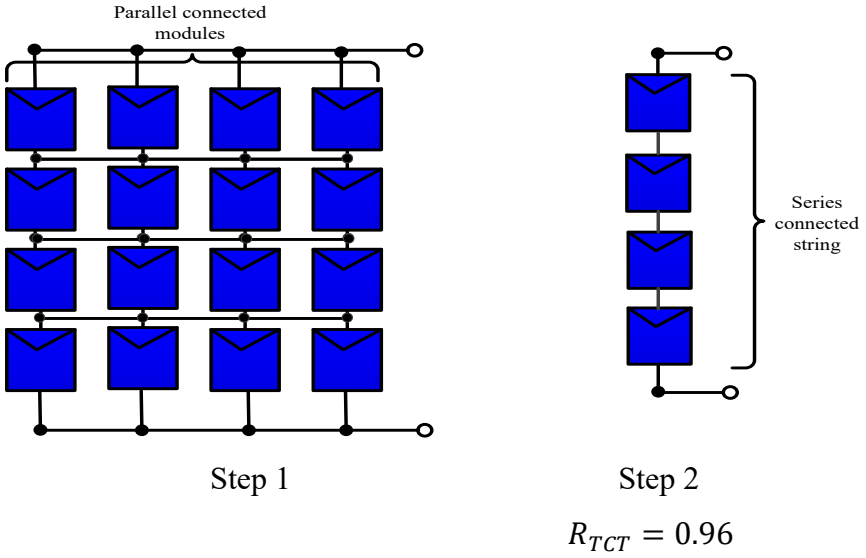


**Fig. 3.17. Reliability calculation of Total Cross Tied PV array configuration**

Case 5 (Bridge Linked): The bridge linked PV array configuration is shown in figure 3.18. In step 1, the reliability of PV modules connected in series is calculated using equation (3.30) and then in step 2 the reliability of PV modules connected in parallel is calculated using equation (3.31). Further, using star to delta conversion, star connection is converted into delta. The reliability of bridge linked PV array configuration is 0.99.

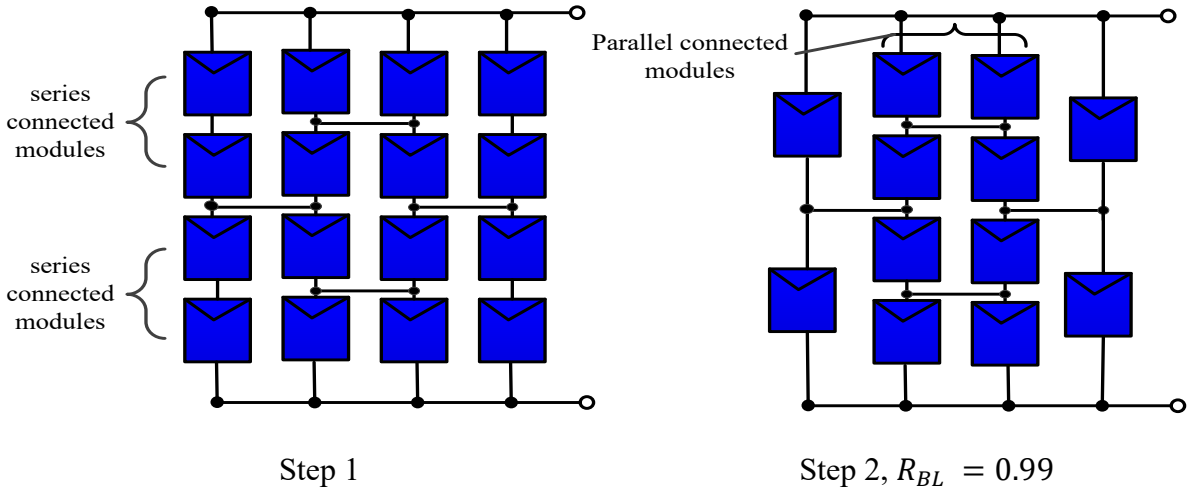


**Fig. 3.18. Reliability calculation of Bridge linked PV array configuration**

Case 6 (Honey Comb): The honey comb PV array configuration is shown in figure 3.19. The reliability of PV modules connected in series is calculated using equation (3.30) and then the reliability of PV modules connected in parallel is calculated using equation (3.31). Further, using

star to delta conversion, star connection is converted into delta. The reliability of honey comb PV array configuration is 0.99.

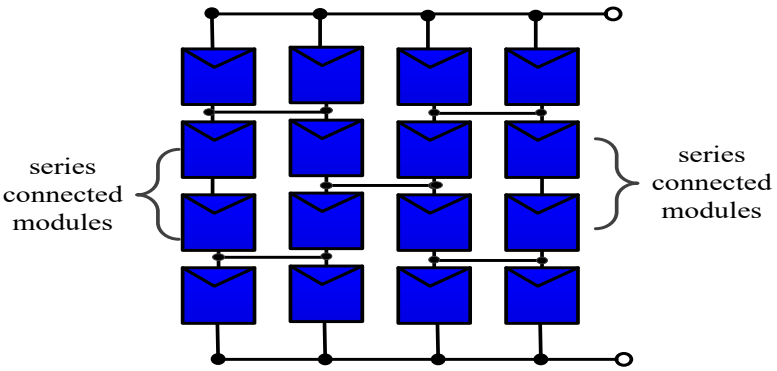


$$R_{HC} = 0.99$$

**Fig. 3.19. Reliability calculation of Honey comb PV array configuration**

**Table 3.5. Reliability of different PV array configuration**

| PV array Configuration | *Reliability* |
|---|---|
| **Series** | 0.85 |
| **Parallel** | ≈1 |
| **TCT** | 0.96 |
| **SP/ BL/HC** | 0.99 |

**3.4.3.3. Reliability of SPV based microgrid**: In this section, the reliability model of SPV based microgrid has been developed using reliability block diagram, FTA and Markov model.

**Reliability Block Diagram**

1) Stand-alone SPV based microgrid:

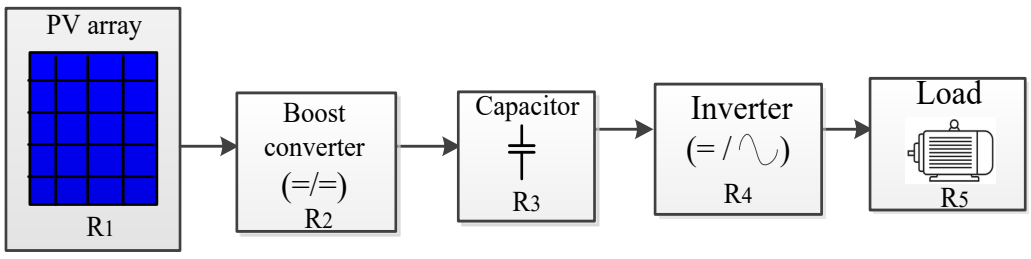


**Fig. 3.20. Reliability block diagram of stand-alone SPV based microgrid**

Figure 3.20 shows the reliability block diagram of stand-alone SPV system. The reliability of the various components is given in appendix D [30].

$$R_{stand-alone} = R_1 * R_2 * R_3 * R_4 * R_5 \quad (3.32)$$

2) Stand-alone SPV based microgrid with BESS: Figure 3.21 shows the reliability block diagram of stand-alone SPV system with BESS.

$$R_{stand-aloneBESS} = [1 - (1 - R_1 * R_2)(1 - R_6 * R_7)]R_3 * R_4 * R_5 \quad (3.33)$$

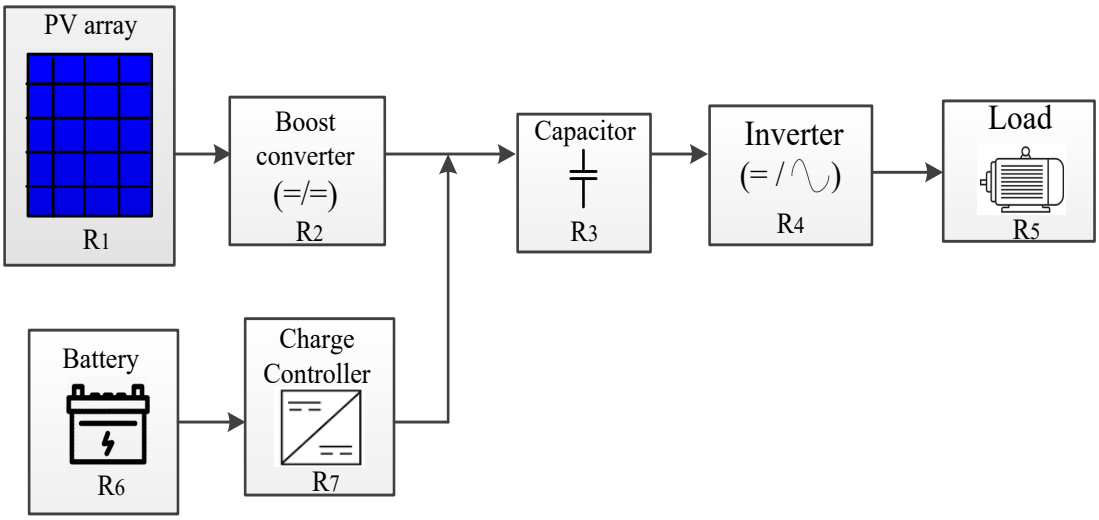


**Fig. 3.21. Reliability block diagram of stand-alone SPV based microgrid with BESS**

3) Grid interfaced SPV based microgrid with BESS: Figure 3.22 shows the reliability block diagram of SPV based microgrid with BESS. The reliability of the complete PV system, $R_{PVB}$, is calculated by series-parallel combination network, so it can be calculated by:

$$R_{PVB} = \left[1 - \left\{\left(1 - \left(1 - (R_1 * R_2)\right)\left(1 - (R_6 * R_7)\right)\right) * R_3 * R_4\right\}\{1 - R_8 * R_9 * R_{10}\}\right] * R_5 \quad (3.34)$$

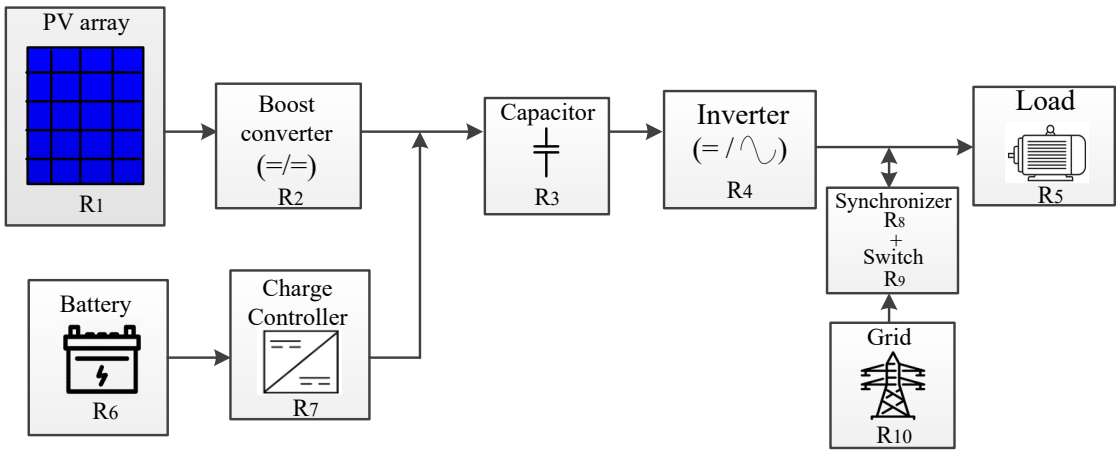


**Fig. 3.22 Reliability block diagram of grid interfaced PV based microgrid with BESS**

### 3.4.3.4. Numerical results and Analysis

The reliability values for different PV array configurations have been given in table 3.5. It can be seen that, the reliability of parallel PV array configuration is highest i.e., approximately equal to 1. This implies, even if any module fails, the PV array still continue to work as all PV modules in an array are connected in parallel with each other. The reliability of series-parallel, bridge link and honey comb PV array configuration is 0.99, while series PV array configuration is least reliable among all.

The reliability values of grid interfaced PV based microgrid with BESS and stand-alone PV system with different configurations can be calculated using equation (3.32) to (3.34) and are shown in table 3.6. It can be concluded, that the grid connected PV based microgrid with BESS is more reliable than stand-alone PV based microgrid.

**Table 3.6. Reliability of stand-alone and PV based microgrid with BESS**

| PV array Configuration | $R_{stand\text{-}alone}$ | $R_{stand\text{-}aloneBESS}$ | $R_{PVB}$ |
|---|---|---|---|
| **Series** | 0.59 | 0.72 | 0.88 |
| **Parallel** | 0.71 | 0.73 | 0.88 |
| **SP/ TCT/BL/HC** | 0.70 | 0.73 | 0.88 |

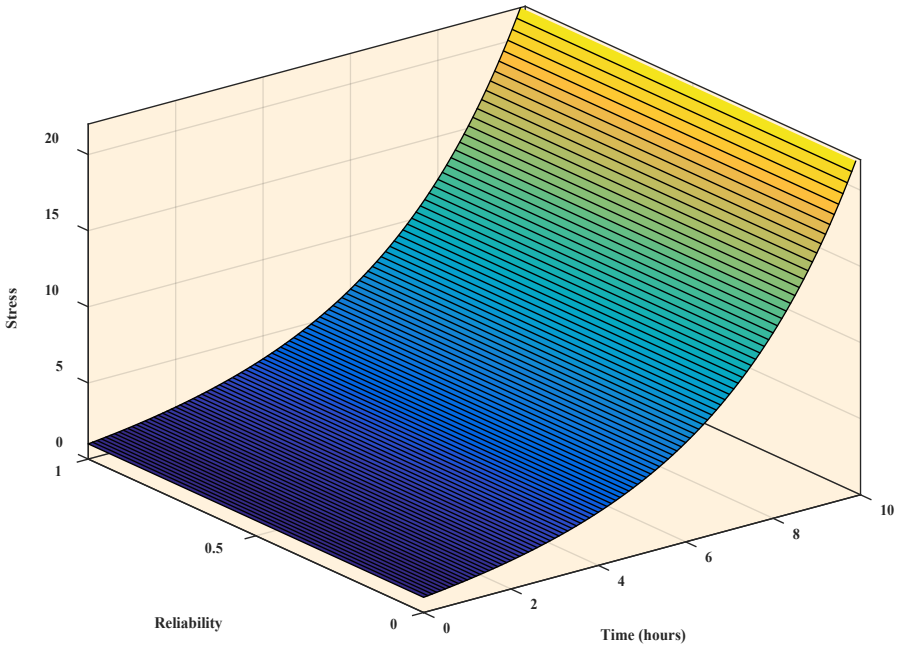


**Fig. 3.23. 3-D Reliability curve of grid interfaced PV based microgrid with BESS considering stress factor.**

Figure 3.23 shows the 3-D curve of reliability vs time vs stress factor considering the dependence of the PV system on inverter functioning. The reliability of inverter depends upon the reliability of its switch, which in turn, depends on various considered stress factors.

### 3.4.3.5. Fault Tree Analysis (FTA) Model

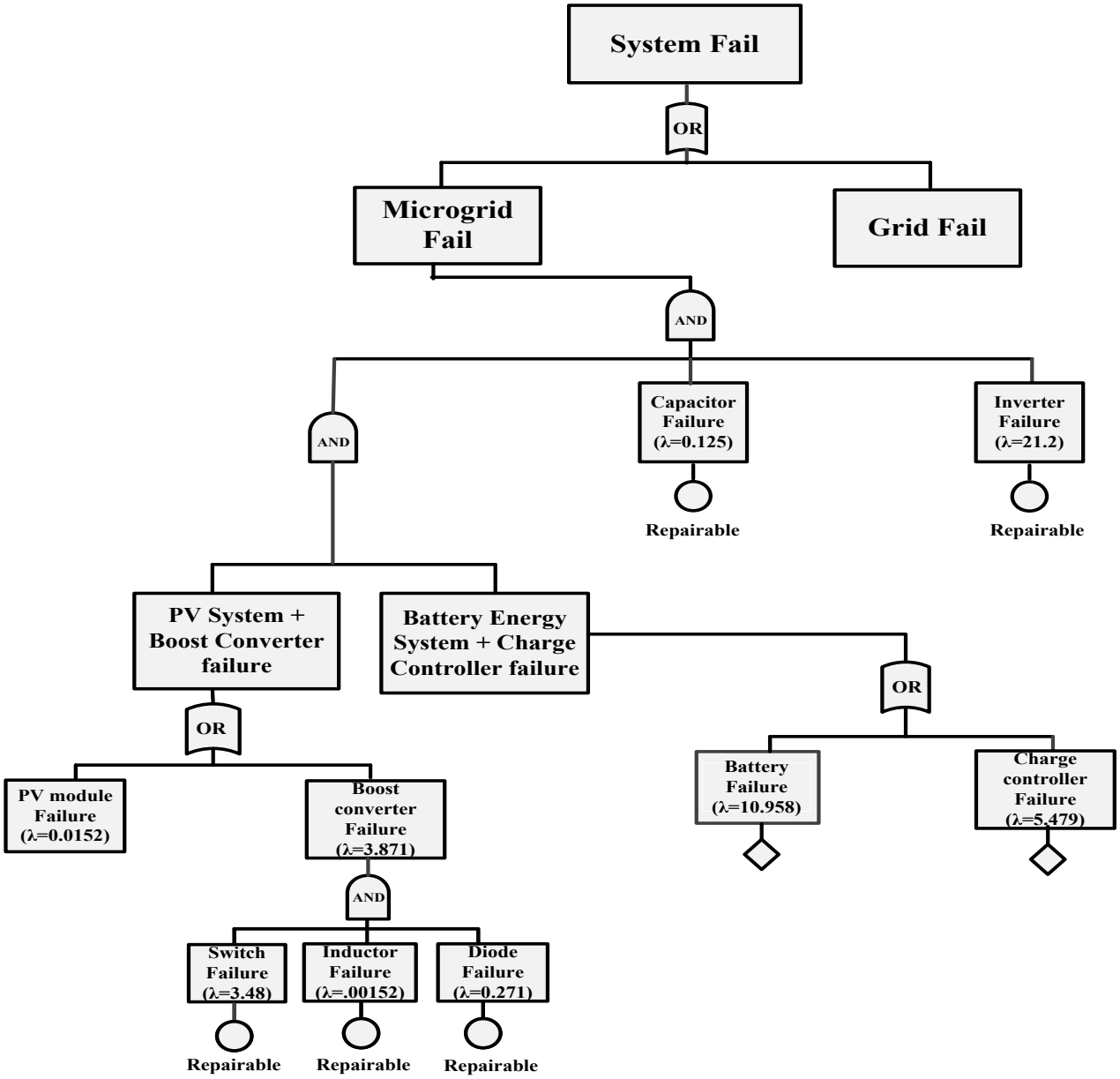


**Fig. 3.24. FTA model of grid interfaced PV based microgrid with BESS**

Fault tree analysis is a graphical tool to find the causes of system level failures. It uses Boolean logic to combine a series of lower-level events and it is basically a top-down approach to identify the component level failures (basic event) that cause the system level failure (top event) to occur. Fault tree comprises of event and logic gates. To determine the reliability, FTA finds the cause of failure or it steps the events serially. The concerned failure event is the top event, and down

events causing the occurrence of top event have been depicted [33]. Fault tree of the proposed system has been developed in occurrence of the events in the system and is shown in figure 3.24. The top event is system failure that can occur due to either failure of microgrid or conventional grid. The down events are listed with their failure rate which lead to the occurrence of top event.

### 3.4.3.6. Markov Reliability Model (MRM)

Markovian methods are useful tools for evaluating the reliability of a system that has multiple states. In the framework of Markovian models, the transitions between various states are characterized by constant transition rates.

Markov reliability modeling is a widely used technique in the study of reliability analysis of system. The MRM is stochastic based approach for modelling the system having many states and transition among states. In Markov model, the transition probability $S_{ij}$, is the probability of transition from *i* (working) to *j* (failed) [31]. The sequence of events occurring at discrete state {S = ($s_o$, $s_1$, $s_2$….$s_n$)} is said to form Markov chain. The transitioning probability $S_{ij}$ of going from i to j is expressed as given in equation (3.35):

$$S_{ij} = P\{S(k) = j | S(0) = i\} \tag{3.35}$$

The probability of each state can be calculated using the Chapman–Kolmogorov equation [154] and is given by the following equation:

$$\frac{dS(k)}{dt} = S(k) * Q \tag{3.36}$$

The transition probabilities $S_{ij}$ of a Markov chain form a n x n square matrix, is called transition matrix,

$$\frac{d}{dt}\overrightarrow{S} = \frac{d}{dt}\begin{bmatrix} s_1 \\ s_2 \\ \vdots \\ s_n \end{bmatrix} = \begin{bmatrix} Q_{11}\, Q_{12} & \cdots & Q_{1n} \\ \vdots & \ddots & \vdots \\ Q_{n1} Q_{n2} & \cdots & Q_{nn} \end{bmatrix} \times \begin{bmatrix} s_1 \\ s_2 \\ \vdots \\ s_n \end{bmatrix} = Q \times \overrightarrow{S} \tag{3.37}$$

where Q is the transition probability matrix and $\overrightarrow{S}$ is the probability vector. The solution of above equation gives the probability of the component transitioning states represented as:

$$\mathrm{S}(k) = e^{Qt} * S(0) \tag{3.38}$$

**Markov model of individual component**

1) PV Array: The PV panel operates in any two states viz working (1) or fail (0). Failure of whole PV array makes the system in failed (0) state. Figure 3.25 (a) shows the two states: 1(working) and 0 (failed). The probability of failure of PV panel is given by:

$$\frac{d}{dt}\begin{bmatrix} S_0 \\ S_1 \end{bmatrix} = \begin{bmatrix} -\left(\lambda_{PV_{Array}}\right) & \left(\lambda_{PV_{Array}}\right) \\ (\upsilon_{PV}) & -(\upsilon_{PV}) \end{bmatrix} \begin{bmatrix} S_0 \\ S_1 \end{bmatrix} \tag{3.39}$$

Initially the PV panel is in working state, the reliability of PV panel to be in working state is given by,

$$R_{PV_{Array}}(t) = S_0(t) = \frac{\upsilon_{PV}}{\lambda_{PV_{Array}} + \upsilon_{PV}} + e^{-\left(\lambda_{PV_{Array}} + \upsilon_{PV}\right)t} \tag{3.40}$$

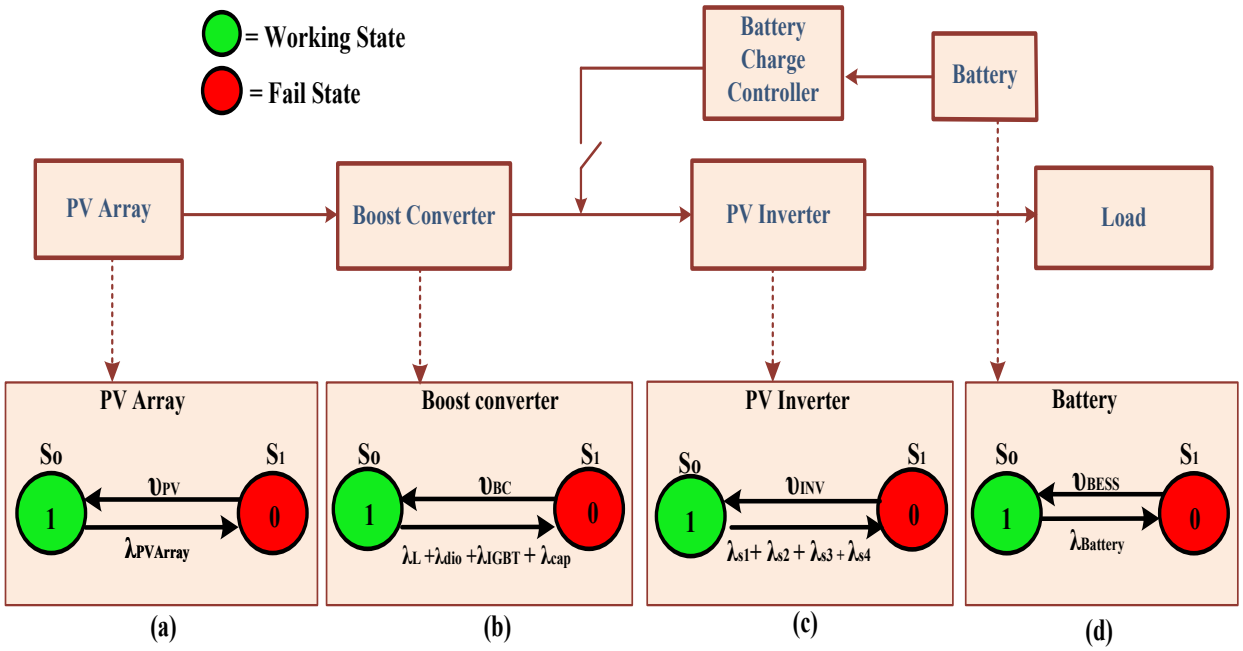


**Fig. 3.25. Markov state transition diagram of (a) PV array (b) Boost Converter (c) PV inverter (d) Battery**

2) Boost Converter: The boost converter (BC) is composed of inductor (L), capacitor (cap), diode (dio) and IGBT. The failure of any of the components makes the converter to be in failed (0) state. So, the Markov transition diagram for boost converter has two states viz. working (1) or fail (0). The probability matrix is given by,

$$\frac{d}{dt}\begin{bmatrix} S_0 \\ S_1 \end{bmatrix} = \begin{bmatrix} -\left(\lambda_L + \lambda_{dio} + \lambda_{IGBT} + \lambda_{cap}\right) & \left(\lambda_L + \lambda_{dio} + \lambda_{IGBT} + \lambda_{cap}\right) \\ (\upsilon_{BC}) & -(\upsilon_{BC}) \end{bmatrix} \begin{bmatrix} S_0 \\ S_1 \end{bmatrix} \tag{3.41}$$

Assuming the boost converter initially is in working state (1), the reliability of the converter is given by,

$$R_{boost}(t) = S_0(t) = \frac{\upsilon_{BC}}{\lambda_L + \lambda_{dio} + \lambda_{IGBT} + \lambda_{cap} + \upsilon_{BC}} + e^{-\left(\lambda_L + \lambda_{dio} + \lambda_{IGBT} + \lambda_{cap} + \upsilon_{BC}\right)t} \tag{3.42}$$

3) PV Inverter: PV inverter (INV) has four IGBT switches ($S_1$, $S_2$, $S_3$, $S_4$) for converting dc voltage into ac voltage of desired magnitude and frequency for supplying ac load. So, failure of

any switch makes the inverter to lie in fail (0) state. The probability matrix for PV inverter is given below and Markov state transition diagram is shown in figure 3.25 (c).

$$\frac{d}{dt}\begin{bmatrix}S_0\\S_1\end{bmatrix}=\begin{bmatrix}-(\lambda_{s1}+\lambda_{s2}+\lambda_{S3}+\lambda_{S4}) & (\lambda_{s1}+\lambda_{s2}+\lambda_{S3}+\lambda_{S4})\\ (\upsilon_{INV}) & -(\upsilon_{INV})\end{bmatrix}\begin{bmatrix}S_0\\S_1\end{bmatrix} \tag{3.43}$$

Assuming the PV inverter initially is in working state (1), the reliability of the inverter is given by,

$$R_{PVinverter}(t)=S_0(t)=\frac{\upsilon_{INV}}{\lambda_{s1}+\lambda_{s2}+\lambda_{S3}+\lambda_{S4}}+e^{-(\lambda_{s1}+\lambda_{s2}+\lambda_{S3}+\lambda_{S4}+\upsilon_{INV})t} \tag{3.44}$$

4) Battery Energy Storage System (BESS): The BESS works in either of the two states viz working (1) or fail (0). The battery failure makes the component to be in non-working stage i.e. fail (0) state. The probability matrix is given by

$$\frac{d}{dt}\begin{bmatrix}S_0\\S_1\end{bmatrix}=\begin{bmatrix}-\lambda_{Battery} & \lambda_{Battery}\\ (\upsilon_{BESS}) & -\upsilon_{BESS}\end{bmatrix}\begin{bmatrix}S_0\\S_1\end{bmatrix} \tag{3.45}$$

Assuming the BESS initially is in working state (1), the reliability is given by,

$$R_{Battery}(t)=S_0(t)=\frac{\upsilon_{BESS}}{\lambda_{Battery}+\upsilon_{BESS}}+e^{-(\lambda_{Battery}+\upsilon_{BESS})t} \tag{3.46}$$

**Markov model of grid interfaced PV based Microgrid with BESS**

Figure 3.26 (a) shows the markov state transition diagram grid interfaced PV based Microgrid with BESS. The system works in five stages: (condition 1(111)) when PV source, BESS and inverter are healthy; (condition 2(011)) - when PV array and boost converter fails; (condition 3(110)) - when BESS and bidirectional boost converter controller fails; (condition 4(000)) - when complete system fails. The failure states are given as ($\lambda_A = (\lambda_{pvarray} + \lambda_{boost})$, $\lambda_B = (\lambda_{BESS} + \lambda_{chargecontroller})$ and $\lambda_{inv} = \lambda_{inverter}$). The probability matrix of grid interfaced PV based Microgrid with BESS is given by:

$$\frac{d}{dt}\begin{bmatrix}S_0\\S_1\\S_2\\S_3\end{bmatrix}=\begin{bmatrix}-(\lambda_A+\lambda_B+\lambda_{inv}) & \lambda_A & \lambda_B & \lambda_{inv}\\ 0 & -\lambda_B & 0 & \lambda_B\\ 0 & 0 & -\lambda_A & \lambda_A\\ -\lambda_{inv} & 0 & 0 & \lambda_{inv}\end{bmatrix}\begin{bmatrix}S_0\\S_1\\S_2\\S_3\end{bmatrix} \tag{3.47}$$

Further, the markov state transition diagram of complete system has been developed considering their repair rate as shown in figure 3.26 (b). The fail states are same as discussed above. The repair rates which is defined as "the frequency of successful repair operations performed on a failed component per unit time" are $\upsilon_A = (\upsilon_{pvarray} + \upsilon_{boost})$, $\upsilon_B = (\upsilon_{BESS} + \upsilon_{birdirectionalconv})$,

$\upsilon_{inv} = \upsilon_{inverter}$. The probability matrix of grid interfaced PV based Microgrid with BESS considering repair rate is given by:

$$\frac{d}{dt}\begin{bmatrix} S_0 \\ S_1 \\ S_2 \\ S_3 \end{bmatrix} = \begin{bmatrix} -(\lambda_A + \lambda_B) & \lambda_A & \lambda_B & 0 \\ \upsilon_A & -(\lambda_B + \upsilon_A) & 0 & \lambda_B \\ \upsilon_B & 0 & -(\lambda_A + \upsilon_B) & \lambda_A \\ (\lambda_{inv} + \upsilon_{inv}) & 0 & 0 & -(\lambda_{inv} + \upsilon_{inv}) \end{bmatrix} \begin{bmatrix} S_0 \\ S_1 \\ S_2 \\ S_3 \end{bmatrix} \tag{3.48}$$

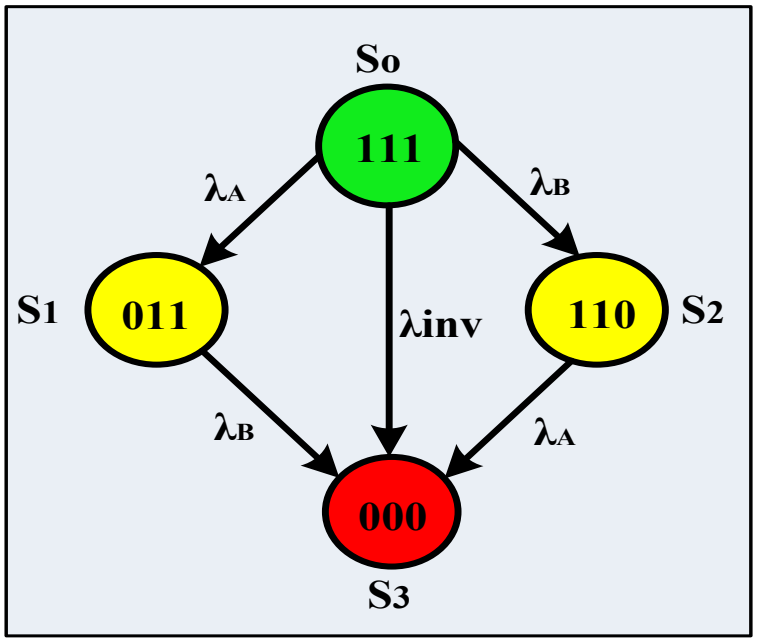


**(a)**

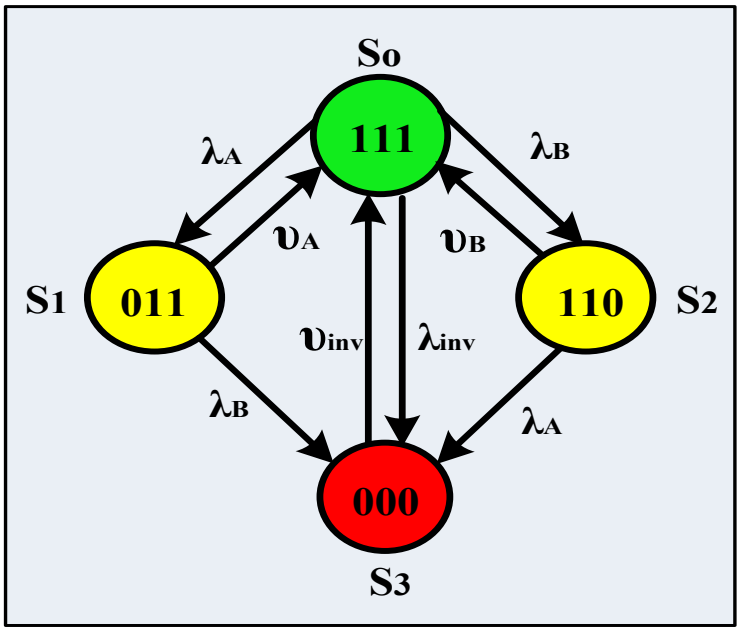


**(b)**

**Fig. 3.26 Markov state transition diagram of (a) Grid interfaced PV based microgrid with BESS (b) Grid interfaced PV based microgrid with BESS considering repair rate**

## 3.5. CONCLUDING REMARKS

In this chapter, modelling and design of stand-alone SPV system and grid integrated SPV based microgrid have been presented. Further, characterization studies for grid interfaced PV based microgrid considering different PV array configurations (S, P, SP, TCT, BL, HC) has been performed. The sensitivity functions for solar cell parameters and boost converter output voltage with respect to parameters of interest have been developed and their numerical values have been calculated.

Reliability model for the system under study has been developed using reliability block diagram, fault tree analysis and Markov model. Pareto analysis is performed to identify the component with highest failure rate. The reliability analysis of the proposed system for various PV array configurations has been carried out and it has been observed that parallel configuration has highest reliability and series configuration has lowest reliability. Also, the reliability of various SPV system viz. stand-alone, stand-alone with BESS and grid connected with BESS has been calculated. It can be concluded that the grid interfaced PV based microgrid with BESS is more reliable than stand-alone PV based microgrid for various PV array configurations considered. The fault tree has been developed for the proposed system. System failure is represented at the top of an event and subsequent down events which make the happening of top event. The down events are indicated with its failure rate. Furthermore, Markov reliability model, considering failure rate and repair rate has been developed for individual component of the system as well as for the complete system and their reliability model has been developed.

# CHAPTER-IV

# MPPT CONTROL ALGORITHMS FOR SOLAR PV SYSTEM UNDER PARTIAL SHADING CONDITION

## INTRODUCTION

In the previous chapter, the modelling and design of solar PV based microgrid has been presented and characterization studies for different PV array configurations have been carried out. This chapter presents the development of maximum power point tracking algorithms for SPV system under partial shading conditions (PSC). Under PSC, P-V curve of SPV exhibits multiple peaks consisting of a single global maximum power point (GMPP) and many local maximum power points (LMPP). The presence of multiple peaks makes tracking of maximum power point more difficult and demands an efficient controller to track the global peak of the P-V curve. In this chapter, two novel MPPT control algorithms viz. Asymmetrical fuzzy logic control (FLC) algorithm and Asymmetrical interval type-2 FLC control algorithm are developed to track maximum power from SPV system under partial shading conditions. The efficacy of the developed control algorithms has been tested for various PV array configurations under different shading scenarios. The performance of the proposed control algorithms has been compared with conventional algorithms.

## 4.2. MAXIMUM POWER POINT TRACKING CONTROL ALGORITHMS FOR PSC

The PV panel gives optimum output under uniform irradiation, and its output is negatively affected by partial shading. Partial shading is the condition when PV array is not uniformly irradiated and can be caused because of shade of nearby buildings/towers, big trees, dense clouds, dust and aging or cracking. A major consequence of partial shading is that the P-V curve of SPV exhibits multiple peaks.

---

This chapter is based on the papers - (i) "Asymmetrical interval type-2 fuzzy logic control based MPPT tuning for PV system under partial shading condition" ISA Transactions, Vol. 100, 2020, pp. 251–263. doi: https://doi.org/10.1016/j.isatra.2020.01.009. (ii) Asymmetrical Fuzzy Logic Control based MPPT algorithm for Stand-alone PV System Under Partially Shaded Conditions" International Journal of Science & technology, Vol. 27, Iss. 6, pp. 3162-3174, 2020. doi: 10.24200/SCI.2019.51737.2338. (iii) "Comparison of intelligent and conventional MPPT algorithms for photovoltaic system under partially shahded conditions" Recent Developments in Control, Automation & Power Engineering (RDCAPE), pp. 505-510, Noida, India, 2017. (iv) "Adaptive MPPT Algorithm for stand-alone PV System under Partial Shading Condition" Journal of Emerging Technologies and Innovative Research, September 2018, Vol 5, Iss. 9, pp.1086-1093.

Figure 4.1 shows the P-V curves of the PV system under different shading patterns. It is evident from figure 4.1 that under PSC, the P-V curve has multiple peaks viz. GMPP and LMPP.

Conventional MPPT algorithms track global peak power under uniform irradiation efficiently as PV array depicts only one peak. Under PSC, conventional MPPT algorithms reaches first peak of PV array i.e., mostly the local peak and lurch around it instead of tracking the highest peak [69], [78], [156]–[161]. Therefore, more efficient MPPT controller is required to track global peak.

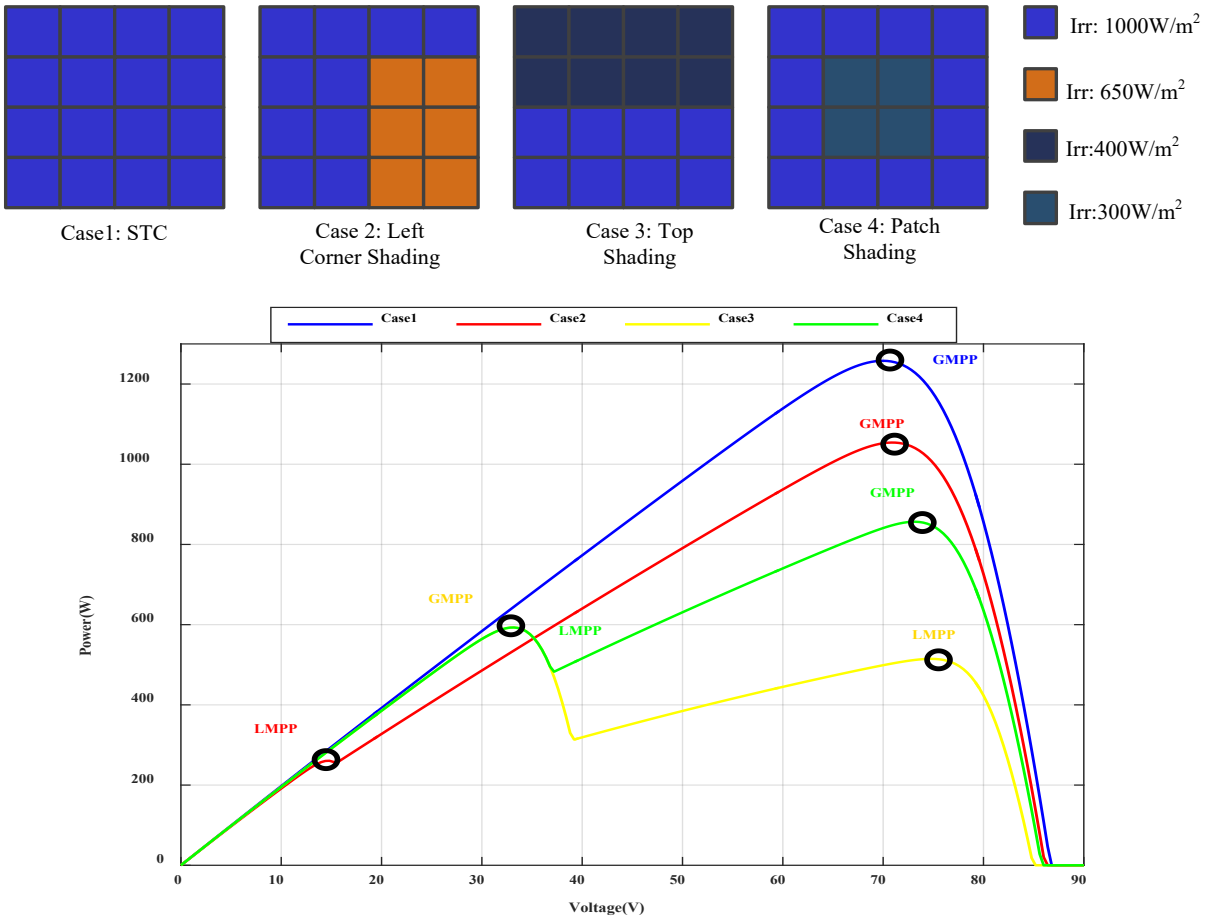


**Fig. 4.1. Simulated Power vs. Voltage curve under partial shading condition**

In the present work, the MPPT control algorithms used to track GMPP under PSC can be classified as and are explained in subsequent sections

- Adaptive Control Algorithm
  - Adaptive Neuro Fuzzy Inference System (ANFIS) Algorithm
- Intelligent Control Algorithms
  - Proposed Asymmetrical Fuzzy Logic Control (AFLC) Algorithm
  - Proposed Asymmetrical interval type-2 FLC (AIT-2 FLC) Algorithm

### 4.2.1. ADAPTIVE CONTROL ALGORITHM

An adaptive control covers a set of techniques which provides a systematic approach for automatic adjustment of controllers, in order to achieve or to maintain a desired level of control system performance when the parameters of the system dynamic model are unknown or change with time. There are many adaptive control algorithms such as model reference adaptive controllers, model identification adaptive controllers, Adaptive Neuro Fuzzy Inference System (ANFIS), nonparametric and parametric adaptive controllers etc. In the present chapter, ANFIS has been used which is explained below.

#### 4.2.1.1. ANFIS Control Algorithm

ANFIS is an adaptive control algorithm which integrates neural networks (learning and parallel data processing abilities) with fuzzy logic (reasoning abilities) [33].

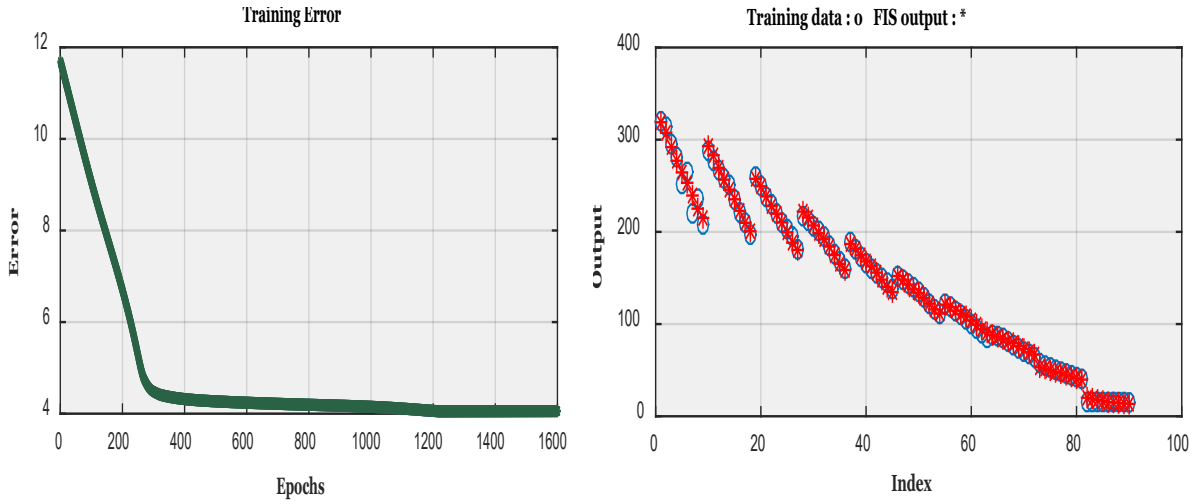


(a) (b)

**Fig. 4.2. (a) Training error v/s Epoch waveform for ANFIS (b) Training Data and FIS output v/s index waveform.**

ANFIS builds a set of fuzzy if-then rules with appropriate membership functions to generate the given input-output pairs and uses a hybrid optimization technique, which is a combination of least square type method and backpropagation algorithm, for training. Solar irradiation and temperature are used to generate the training data set by varying the irradiation level from 0.1kW/m$^2$ to 1kW/m$^2$ in a fixed step of 0.05kW/m$^2$ and temperature from 20$^{\circ}$C to 60$^{\circ}$C in step of 5$^{\circ}$C. The retrieved training data is saved in a workspace of MATLAB Figure 4.2 (a) shows training error v/s epoch waveform. The training error has been reduced to approximately 4% as seen from the figure. Figure 4.2 (b) shows the training data and FIS output v/s index waveform. Figure 4.3 shows the 3-D surface view generated by ANFIS. As shown in figure 4.4, the ANFIS

structure consists of five layers with two inputs (irradiation and temperature) and one output (power).

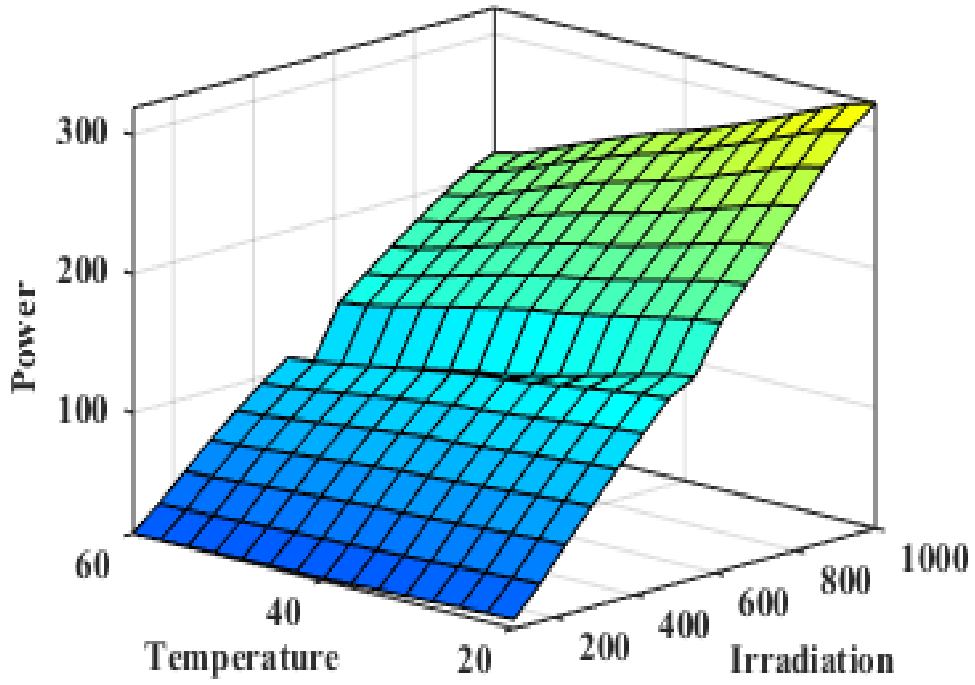


**Fig. 4.3. 3-D surface view representation between two inputs (irradiation and temperature) and one output (Power) generated by ANFIS**

The ANFIS model is generally summarised as follows.

Layer 1- The fuzzification process is performed by applying the membership functions to the input data. Every node in this layer is an adaptive node. The values of parameters of this layer change according to the error signal and generate the proper value of each membership function.

Layer 2- Rules are created based on the fuzzy logic inference system. All the nodes of this layer are fixed and each rule is represented by one node. In this layer, the outputs of the first layer have been multiplied with each other to determine the degree of fulfilment of the rule and forwarded it to the next layer.

Layer 3- The normalisation process is applied using the weighted average to each node coming from the rule layer. All the nodes of this layer are fixed.

Layer 4- The consequent of the rule are computed. All the nodes in this layer are adaptive nodes. Each junction in this layer computes the output for the rule.

Layer 5- The single node in this layer is a fixed node. Defuzzification process converts each fuzzy result into crisp output, single output value of the system is generated by collecting the output values of all nodes.

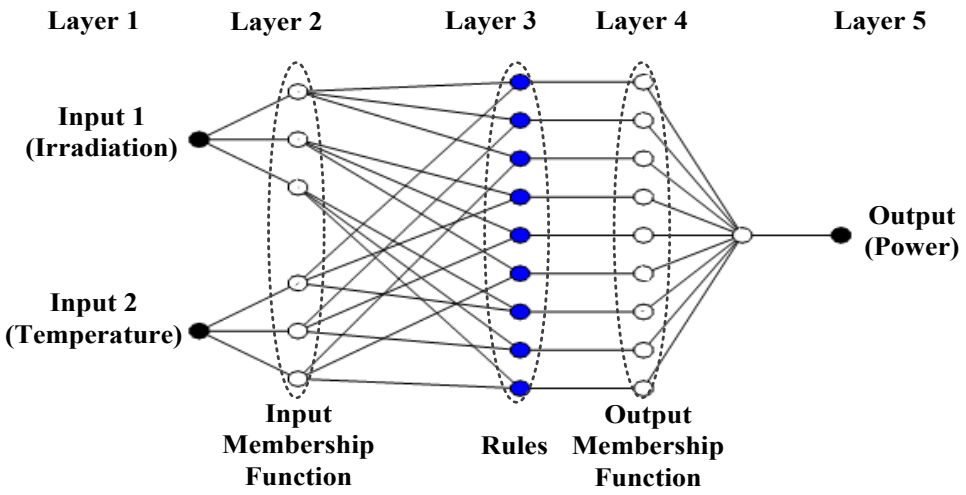


**Fig. 4.4. Structure of ANFIS**

### 4.2.2. INTELLIGENT CONTROL ALGORITHM

Intelligent controllers are envisioned emulating human mental faculties such as adaptation and learning, planning under large uncertainty, coping with large amounts of data etc. in order to effectively control complex processes; and this is the justification for the use of the term intelligent in intelligent control, since these mental faculties are considered to be important attributes of human intelligence. Intelligent control, typically, combines planning with on-line error compensation; it requires learning of both the system and the environment to be a part of the control process. It is a class of control techniques that use various artificial intelligence computing approaches like Bayesian probability, fuzzy logic, machine learning, reinforcement learning etc. In the present chapter, fuzzy logic control has been used and is explained below.

#### 4.2.2.1. Proposed Asymmetrical FLC (AFLC) Algorithm

Fuzzy logic was proposed by Lotfi A. Zadeh of the University of California at Berkeley in 1965. Fuzzy logic is a multi-level logic system and is a mathematical tool for analysing the uncertainties in the data. It exploits the tolerance for imprecision, uncertainty and partial truth to achieve tractability, robustness and efficient model. It analysis the problem in three steps

- Fuzzification – a process of mapping/ transformation of approximate crisp value into fuzzy set of values.
- Inferencing – processing of fuzzy set of values using the knowledge-based rule.
- Defuzzification – obtaining back the crisp value

**Fuzzification:** It is the process of converting the crisp value of the input into the fuzzy value. The universe of discourse (UOD) or membership function is a curve that denotes how each point in the input space is mapped between 0 and 1. The configuration of fuzzy logic membership functions can be of two types-

(i) Symmetrical, and

(ii) Asymmetrical

In the present studies, asymmetrical membership functions are proposed since the parameters associated with PV systems such as photon energy and the load are uncertain and random in nature. In the proposed AFLC (type-1) based intelligent algorithm, the input membership functions of FLC are further fine-tuned by the heuristic approach using fine tuning and coarse tuning features that can provide better controlling and stability. The membership functions are denser at the centre to provide greater sensitivity in the near MPP and become less dense gradually. Input membership functions are normalized, and suitable tuning gains are used. Figure 4.5 shows the fuzzy input and output membership functions used in the proposed system for tracking maximum power under steady-state as well as dynamic condition. The universe of discourse for input and output variables are divided into seven fuzzy sets: S1 (Small 1), S2 (Small 2), S3 (Small 3), ZO (Zero), B1 (Big 1), B2 (Big 2) and B3 (Big 3).

The asymmetrical FLC has two inputs i.e., error and change in error and one output (duty ratio). For the developed AFLC based MPPT algorithm, the two inputs are obtained from power and current of PV array. An error is calculated using equation (4.1). Change in error is derived from the derivative of error and can be calculated using equation (4.2).

$$E_r(n) = \frac{P_{o/p}(n) - P_{o/p}(n-1)}{I_{o/p}(n) - I_{o/p}(n-1)} \tag{4.1}$$

$$\Delta E_r(n) = E_r(n) - E_r(n-1) \tag{4.2}$$

where, $E_r$ is the error calculated, $P_{o/p}$ and $I_{o/p}$ are the power and current output of the proposed PV system and $\Delta E_r$ is the change in error.

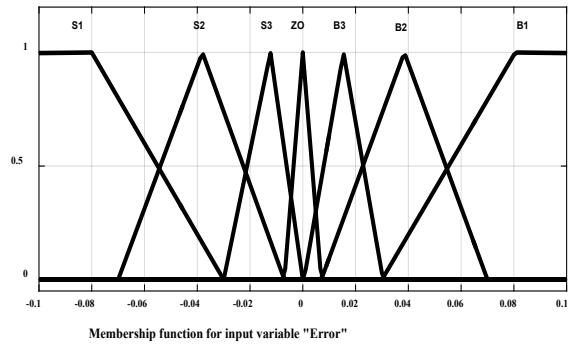


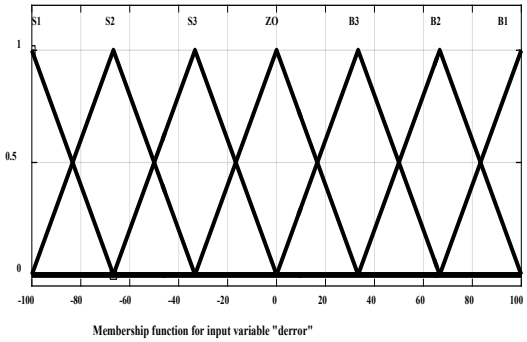

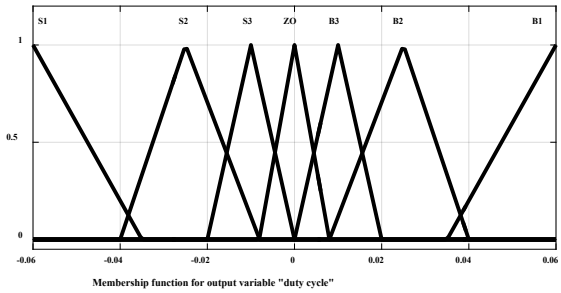


**Fig. 4.5. Membership functions for input variable 'Error', 'Error Change' and Output variable 'Duty Ratio' for Asymmetrical FLC**

## Inferencing

The inference method implements the rules to the fuzzy input to determine the fuzzy output as shown in table 4.1. The fuzzy inference system can be Mamdani or Sugeno, and depends upon the designer's requirement. Rules are made based on membership functions of input variables viz. error and change in error. In the proposed system, the rules have been made using "If…Then…" logic.

**Table 4.1 Fuzzy rule base for computing output variable 'Duty ratio'**

| E / ΔE | S1 | S2 | S3 | ZO | B3 | B2 | B1 |
|---|---|---|---|---|---|---|---|
| S1 | ZO | ZO | ZO | S1 | S1 | S1 | S1 |
| S2 | ZO | ZO | ZO | S2 | S2 | S2 | S2 |
| S3 | S3 | S3 | ZO | ZO | ZO | B3 | B3 |
| ZO | S3 | ZO | ZO | ZO | ZO | ZO | B3 |
| B3 | B3 | B3 | ZO | ZO | ZO | S3 | S3 |
| B2 | B2 | B2 | B2 | B2 | ZO | ZO | ZO |
| B1 | B1 | B1 | B1 | B1 | ZO | ZO | ZO |

In table 4.1, rule base consisting of 49 fuzzy control rules are given. These rules can also be represented in a 3-D graph known as a surface viewer as shown in figure 4.6. The output membership function of each rule is given by the minimum operator whereas collective fuzzy output is provided by maximum operator.

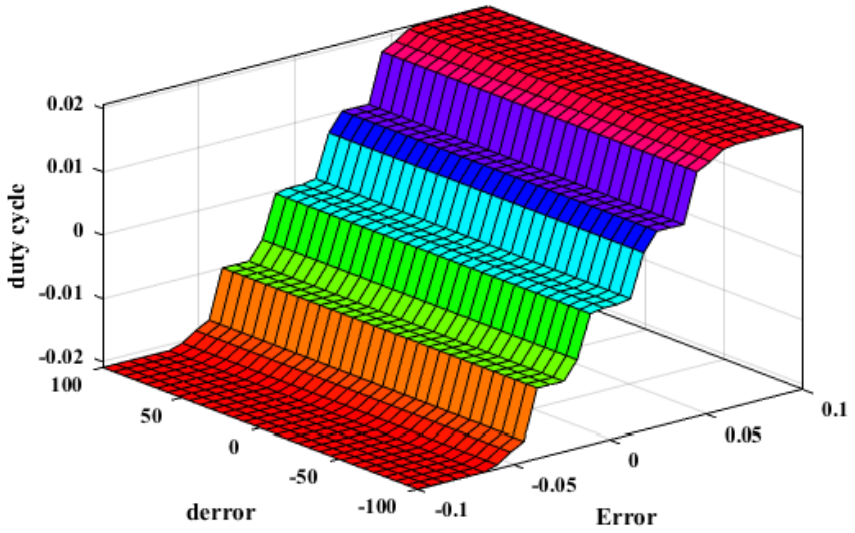


**Fig. 4.6. 3-D surface view representation between two inputs (error and change in error) and output (duty ratio) generated by AFLC for the proposed PV system**

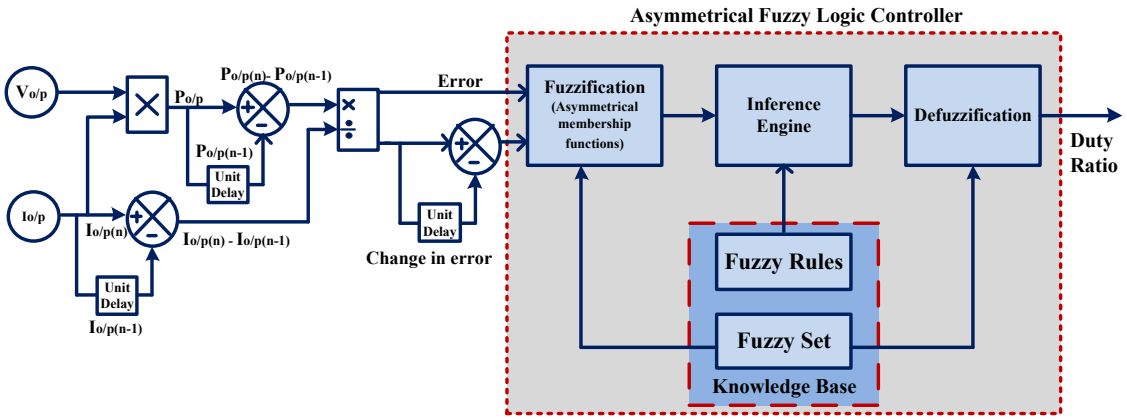


**Fig. 4.7. Block diagram of Asymmetrical FLC based control algorithm for MPPT**

## Defuzzification

Defuzzification is used to convert the fuzzy inference output into crisp output which can be given by equation (4.3):

$$z_o = defuzzifier(x) \tag{4.3}$$

where, x is the aggregate output and defuzzifier is defuzzification operator.

In the present work, Center of Area (CoA) is used for defuzzification and is represented by equation (4.4):

$$x = \frac{\sum_{i=1}^{n} \mu(x_i) x_i}{\sum_{i=1}^{n} \mu x_i} \tag{4.4}$$

where, $\mu x_i$ is the activation degree on rule 'i', $x_i$ is the center of the Max-Min composition of the output membership functions and x is the required output i.e. duty cycle.

#### 4.2.2.2. Proposed Asymmetrical Interval Type-2 FLC (AIT-2 FLC) Algorithm

The interval type-2 fuzzy membership function is 3-D fuzzy set. The blurred type-1 membership function represents footprint of uncertainty (FOU) and it has two bounded membership functions i.e. called as lower membership function (LMF) and upper membership function (UMF). The IT-2 FLC are expansion of type-1 fuzzy control. Figure 4.8 (a) represents the type-1 fuzzy control and (b) blurring of type-1 membership function. Blurred membership function is 3-D, having UMF, LMF along with footprint of uncertainty (third dimension of IT-2 FLC). Blurring of type-1 FLC by moving the points on left and right of the membership function achieves IT-2 FLC. Assuming this is repeated for all x∈ X, the interval type-2 3-D membership function of fuzzy set will be created. FOU provides degree of freedom and it is also capable of handling uncertainties.

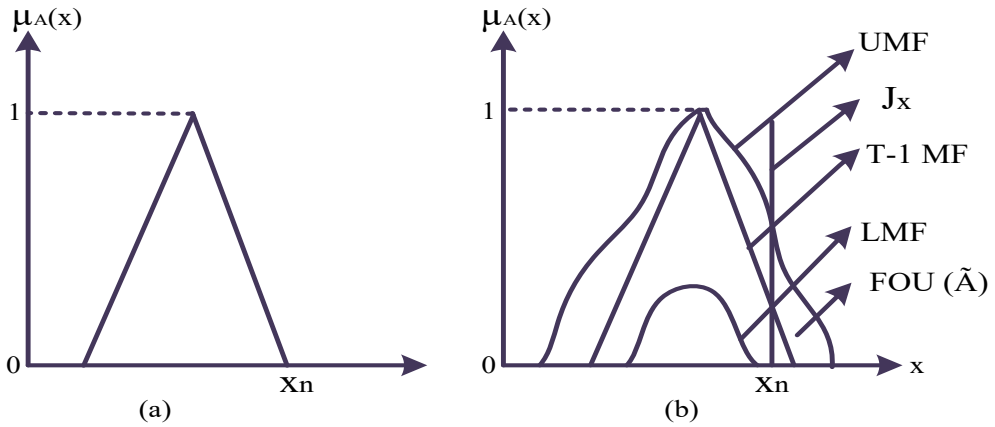


**Fig. 4.8. (a) Type-1 FLC and (b) Blurring of type-1 membership function**

The reasoning methodology of interval T-2 FLC has been expressed by "IF-THEN" rules or commands. The IT-2 FLC, like T-1 FLC, has same logical system except output processing stage which has type-reducer followed by defuzzification. In the interval type-2 fuzzy set, Takagi-Sugeno (TS) FLC architecture is used. The antecedent and consequent of rule base are linguistic term and mathematical function of the input respectively.

The AIT-2 FLC set, represented by $\tilde{A}$, is defined by a type-2 membership function $\mu_{\tilde{A}}(x,u)$, where $x \in X$ (X is universe of discourse) and $u \in J_x \subseteq [0,1]$, i. e. given by equation (4.5),

$$\tilde{A} = \left\{ \left((x,u), \mu_{\tilde{A}}(x,u)\right) \mid \forall x \in X, J_x \subseteq [0,1] \right\} \tag{4.5}$$

Set $\tilde{A}$ can also be defined expressed in equation (4.6),

$$\tilde{A} = \int_{x \in X} \int_{u \in J_x} \frac{\mu_{\tilde{A}}(x,u)}{(x,u)} \qquad J_x \subseteq [0,1] \tag{4.6}$$

where ∫ represents union. Set $\tilde{A}$ (discrete) can also be defined as,

$$\tilde{A} = \sum_{x \in X} \sum_{u \in J_x} \frac{\mu_{\tilde{A}}(x,u)}{(x,u)} \qquad J_x \subseteq [0,1] \tag{4.7}$$

The asymmetrical IT-2 type FLC has two inputs i.e., error and change in error and one output (duty ratio). Input variable and output variable fuzzy set consist of five membership functions as shown in figure 4.9. The membership functions are labelled as; *-B*: negative big, *-S*: negative small, *ZO*: zero, *+S*: positive small and *+B*: positive big as shown in table 4.2.

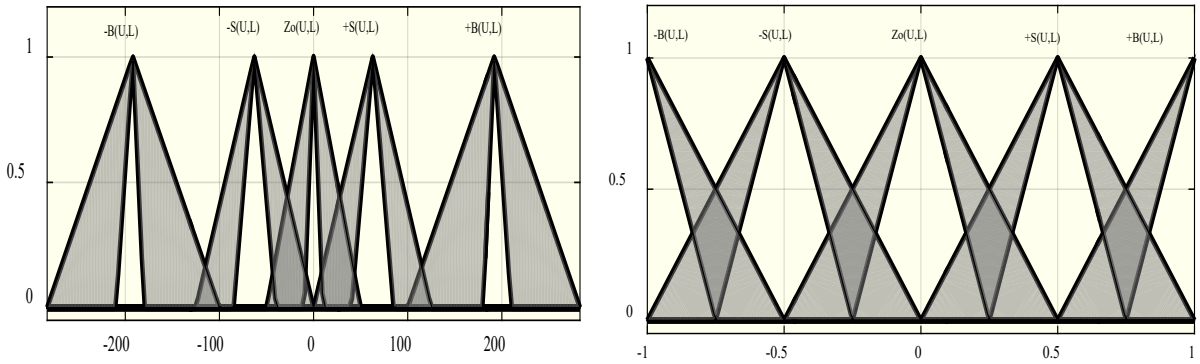


(a) (b)

**Fig. 4.9. Membership functions of (a) Error (E) (b) Change in Error (ΔE)**

**Table 4.2 Fuzzy rule base for computing output variable 'Duty ratio'**

| E / ΔE | **-B** | **-S** | **Zo** | **+S** | **+B** |
|---|---|---|---|---|---|
| **-B** | Zo | Zo | +S | -S | -B |
| **-S** | Zo | Zo | Zo | -S | -B |
| **Zo** | +B | +S | Zo | -S | -B |
| **+S** | +B | +S | Zo | Zo | Zo |
| **+B** | +B | +S | -S | Zo | Zo |

For output processing, type-2 fuzzy sets are reduced to type-1 fuzzy sets by centroid calculation in type reducer block. Then, similar to type-1 defuzzification, fuzzy inferred output is converted to crisp output and which is given by:

$z_o = defuzzifier(x)$

where, x indicates combined output.

There are number of methods for type reducing and defuzzification viz. Karnik-Mendel (KM) method, enhanced Karnik Mendel (EKM), enhanced iterative algorithm with stopping condition (EIASC) etc. In the proposed system, output processing has been done by Karnik-Mendel (KM) method.

Figure 4.10 shows the block diagram of the asymmetrical interval type -2 FLC. The sensed PV array voltage and current are given to the fuzzifier. The output from fuzzifier is fed to inference engine based on the knowledge base which is further defuzzified using output processing block.

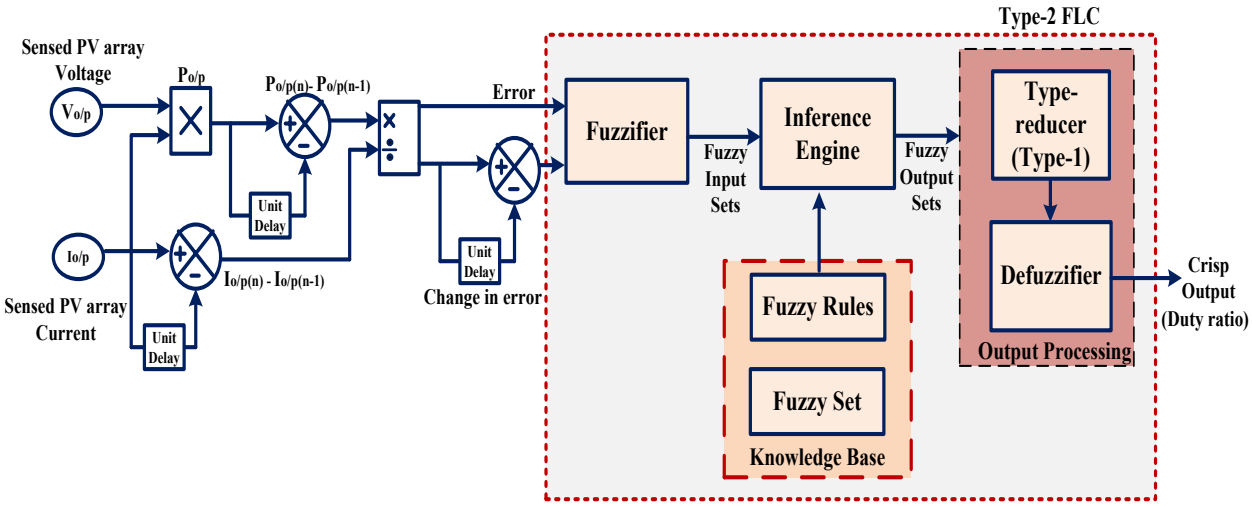


**Fig. 4.10. Block Diagram of Interval type-2 fuzzy logic based MPPT algorithm under PSC**

## 4.3. RESULTS AND DISCUSSIONS

This section presents simulation performance and the analysis of the proposed MPPT control algorithms under various shading scenarios with different PV array configurations. A 4x4 PV array of 1.28 kW has been considered for the present studies. The shading scenario considered for all the PV array configurations is shown in figure 4.11. The different PV configurations studied are given in figure 4.12. The P-V curves under different shading scenarios is shown in figure 4.1.

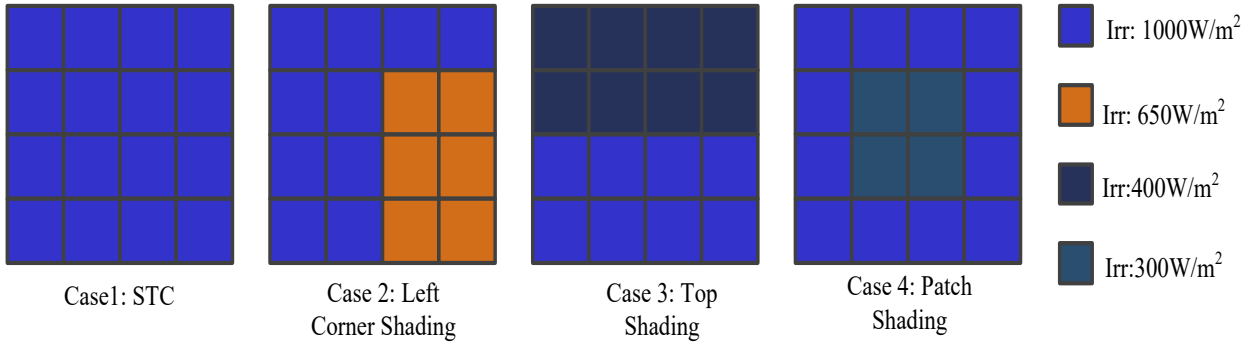


**Fig. 4.11. Various shading scenarios under STC and PSC**

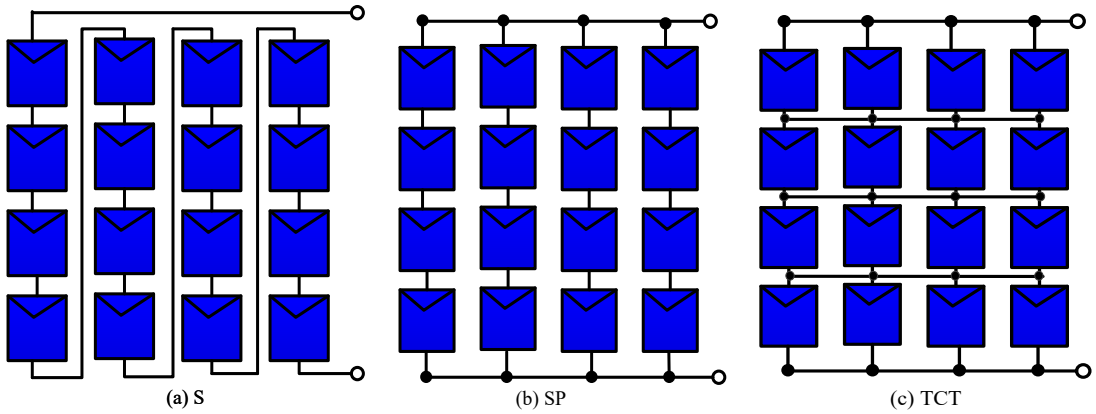


**Fig. 4.12. Schematic diagram of various PV array configurations**

The proposed MPPT algorithms have been tested under dynamic change in irradiation level. The algorithms have been tested with EN 50530 MPPT efficiency standard. Figure 4.13 shows trapezoidal waveform representing slow and medium change at irradiation level of 400 W/m$^2$/s and 800 W/m$^2$/s respectively. The irradiation level changes slowly from 1-6 seconds and the irradiation level change is faster from 7-10 seconds.

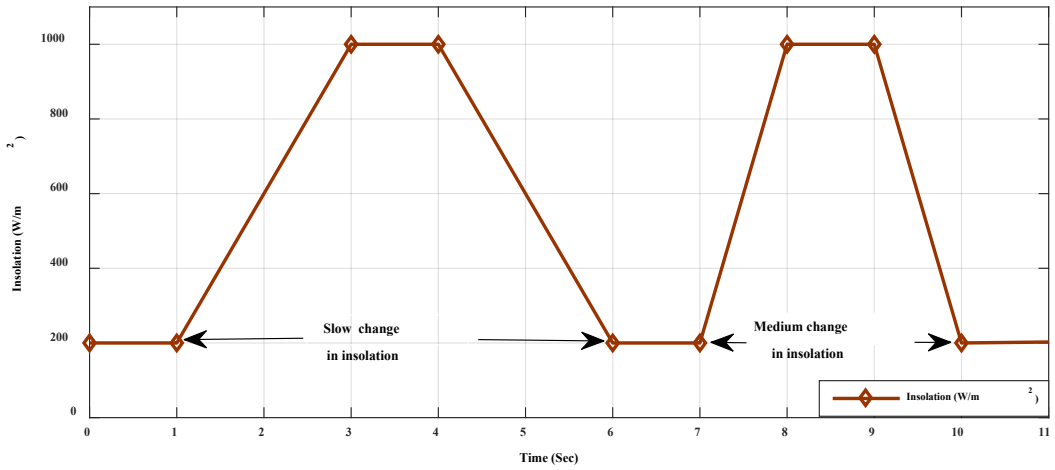


**Fig. 4.13. Dynamic change in irradiation level for EN 50530 standard MPPT efficiency test**

## 4.3.1. PERFORMANCE EVALUATION OF ANFIS BASED MPPT CONTROL ALGORITHM UNDER PSC

### 4.3.1.1. Under Steady State Condition

Case1(STC): In case 1, the STC (All PV panels are uniformly irradiated at 1000W/m$^2$) has been considered. Figure 4.14 shows the power output for various PV array arrangements under this condition. It can be seen that, the TCT arrangement tracks maximum power of 998 W while series PV arrangement tracks lowest power of 978W.

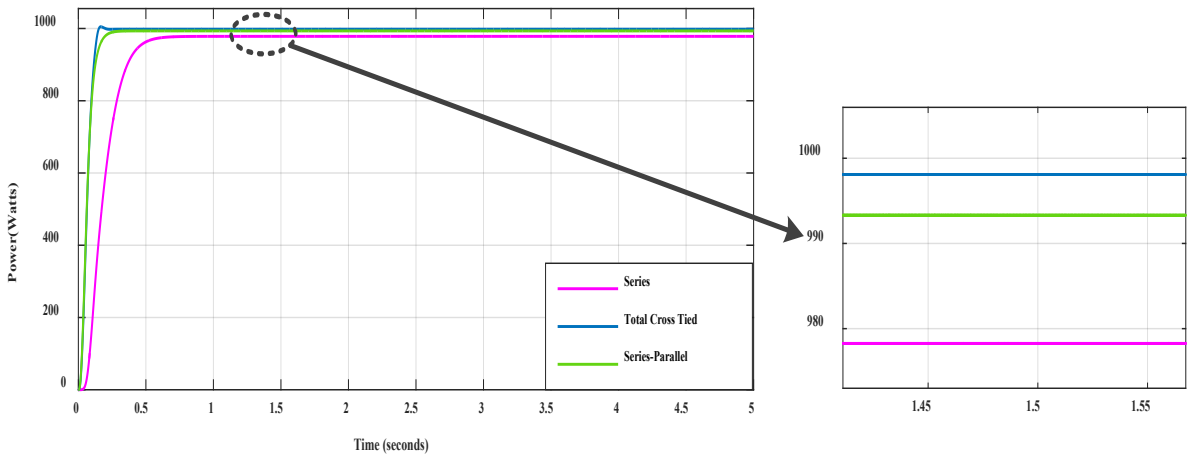


**Fig. 4.14. Power vs. Time plot for ANFIS MPPT technique with different PV array arrangements under STC (case 1)**

Case 2 (Left corner shading): In case 2, the left shading pattern (left corner irradiated at 650W/m$^2$) has been considered. Figure 4.15 shows the power output for various PV array arrangements under this condition. It can be seen that, the TCT arrangement tracks maximum power of 950 W while series PV arrangement tracks lowest power of 938 W.

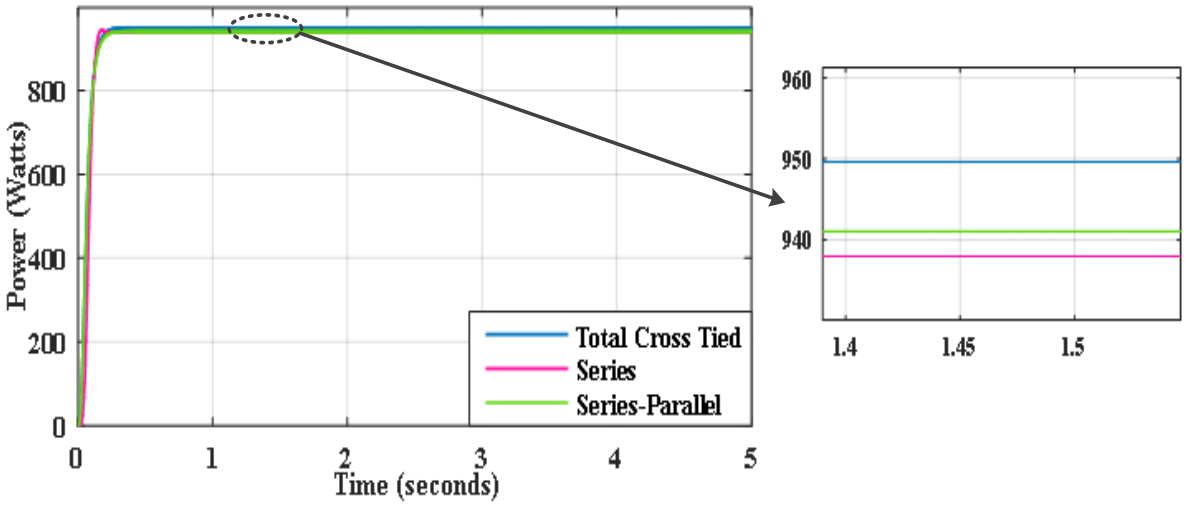


**Fig. 4.15. Power vs. Time plot for ANFIS MPPT technique with different PV array arrangements under Left corner shading (case 2)**

Case 3 (Top shading): In case 3, the top shading pattern (top PV panels are irradiated at 400W/m$^2$) has been considered. Figure 4.16 shows the power output for various PV array

arrangements under this condition. It can be seen that, the TCT arrangement tracks maximum power of 528 W while series PV arrangement tracks lowest power of 514W.

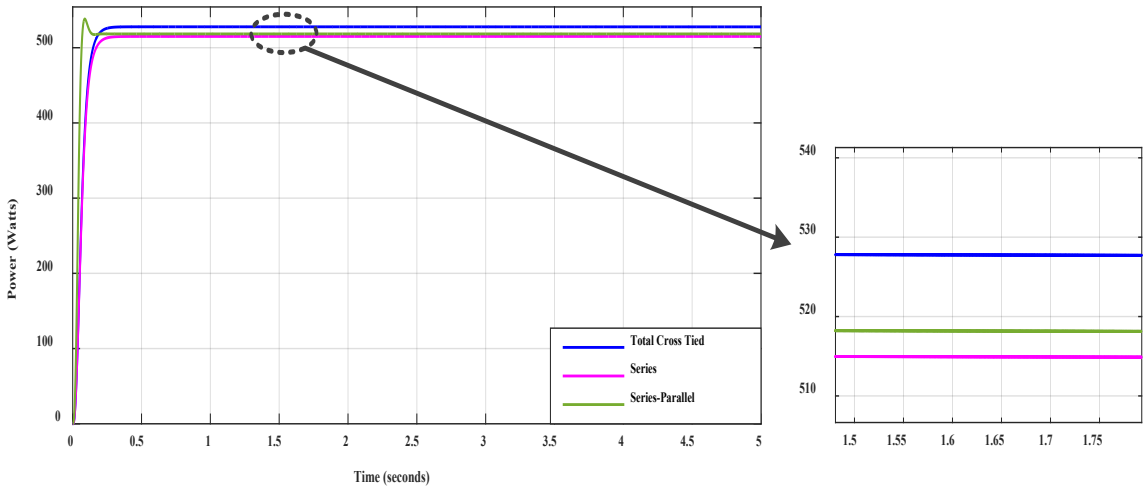


**Fig. 4.16. Power vs. Time plot for ANFIS MPPT technique with different PV array arrangements under Top shading (case 3)**

Case 4 (Patch Shading): In case 4 the patch shading pattern (patch is irradiated at 300W/m$^2$) has been considered. Figure 4.17 shows the power output for various PV array arrangements under this condition. It can be seen that, the TCT arrangement tracks maximum power of 725 W while series PV arrangement tracks lowest power of 706 W.

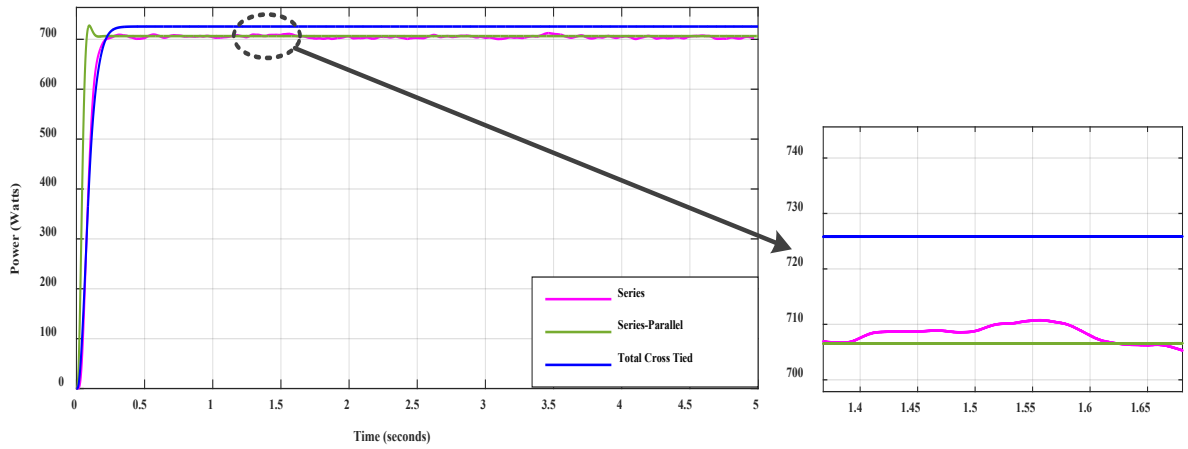


**Fig. 4.17. Power vs. Time plot for ANFIS MPPT technique with different PV array arrangements under Patch Shading (case 4)**

### 4.3.1.2. Under dynamic change in irradiation level

In this case, the dynamic change in irradiation level, as shown in figure 4.13 has been considered. Figure 4.18 shows the power output for various PV array arrangements. It can be

seen that, the TCT arrangement tracks maximum power of 997 W while series PV arrangement tracks lowest power of 978 W. Also, the settling time with TCT arrangement is lesser while series arrangement has more settling time.

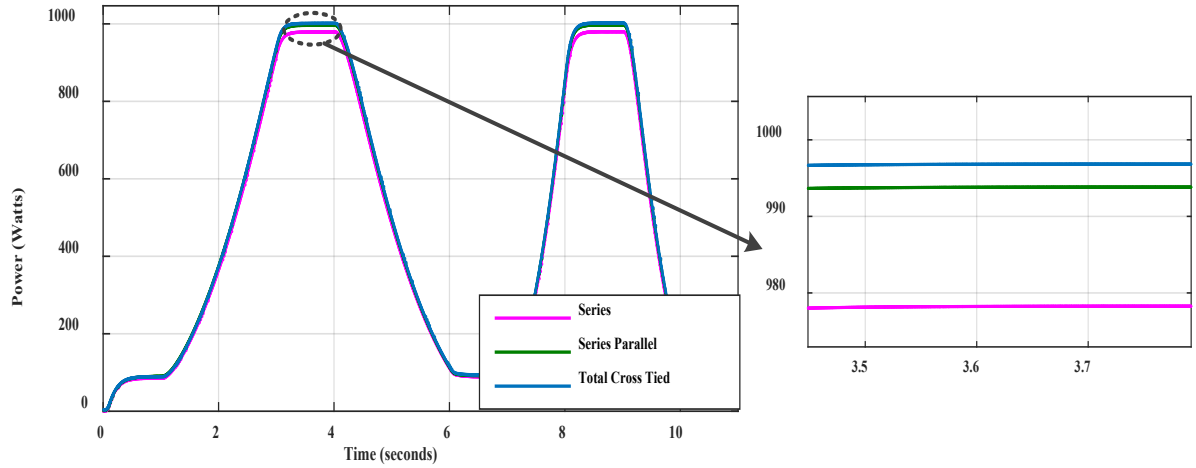


**Fig. 4.18. Power vs. Time plot for ANFIS MPPT technique with different PV array arrangements under dynamic change in irradiation level**

## 4.3.2. PERFORMANCE EVALUATION OF ASYMMETRICAL FLC BASED MPPT CONTROL ALGORITHM UNDER PSC

### 4.3.2.1. Under Steady State Condition

Case1(STC): In case 1 the STC (All PV panels are uniformly irradiated at 1000W/m$^2$) has been considered. Figure 4.19 shows the power output for various PV array arrangements under this condition. It can be seen that, the TCT arrangement tracks maximum power of 1028 W while series PV arrangement tracks lowest power of 983 W.

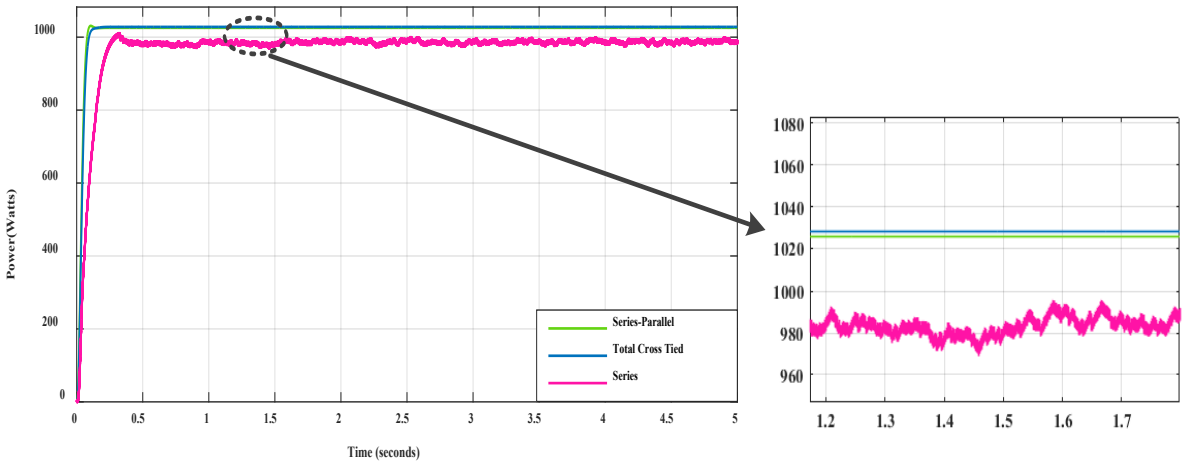


**Fig. 4.19. Power vs. Time plot for AFLC MPPT technique with different PV array arrangements under STC (case 1)**

Case 2 (Left corner shading): In case 2 the left shading pattern (left corner irradiated at 650W/m$^2$) has been considered. Figure 4.20 shows the power output for various PV array arrangements under this condition. It can be seen that, the TCT arrangement tracks maximum power of 954 W while series PV arrangement tracks lowest power of 939 W.

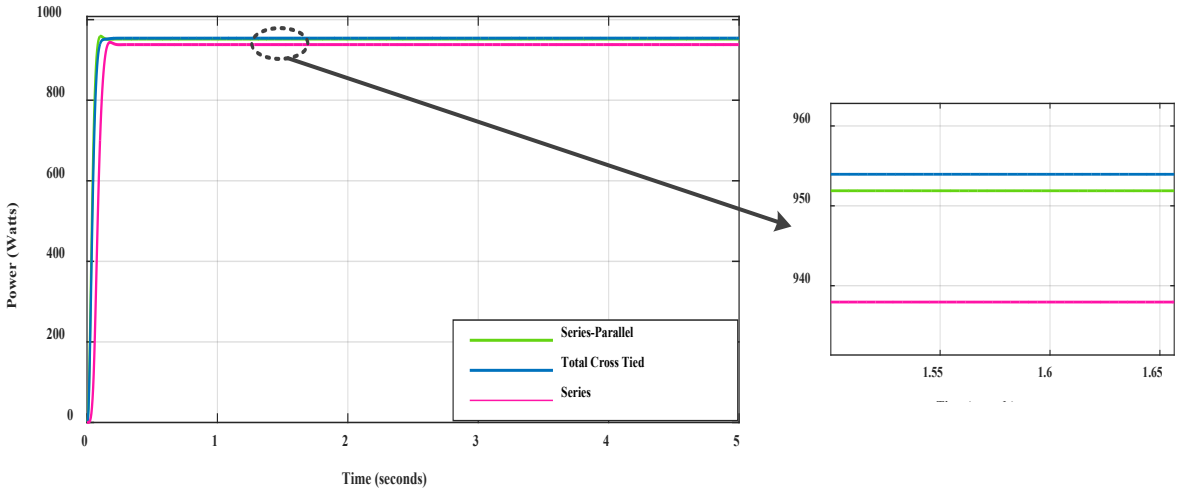


**Fig. 4.20. Power vs. Time plot for AFLC MPPT technique with different PV array arrangements under Left corner shading (case 2)**

Case 3 (Top shading): In case 3 the top shading pattern (top PV panels are irradiated at 400W/m$^2$) has been considered. Figure 4.21 shows the power output for various PV array arrangements under this condition. It can be seen that, the TCT arrangement tracks maximum power of 533 W while series PV arrangement tracks lowest power of 519 W.

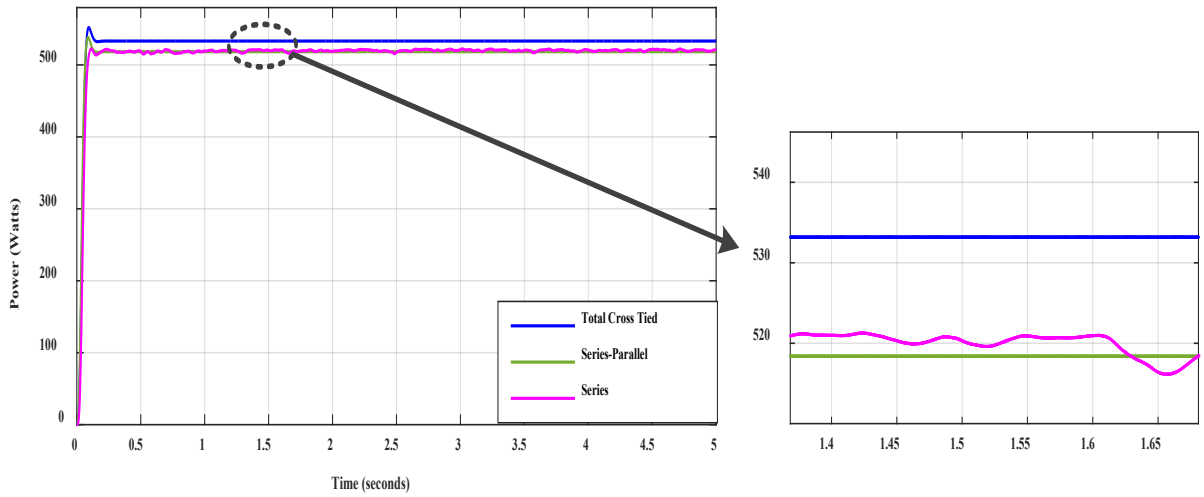


**Fig. 4.21. Power vs. Time plot for AFLC MPPT technique with different PV array arrangements under Top shading (case 3)**

Case 4 (Patch Shading): In case 4 the patch shading pattern (patch is irradiated at 300W/m$^2$) has been considered. Figure 4.22 shows the power output for various PV array arrangements under this condition. It can be seen that, the TCT arrangement tracks maximum power of 725 W while series PV arrangement tracks lowest power of 708 W.

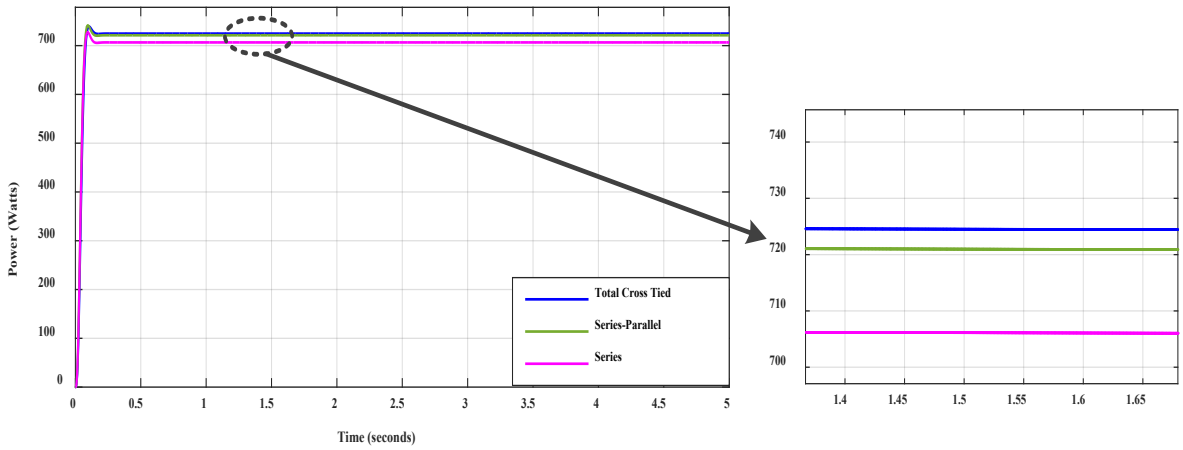


**Fig. 4.22. Power vs. Time plot for AFLC MPPT technique with different PV array arrangements under Patch Shading (case 4)**

### 4.3.2.2. Under dynamic change in irradiation level

In this case, the dynamic change in irradiation level, as shown in figure 4.13 has been considered. Figure 4.23 shows the power output for various PV array arrangements. It can be seen that, the TCT arrangement tracks maximum power of 1028 W while series PV arrangement tracks lowest power of 983 W. Also, the settling time with TCT arrangement is lesser while series arrangement has more settling time.

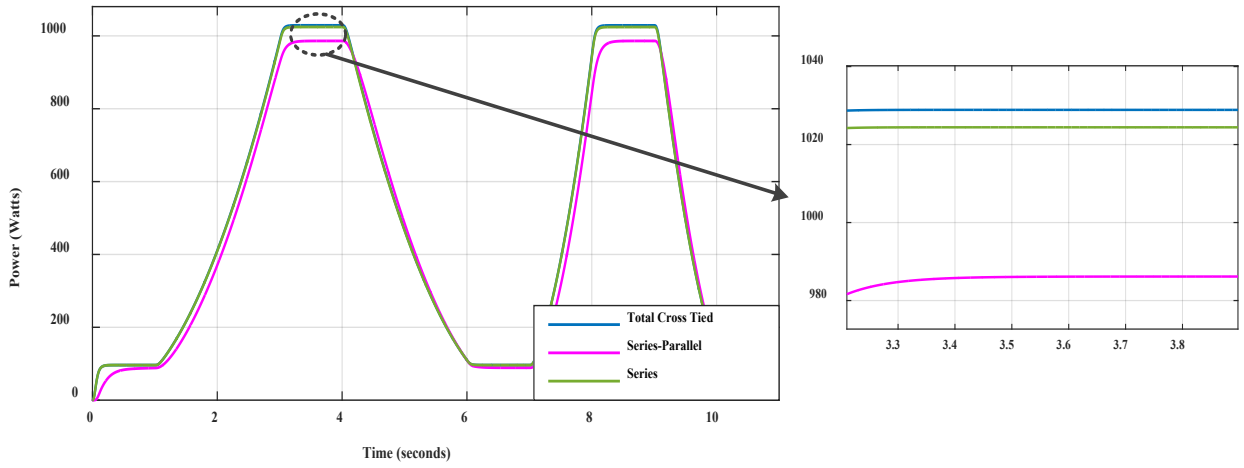


**Fig. 4.23. Power vs. Time plot for Asymmetrical FLC MPPT technique with different PV array arrangements under dynamic change in irradiation level**

### 4.3.3. PERFORMANCE EVALUATION OF ASYMMETRICAL INTERVAL TYPE-2 FLC BASED MPPT CONTROL ALGORITHM UNDER PSC

#### 4.3.3.1. Under Steady State Condition

Case1(STC): In case 1 the STC (All PV panels are uniformly irradiated at 1000W/m$^2$) has been considered. Figure 4.24 shows the power output for various PV array arrangements under this condition. It can be seen that, the TCT arrangement tracks maximum power of 1028 W while series PV arrangement tracks lowest power of 1027 W.

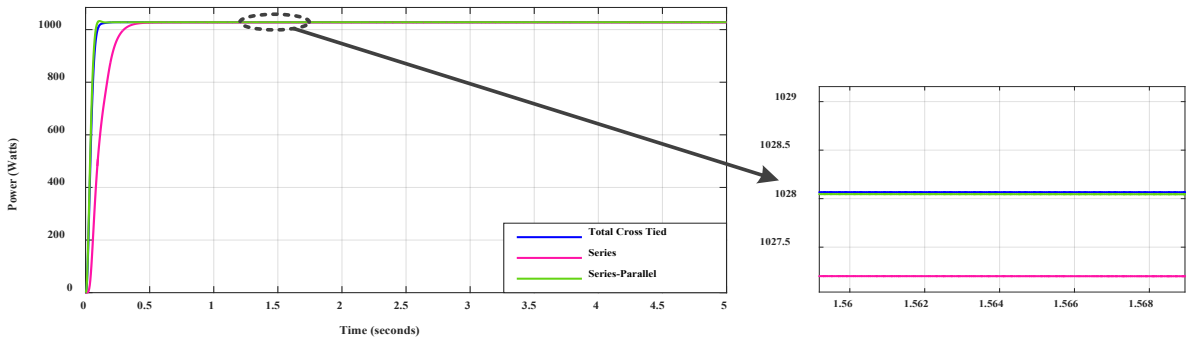


**Fig. 4.24. Power vs. Time plot for AIT-2 FLC MPPT technique with different PV array arrangements under STC (case 1)**

Case 2 (Left corner shading): In case 2 the left shading pattern (left corner irradiated at 650W/m$^2$) has been considered. Figure 4.25 shows the power output for various PV array arrangements under this condition. It can be seen that, the TCT arrangement tracks maximum power of 978 W while series PV arrangement tracks lowest power of 960 W.

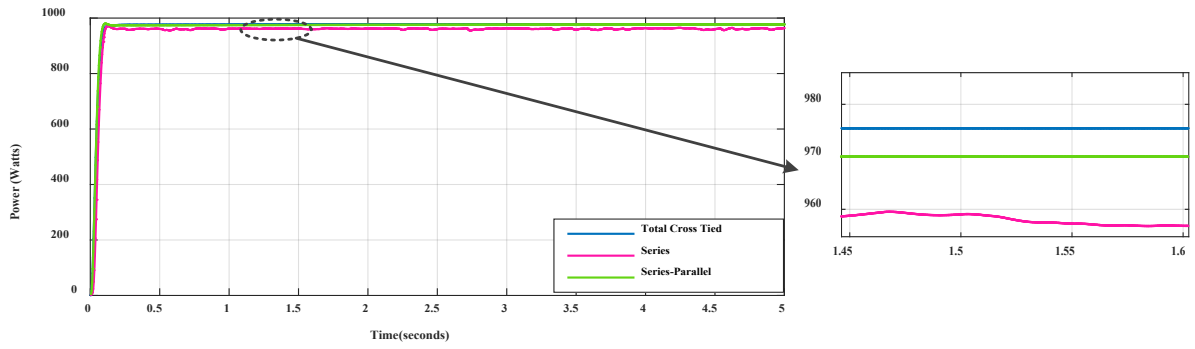


**Fig. 4.25. Power vs. Time plot for AIT-2 FLC MPPT technique with different PV array arrangements under Left corner shading (case 2)**

Case 3 (Top shading): In case 3 the top shading pattern (top PV panels are irradiated at 400W/m$^2$) has been considered. Figure 4.26 shows the power output for various PV array

arrangements under this condition. It can be seen that, the TCT arrangement tracks maximum power of 563.5 W while series PV arrangement tracks lowest power of 520 W

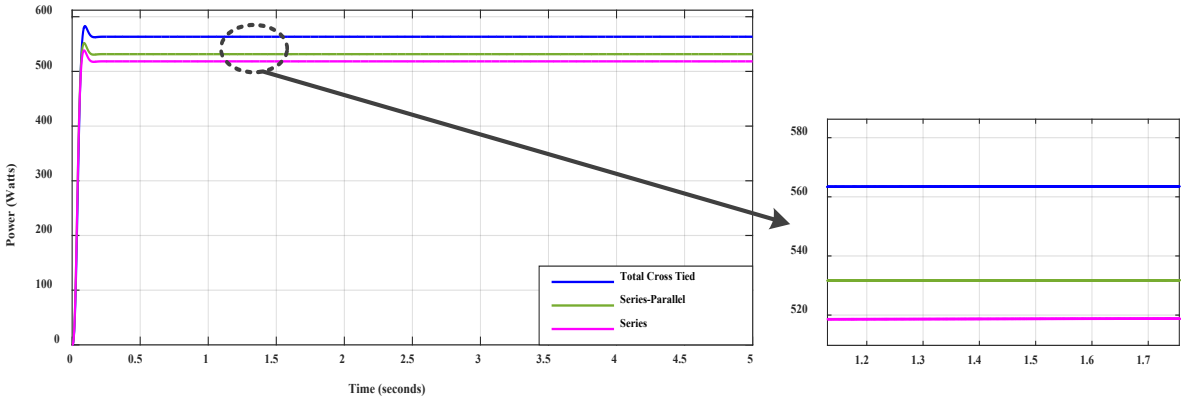


**Fig. 4.26. Power vs. Time plot for AIT-2 FLC MPPT technique with different PV array arrangements under Top shading (case 3)**

Case 4 (Patch Shading): In case 4 the patch shading pattern (patch is irradiated at 300W/m$^2$) has been considered. Figure 4.27 shows the power output for various PV array arrangements under this condition. It can be seen that, the TCT arrangement tracks maximum power of 845 W while series PV arrangement tracks lowest power of 827 W.

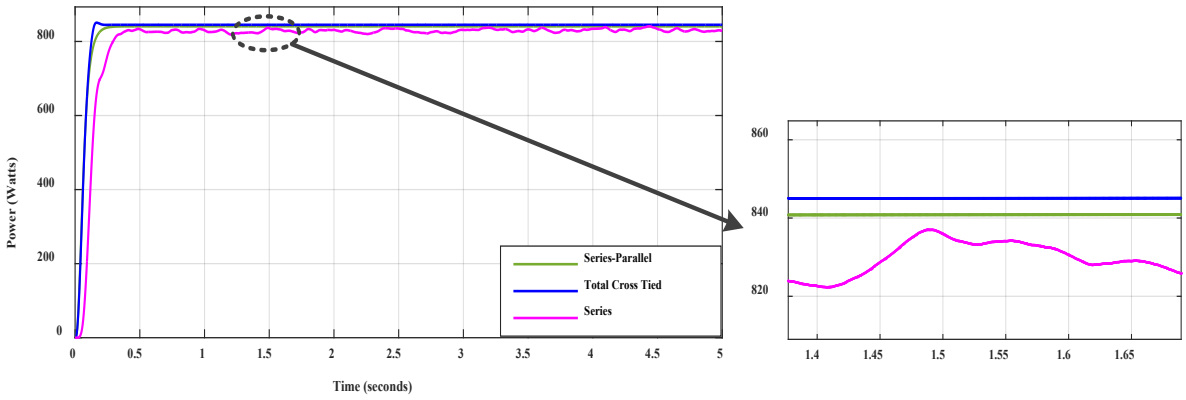


**Fig. 4.27. Power vs. Time plot for AIT-2 FLC MPPT technique with different PV array arrangements under Patch Shading (case 4)**

### 4.3.3.2. Under dynamic change in irradiation level

In this case, the dynamic change in irradiation level, as shown in figure 4.13 has been considered. Figure 4.28 shows the power output for various PV array arrangements. It can be seen that, the TCT arrangement tracks maximum power of 1029 W while series PV arrangement tracks lowest power of 1027 W. Also, the settling time with TCT arrangement is lesser while series arrangement has more settling time.

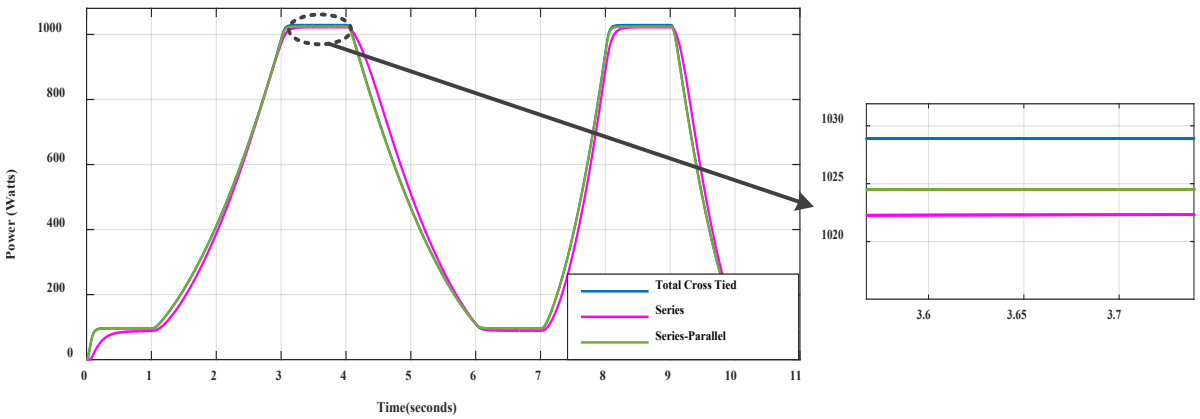


**Fig. 4.28. Power vs. Time plot for Asymmetrical interval type-2 FLC MPPT technique with different PV array arrangements under dynamic change in irradiation level**

Table 4.3 tabulates the power tracked by various MPPT techniques with different PV array configurations under considered shading patterns. Table 4.4 gives the dynamic response of the various MPPT techniques.

**Table 4.3 GMPP (W) tracking by various MPPT techniques with different PV array arrangements**

| | MPPT techniques | Series | Series-Parallel | Total cross tied |
|---|---|---|---|---|
| **Case 1** | ANFIS | 978 | 983 | 1027 |
| | AFLC | 993 | 1025.5 | 1028 |
| | AIT-2 FLC | 998 | 1028 | 1028 |
| **Case 2** | ANFIS | 938 | 935 | 950 |
| | AFLC | 941 | 952 | 954 |
| | AIT-2 FLC | 950 | 970 | 978 |
| **Case 3** | ANFIS | 514 | 218 | 516.5 |
| | AFLC | 515 | 518.5 | 531.5 |
| | AIT-2 FLC | 528 | 533 | 563.5 |
| **Case 4** | ANFIS | 706 | 719 | 827 |
| | AFLC | 706 | 721 | 841 |
| | AIT-2 FLC | 725 | 725 | 845 |

**Table 4.4 Dynamic response of various MPPT techniques**

| PV array arrangement | MPPT techniques | Initial | | Slow | | Medium | |
|---|---|---|---|---|---|---|---|
| | | Power (W) | Settling Time (sec) | Power (W) | Settling Time (sec) | Power (W) | Settling Time (sec) |
| SERIES | ANFIS | 84 | 0.67 | 975 | 0.33 | 975 | 0.33 |
| | AFLC | 86 | 0.64 | 993 | 0.33 | 993 | 0.33 |
| | AIT-2 FLC | 86 | 0.64 | 998 | 0.33 | 998 | 0.33 |
| SERIES-PARALLEL | ANFIS | 85 | 0.65 | 983 | 0.35 | 983 | 0.35 |
| | AFLC | 96 | 0.65 | 1025 | 0.15 | 1025 | 0.15 |
| | AIT-2 FLC | 96 | 0.64 | 1028 | 0.15 | 1028 | 0.15 |
| TOTAL CROSS TIED | ANFIS | 85 | 0.65 | 1022 | 0.26 | 1022 | 0.26 |
| | AFLC | 96 | 0.64 | 1024 | 0.10 | 1024 | 0.10 |
| | AIT-2 FLC | 96 | 0.62 | 1028 | 0.10 | 1028 | 0.10 |

Further, simulation results of the ANFIS, Asymmetrical FLC, Asymmetrical interval type-2 FLC under partial shading condition along with different PV arrangements has been compared for shading losses, mismatch loss, fill factor and the EN 50530 MPPT efficiency test.

(a) Shading Losses: The power loss due to shading is called shading loss. Shading loss is the difference in power between the maximum power obtained from an array under STC ($P_{MP,\ withoutshading}$) and the total maximum available power under PSC ($P_{MP,\ shading}$) [162]. It can be represented as:

$$P_{MP,\ shadinglosses} = P_{MP,withoutshading} - P_{MP,shading} \quad (4.8)$$

(b) Mismatch Losses: It can be defined as, the difference of individual maximum power ($P_{mpi}$) of PV array and global maximum power ($P_{GMPP}$). Table 4.3 shows the individual maximum powers under different shading scenarios. Mismatch loss ($P_{mml}$) is given by equation (4.9):

$$P_{mml} = P_{mpi} - P_{GMPP} \quad (4.9)$$

(c) Fill Factor (FF): It can be defined as the ratio of maximum global power ($P_{GMPP}$) to the product of open circuit voltage ($V_{oc}$) and short circuit current ($I_{scc}$) (Appendix B (a)) of the PV system. The value of fill factor can be calculated by equation (4.10).

$$FF = \frac{P_{GMPP}}{V_{oc} * I_{scc}} \tag{4.10}$$

(d) MPPT Efficiency test EN50530: Under dynamic weather condition, the assessment of the proposed algorithm is done with EN 50530 MPPT efficiency test. MPPT tracking efficiency of the proposed controller is evaluated using the given by equation (4.11) [163]:

$$\eta_{MPPT} = \frac{P_{mpi}}{P_{GMPP}} \tag{4.11}$$

Table 4.5, 4.6, 4.7 and 4.8 represents shading loss, fill factor, mismatch loss (%) and efficiency respectively in various MPPT algorithms with different PV array arrangements.

**Table 4.5 Shading loss (W) in various MPPT techniques under study with different PV array arrangements**

| | **MPPT techniques** | **Series** | **Series-Parallel** | **Total cross tied** |
|---|---|---|---|---|
| **Case 1** | ANFIS | 302 | 297 | 253 |
| | AFLC | 287 | 254.5 | 252 |
| | AIT-2 FLC | 282 | 252 | 252 |
| **Case 2** | ANFIS | 342 | 345 | 321.5 |
| | AFLC | 339 | 328 | 310 |
| | AIT-2 FLC | 330 | 326 | 305 |
| **Case 3** | ANFIS | 766 | 762 | 763.5 |
| | AFLC | 765 | 761.5 | 748.5 |
| | AIT-2 FLC | 752 | 747 | 716.5 |
| **Case 4** | ANFIS | 574 | 561 | 453 |
| | AFLC | 574 | 559 | 439 |
| | AIT-2 FLC | 555 | 555 | 435 |

**Table 4.6 Mismatch losses (%) in various MPPT techniques under study with different PV array arrangements**

| | MPPT techniques | Series | Series-Parallel | Total cross tied |
|---|---|---|---|---|
| **Case 1** | ANFIS | 22.07 | 21.6 | 18.16 |
| | AFLC | 20.8 | 18.2 | 18.0 |
| | AIT-2 FLC | 20.4 | 18.0 | 18.0 |
| **Case 2** | ANFIS | 11.0 | 11.2 | 9.06 |
| | AFLC | 10.72 | 9.67 | 7.7 |
| | AIT-2 FLC | 9.86 | 9.48 | 7.4 |
| **Case 3** | ANFIS | 13.1 | 12.5 | 12.7 |
| | AFLC | 13.0 | 12.0 | 10.2 |
| | AIT-2 FLC | 10.8 | 9.9 | 4.8 |
| **Case 4** | ANFIS | 17.6 | 16.1 | 3.5 |
| | AFLC | 17.6 | 15.8 | 1.8 |
| | AIT-2 FLC | 15.4 | 15.4 | 1.4 |

**Table 4.7 Fill Factor in various MPPT techniques under study with different PV array arrangements**

| | MPPT techniques | Series | Series-Parallel | Total cross tied |
|---|---|---|---|---|
| **Case 1** | ANFIS | 0.558 | 0.561 | 0.586 |
| | AFLC | 0.566 | 0.585 | 0.586 |
| | AIT-2 FLC | 0.569 | 0.586 | 0.586 |
| **Case 2** | ANFIS | 0.535 | 0.533 | 0.547 |
| | AFLC | 0537 | 0.543 | 0.553 |
| | AIT-2 FLC | 0.542 | 0.544 | 0.556 |
| **Case 3** | ANFIS | 0.301 | 0.310 | 0.309 |
| | AFLC | 0.301 | 0.311 | 0.319 |
| | AIT-2 FLC | 0.309 | 0.319 | 0.338 |
| **Case 4** | ANFIS | 0.412 | 0.426 | 0.491 |
| | AFLC | 0.412 | 0.428 | 0.499 |
| | AIT-2 FLC | 0.423 | 0.430 | 0.501 |

**Table 4.8 Efficiency (%) of various MPPT techniques under study with different PV array arrangements**

| | MPPT techniques | Series | Series-Parallel | Total cross tied |
|---|---|---|---|---|
| **Case 1** | ANFIS | 77.90 | 78.32 | 81.83 |
| | AFLC | 79.12 | 81.71 | 81.91 |
| | AIT-2 FLC | 79.52 | 81.91 | 81.91 |
| **Case 2** | ANFIS | 88.99 | 88.70 | 90.93 |
| | AFLC | 89.21 | 90.23 | 92.03 |
| | AIT-2 FLC | 90.13 | 90.51 | 92.50 |
| **Case 3** | ANFIS | 86.82 | 87.50 | 87.24 |
| | AFLC | 86.94 | 87.58 | 89.78 |
| | AIT-2 FLC | 89.18 | 90.33 | 95.18 |
| **Case 4** | ANFIS | 82.38 | 83.89 | 96.49 |
| | AFLC | 82.38 | 84.13 | 98.13 |
| | AIT-2 FLC | 84.39 | 84.59 | 98.59 |

It has been observed that the proposed AFLC and AIT-2 FLC algorithms performs better as compared to ANFIS. The maximum power is tracked by AIT-2 FLC. Also, the proposed asymmetrical interval type-2 FLC algorithm has minimum shading losses, improved fill factor and minimum mismatch losses as compared to the other algorithm It can be seen that for all the MPPT algorithms the performance of TCT PV array arrangement is better than any other configuration. From table 4.8, it can be seen AIT-2 FLC with TCT PV array arrangement has highest efficiency.

## 4.4. CONCLUDING REMARKS

In this chapter novel MPPT techniques viz. asymmetrical FLC and asymmetrical interval type-2 FLC have been developed for tracking maximum power in a solar PV system under PSC. The simulation studies for the considered system have been carried out using these developed algorithms for different PV array configurations. The performance of ANFIS, AFLC, AIT-2 FLC algorithm has been compared in terms of GMPP tracking, shading losses, fill factor, mismatch loss (%) and efficiency. The MPPT algorithms have also been tested under dynamic

condition by performing EN50530 MPPT efficiency test. The simulation results shows that the proposed asymmetrical interval type -2 based MPPT algorithm tracks highest power for all the PV array configurations under all the considered shading patterns. Also, it has higher tracking efficiency with minimum shading loss and mismatch loss. Further, it has been observed that TCT configuration gives best results under all the conditions for all the algorithms considered.

# CHAPTER-V

# DC LINK VOLTAGE CONTROL OF STAND-ALONE SPV SYSTEM WITH BATTERY ENERGY STORAGE SYSTEM

## INTRODUCTION

Stand-alone SPV system is self-reliant energy system. It is preferred in those areas where there is little access to utility grid. But the output of SPV system is not constant, due to which it become difficult to maintain continuous power to load in this system. This problem can be addressed by adding an energy storage system along with PV system. Battery is most commonly used storage device and it is very pivotal in maintaining continuity of power to the load. But when two or more energy sources are connected, then control of dc link voltage at common coupling point (CCP) is an area of concern as the inverter output depends upon dc link voltage and hence any variation in dc-link voltage is undesirable for reliable operation of the system. In this chapter, a novel nonlinear autoregressive moving average-L2 (NARMA-L2) control algorithm is proposed and developed for the dc link voltage regulation of stand-alone PV system with battery energy storage system (BESS) and is compared with conventional PI controller. The proposed DC link voltage control algorithm is tested using MATLAB-Simulink and Sim-Power System toolbox.

## 5.2. DESIGN AND MODELLING OF STAND-ALONE PV SYSTEM WITH BESS

Schematic diagram for dc-link voltage control of stand-alone PV system with BESS is shown in figure 5.1. Stand-alone PV system with BESS comprises of PV array, battery, bidirectional dc-dc converter, boost converter, inverter and load. BESS has been connected in parallel to PV system for uninterrupted power supply to load. BESS consists of battery connected to bidirectional dc-dc converter. Modelling of PV array, boost converter and inverter are already explained in chapter 3. In the subsequent section the modeling of BESS has been explained.

**5.2.1. Modelling of Battery:** Battery is most commonly used storage system. When SPV generates power more than the load requirement, the surplus power may be used to charge the battery and when power generated by SPV system is less than load demand, battery can supply power to the load.

---

This chapter is based on the papers - (i) "DC Link Voltage Control of Stand-Alone PV Tied with Battery Energy Storage System" 20th International Conference on Intelligent Systems Design and Applications (ISDA 2020) held December 12-15, 2020, pp. 1–11, 2021.https://doi.org/10.1007/978-3-030-71187-0_86.

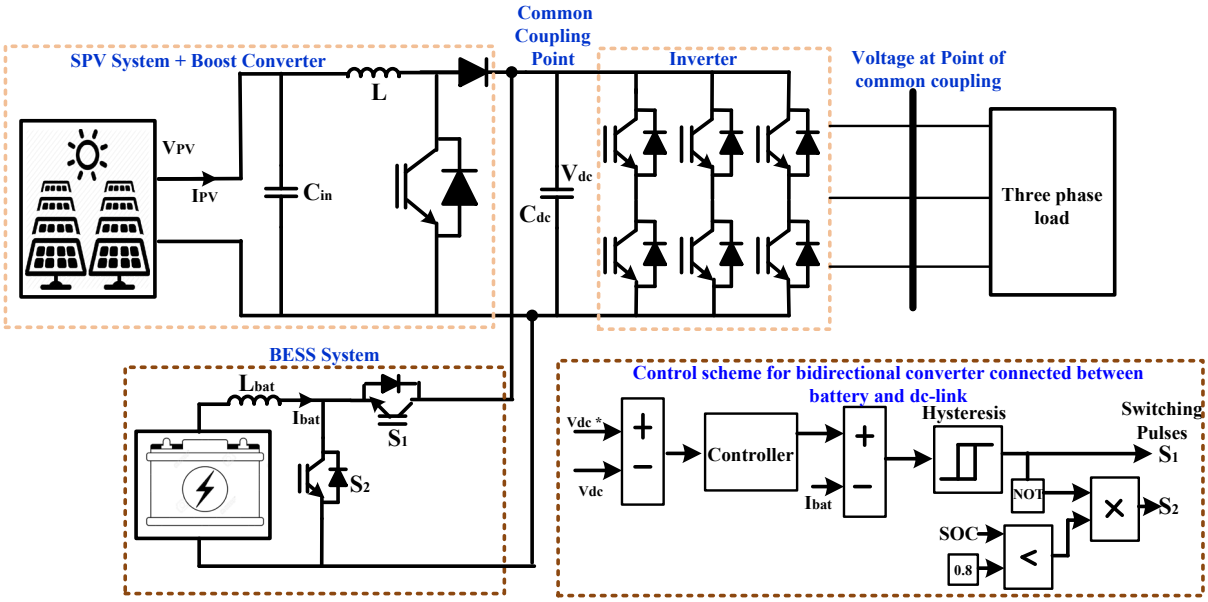


**Fig. 5.1. Schematic Diagram for DC link voltage control of stand-alone PV system with BESS**

The equivalent circuit diagram of battery, consisting of voltage-controlled source connected in series with resistance, is shown in figure 5.2.

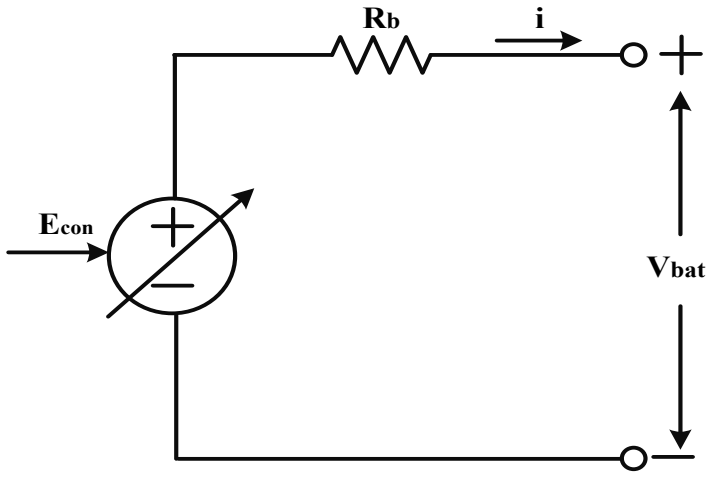


**Fig. 5.2. Equivalent circuit diagram of battery**

From figure 5.2 it can be seen that;

$$V_{bat} = E_{con} - R_b . i \quad (5.1)$$

where, $V_{bat}$ is actual battery voltage, $E_{con}$ is the controlled battery voltage, $i$ is battery current, $R_b$ is battery internal resistance. The controlled voltage of battery $E_{con}$ is given by:

$$E_{con} = E_{con0} - K\frac{Q_{bat}}{Q_{bat}-it}.it - K\frac{Q_{bat}}{Q_{bat}-it}.i^* + Exp(t) \text{ [For Discharging]} \quad (5.2)$$

$$E_{con} = E_{con0} - K\frac{Q_{bat}}{Q_{bat}-it}.it - K\frac{Q_{bat}}{it-0.1.Q_{bat}}.i^* + Exp(t) \text{ [For charging]} \quad (5.3)$$

where, $E_{con0}$ is constant open circuit voltage, K is polarization voltage, $Q_{bat}$ is the battery

capacity, $it = \int i\,dt$ is the battery actual charge, $i^*$ is the reference current of battery, $Exp(t)$ is the exponential zone voltage.

In the system considered, an inbuilt Lithium-ion battery of MATLAB/Simulink has been used. The specifications of the battery are as:

- Rated nominal voltage is 300V
- Rated capacity is 6.5Ah and
- Initial state of charge of 79.80%.

**Discharge characteristics of Battery**

The capacity of battery is related to its discharge current. In figure 5.3, the discharge characteristics of battery used in the present work has been shown for different discharge current ratings. From the discharge characteristics it can be seen that with increase in the current drawn, the battery discharge rate is also increased. If the demand is 28.3 A, then the battery will supply it for approximately 10 minutes where as if the demand is 1.4 A, then the battery will supply it for approximately 250 minutes.

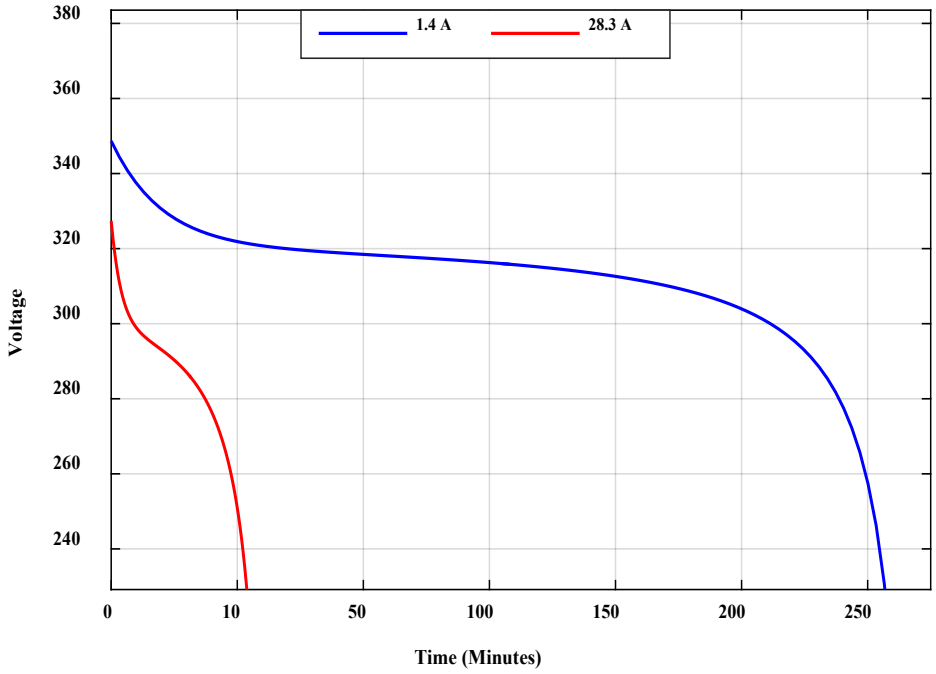


**Fig. 5.3. Discharge characteristics of the battery**

### 5.2.2. Bidirectional dc-dc converter

Bidirectional dc-dc converter is used for bidirectional power flow from or to the battery. In figure 5.4, the bidirectional dc-dc converter is shown which is connected in parallel with solar PV system. The converter has two IGBT switches $S_1$, $S_2$, diodes $D_1$, $D_2$, inductor (L) and

capacitor ($C_{dc}$). The output of converter is connected to the CCP through $C_{dc}$. The converter works in two modes i.e., boost and buck.

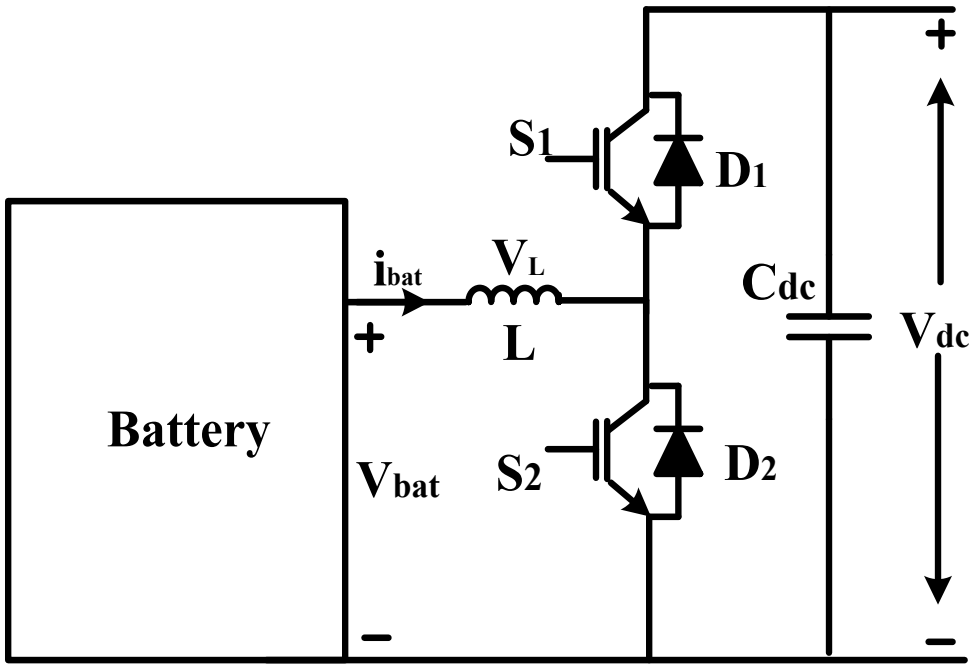


**Fig. 5.4. Bidirectional converter in buck-boost mode**

The bidirectional operation of the above circuit in two modes is as explained below:

**Mode 1 (Boost Mode):** In this mode switch $S_2$ and diode $D_1$ enters into conduction depending on the duty cycle whereas the switch $S_1$ and diode $D_2$ are off all the time. This mode can further be divided into two intervals depending on the conduction of the switch $S_2$ and diode $D_1$.

- *Interval 1: ($S_1$-OFF, $D_1$-OFF; $S_2$-ON, $D_2$-OFF)* In this mode $S_2$ is on and hence can be considered to be short circuited, therefore battery charges the inductor and the inductor current goes on increasing till the gate pulse is removed from the $S_2$. Also, since the diode $D_1$ is reversed biased in this mode and the switch $S_1$ is off, no current flows through the switch $S_1$.
- *Interval 2: ($S_1$-OFF, $D_1$-ON; $S_2$-OFF, $D_2$-OFF)* In this mode $S_2$ and $S_1$ both are off and hence can be considered to be opened circuited. Now since the current owing through the inductor cannot change instantaneously, the polarity of the voltage across it reverses and hence it starts acting in series with the input voltage ($V_{bat}$). Hence, the diode $D_1$ is forward biased and the inductor current charges the output capacitor $C_{dc}$ to a higher voltage. Therefore, the output voltage boosts up.

**Mode 2 (Buck Mode):** In this mode switch $S_1$ and diode $D_2$ enters into conduction depending on the duty cycle whereas the switch $S_2$ and diode $D_1$ are off all the time. This mode can further be divided into two intervals depending on the conduction on the switch $S_2$ and diode $D_1$.

- *Interval 1: ($S_1$-ON, $D_1$- OFF; $S_2$- OFF, $D_2$- OFF)* In this mode $S_1$ is on and hence can be considered to be short circuited. The higher voltage battery will charge the inductor and the output capacitor will get charged by it.
- *Interval 2: ($S_1$- OFF, $D_1$- OFF; $S_2$- OFF, $D_2$-ON)* In this mode $S_2$ and $S_1$ both are off. Since the inductor current cannot change instantaneously, it gets discharged through the freewheeling diode $D_2$. The output voltage is decreased as compared to the input voltage.

## 5.3. CONTROL ALGORITHMS FOR DC LINK VOLTAGE CONTROL OF STAND-ALONE PV SYSTEM WITH BESS

Due to intermittent nature of solar energy, PV power cannot always meet the load demand and requires an energy storage device. When more than one energy source is connected, the voltage at common coupling point may fluctuate. This requires regulation and control of dc-link voltage at CCP under both variable irradiation as well as variable load condition. There are several control algorithms such as PI, ANFIS, FLC, model predictive controller, adaptive based etc. available in literature for dc link voltage control of stand-alone PV system with BESS.
The control algorithms used in the present work are as follows:

- Conventional PI controller
- Proposed NARMA-L2 controller

### 5.3.1. Proportional Integral-based conventional control algorithm

Both power output from solar PV and load demand are dynamic in nature. For continuous supply of power to load and to address the intermittency, battery energy storage system is connected in parallel with SPV system. This causes the voltage at dc-link to vary. In present work, PI controller is used for control of dc-link voltage of stand-alone PV system with BESS. A PI controller is a control loop feedback mechanism and is mainly used in industrial control systems.
The PI controller involves calculation of two different parameters, Proportional (P) and the Integral (I) values. The proportional component depends only on the difference between the set point and the process variable. This difference is referred to as the error term. The integral component sums the error term over time. The result is that even a small error term will cause the integral component to increase slowly. The integral response will continually increase over time unless the error is zero, so the effect is to drive the steady-State error to zero.

The overall control action is governed by mathematical formula given below:

$$u(t) = K_P(t) + K_i \int_0^t e(t)dt \quad (5.4)$$

where, $K_p$ and $K_i$ are all non-negative, denote the coefficients for the proportional, integral terms respectively.

In figure 5.5, the block diagram for controlling dc link voltage using PI controller is shown. The INC MPPT technique is used to track the maximum power available from PV array and using dc-dc converter voltage output of SPV is maintained at fixed value. Now, the maintained dc link voltage has been compared with reference dc voltage and the generated error is given to proportional-integral (PI) controller to generate battery current ($I_{bat}$). The battery current and reference battery current are compared and the resultant signal is given to hysteresis band for gating battery switches $S_1$ or $S_2$. The switching ON/OFF of $S_2$ takes places by comparing the SoC (State of charge) with fixed value. If SoC is greater than the fixed value (0.8) then the triggering of $S_2$ switch comes into action.

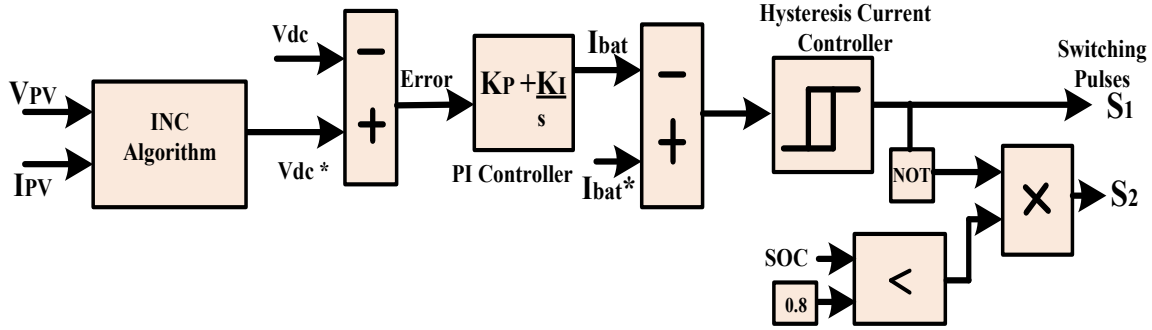


**Fig. 5.5. Block diagram for controlling dc link voltage of stand-alone PV system with BESS using PI controller**

### 5.3.2. Nonlinear Autoregressive Moving Average control algorithm (NARMA)

The non-linear autoregressive moving average model is the most discernible form of non-linear discrete time system. In a NARMA model the past, present input and output values are used to determine future output values. The equation for the approximate model is shown in equation (5.5)

$$Y_{(k+d)} = f\,[Y_{(k)}, Y_{(k-1)}, \ldots . Y_{(k-n+1)}, U_{(k)}, U_{(k-1)}, \ldots . U_{(k-n+1)}] \quad (5.5)$$

where $Y_{(k)}$, , $U_{(k)}$ are the input and output of the system respectively, d is the relative degree and $f\,[.]$ is a nonlinear approximation of input and output of the system. For the identification stage, a global approximation can be used to evaluate $f\,[.]$. For control purposes, using backpropagation ANN, for finding a control signal , $U_{(k)}$ is noted to be quite slow because of the involving dynamic gradient methods. Therefore, an efficient method is proposed by

Narendra and Mukhopadhyay by introducing approximation models to overcome computational difficulties. Two NARMA models viz. NARMA L1 and NARMA L2 have been discussed in literature [89]. It was found that the NARMA-L2 involving two sub-approximation functions is more efficient and adequate in the identification and adaptation of control contexts [91] and hence has been proposed in this work for dc-link voltage regulation.

### 5.3.3. Nonlinear Autoregressive Moving Average-L2 control algorithm (NARMA-L2)

The primary goal of this control is to linearize the nonlinear dynamics. The NARMA-L2 controller formed by two neural networks: The 1st network is NARMA model, which is the standard model, used to represent general discrete-time nonlinear systems in the system identification to identify the system to be controlled and the second network is used for the control design. The NARMA-L2 model is shown using equation (5.6):

$$\hat{Y}_{(k+d)} = f\left[Y_{(k)}, Y_{(k-1)}, \ldots . Y_{(k-n+1)}, U_{(k)}, U_{(k-1)}, \ldots . U_{(k-n+1)}\right] + g\left[Y_{(k)}, Y_{(k-1)}, \ldots . Y_{(k-n+1)}, U_{(k)}, U_{(k-1)}, \ldots . U_{(k-n+1)}\right] * U_{(k)} \quad (5.6)$$

The two sub-functions, $f$ and $g$, are used in the identification phase as well as to compute the control signal as follows:

$$U_{(k)} = \frac{Y_{(k+d)} - f[Y_{(k)}, Y_{(k-1)}, \ldots . Y_{(k-n+1)}, U_{(k)}, U_{(k-1)}, \ldots . U_{(k-n+1)}]}{g[Y_{(k)}, Y_{(k-1)}, \ldots . Y_{(k-n+1)}, U_{(k)}, U_{(k-1)}, \ldots . U_{(k-n+1)}]} \quad (5.7)$$

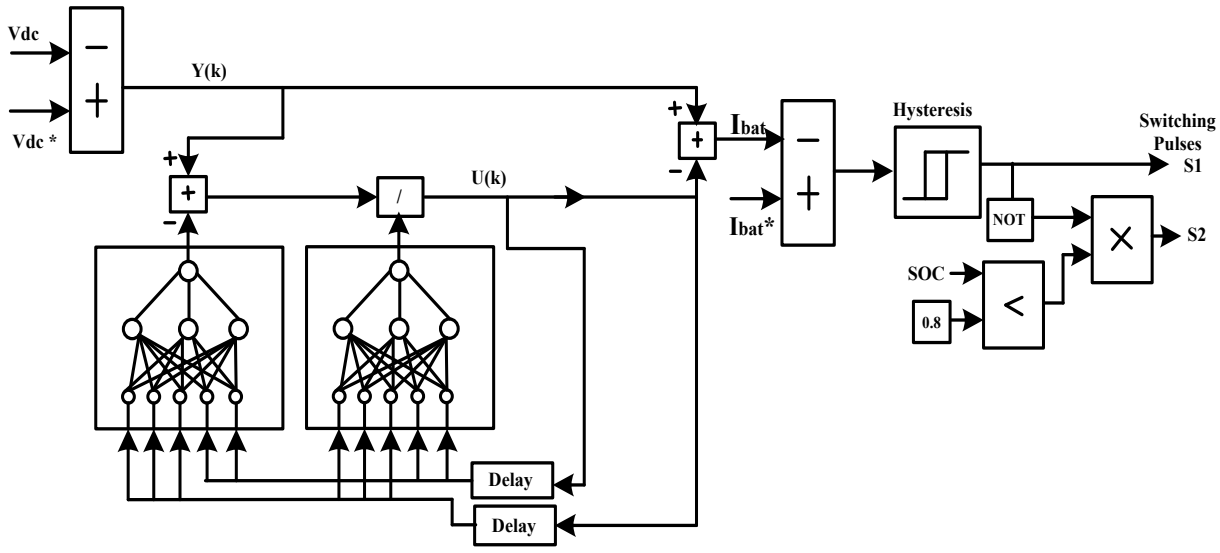


**Fig. 5.6. Block diagram for controlling dc link voltage of stand-alone PV system with BESS using NARMA-L2 controller**

Here, NARMA-L2 is used for controlling dc-link voltage of stand-alone PV system with BESS. It maintains the dc link voltage under input/output variation condition. Figure 5.6 shows the

block diagram for controlling dc link voltage of stand-alone PV system with BESS using NARMA-L2 controller.

## 5.4. RESULTS AND DISCUSSIONS

Simulation results and analysis for dc-link voltage regulation of stand-alone PV system with BESS (Appendix B (c)) using above mentioned control algorithms have been shown in this section. The efficacy of the novel control algorithm is tested under variable irradiation at input side and load variation at output side has been considered.

### 5.4.1. Proportional Integral control algorithm

#### 5.4.1.1. Linear Load

In this section, the performance of conventional PI controller with linear load is presented. The system is considered to be working under standard test condition (STC) i.e., solar irradiation 1000W/m$^2$ and temperature 25°C at a load of 2.5 kW.

**Performance under variable irradiation condition**

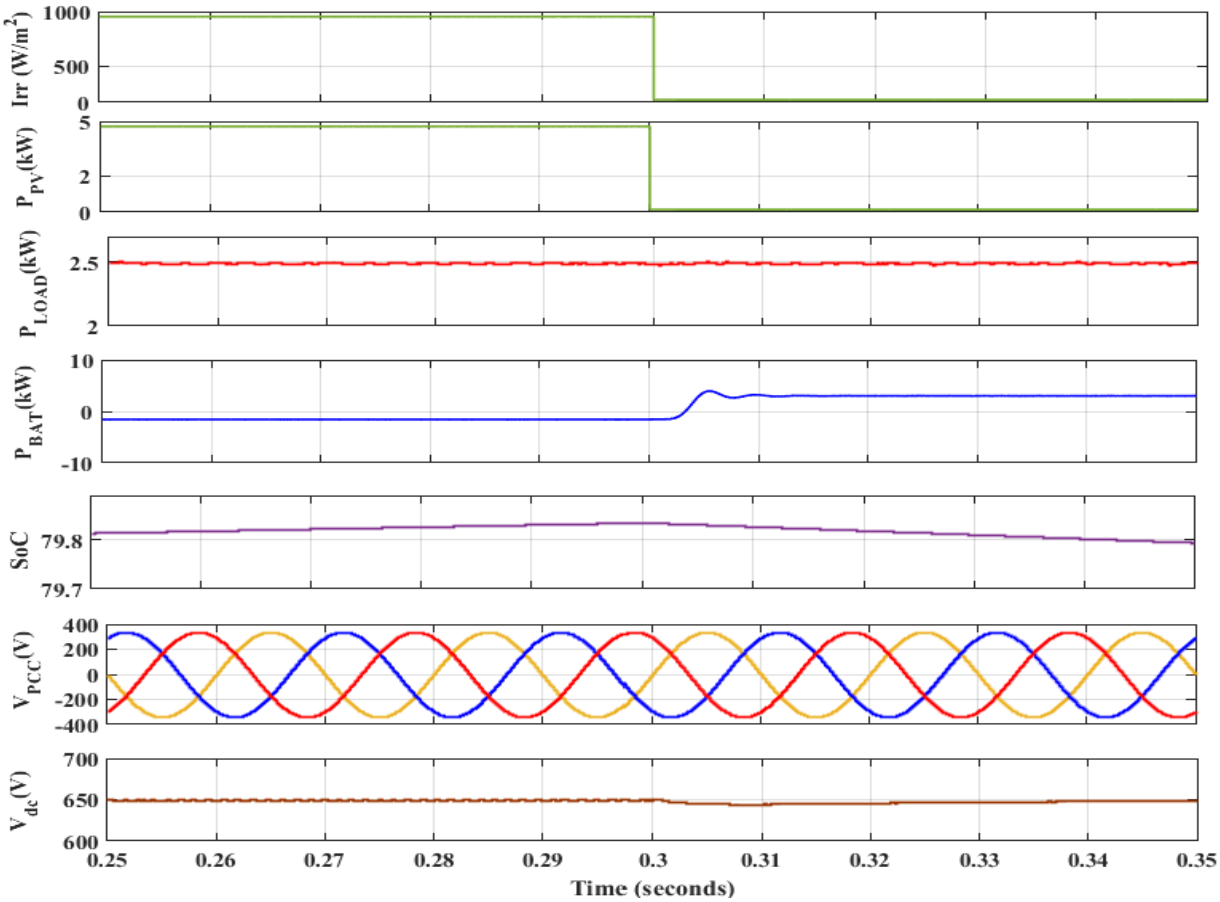


**Fig. 5.7. Performance under variable irradiation condition with PI controller**

Figure 5.7 shows, the waveforms of solar irradiation (W/m$^2$), power of PV array (kW), load requirement (kW), power of battery (kW), state of charge (SoC) of the battery, point of common coupling voltage ($V_{PCC}$), dc-link voltage ($V_{dc}$) under variable irradiation condition. The SPV system generates ≈ 4.7 kW power and the load demand is 2.5 kW. Load demand is fulfilled by solar PV system alone and surplus power (2.2 kW) from PV system is used to charge the battery. At t=0.3 second, irradiation is changed from 1000W/m$^2$ to 100W/m$^2$. With the decrease in the irradiation level, the power generated from the PV decreases from 4.7 kW to 0.14 kW. Now, the deficit power (2.36 kW) is taken from battery to meet the load demand. The state of charge of battery is decreasing. The voltage across dc link is maintained at 650V and common coupling point voltage is found to be balanced and sinusoidal.

**Performance under variable load condition**

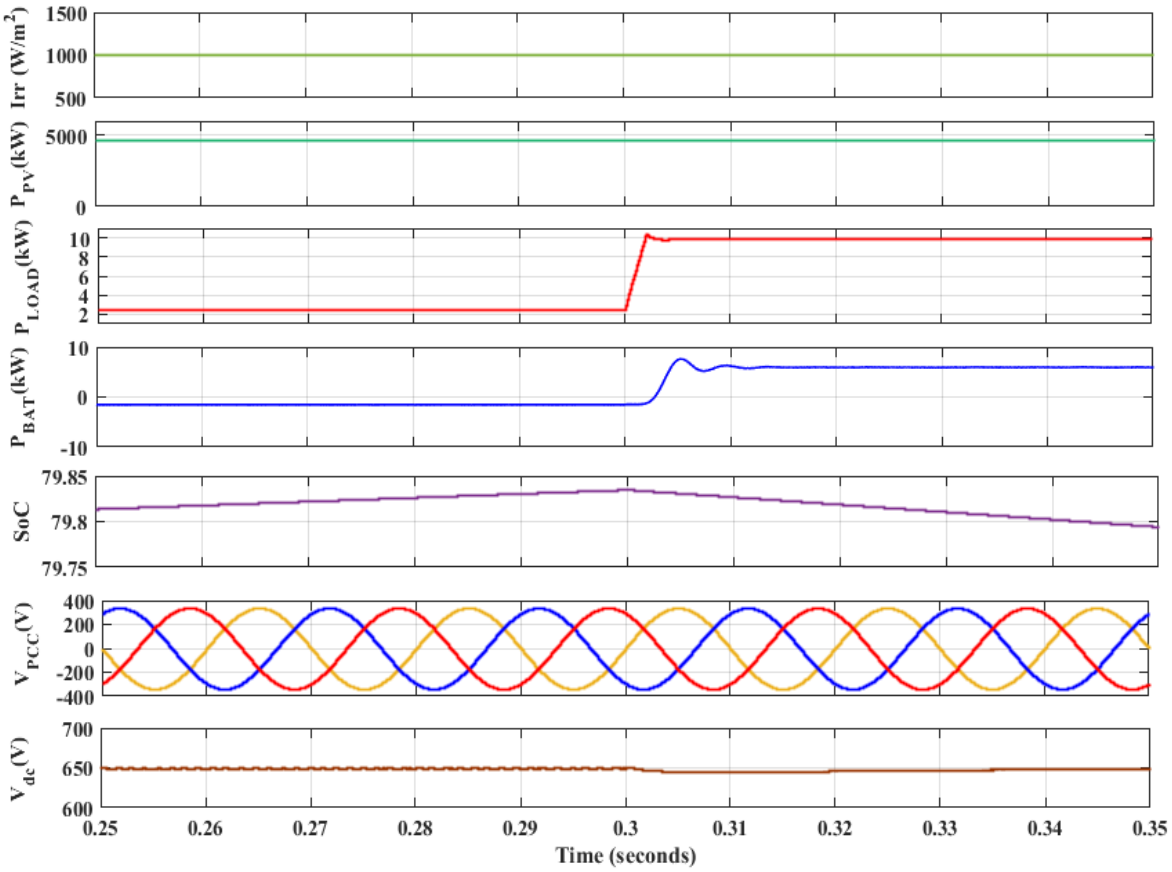


**Fig. 5.8. Performance under variable load conditions with PI controller**

Figure 5.8 shows the waveforms of solar irradiation (W/m$^2$), power of PV array (kW), load requirement (kW), power of battery (kW), state of charge (SoC) of the battery, point of common coupling voltage ($V_{PCC}$), dc-link voltage ($V_{dc}$) under variable load condition. The SPV system generates ≈ 4.7 kW power and the load demand is 2.5 kW. Load demand is fulfilled by

solar PV system alone and surplus power (2.2 kW) from PV system is used to charge the battery. At t=0.3 second, load demand is increased from 2.5 kW to 10 kW. Now, the deficit power (5.3 kW) is taken from battery to meet the load demand. The state of charge of battery is decreasing. The voltage across dc link is maintained at 650V and common coupling point voltage is found to be balanced and sinusoidal.

### 5.4.1.2. Non-Linear Load

In this section, the performance of conventional PI controller with non-linear load is presented. The system is considered to be working under standard test condition (STC) i.e., solar irradiation 1000W/m$^2$ and temperature 25°C at a non-linear load (3-ϕ bridge rectifier R=80-ohm, L=80 mH).

**Performance under variable irradiation condition**

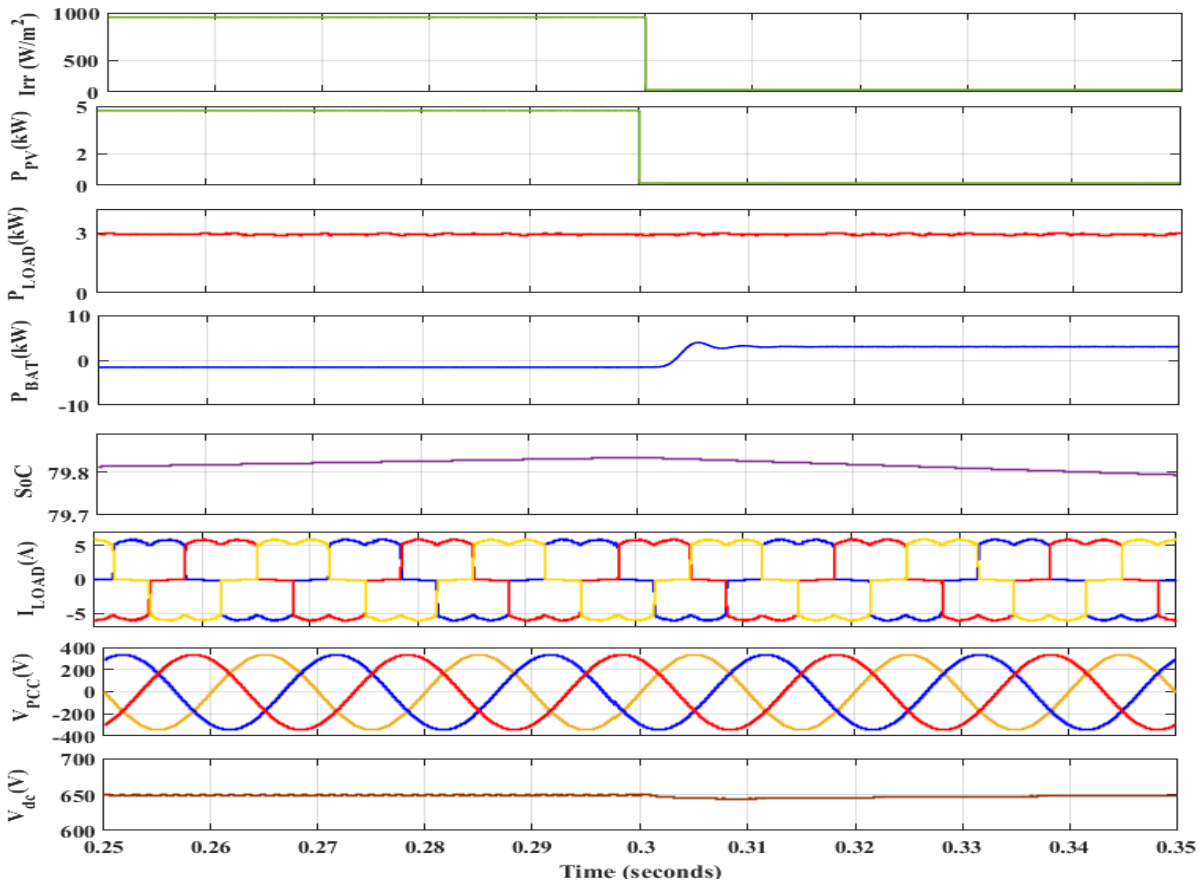


**Fig. 5.9. Performance under variable irradiation condition with PI controller**

Figure 5.9 shows, the waveforms of solar irradiation (W/m$^2$), power of PV array (kW), load requirement (kW), power of battery (kW), state of charge (SoC) of the battery, point of common coupling voltage ($V_{PCC}$), dc-link voltage ($V_{dc}$) under variable irradiation condition.

The SPV system generates ≈ 4.7 kW power and the load demand is 3 kW. Load demand is fulfilled by solar PV system alone and surplus power (1.7 kW) from PV system is used to charge the battery. At t=0.3 second, irradiation is changed from 1000W/m$^2$ to 100W/m$^2$. With the decrease in the irradiation level, the power generated from the PV decreases from 4.7 kW to 0.14 kW. Now, the deficit power (2.86 kW) is taken from battery to meet the load demand. The state of charge of battery is decreasing. The voltage across dc link is maintained at 650V and common coupling point voltage is found to be balanced and sinusoidal.

**Performance under variable load condition**

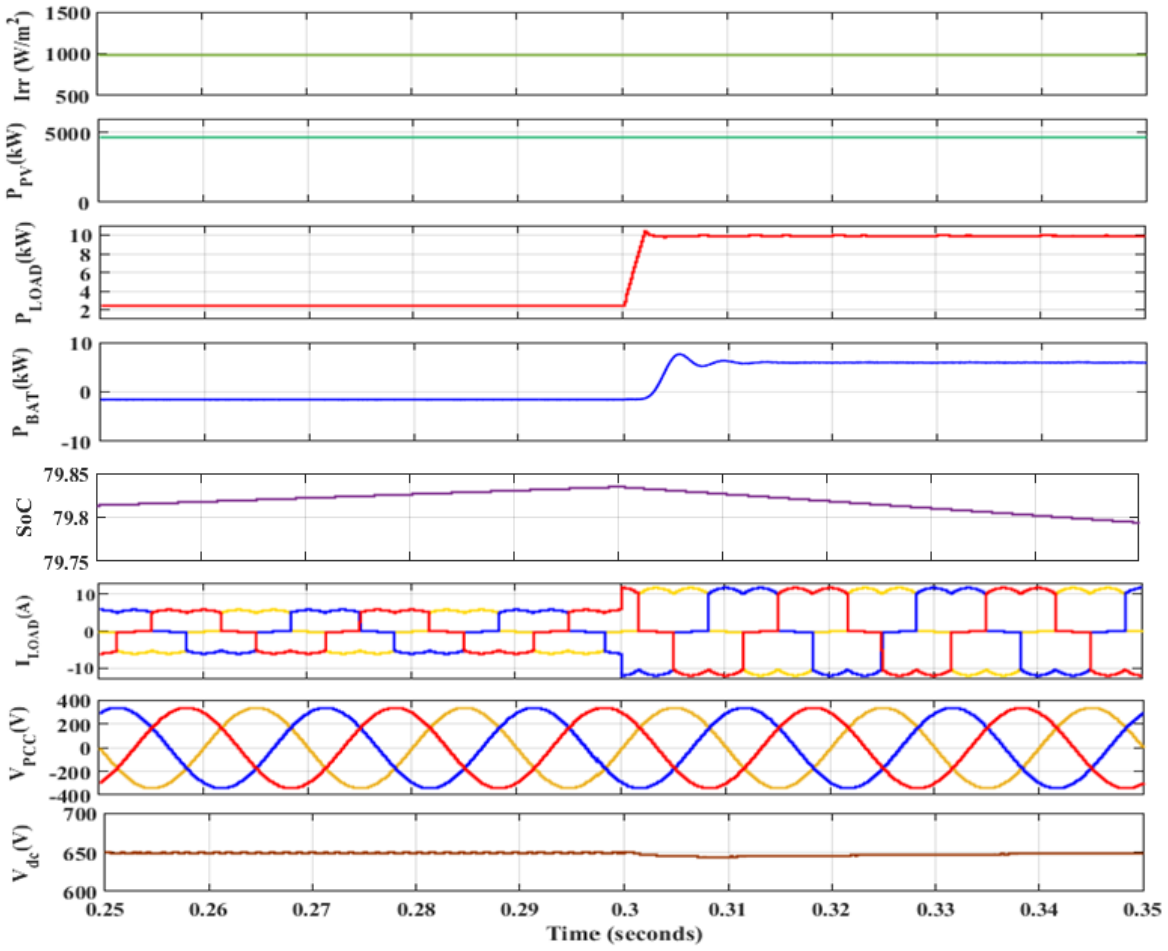


**Fig. 5.10. Performance under variable load condition with PI controller**

Figure 5.10 shows the waveforms of solar irradiation (W/m$^2$), power of PV array (kW), load requirement (kW), power of battery (kW), state of charge (SoC) of the battery, point of common coupling voltage ($V_{PCC}$), dc-link voltage ($V_{dc}$) under variable load condition. The SPV system generates ≈ 4.7 kW power and the load demand is 3 kW. Load demand is fulfilled by solar PV system alone and surplus power (1.7 kW) from PV system is used to charge the battery. At t=0.3 second, load demand is increased from 3 kW to 10 kW. Now, the deficit power

(5.3 kW) is taken from battery to meet the load demand. The state of charge of battery is decreasing. The voltage across dc link is maintained at 650V and common coupling point voltage is found to be balanced and sinusoidal.

### 5.4.2. Proposed NARMA-L2 Controller

#### 5.4.2.1. Linear Load

In this section, the performance proposed NARMA-L2 controller with linear load is presented. The system is considered to be working under standard test condition (STC) i.e., solar irradiation 1000W/m$^2$ and temperature 25°C at a load of 2.5 kW

**Performance under variable irradiation condition**

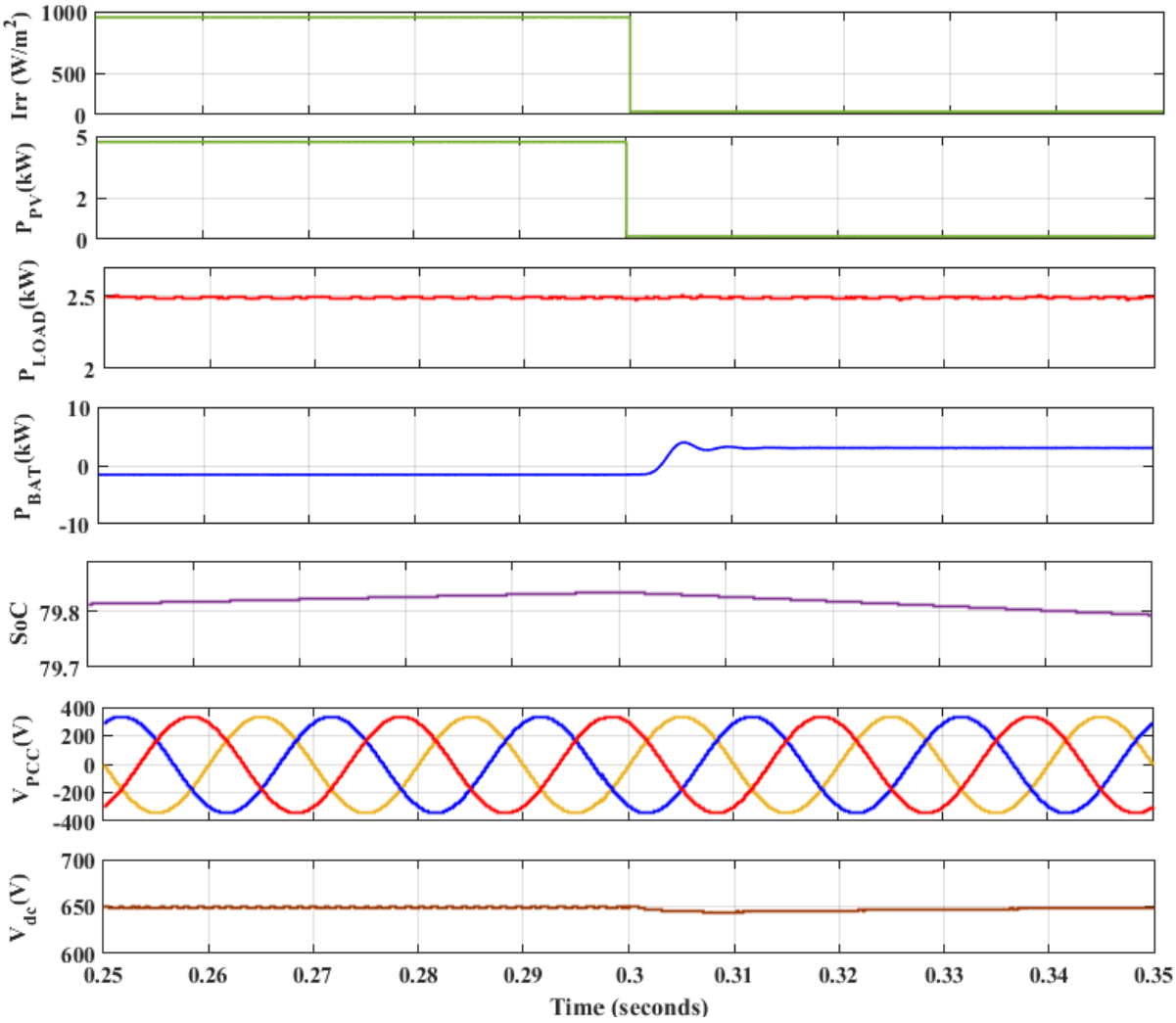


**Fig. 5.11. Performance under variable irradiation condition with PI controller**

Figure 5.11 shows, the waveforms of solar irradiation (W/m$^2$), power of PV array (kW), load requirement (kW), power of battery (kW), state of charge (SoC) of the battery, point of

common coupling voltage ($V_{PCC}$), dc-link voltage ($V_{dc}$) under variable irradiation condition. The SPV system generates ≈ 4.7 kW power and the load demand is 2.5 kW. Load demand is fulfilled by solar PV system alone and surplus power (2.2 kW) from PV system is used to charge the battery. At t=0.3 second, irradiation is changed from 1000W/m$^2$ to 100W/m$^2$. With the decrease in the irradiation level, the power generated from the PV decreases from 4.7 kW to 0.14 kW. Now, the deficit power (2.36 kW) is taken from battery to meet the load demand. The state of charge of battery is decreasing. The voltage across dc link is maintained at 650V and common coupling point voltage is found to be balanced and sinusoidal.

**Performance under variable load condition**

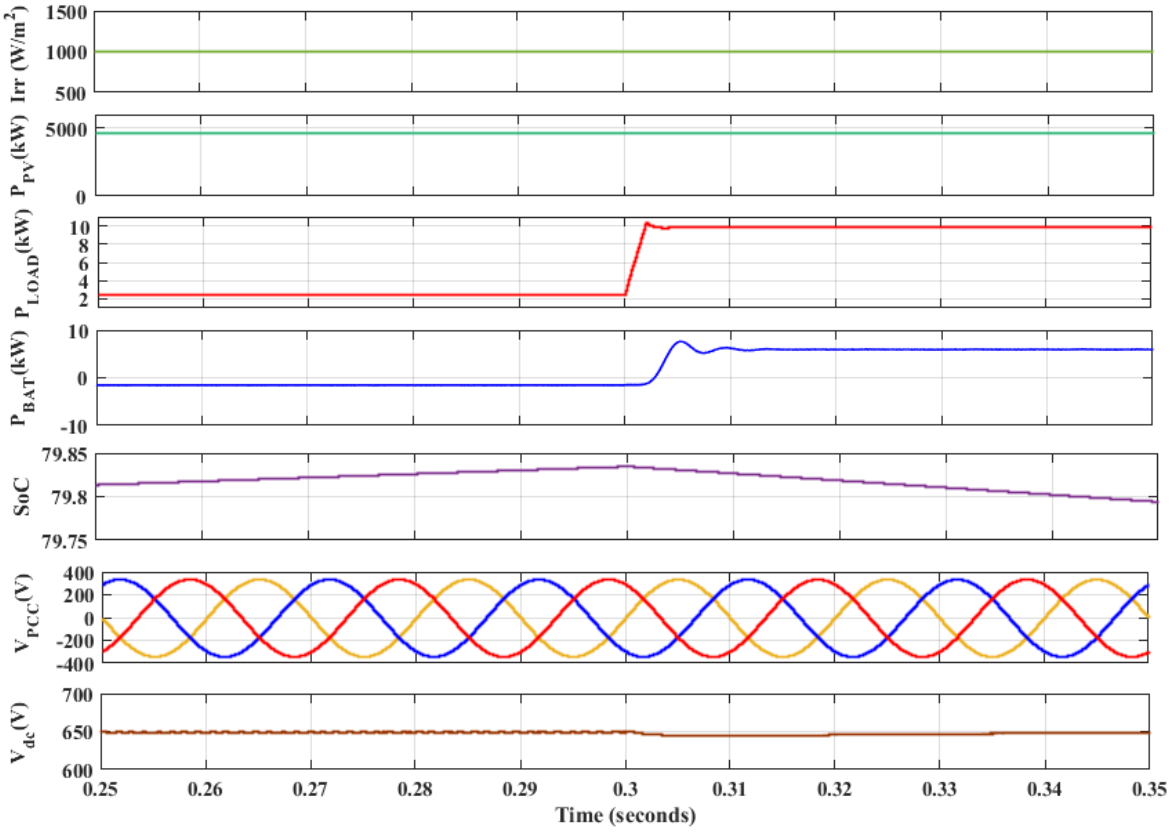


**Fig. 5.12. Performance under variable load conditions with PI controller**

Figure 5.12 shows the waveforms of solar irradiation (W/m$^2$), power of PV array (kW), load requirement (kW), power of battery (kW), state of charge (SoC) of the battery, point of common coupling voltage ($V_{PCC}$), dc-link voltage ($V_{dc}$) under variable load condition. The SPV system generates ≈ 4.7 kW power and the load demand is 2.5 kW. Load demand is fulfilled by solar PV system alone and surplus power (2.2 kW) from PV system is used to charge the battery. At t=0.3 second, load demand is increased from 2.5 kW to 10 kW. Now, the deficit

power (5.3 kW) is taken from battery to meet the load demand. The state of charge of battery is decreasing. The voltage across dc link is maintained at 650V and common coupling point voltage is found to be balanced and sinusoidal.

### 5.4.2.2. Non-Linear Load

In this section, the performance of conventional PI controller with non-linear load is presented. The system is considered to be working under standard test condition (STC) i.e., solar irradiation 1000W/m$^2$ and temperature 25°C at a non-linear load (3-ϕ bridge rectifier R=80-ohm, L=80 mH).

**Performance under variable irradiation condition**

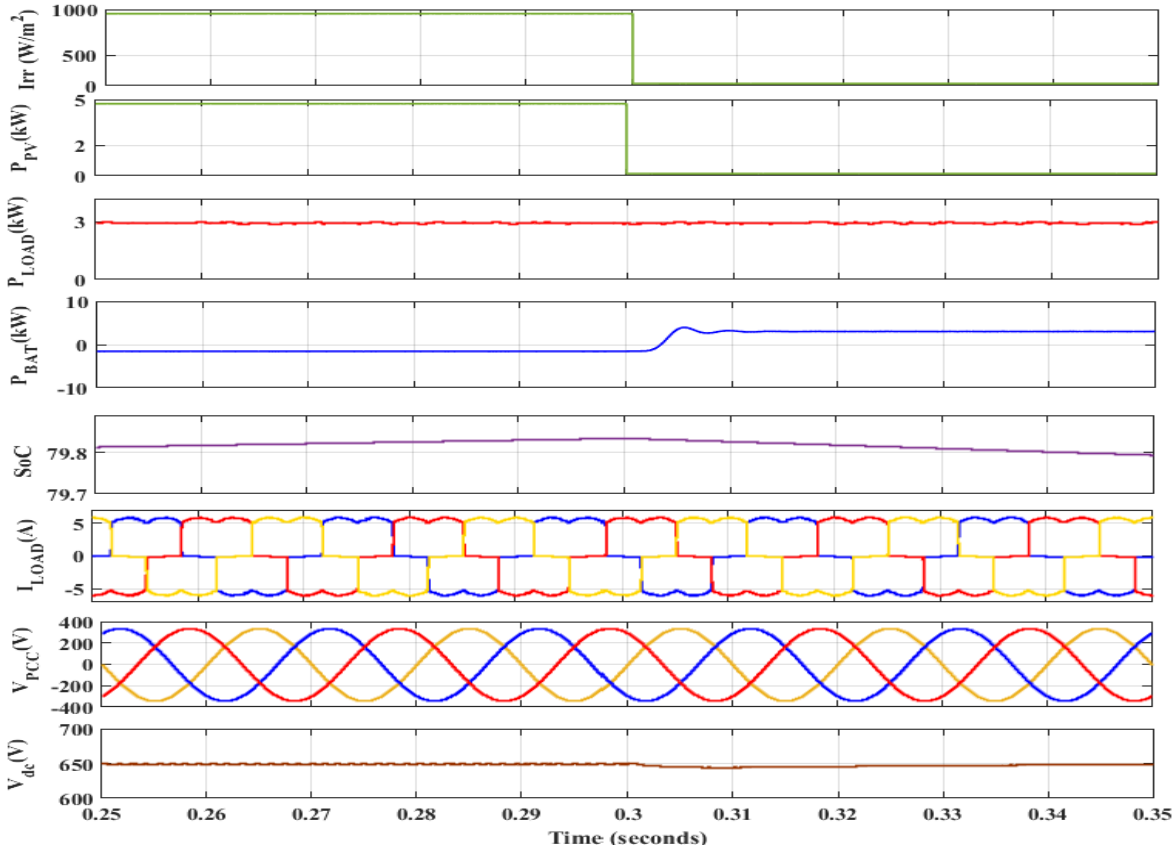


**Fig. 5.13. Performance under variable irradiation condition with PI controller**

Figure 5.13 shows, the waveforms of solar irradiation (W/m$^2$), power of PV array (kW), load requirement (kW), power of battery (kW), state of charge (SoC) of the battery, point of common coupling voltage ($V_{PCC}$), dc-link voltage ($V_{dc}$) under variable irradiation condition. The SPV system generates ≈ 4.7 kW power and the load demand is 3 kW. Load demand is fulfilled by solar PV system alone and surplus power (1.7 kW) from PV system is used to

charge the battery. At t=0.3 second, irradiation is changed from 1000W/m$^2$ to 100W/m$^2$. With the decrease in the irradiation level, the power generated from the PV decreases from 4.7 kW to 0.14 kW. Now, the deficit power (2.86 kW) is taken from battery to meet the load demand. The state of charge of battery is decreasing. The voltage across dc link is maintained at 650V and common coupling point voltage is found to be balanced and sinusoidal.

**Performance under variable load condition**

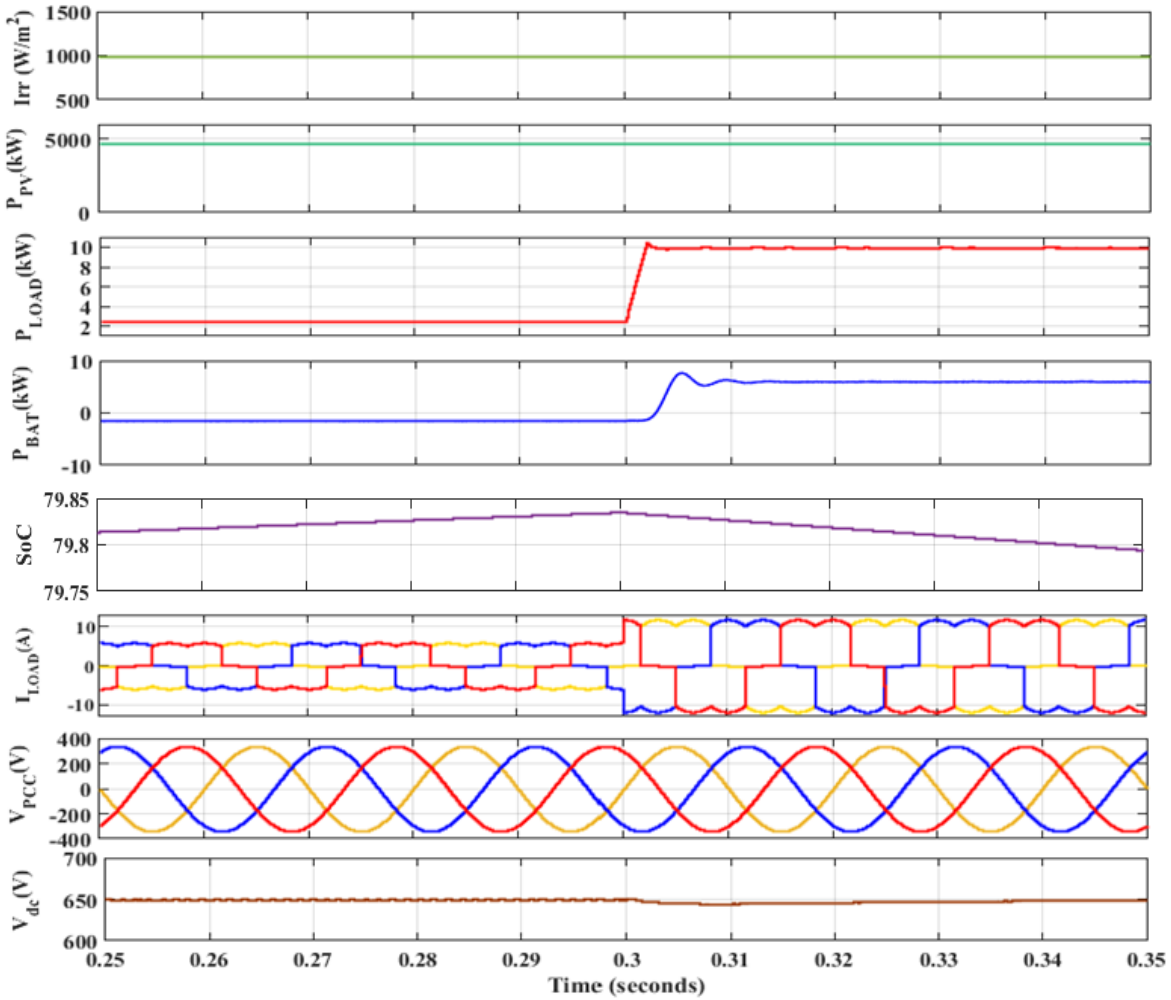


**Fig. 5.14. Performance under variable load condition with PI controller**

Figure 5.14 shows the waveforms of solar irradiation (W/m$^2$), power of PV array (kW), load requirement (kW), power of battery (kW), state of charge (SoC) of the battery, point of common coupling voltage ($V_{PCC}$), dc-link voltage ($V_{dc}$) under variable load condition. The SPV system generates ≈ 4.7 kW power and the load demand is 3 kW. Load demand is fulfilled by solar PV system alone and surplus power (1.7 kW) from PV system is used to charge the battery. At t=0.3 second, load demand is increased from 3 kW to 10 kW. Now, the deficit power (5.3 kW) is taken from battery to meet the load demand. The state of charge of battery is

decreasing. The voltage across dc link is maintained at 650V and common coupling point voltage is found to be balanced and sinusoidal.

### 5.4.3. COMPARISON OF NARMA-L2 CONTROL ALGORITHM WITH P-I CONTROLLER

In this section, the proposed control algorithm NARMA-L2 has been compared with conventional PI control scheme in terms of dc link voltage. Figure 5.15 (a) shows the comparison of NARMA-L2 and PI controller with irradiation variation. At time t = 0.3 seconds, irradiation is changed from 1000W/m$^2$ to 100W/m$^2$. It can be observed that during initial period and irradiation variation, the NARMA-L2 gives better control of dc-link voltage in terms of undershoot, overshoot and settling time.

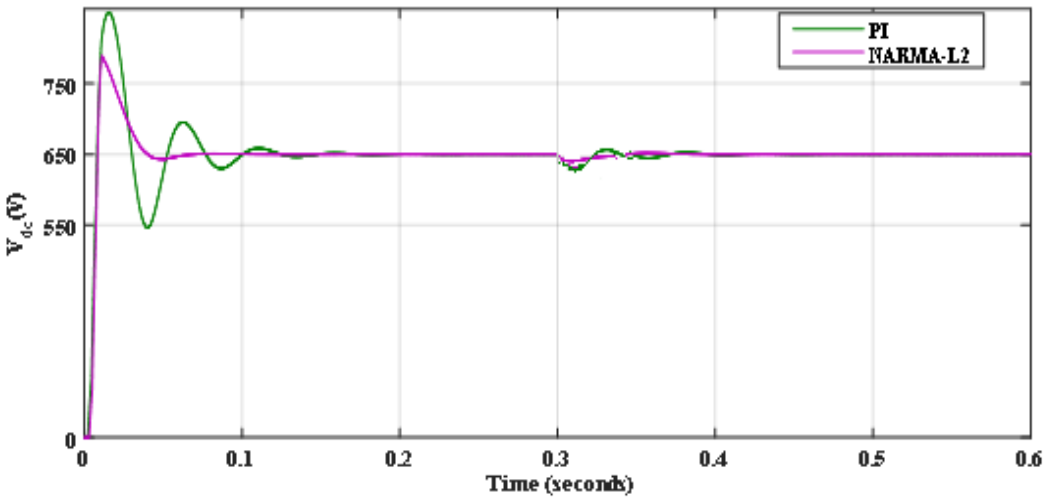


**(a) Irradiation variation**

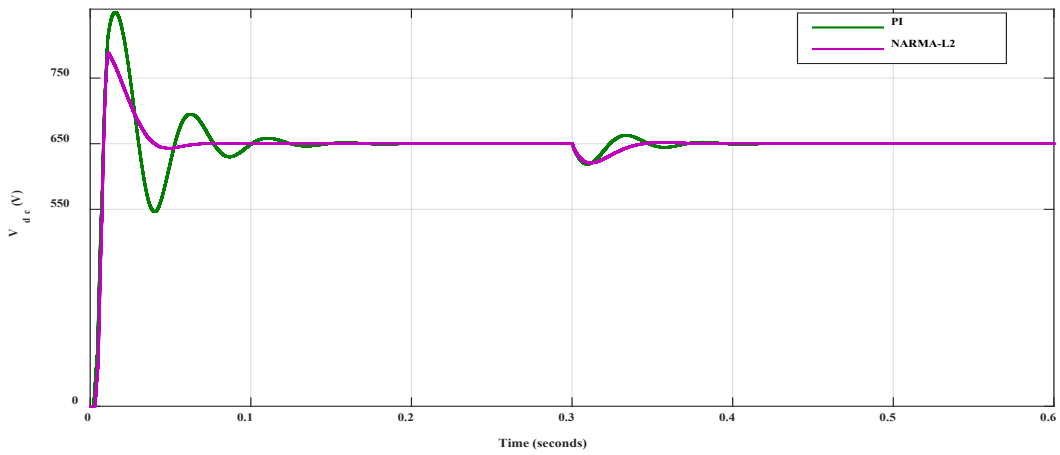


**(b) Load variation**

**Fig. 5.15. DC bus voltage ($V_{dc}$) comparison of NARMA-L2 with PI control algorithm**

Figure 5.15 (b) shows the comparison of NARMA-L2 and PI controller with load variation. At time t = 0.3 seconds, load demand is increased from 2.5 kW to 10 kW. It can be observed that during initial period and load variation, the NARMA-L2 gives better control of dc-link voltage in terms of undershoot, overshoot and settling time.

**Table 5.1.(a) Comparison of dc-link voltage of NARMA-L2 control algorithm with PI controller with irradiation variation**

| Algorithm | Initial Condition | | | Irradiation Variation | | |
|---|---|---|---|---|---|---|
| | Undershoot voltage of dc-link (V) | Overshoot voltage of dc-link (V) | Settling Time (sec) | Undershoot voltage of dc-link (V) | Overshoot voltage of dc-link (V) | Settling Time (sec) |
| **NARMA-L2** | - | 760 | 0.14 | 610 | - | 0.11 |
| **PI** | 550 | 850 | 0.18 | 625 | 652 | 0.19 |

**Table 5.1.(b) Comparison of dc-link voltage of NARMA-L2 control algorithm with PI controller with load variation**

| Algorithm | Initial Condition | | | Load Increment | | |
|---|---|---|---|---|---|---|
| | Undershoot voltage of dc-link (V) | Overshoot voltage of dc-link (V) | Settling Time (sec) | Undershoot voltage of dc-link (V) | Overshoot voltage of dc-link (V) | Settling Time (sec) |
| **NARMA-L2** | - | 760 | 0.14 | 625 | - | 0.12 |
| **PI** | 550 | 850 | 0.18 | 627 | 655 | 0.18 |

Table 5.1 shows the comparison of voltage across dc bus of NARMA-L2 control algorithm with PI controller. Table 5.1 (a) and (b) gives the results in tabular form. It can be seen that, the NARMA-L2 gives better control of dc-link voltage in terms of undershoot, overshoot and settling time.

## 5.5. CONCLUDING REMARKS

In this chapter, control algorithms for the regulation of dc-link voltage in the stand-alone PV system with battery energy storage system is presented. Novel NARMA-L2 algorithm has been developed to control dc-link voltage. The developed control algorithm was tested in MATLAB/Simulink 2018a. The voltage across dc-link have been maintained under variable irradiation and load condition. Also, the continuous power to the load have been supplied either by solar PV system or by battery energy storage system. The simulation results show the efficacy of the proposed control algorithm under steady state and transient conditions. The point of common coupling voltage has been found to be balanced and sinusoidal. To establish the superiority of the developed algorithm, the results of NARMA-L2 algorithm are compared with conventional PI controller. Under transient conditions, the developed NARMA-L2 gives better control of dc-link voltage in terms of undershoot, overshoot and settling time.

# CHAPTER-VI

# PV INVERTER CONTROL ALGORITHM FOR GRID-TIED PV BASED MICROGRID

## INTRODUCTION

The output of solar PV based microgrid depends largely on atmospheric conditions and hence is intermittent. To take care of this intermittency and to supply good quality power at load end, PV based microgrid is connected to utility grid through PV inverter. In this chapter, PV inverter interfacing control algorithms for two stage three-phase grid interfaced PV system have been presented. The voltage source inverter is connected at point of common coupling via interfacing inductors ($L_f$) for compensating current ripples. The interfacing control algorithms are used to control the PV inverter for its efficient utilization and provides reactive power compensation, harmonics compensation and load balancing. In the present work, Novel Smooth Least Mean Square (SLMS), improved zero attracting LMS (IZALMS) and reweighted $L_0$ norm variable step size continuous mixed p-norm (RL$_0$-VSSCMPN) based adaptive control algorithms are proposed and developed for the SPV based microgrid. The performance of the proposed interfacing control algorithms is analysed and compared with conventional control algorithms using MATLAB-Simulink and Sim-Power System toolbox by carrying out simulation studies. The proposed algorithms are also tested in real time on the prototype hardware setup developed in the laboratory using dSPACE1202.

## 6.2. SYSTEM DESCRIPTION

Figure 6.1 shows the schematic diagram of two stage three phase grid interfaced SPV system consisting of 11.78 kW SPV array, dc-dc converter (boost), dc-link capacitor, PV inverter, interfacing inductors, grid and load. MPPT (P&O) is used to extract maximum power from PV array under varying environmental scenarios. PV inverter control algorithms are used for generation of reference currents which in turn are used to generate the gate pulses for the inverter. The PV inverter control scheme basically comprises of (i) voltage control (ii) network synchronization control and (iii) generation of gating pulses.

---

This chapter is based on the paper - (i) "Smooth LMS-based adaptive control of SPV system tied to grid for enhanced power quality," IET Power Elec., Vol. 13, Iss.. 15, pp. 3456-3466, 2020. doi: 10.1049/iet-pel.2020.0134. (ii) "Grid integration of Renewable Energy systems: Power electronics topologies for grid integration, Advanced control techniques of grid connected PV inverters" accepted in Renewable Energy Systems: Modelling, Optimization, and Applications (RESMOA 2021) (iii) "Design and Implementation of Improved Zero Attracting LMS adaptive filter for power quality refinement of PV system interfaced to grid" R2 submitted in AJSE (Springer)

In voltage control block, the voltage across the dc-link capacitor is controlled. Here, reference and sensed dc-link voltage are processed, to generate loss component ($I_{loss}$). Fundamental component obtained from network synchronization block together with loss component are used to calculate the reference current signals. Reference current signals and sensed grid current are used to generate the gating pulse signals for switching of PV inverter [46], [162]–[166]. Hysteresis Current Control (HCC) technique is used for gating pulse generation.

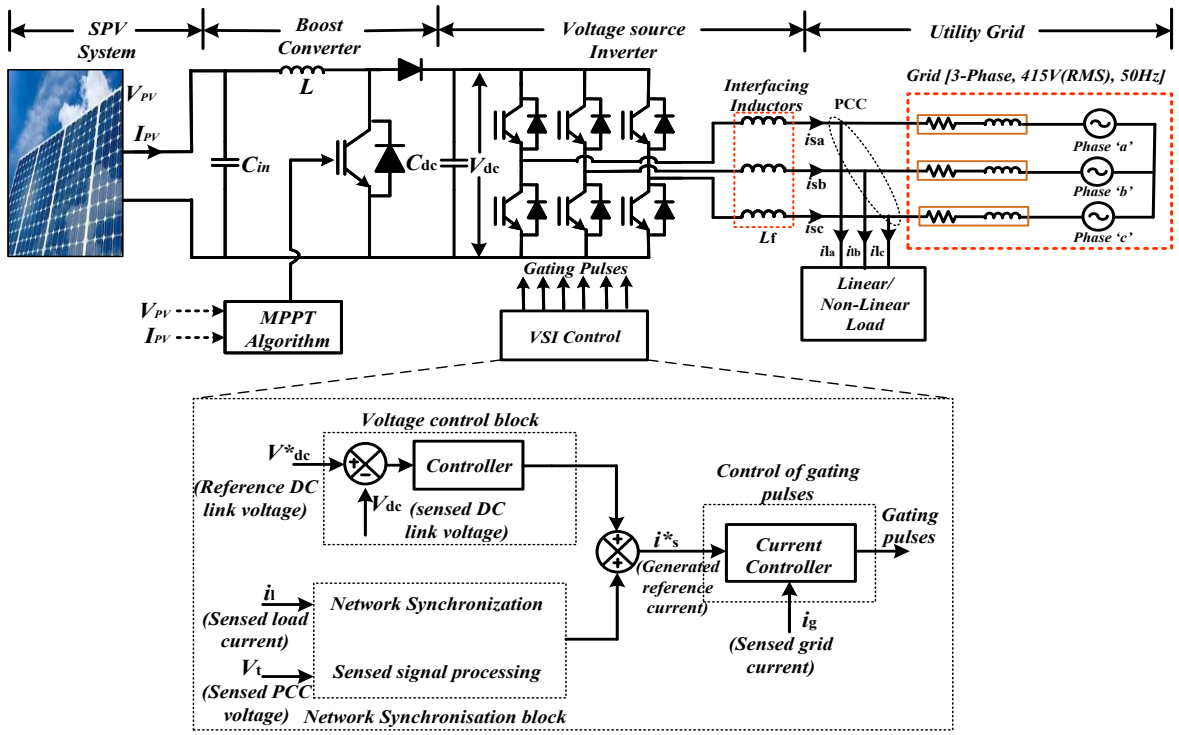


**Fig. 6.1. Schematic Diagram of Grid interfaced SPV system**

## 6.3. PV INVERTER CONTROL ALGORITHMS

There are several control algorithms available that generate reference currents for the voltage source inverter (VSI). The control algorithms used in the present work are as follows:

- Conventional Control Algorithms
  - Synchronous reference frame theory
  - Unit Template
- Adaptive Control Algorithms
  - LMS
  - Proposed adaptive control algorithms
    - Smooth LMS
    - Improved zero attracting LMS
    - Reweighted $L_0$ norm variable step size continuous mixed p-norm

### 6.3.1. Synchronous Reference Frame Theory-based Conventional Control Algorithm

Block diagram of SRFT based control algorithm is shown in figure 6.2. The sensed dc link voltage, three phase load currents and PCC voltage are given to voltage control and network synchronization block respectively for the generation of reference grid currents.

Three phases *'a-b-c'* can be transformed into *'α-β'* coordinates by Clark's transformation as given by equation (6.1). Phase-locked loop (PLL) is used for synchronization of inverter with the grid.

$$\begin{bmatrix} i_\alpha \\ i_\beta \end{bmatrix} = \sqrt{2/3}\begin{bmatrix} 1 & -1/2 & -1/2 \\ 0 & \sqrt{3}/2 & -\sqrt{3}/2 \end{bmatrix} \cdot \begin{bmatrix} i_{la} \\ i_{lb} \\ i_{lc} \end{bmatrix} \tag{6.1}$$

Using Park's transformation, these currents can be transformed from *'α-β'* to *'d-q'* frame as given by equation (6.2)

$$\begin{bmatrix} i_d \\ i_q \end{bmatrix} = \sqrt{2/3}\begin{bmatrix} \cos(\omega t) & \sin(\omega t) \\ -\sin(\omega t) & \cos(\omega t) \end{bmatrix} \cdot \begin{bmatrix} i_\alpha \\ i_\beta \end{bmatrix} \tag{6.2}$$

Where, $\omega$ is the angular frequency of the synchronous rotating frame

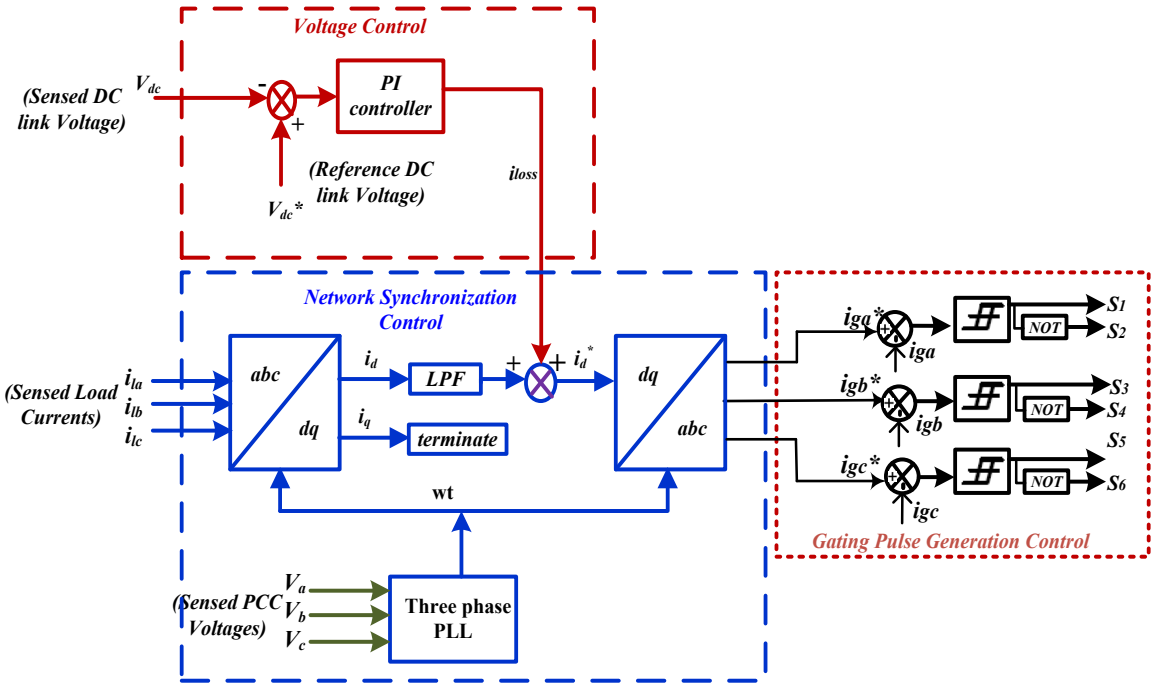


**Fig. 6.2. Block diagram of control scheme for SRF theory based conventional control algorithm**

The loss component of PV inverter given by $i_{loss}$, is the output of the proportional integral (PI) controller in the voltage control loop which is by equation (6.3).

$$i_{loss}(i+1) = i_{loss}(i) + K_p\{v_e(i) - v_e(i)\} + K_i v_e(i) \tag{6.3}$$

where, $K_p$ is proportional gain, $K_i$ is integral gain, $v_e(i)$ is voltage error signal at $i^{th}$ instant. The reference active component of supply current ($i_d^*$) is the summation of output of DC bus PI controller ($i_{loss}$) and fundamental DC current component of load current ($i_d$) which is given by equation (6.4).

$$i_d^* = (i_d + i_{loss}) \tag{6.4}$$

Inverse Clark's and Park's transformation are then used to obtain three-phase reference source current using equation (6.5) and equation (6.6). Reverse Park's transformation is given by equation (6.5):

$$\begin{bmatrix} i_\alpha^* \\ i_\beta^* \end{bmatrix} = \sqrt{\frac{2}{3}} \begin{bmatrix} \cos(\omega t) & \sin(\omega t) \\ -\sin(\omega t) & \cos(\omega t) \end{bmatrix} \begin{bmatrix} i_d \\ 0 \end{bmatrix} \tag{6.5}$$

Reverse Park's transformation is given equation (6.6) :

$$\begin{bmatrix} i_{ga}^* \\ i_{gb}^* \\ i_{gc}^* \end{bmatrix} = \sqrt{\frac{2}{3}} \begin{bmatrix} 1 & 0 \\ -1/2 & \sqrt{3/2} \\ -1/2 & -\sqrt{3/2} \end{bmatrix} \begin{bmatrix} i_\alpha^* \\ i_\beta^* \end{bmatrix} \tag{6.6}$$

In hysteresis current controller (HCC) the reference currents are compared with actual current within a hysteresis band and switching pulses are generated accordingly.

### 6.3.2. Unit Template-based Conventional Control Algorithm

In unit template based conventional control algorithm, the three phase PCC voltage and dc-link voltage are sensed to generate reference currents for the generation of gating signals for VSI. Figure 6.3 shows the schematic diagram of unit template based conventional control algorithm.

The peak value of per phase PCC voltage ($V_t$) is given by equation (6.7):

$$V_t = \sqrt{\frac{2}{3}(V_a^2 + V_b^2 + V_c^2)} \tag{6.7}$$

The in-phase unit template ($U_{aa}$, $U_{ab}$, $U_{ac}$) can be calculated by equation (6.8) [167]

$$\mathrm{U}_{aa} = \frac{V_a}{V_t}, \mathrm{U}_{ab} = \frac{V_b}{V_t}, \mathrm{U}_{ac} = \frac{V_c}{V_t} \tag{6.8}$$

The reference grid currents are obtained by multiplying the obtained unit template with output of dc-link PI controller $I_{loss}$ as given by equation (6.9).

$$i_{ga}^* = i_{loss}\mathrm{U}_{aa}, i_{gb}^* = i_{loss}\mathrm{U}_{ab}, i_{gc}^* = i_{loss}\mathrm{U}_{ac} \tag{6.9}$$

$i_{ga}^*$, $i_{gb}^*$, $i_{gc}^*$ are instantaneous values of reference grid currents. In HCC, the reference currents

are compared with actual current within a hysteresis band and switching pulses are generated accordingly.

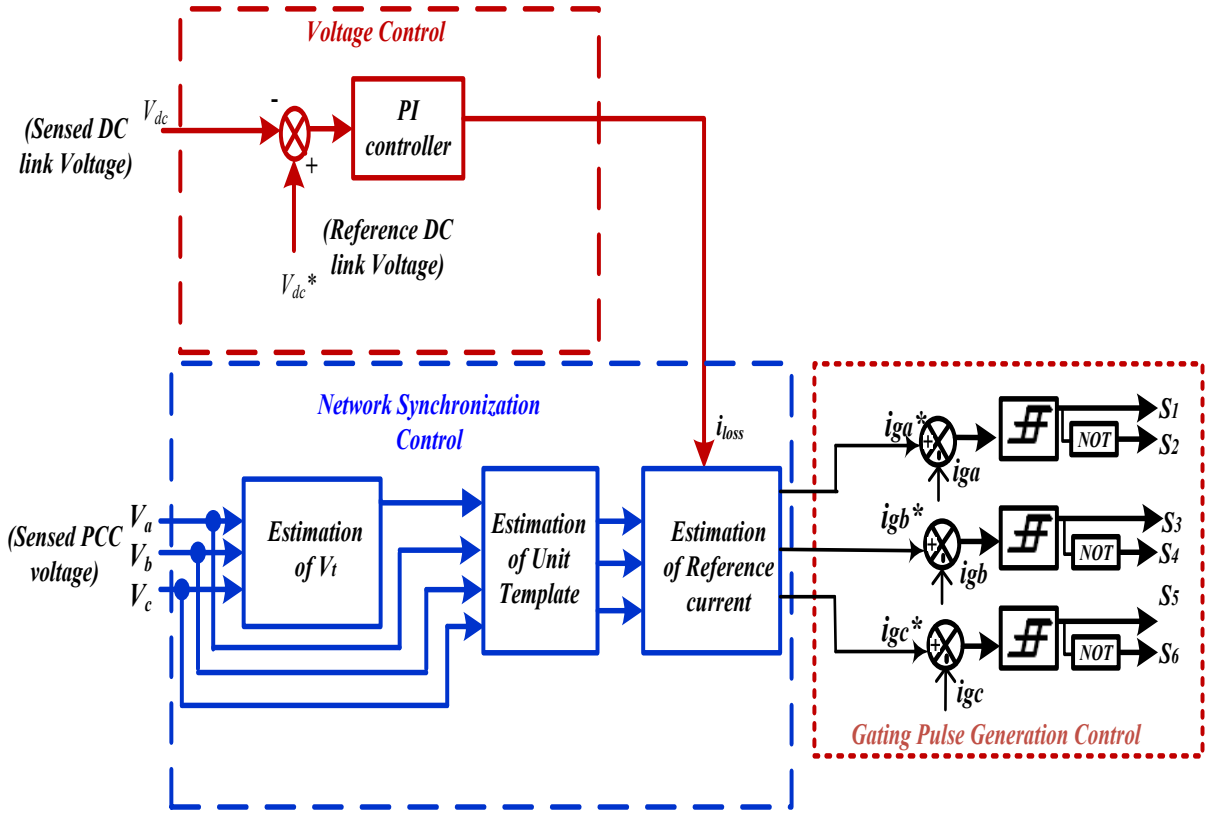


**Fig. 6.3. Block diagram of control scheme for Unit template based conventional control algorithm**

### 6.3.3. Least Mean Square (LMS) based Adaptive Control Algorithm

Fig. 6.4 shows the LMS based adaptive control algorithm of the SPV generating system used to estimate the fundamental part of the weight component.

The load current ($i_{la}$, $i_{lb}$, $i_{lc}$), unit templates ($U_{aa}$, $U_{ab}$, $U_{ac}$) obtained from sensed grid voltages ($V_a$, $V_b$, $V_c$), the dc-link voltage ($V_{dc}$) and voltage magnitude ($V_t$) are used to produce reference current. Using LMS control algorithm, active and reactive weight components are computed. Then reference grid current is generated with respect to active and reactive components. The reference grid currents produced from the algorithm are compared with the sensed grid currents and the error generated is used by the controller to produce the suitable gating signals for the voltage source inverter.

***Weight extraction by LMS control algorithm***

The LMS weight extraction is given by equation (6.10) [168]:

$$w(i+1) = w(i) + \varrho(i) * e(i) \tag{6.10}$$

$$e(i) = d(i) - x^T(i)\, w(i) \tag{6.11}$$

where $\varrho$ is step size, *e(i)* is estimated error signal, $x^T(i)$ is input vector, $d(i)$ is desired response and $w(i)$ weight value.

The active weights $w_{aa}, w_{ab}, w_{ac}$ at (i+1) instant for phase '*a*', '*b*' and '*c*' respectively can be computed as given in equation (6.12):

$$w_{aa}(i+1) = w_{aa}(i) + \varrho_{aa}(i) * e_{aa}(i)$$

$$w_{ab}(i+1) = w_{ab}(i) + \varrho_{ab}(i) * e_{ab}(i) \quad (6.12)$$

$$w_{ac}(i+1) = w_{ac}(i) + \varrho_{ac}(i) * e_{ac}(i)$$

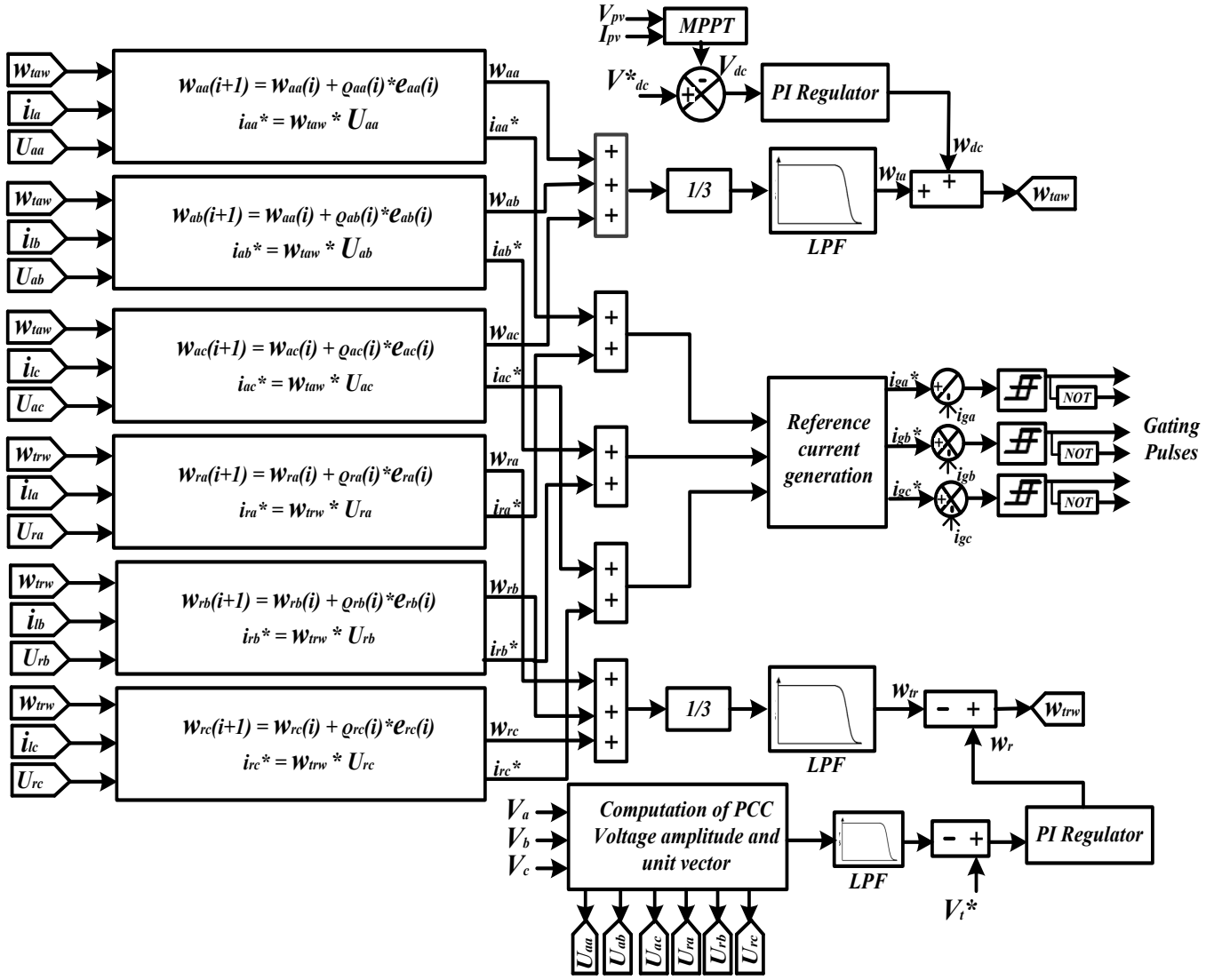


**Fig. 6.4. Block Diagram of LMS based adaptive control algorithm**

Similarly, the reactive weights $w_{ra}, w_{rb}, w_{rc}$ at (i+1) instant for phase '*a*', '*b*' and '*c*' respectively can be computed as given in equation (6.13):

$$w_{ra}(i+1) = w_{ra}(i) + \varrho_{ra}(i) * e_{ra}(i)$$

$$w_{rb}(i+1) = w_{rb}(i) + \varrho_{rb}(i) * e_{rb}(i) \quad (6.13)$$

$$w_{rc}(i+1) = w_{rc}(i) + \varrho_{rc}(i) * e_{rc}(i)$$

The average of fundamental active and reactive weight components can be computed as given in equation (6.14):

$$w_{ta} = \frac{(w_{aa}+w_{ab}+w_{ac})}{3} \quad (6.14)$$

$$w_{tr} = \frac{(w_{ra}+w_{rb}+w_{rc})}{3} \quad (6.15)$$

***Reference grid current generation with respect to active power components***

The in-phase unit template ($U_{aa,}\ U_{ab,}\ U_{ac}$) can be calculated as given in equation (6.16):

$$\mathrm{U}_{aa} = \frac{V_a}{V_t}\ , \mathrm{U}_b = \frac{V_b}{V_t}, \mathrm{U}_c = \frac{V_c}{V_t} \quad (6.16)$$

The sensed dc-link ($V_{dc}^*$) and reference dc link voltage ( $V_{dc}$) voltages are compared in order to generate error and given to proportional integral (PI) controller. The output is dc loss weight ($w_{dc}$) which is given by equation (6.17) :

$$w_{dc}(i+1) = w_{dc}(i) + K_{pd}\{v_{de}(i+1) - v_{de}(i)\} + K_{id}v_{de}(i+1) \quad (6.17)$$

where $K_{pd}, K_{id}$ are proportional and integral gain of DC bus PI. $v_{de}(i+1)$ is generated error of the reference and sensed dc bus voltage at (i+1)$^{th}$ time.

The total active weight ($w_{taw}$) of the reference current is given by equation (6.18):

$$w_{taw} = w_{ta} + w_{dc} \quad (6.18)$$

The active in-phase reference current components can be evaluated as shown in equation (6.19):

$$i_{aa}^* = w_{taw}\mathrm{U}_{aa},\ i_{ab}^* = w_{taw}\mathrm{U}_{ab},\ i_{ac}^* = w_{taw}\mathrm{U}_{ac} \quad (6.19)$$

***Generation of reference grid current with respect to reactive power components***

The reactive unit templates ($U_{\mathrm{ra,}}\ U_{\mathrm{rb,}}\ U_{\mathrm{rc}}$) components can be obtained as shown in equation (6.20):

$$U_{ra} = -\frac{U_{aa}}{\sqrt{3}} + \frac{U_{ac}}{\sqrt{3}}\ , U_{rb} = \frac{\sqrt{3}\,U_{aa}}{2} + \frac{(U_{ab}-U_{ac})}{2\sqrt{3}}, U_{rc} = -\frac{\sqrt{3}\,U_{aa}}{2} + \frac{(U_{ab}-U_{ac})}{2\sqrt{3}} \quad (6.20)$$

The sensed average magnitude of supply voltage is compared with set reference magnitude and the generated error is given to the PI controller. The output of the controller is ac loss weight ($w_{ac}$) and is given as shown in equation (6.21):

$$w_{ac}(i+1) = w_{ac}(i) + K_{pa}\{v_{te}(i+1) - v_{te}(i)\} + K_{ia}v_{te}(i+1) \quad (6.21)$$

where $K_{pa}, K_{ia}$ are proportional and integral gain of ac voltage controller. $v_{te}(i+1)$ is the error of the sensed and reference ac bus voltage at (i+1)$^{th}$ time.

The total reactive weight, $w_{trw}$, of the reference current is given by equation (6.22):

$$w_{trw} = w_r - w_{tr} \tag{6.22}$$

The reactive reference current components can be evaluated as given by equation (6.23):

$$i_{ra}^* = w_{trw}\mathrm{U}_{ra},\ i_{rb}^* = w_{trw}\mathrm{U}_{rb},\ i_{rc}^* = w_{trw}\mathrm{U}_{rc} \tag{6.23}$$

***Generation of gating signal for three-phase Voltage source inverter***

The summation of reference active and reactive$(i_{aa}^*, i_{ab}^*, i_{ac}^*)$, $(i_{ra}^*, i_{rb}^*, i_{rc}^*)$ respectively are used to generate reference grid current $(i_{ga}^*, i_{gb}^*, i_{gc}^*)$ which is given by equation (6.24):

$$i_{ga}^* = i_{aa}^* + i_{ra}^*, i_{gb}^* = i_{ab}^* + i_{rb}^*, I_{gc}^* = i_{ac}^* + i_{rc}^* \tag{6.24}$$

The sensed grid current is compared with reference grid current. Hysteresis current control scheme is used for the generation of gating signal for six switches of voltage source inverter.

### 6.3.4. Proposed Smooth LMS based Adaptive Control Algorithm

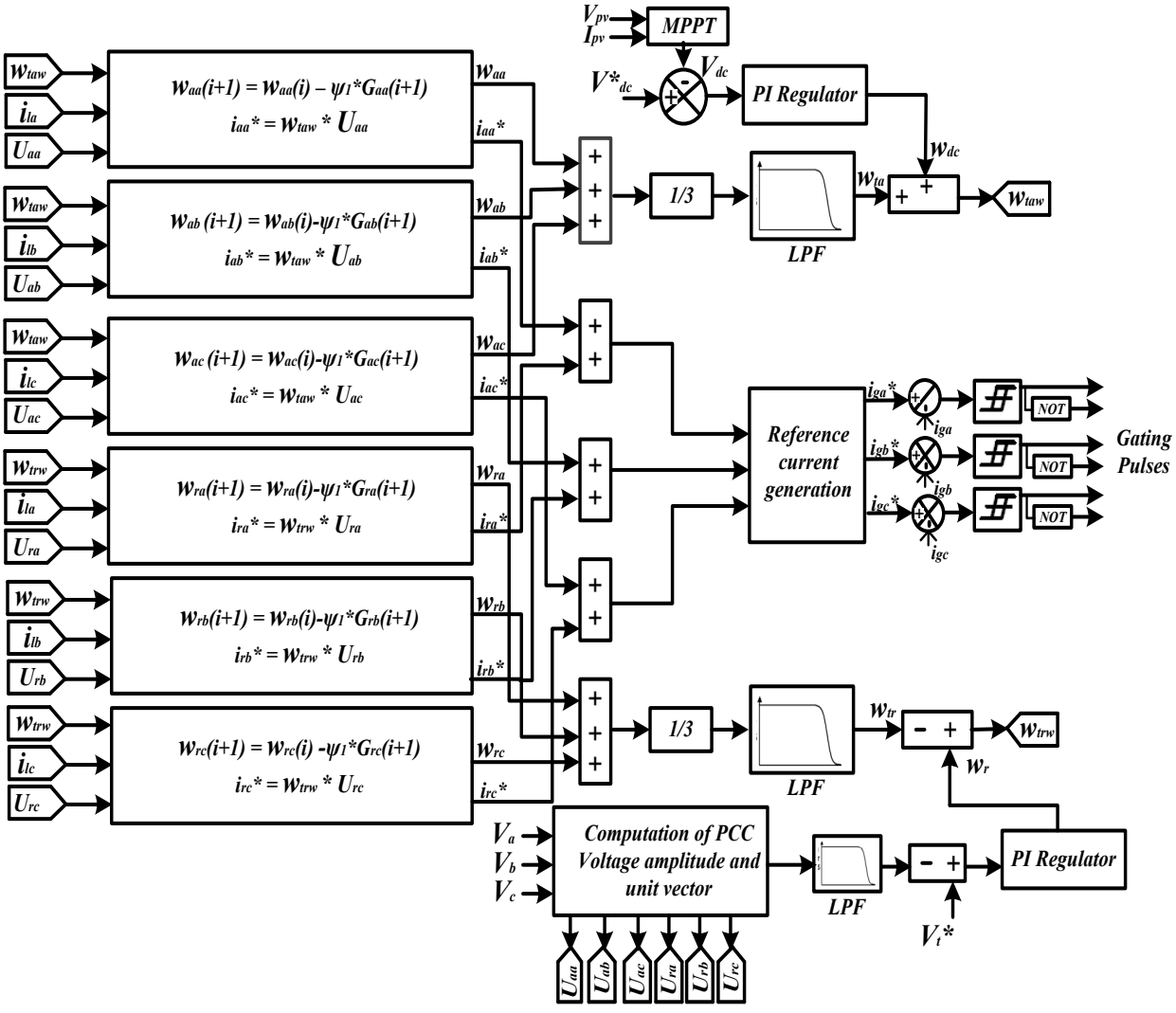


**Fig. 6.5. Block Diagram of Smooth LMS Control Algorithm**

The basic schematic diagram of the proposed Smooth LMS control algorithm is shown on figure 6.5. The basic LMS algorithm has been widely implemented due to its simplicity but its performance is often unsatisfactory due to slower convergence speed. So, smooth LMS has been attempted to preserve its simplicity and to enhance its performance by adding a smoothing gradient.

***Weight extraction by Smooth LMS***

The Smooth LMS [170] weight extraction equation is given by equations (6.25) to (6.27):

$$w(i+1) = w(i) - \psi_1 G(i+1) \tag{6.25}$$

where $G(i+1) = (1-\psi_2)G(i) - \psi_2 e(i)x(i)$ (6.26)

$$e(i) = d(i) - x^T(i)\, w(i) \tag{6.27}$$

where $\psi_1$ and $\psi_2$ are decaying sequence, *e(i)* is estimated error signal, $x^T(i)$ is input vector and $w(i)$ weight value, $G(i)$ is smoothing gradient.

The active weights $w_{aa}, w_{ab}, w_{ac}$ at (i+1) instant for phase '*a'*, '*b'* and '*c'* respectively can be computed as given by equation (6.28):

$$\begin{aligned} w_{aa}(i+1) &= w_{aa}(i) - \psi_1 G_{aa}(i+1) \\ w_{ab}(i+1) &= w_{ab}(i) - \psi_1 G_{ab}(i+1) \\ w_{ac}(i+1) &= w_{ac}(i) - \psi_1 G_{ac}(i+1) \end{aligned} \tag{6.28}$$

Similarly, the reactive weights $w_{ra}, w_{rb}, w_{rc}$ for phase '*a'*, '*b'* and '*c'* respectively can be computed as given by equation (6.29):

$$\begin{aligned} w_{ra}(i+1) &= w_{ra}(i) - \psi_1 G_{ra}(i+1) \\ w_{rb}(i+1) &= w_{rb}(i) - \psi_1 G_{rb}(i+1) \\ w_{rc}(i+1) &= w_{rc}(i) - \psi_1 G_{rc}(i+1) \end{aligned} \tag{6.29}$$

The average of fundamental active and reactive weight components can be computed as given by equation (6.30) and (6.31):

$$w_{ta} = \frac{(w_{aa}+w_{ab}+w_{ac})}{3} \tag{6.30}$$

$$w_{tr} = \frac{(w_{ra}+w_{rb}+w_{rc})}{3} \tag{6.31}$$

Using hysteresis current control scheme, the gating signal for six switches of voltage source inverter are generated as already explained in previous section.

### 6.3.5. Proposed Improved Zero Attracting LMS (IZALMS) based Adaptive Control Algorithm

Block Diagram of proposed improved zero attracting control algorithm is shown in figure 6.6. The basic LMS and $L_1$ –norm regularization is collectively used to generate zero attractor in

iteration to remove harmonic content of load current [173]. Also, the step size varies in accordance with the change in environment as well as load conditions.

***Weight extraction by IZALMS algorithm***

The zero attracting LMS weight extraction calculation at *'i+1'* instant is given by equation (6.32):

$$w(i+1) = w(i) + \varrho_v\, e(i)x(i) - Qsgn\big(w(i)\big) \tag{6.32}$$

where $sgn\big(w(i)\big)$ is component wise sign function given by equation (6.33):

$$sgn\big(w(i)\big) = \begin{cases} \frac{w(i)}{|w(i)|}, & if\ w(i) \neq 0 \\ 0, & if\ w(i) \neq 0 \end{cases} \tag{6.33}$$

and $\varrho_v$ is variable-step size [174] and is given by equation (6.34):

$$\varrho_v = \delta\, \varrho(i) + (1-\delta)e(i) \tag{6.34}$$

where, $e(i) = d(i) - x^T(i)\, w(i)$ (6.35)

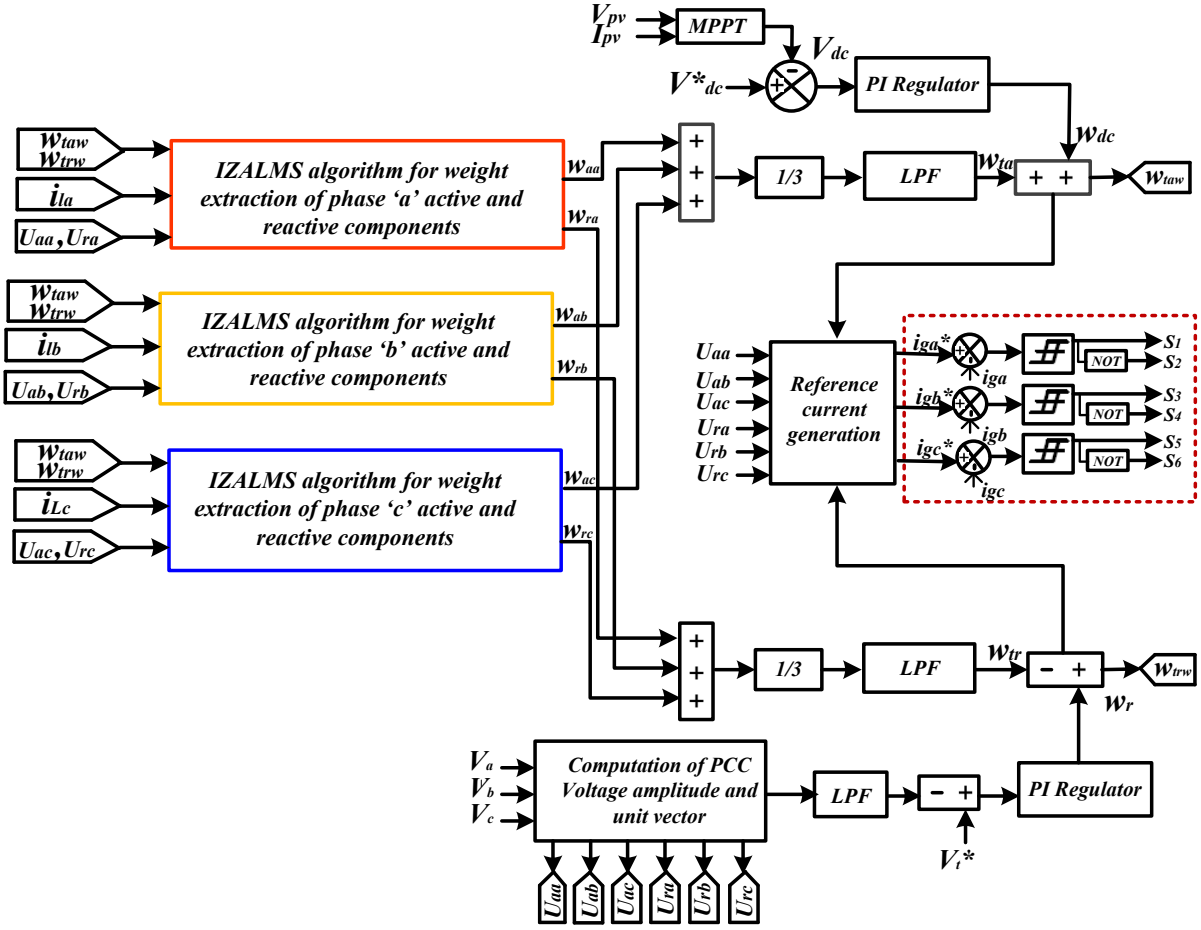


**Fig. 6.6. Block Diagram of improved zero attracting control algorithm**

where Q is the zero-attractor controller which decide the strength of attraction, δ values lies between (0,1), *e(i)* is estimated error signal, $x^T(i)$ is input vector and $w(i)$ is the weight value.

The active weights $w_{aa}, w_{ab}, w_{ac}$ at (i+1) instant for phase '*a*', '*b*' and '*c*' respectively can be computed as given by equation (6.36):

$$\begin{aligned} w_{aa}(i+1) &= w_{aa}(i) + \varrho_v\, e(i)x(i) - Qsgn\big(w(i)\big) \\ w_{ab}(i+1) &= w_{ab}(i) + \varrho_v\, e(i)x(i) - Qsgn\big(w(i)\big) \\ w_{ac}(i+1) &= w_{ac}(i) + \varrho_v\, e(i)x(i) - Qsgn\big(w(i)\big) \end{aligned} \tag{6.36}$$

Similarly, the reactive weights $w_{ra}, w_{rb}, w_{rc}$ for phase '*a*', '*b*' and '*c*' respectively can be computed as given by equation (6.29):

$$\begin{aligned} w_{ra}(i+1) &= w_{ra}(i) + \varrho_v\, e(i)x(i) - Qsgn\big(w(i)\big) \\ w_{rb}(i+1) &= w_{rb}(i) + \varrho_v\, e(i)x(i) - Qsgn\big(w(i)\big) \\ w_{rc}(i+1) &= w_{rc}(i) + \varrho_v\, e(i)x(i) - Qsgn\big(w(i)\big) \end{aligned} \tag{6.37}$$

The average of fundamental active and reactive weight components can be computed as given by equation (6.38) and (6.39):

$$w_{ta} = \frac{(w_{aa}+w_{ab}+w_{ac})}{3} \tag{6.38}$$

$$w_{tr} = \frac{(w_{ra}+w_{rb}+w_{rc})}{3} \tag{6.39}$$

The gating signal for six switches of voltage source inverter are generated using hysteresis current control scheme.

### 6.3.6. Proposed Reweighted $L_0$ VSS-CMPN control algorithm

Block diagram of proposed reweighted $L_0$ VSS-CMPN control algorithm is shown in figure 6.7. Fixed step size in continuous mixed p-norm (CMPN) is made variable which changes in accordance to change in input/output parameters. In the present work, optimal novel reweighted $L_0$ norm is combined with CMPN ($RL_0$-VSSCMPN). Here, reweighting component is added which gives fast convergence speed and makes system adaptable to complicated circuits.

#### *Weight extraction by $RL_0$-VSSCMPN algorithm*

The equations given below are involved in $RL_0$-VSSCMPN control algorithm [172].

The cost function $C_{RL0}(i)$ with reweighted $L_0$ norm function of the algorithm is given as shown in equation (6.40) [29]:

$$C_{RL_0}(i) = \int_1^2 \lambda_i(p)\, E\{|e(i)|\}^p \mathrm{d}p + \gamma \underbrace{\|f(i)\, w(i)\|_0}_{reweighted L_0 norm} \tag{6.40}$$

where, $\lambda_i(p)$ is a probability density-like weighting function with constraint the $\int_1^2 \lambda_i(p)\mathrm{d}p =$

1, $\|.\|_0$ is $L_0$ norm, γ is regularization parameter which makes convergence faster and smoothens transitions.

The error function of phase 'a' load is given by equation (6.41):

$$e(i) = i_{la}(i) - w_{aa}(i)U_{aa}(i) \tag{6.41}$$

$$f(i) = \frac{1}{\epsilon + |w_{aa}(i)|}$$

where $U_{aa}$ is unit template, $\epsilon > 0$ and $w_{aa}(i)$ weight value.

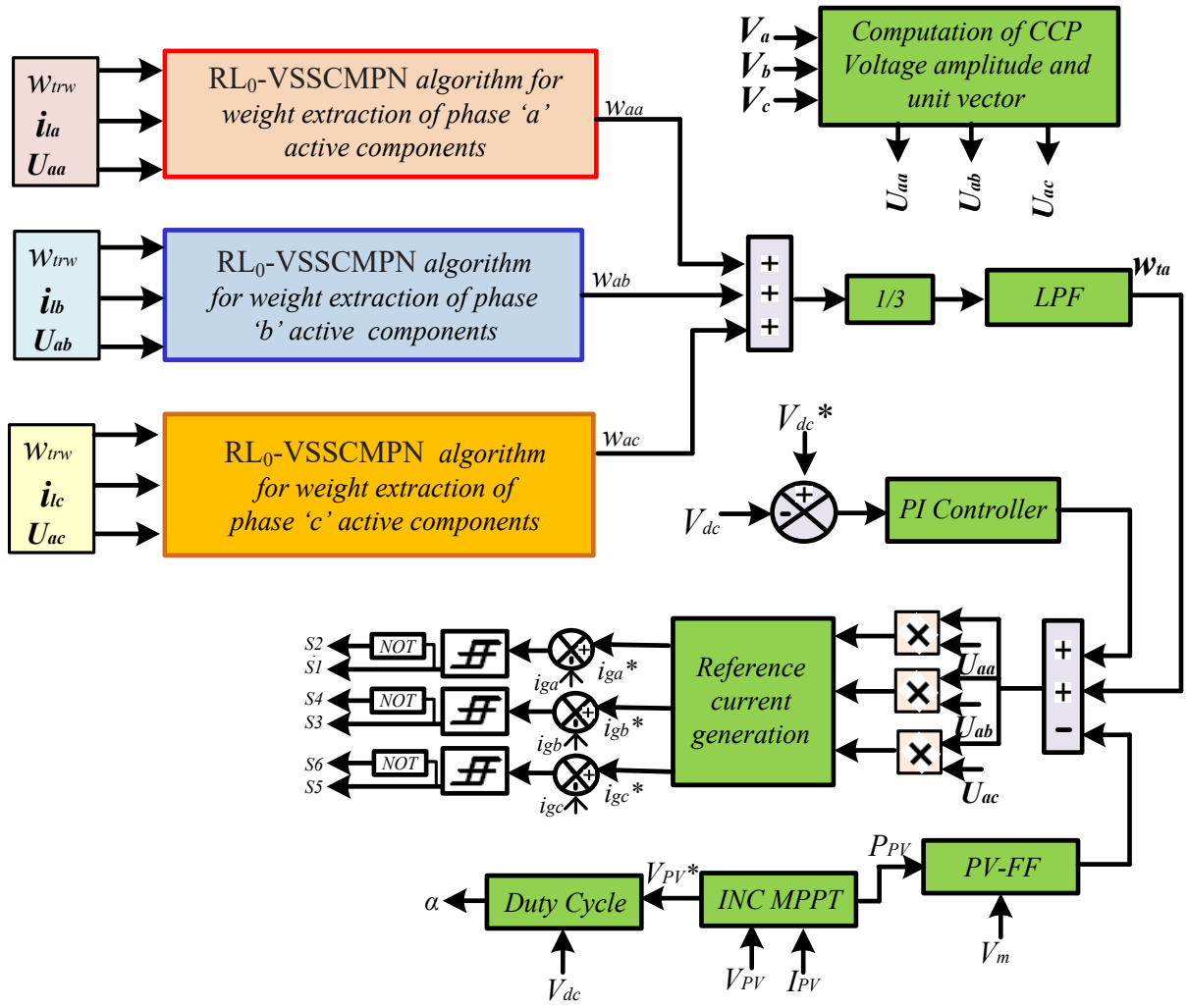


**Fig. 6.7. Block Diagram of Reweighted $L_0$ VSS-CMPN control algorithm**

The weight ($w_{aa}$) of fundamental load current component is given by equations [173] (6.42) to (6.44):

$$w_{aa}(i+1) = w_{aa}(i) + \varrho \frac{\partial C_{RL_0}(i)}{\partial w_{aa}(i)} \tag{6.42}$$

$$w_{aa}(i+1) = w_{aa}(i) + \varrho \int_1^2 \lambda_i(p) \frac{\partial E\{|e(i)|\}^p}{w_{aa}(i)} dp - \varrho\, \gamma\, f_\beta\{f(i)\, w(i)\} \tag{6.43}$$

$$w_{aa}(i+1) = w_{aa}(i) + \varrho\, \lambda_i sgn\big(e(i)\big)x(i) - \varrho\, \gamma\, f_\beta\{f(i)\, w(i)\} \tag{6.44}$$

where $\varrho$ is the step size, sgn is signum function, $f_\beta$ is threshold parameter, $\lambda_i$ is variable step size that depends on e(i).

$$\lambda_i = \frac{(2|e(i)|-1)ln(|e(i)|)-|e(i)|+1}{ln^2(|e(i)|)} \quad (6.45)$$

Similarly, the fundamental component of weight for other two phases are given by equations (6.46) to (6.47) [174}:

$$w_{ab}(i+1) = w_{ab}(i) + \varrho\, \lambda_i sgn\big(e(i)\big)x(i) - \varrho\, \gamma\, f_\beta\{f(i)\, w(i)\} \quad (6.46)$$

$$w_{ac}(i+1) = w_{ac}(i) + \varrho\, \lambda_i sgn\big(e(i)\big)x(i) - \varrho\, \gamma\, f_\beta\{f(i)\, w(i)\} \quad (6.47)$$

The average of fundamental active weight components can be computed as given by equation (6.48):

$$w_{ta} = \frac{(w_{aa}+w_{ab}+w_{ac})}{3} \quad (6.48)$$

Hysteresis current control scheme has been used for generating the gating signal for six switches of voltage source inverter.

## 6.4. RESULTS AND DISCUSSIONS (MATLAB/Simulink)

In this section, simulation results of the proposed smooth LMS, IZALMS and $RL_0$-VSSCMPN based adaptive control algorithms for two-stage three-phase grid interfaced SPV system of 11.78 kW (Appendix B (b)) are shown.

### 6.4.1. Smooth LMS Control Algorithm

#### 6.4.1.1. System performance with linear load under load variation and irradiation variation

Figure 6.8 shows the simulation results of the system for load variation and irradiation variation. A linear load of 14.14 kVA, 0.71 lagging p.f. is connected at the PCC. In figure 6.8 (a), waveforms of solar irradiation ($I_{rr}$), output power of SPV system ($P_{PV}$), three phase waveforms of grid voltage ($V_g$), load current ($I_L$), source i.e., inverter current ($I_s$), grid current ($I_g$) and dc-link voltage ($V_{dc}$) are shown.

Figure 6.8 (b) depicts active, reactive power of load, source and grid in power factor correction mode. The SPV system generates 11.78 kW power and active power demand of the load is 10 kW. The surplus power (1.78 kW) is given to grid. The system works in UPF mode. The reactive power requirement of the load (10 kVAR) is fulfilled by inverter alone. At t=0.3sec, an extra load of 10 kW UPF is added to the existing load. The new active power demand of

the load (20 kW) is fulfilled by both inverter (11.78 kW) and grid (8.22 kW) as shown in figure 6.8 (a). At t = 0.5 sec, the irradiation is changed from 1000 W/m$^2$ to 500 W/m$^2$. With the decrease in the irradiation level, the active power generated from the PV decreases from 11.78 kW to 5.2 kW. The deficit power (14.2 kW) is taken from the grid. Even, with change in irradiation reactive power generated by the PV inverter remains the same. The grid currents remain balanced and sinusoidal irrespective of change in load and irradiation. The $V_{dc}$ is maintained at 800V.

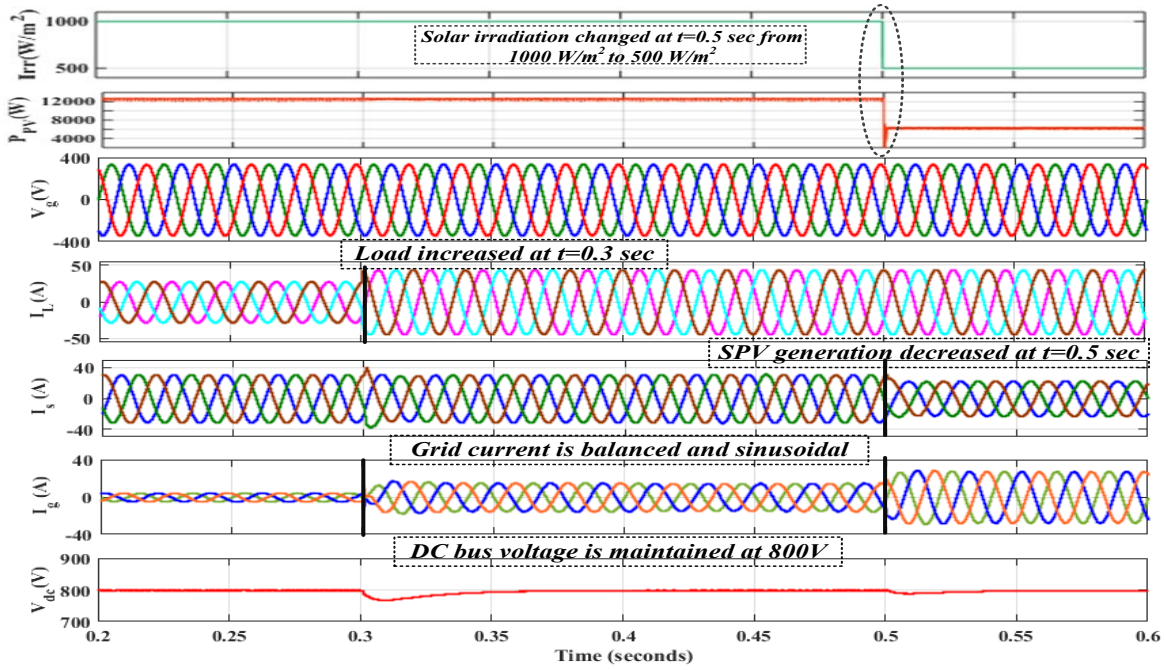


**(a)**

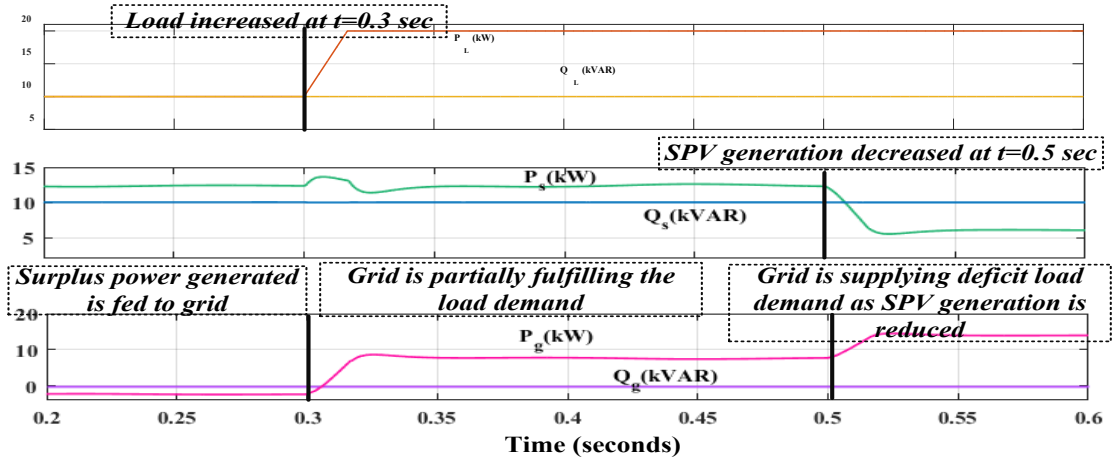


**(b)**

**Fig. 6.8. System performance with linear load under load variation and irradiation variation (a) waveform of solar irradiation ($I_{rr}$), output power of SPV system ($P_{PV}$), Three phase waveform of grid voltage ($V_g$), load current ($I_L$), source current ($I_s$) and grid current ($I_g$), and voltage at DC bus ($V_{dc}$) (b) Active and reactive power of load, source and grid.**

### 6.4.1.2. System performance with non-linear load

In this section, the performance of Smooth LMS control algorithm with non-linear load (Three-phase bridge rectifier with RL load, R=20ohm, L=10mH) is shown.

**(a) Load variation and irradiation variation**

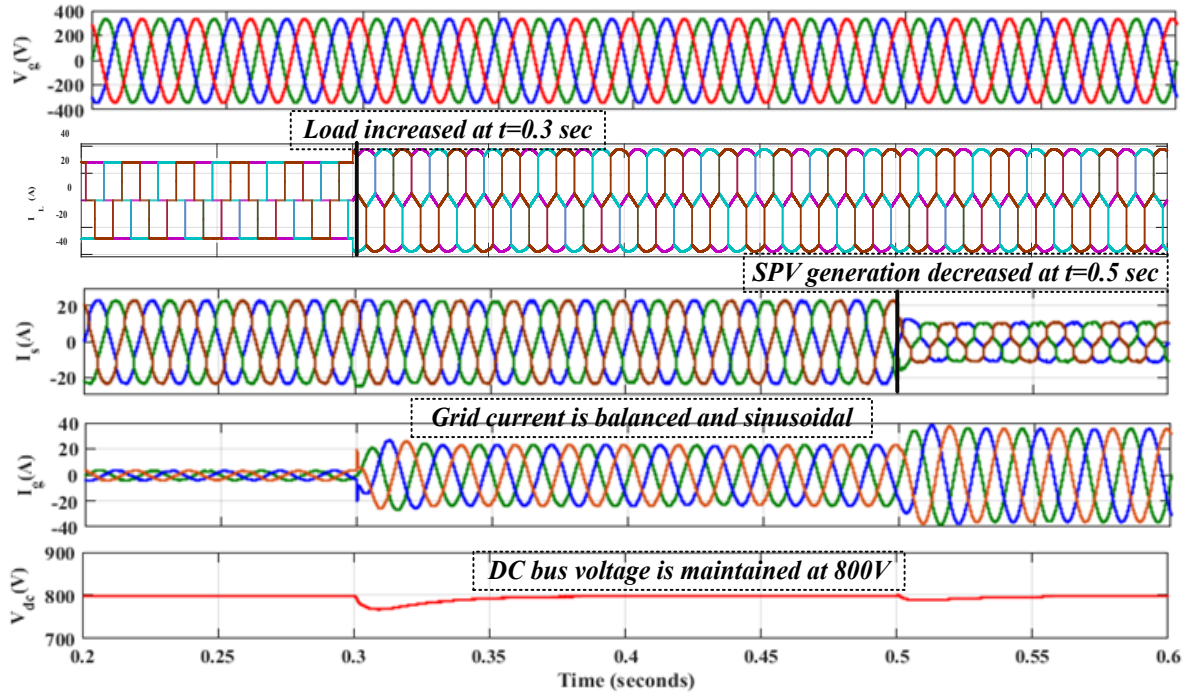


**(a)**

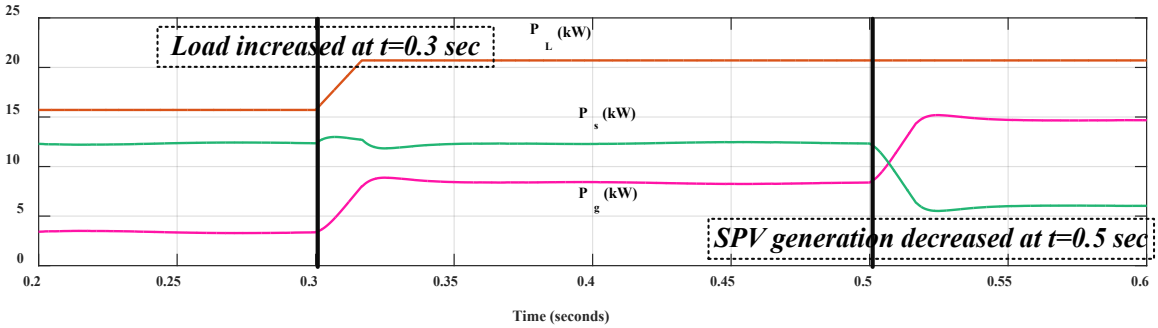


**(b)**

**Fig.6.9. System performance with non-linear load under load/irradiation variation) (a) Three phase waveform of grid voltage ($V_g$), load current ($I_L$), source current ($I_s$) and grid current ($I_g$) and voltage at DC bus ($V_{dc}$) (b) Active power of load, source and grid**

Figure 6.9 shows the simulation results of the given system for load variation and irradiation variation. A three-phase diode bridge rectifier with RL load (20Ω, 100mH) is connected at the PCC. The SPV system generates 11.78 kW power and active power demand of the load is 15.7 kW. In order to meet the load demand, deficit power i.e., 3.92 kW is taken from grid.

At t=0.3sec, an extra load of 5 kW UPF is added to the existing load. The load demand (20.5 kW) is fulfilled by both inverter (11.78 kW) and grid (8.72 kW) as shown in figure 6.9. At t = 0.5 sec, the irradiation is changed from 1000W/m$^2$ to 500W/m$^2$. With the decrease in the irradiation level, the active power generated from the PV decreases from 11.78kW to 5.2 kW. Hence, deficit power (15.3 kW) is demanded from the grid. The grid currents remain balanced and sinusoidal irrespective of change in load and irradiation. The system works in unity power factor mode. The $V_{dc}$ is maintained at 800V. Figure 6.9 (b) depicts active power of load, source and grid.

### (b) Unbalanced non-linear load condition

Figure 6.10 shows the simulation results of the system for unbalanced non-linear load. Phase 'b' of non-linear load is removed from time t=0.3 sec to t=0.5 sec and reconnecting it at t=0.5 sec. Even when the load is unbalanced, the grid current was found to be balanced and sinusoidal. The $V_{dc}$ is maintained at 800V.

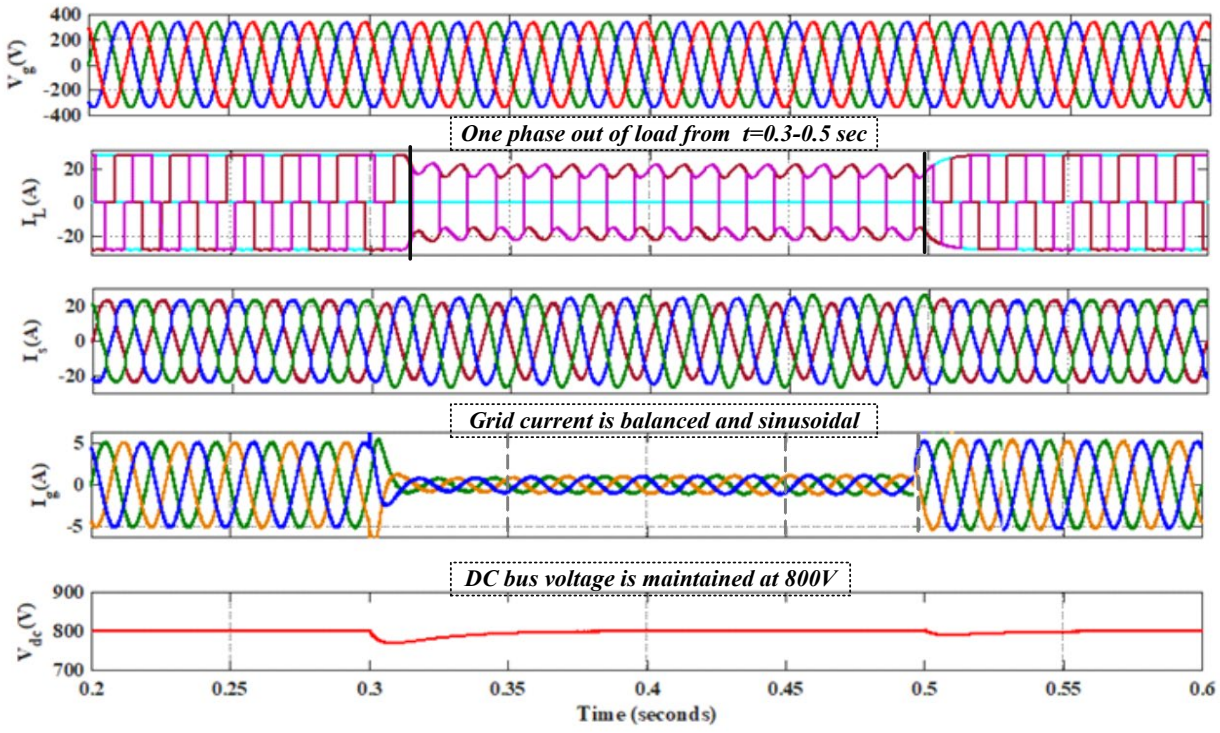


**Fig. 6.10. System performance with unbalanced non-linear load**

### (c) Unbalanced grid condition

Figure 6.11 shows the simulation results of the system for unbalanced grid voltage condition. From t= 0.4 to t= 0.6sec, grid unbalancing is created by increasing the voltage of phase 'b' to

370 V and reducing the voltage of phase ‘c’ to 315 V. The grid current under grid unbalanced condition is found to be balanced and sinusoidal. The $V_{dc}$ is maintained at 800V.

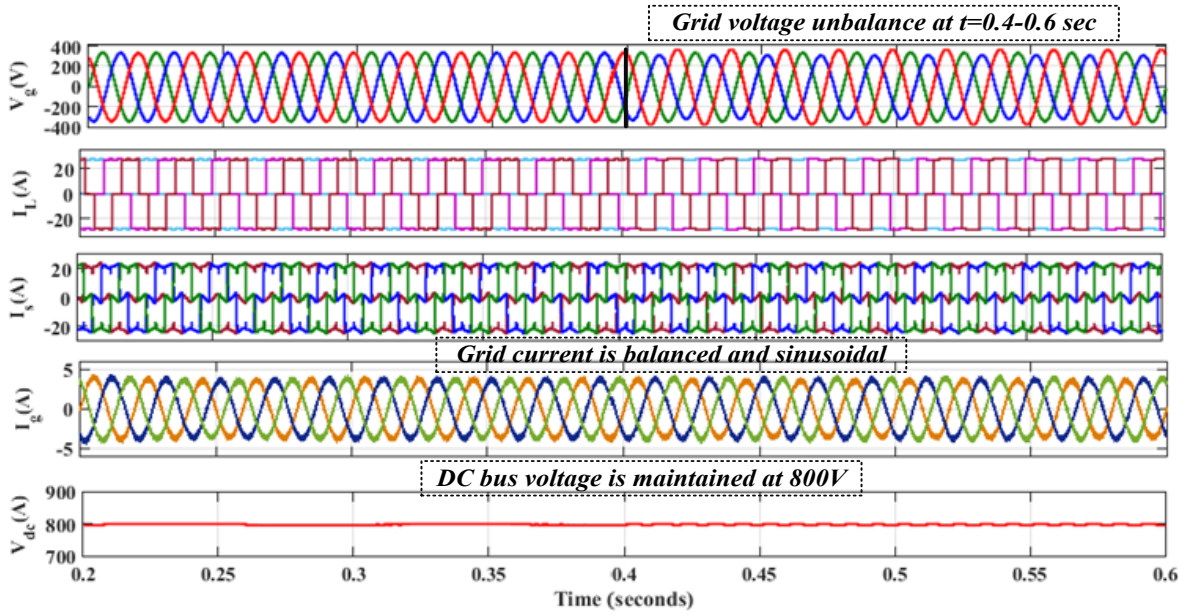


**Fig. 6.11. System performance with non-linear load under unbalanced grid**

### (d) Grid voltage sag and voltage swell condition

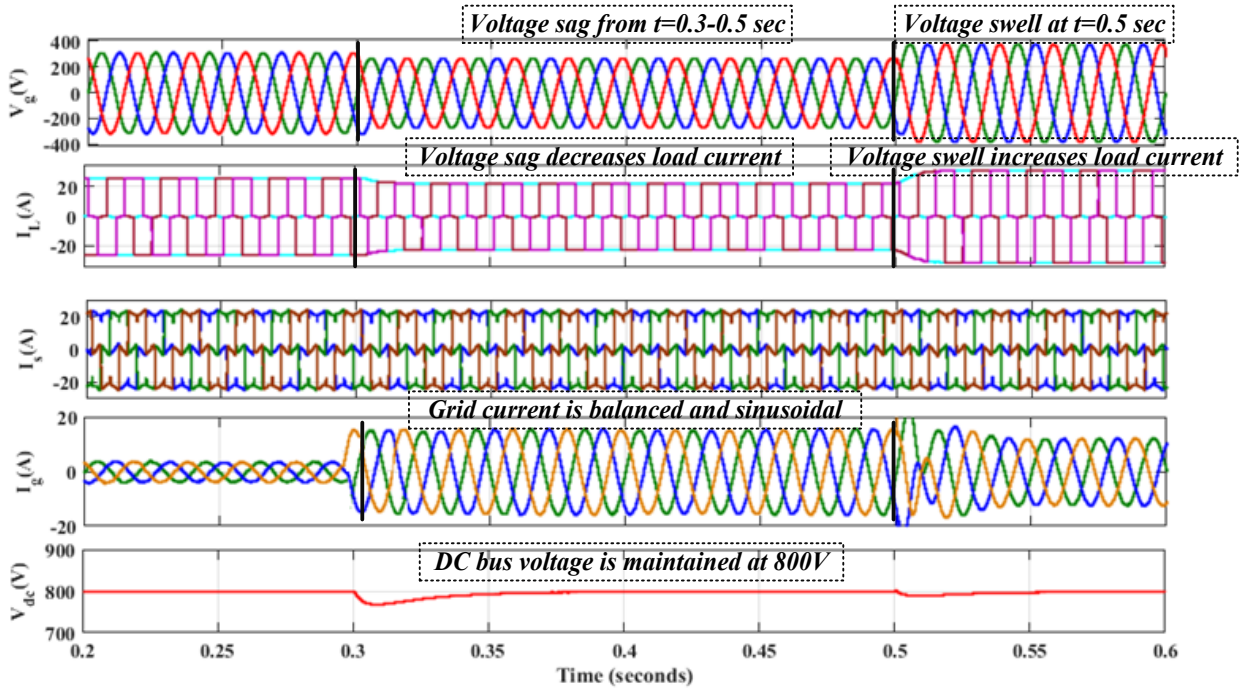


**Fig. 6.12. System performance with non-linear load under grid voltage swell and sag**

Figure 6.12 shows the simulation results of the system under grid voltage sag and swell condition. Voltage sag from t= 0.3 to 0.5sec and voltage swell from t= 0.5 to 0.6 sec is given in grid voltage. Voltage sag of 270 V at t= 0.3 to 0.5sec, decreases the current across the load.

Alike, the voltage swell of 378 V at t= 0.5 sec, increases current across the load. Under this dynamic condition, the grid current was found to be balanced and sinusoidal. The $V_{dc}$ is maintained at 800V.

### 6.4.2. Improved Zero Attracting LMS Control Algorithm

#### 6.4.2.1. System performance with linear load under load variation and irradiation variation

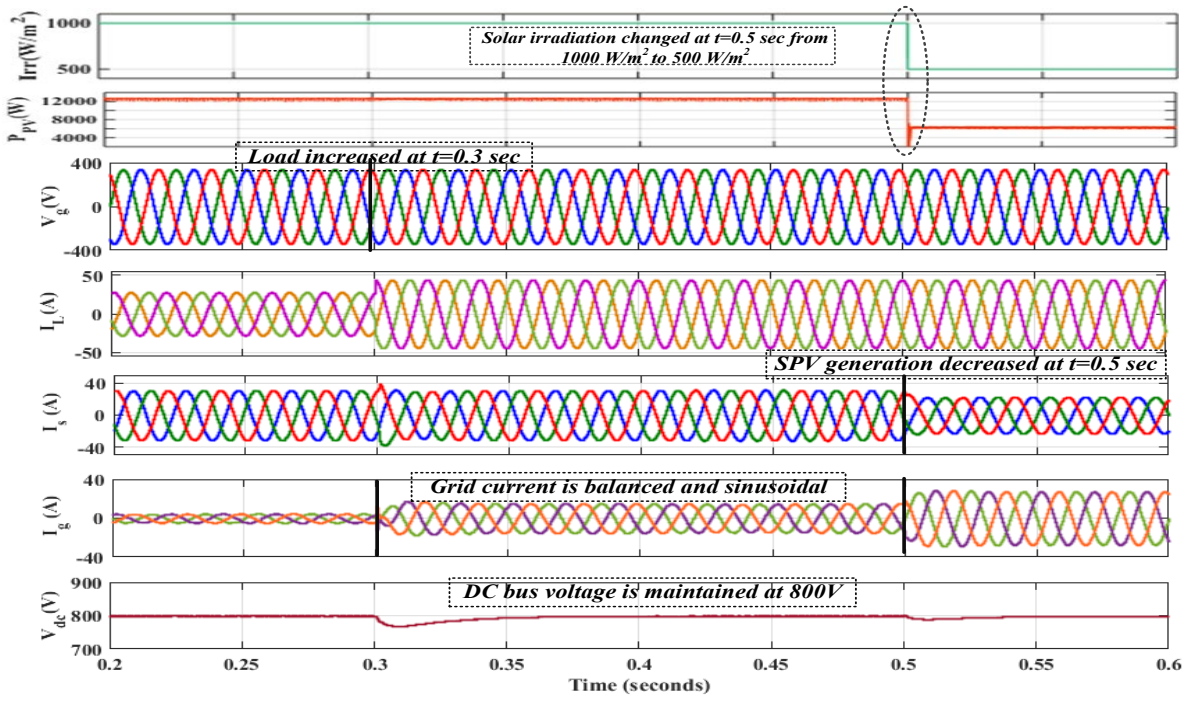


(a)

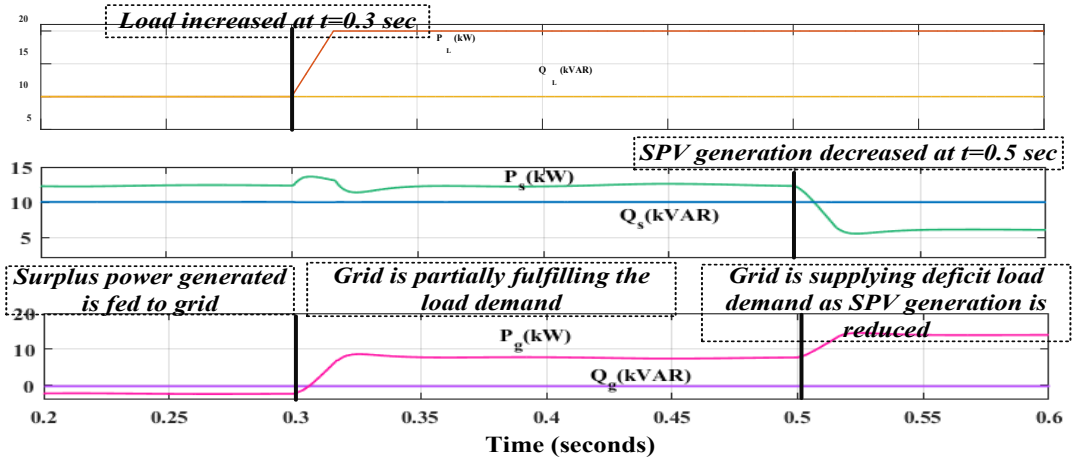


(b)

**Fig. 6.13. System performance with linear load under load variation and irradiation variation (a) waveform of solar irradiation ($I_{rr}$), output power of SPV system ($P_{PV}$), Three phase waveform of grid voltage ($V_g$), load current ($I_L$), source current ($I_s$) and grid current ($I_g$), and voltage at DC bus ($V_{dc}$) (b) Active and reactive power of load, source and grid.**

Figure 6.13 shows the simulation results of the system for load variation and irradiation variation. A linear load of 14.14 kVA, 0.71 lagging p.f. is connected at the PCC. In figure 6.13 (a), waveforms of solar irradiation ($I_{rr}$), output power of SPV system ($P_{PV}$), three phase waveforms of grid voltage ($V_g$), load current ($I_L$), source i.e., inverter current ($I_s$), grid current ($I_g$) and dc-link voltage ($V_{dc}$) are shown. In figure 6.13 (b) depicts active, reactive power of load, source and grid in power factor correction mode. The SPV system generates 11.78 kW power and active power demand of the load is 10 kW. The surplus power (1.78 kW) is given to grid. The system works in UPF mode. The reactive power requirement of the load (10 kVAR) is fulfilled by inverter alone. At t=0.3sec, an extra load of 10 kW UPF is added to the existing load. The new active power demand of the load (20 kW) is fulfilled by both inverter (11.78 kW) and grid (8.22 kW) as shown in figure 6.8 (a). At t = 0.5 sec, the irradiation is changed from 1000 W/m$^2$ to 500 W/m$^2$. With the decrease in the irradiation level, the active power generated from the PV decreases from 11.78 kW to 5.2 kW. Hence, deficit power (14.2 kW) is taken from the grid. Even, with change in irradiation reactive power generated by the PV inverter remains the same. The grid currents remain balanced and sinusoidal irrespective of change in load and irradiation. The $V_{dc}$ is maintained at 800V.

Figure 6.13 (b) depicts active, reactive power of grid, load and source in power factor correction mode.

### 6.4.2.2. System performance with non-linear load

In this section, the performance of proposed IZALMS control algorithm with non-linear load (Three phase bridge rectifier with RL load, R=20ohm, L=10mH) is shown.

**(a) Load variation and irradiation variation**

Figure 6.14 shows the simulation results of the system for load variation and irradiation variation SPV system generates 11.78 kW power and active power demand of the load is 15.7 kW. In order to meet the load demand, deficit power i.e., 3.92 kW is taken from grid. At t=0.3sec, an extra load of 5 kW UPF is added to the existing load. The load demand (20.5 kW) is fulfilled by both inverter (11.78 kW) and grid (8.72 kW) as shown in figure 6.9. At t = 0.5 sec, the irradiation is changed from 1000W/m$^2$ to 500W/m$^2$. With the decrease in the irradiation level, the active power generated from the PV decreases from 11.78kW to 5.2 kW. Hence, deficit power (15.3 kW) is demanded from the grid. The grid currents remain balanced and sinusoidal irrespective of change in load and irradiation. The $V_{dc}$ is maintained at 800V. Figure 6.14 (b) depicts active power of load, source and grid.

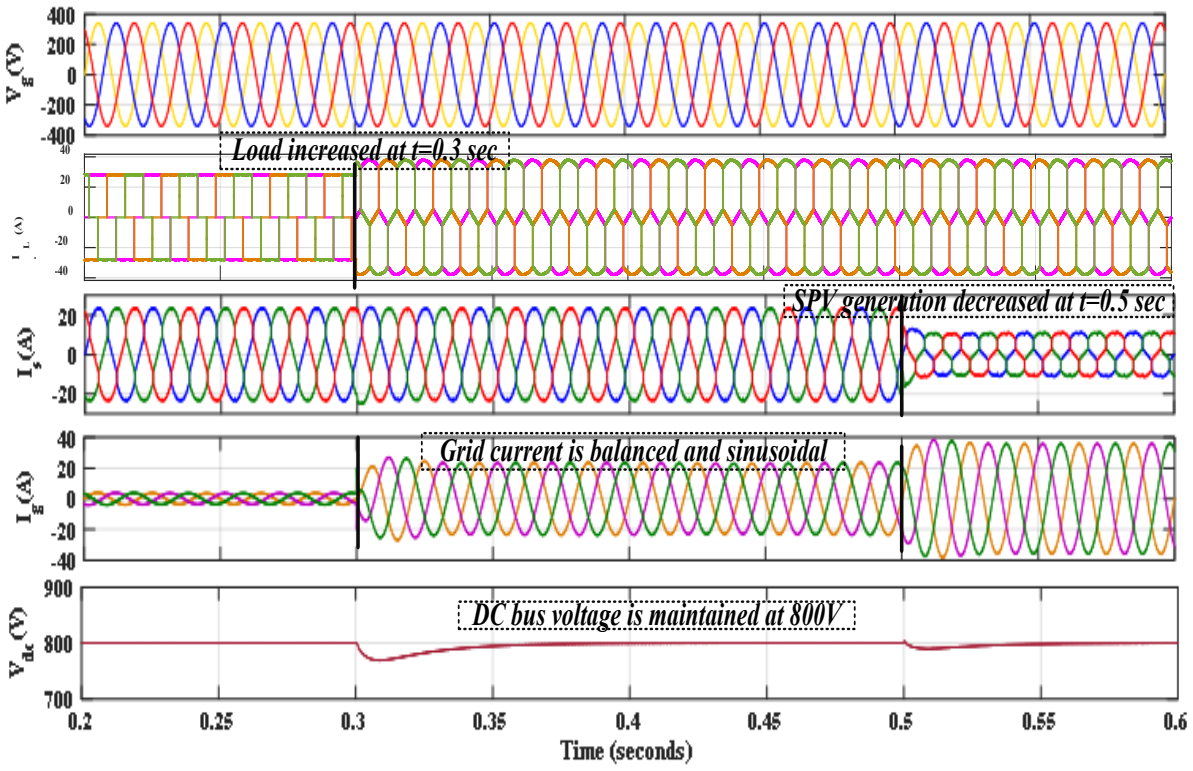


**(a)**

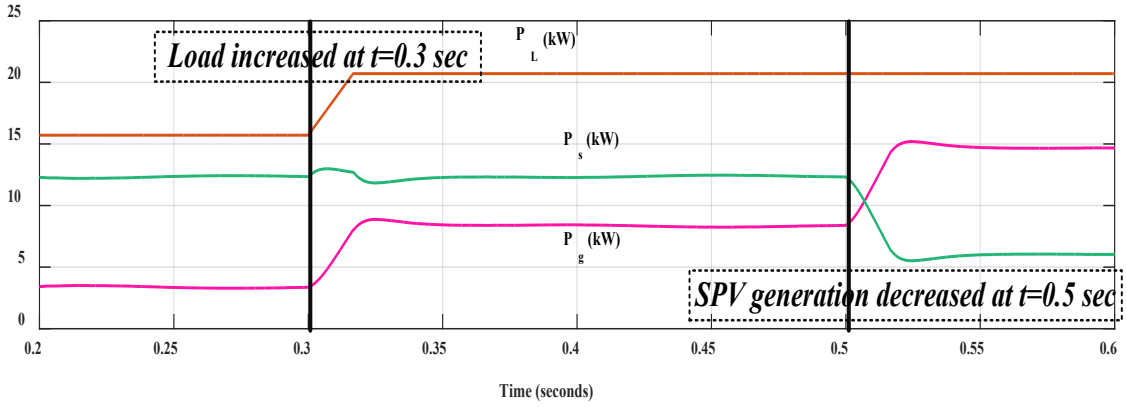


**(b)**

**Fig. 6.14. System performance with non-linear load under load/irradiation variation) (a) Three phase waveform of grid voltage ($V_g$), load current ($I_L$), source current ($I_s$) and grid current ($I_g$), and voltage at DC bus (b) Active power of load, source and grid.**

### (b) Unbalanced non-linear load condition

Figure 6.15 shows the simulation results of the system for unbalanced non-linear load. Phase 'b' of non-linear load is removed from time t=0.3 sec to t=0.5 sec and reconnecting it at t=0.5 sec. Even when the load is unbalanced, the grid current was found to be balanced and sinusoidal. The $V_{dc}$ is maintained at 800V.

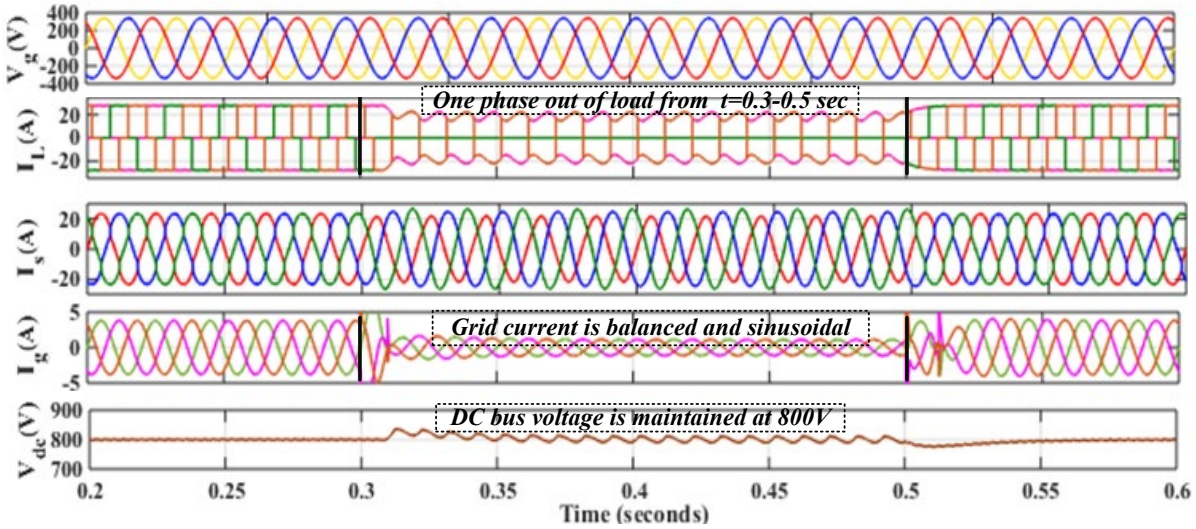


**Fig. 6.15. System performance with unbalanced non-linear load**

### (c) Unbalanced grid condition

Figure 6.16 shows the simulation results of the system for unbalanced grid condition. From t= 0.4 to t= 0.6sec, grid unbalancing is created by increasing the voltage of phase 'b' to 370 V and reducing the voltage of phase 'c' to 315 V. The grid current under grid unbalanced condition is found to be balanced and sinusoidal. The $V_{dc}$ is maintained at 800V.

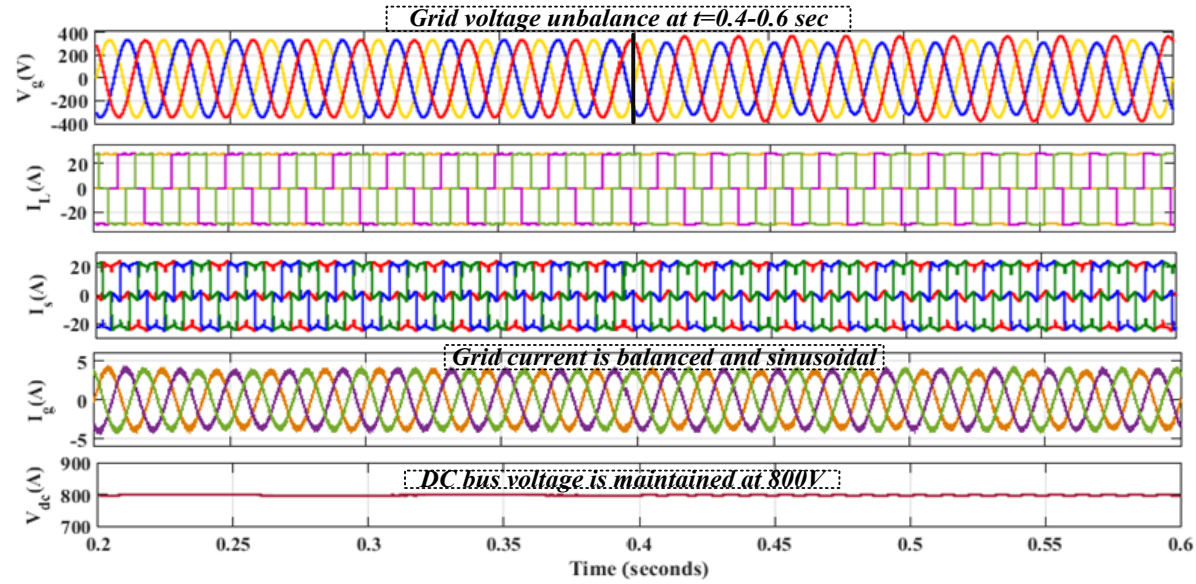


**Fig. 6.16. System performance with non-linear load under unbalanced grid**

### (d) Grid voltage sag and voltage swell condition

Figure 6.17 shows the simulation results of the system for grid voltage sag and swell. Voltage sag from t= 0.3 to 0.5sec and swell from t= 0.5 to 0.6sec is given in grid voltage. Voltage sag of 270 V at t= 0.3 to 0.5sec, decreases the current across the load. Alike, the voltage swell of

378 V at t= 0.5 sec, increases current across the load. Under this dynamic condition, the grid current was found to be balanced and sinusoidal. The $V_{dc}$ is maintained at 800V.

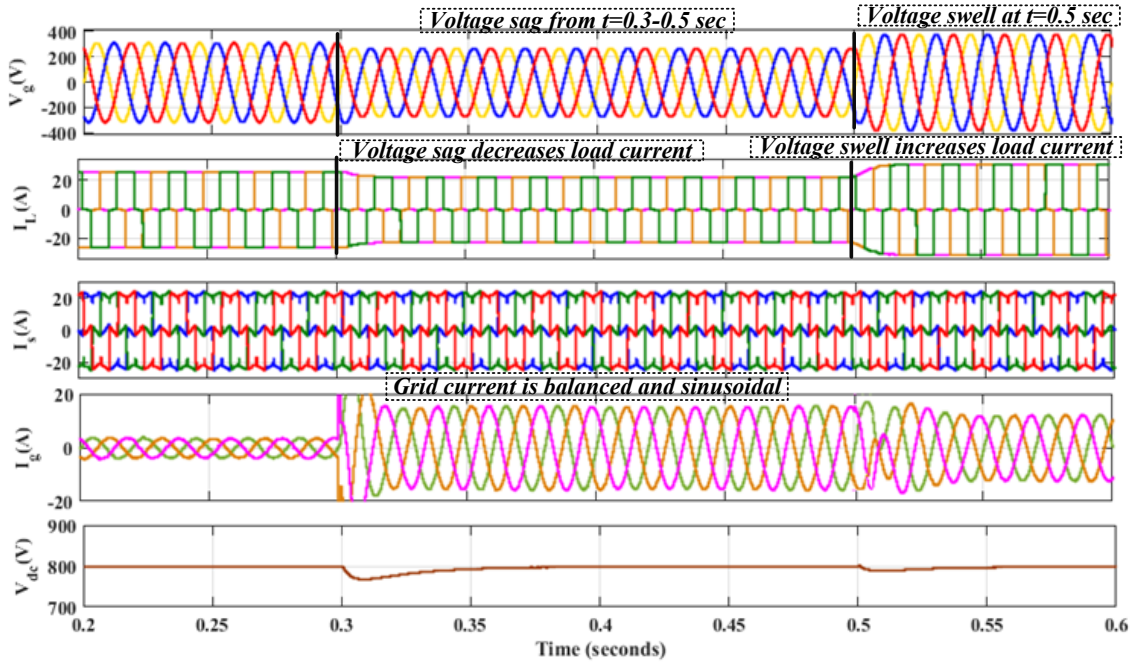


**Fig. 6.17. System performance with non-linear load under grid voltage swell and sag**

### 6.4.3. $RL_0$-VSSCMPN Control Algorithm

#### 6.4.3.1. System performance with linear load under load variation and irradiation variation

Figure 6.18 shows the simulation results of the system for load variation and irradiation variation. A linear load of 14.14 kVA, 0.71 lagging p.f. is connected at the PCC. In figure 6.18 (a), waveforms of solar irradiation ($I_{rr}$), output power of SPV system ($P_{PV}$), three phase waveforms of grid voltage ($V_g$), load current ($I_L$), source i.e., inverter current ($I_s$), grid current ($I_g$) and dc-link voltage ($V_{dc}$) are shown. In figure 6.18 (b) depicts active, reactive power of load, source and grid in power factor correction mode. The SPV system generates 11.78 kW power and active power demand of the load is 10 kW. The surplus power (1.78 kW) is given to grid. The system works in UPF mode. The reactive power requirement of the load (10 kVAR) is fulfilled by inverter alone. At t=0.3sec, an extra load of 10 kW UPF is added to the existing load. The new active power demand of the load (20 kW) is fulfilled by both inverter (11.78 kW) and grid (8.22 kW) as shown in figure 6.8 (a). At t = 0.5 sec, the irradiation is changed from 1000 W/m$^2$ to 500 W/m$^2$. With the decrease in the irradiation level, the active power generated from the PV decreases from 11.78 kW to 5.2 kW. Hence, deficit power

(14.2 kW) is taken from the grid. Even, with change in irradiation reactive power generated by the PV inverter remains the same. The grid currents remain balanced and sinusoidal irrespective of change in load and irradiation. The $V_{dc}$ is maintained at 800V.

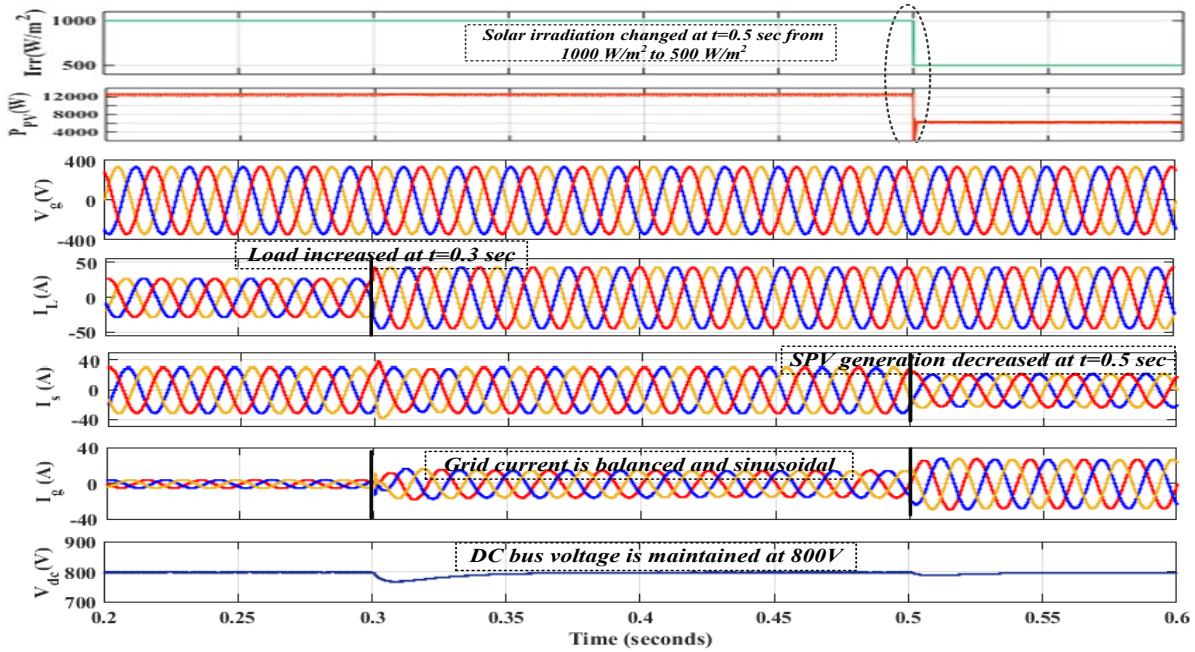


**(a)**

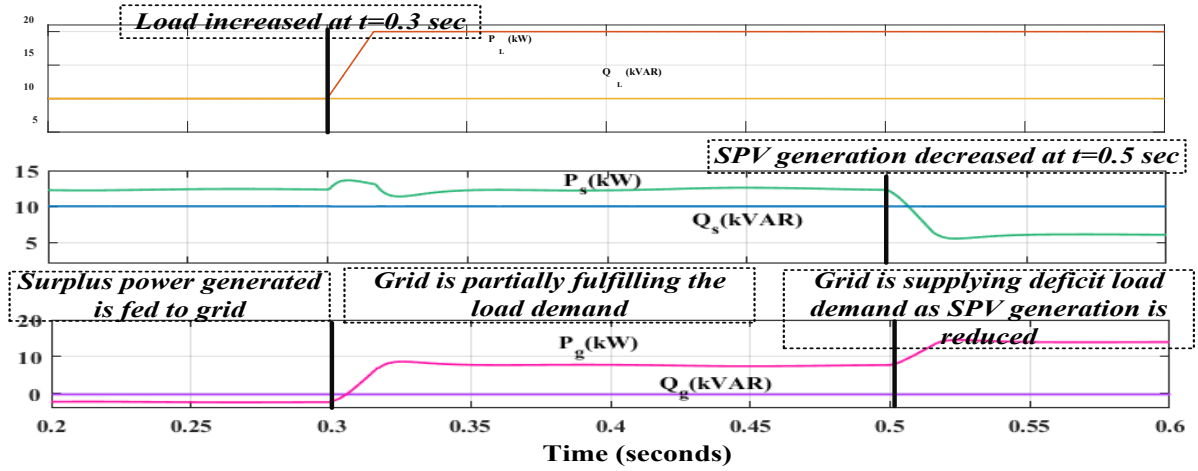


**(b)**

**Fig. 6.18. System performance with linear load under load variation and irradiation variation (a) waveform of solar irradiation ($I_{rr}$), output power of SPV system ($P_{PV}$), Three phase waveform of grid voltage ($V_g$), load ($I_L$), source ($I_s$) and grid current ($I_g$), and voltage at DC bus ($V_{dc}$) (b) Active and reactive power of grid, load and source**

### 6.4.3.2. System performance with non-linear load

In this section, the performance of proposed $RL_0$-VSSCMPN control algorithm with non-linear load (Three phase bridge rectifier with RL load, R=20ohm, L=10mH) is shown.

**(a) Load variation and irradiation variation**

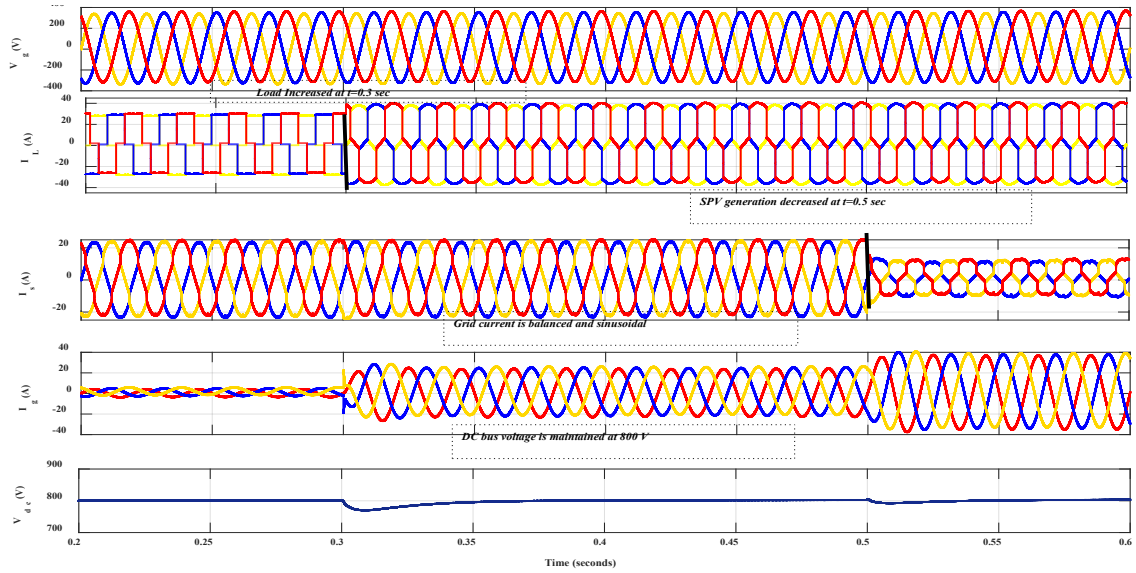


**(a)**

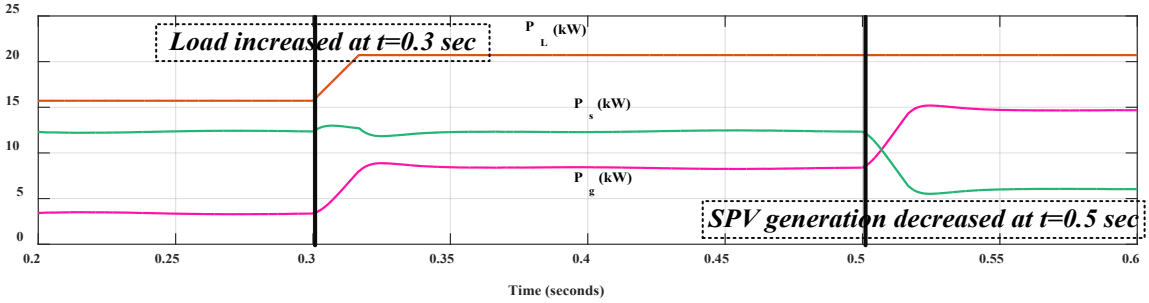


**(b)**

**Fig.6.19. System performance with non-linear load under load/irradiation variation) (a) Three phase waveform of grid voltage ($V_g$), load current ($I_L$), source current ($I_s$) and grid current ($I_g$), and voltage at DC bus (b) Active power of load, source and grid**

Figure 6.19 shows the simulation results of the system for load variation and irradiation variation. SPV system generates 11.78 kW power and active power demand of the load is 15.7 kW. In order to meet the load demand, deficit power i.e., 3.92 kW is taken from grid. At t=0.3sec, an extra load of 5 kW UPF is added to the existing load. The load demand (20.5 kW) is fulfilled by both inverter (11.78 kW) and grid (8.72 kW) as shown in figure 6.9. At t = 0.5 sec, the irradiation is changed from 1000W/m$^2$ to 500W/m$^2$. With the decrease in the irradiation level, the active power generated from the PV decreases from 11.78kW to 5.2 kW. Hence, deficit power (15.3 kW) is demanded from the grid. The grid currents remain balanced and sinusoidal irrespective of change in load and irradiation. The $V_{dc}$ is maintained at 800V. Figure 6.19 (b) depicts active power of load, source and grid.

### (b) Unbalanced non-linear load condition

Figure 6.20 shows the simulation results of the system for unbalanced non-linear load. Phase 'b' of non-linear load is removed from time t=0.3 sec to t=0.5 sec and reconnecting it at t=0.5 sec. Even when the load is unbalanced, the grid current was found to be balanced and sinusoidal. The $V_{dc}$ is maintained at 800V.

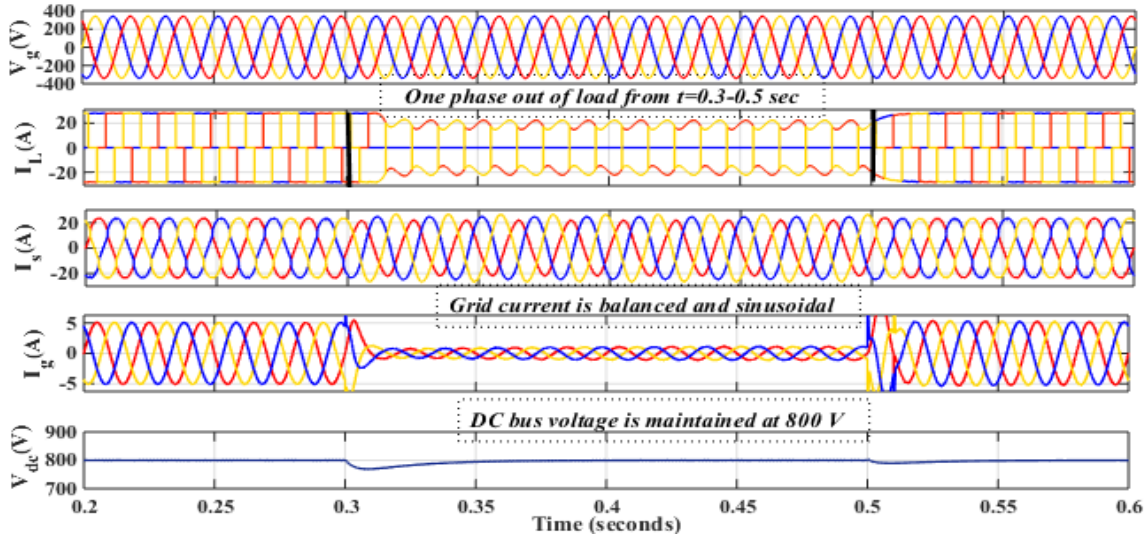


**Fig. 6.20. System performance with unbalanced non-linear load**

### (c) Unbalanced grid condition

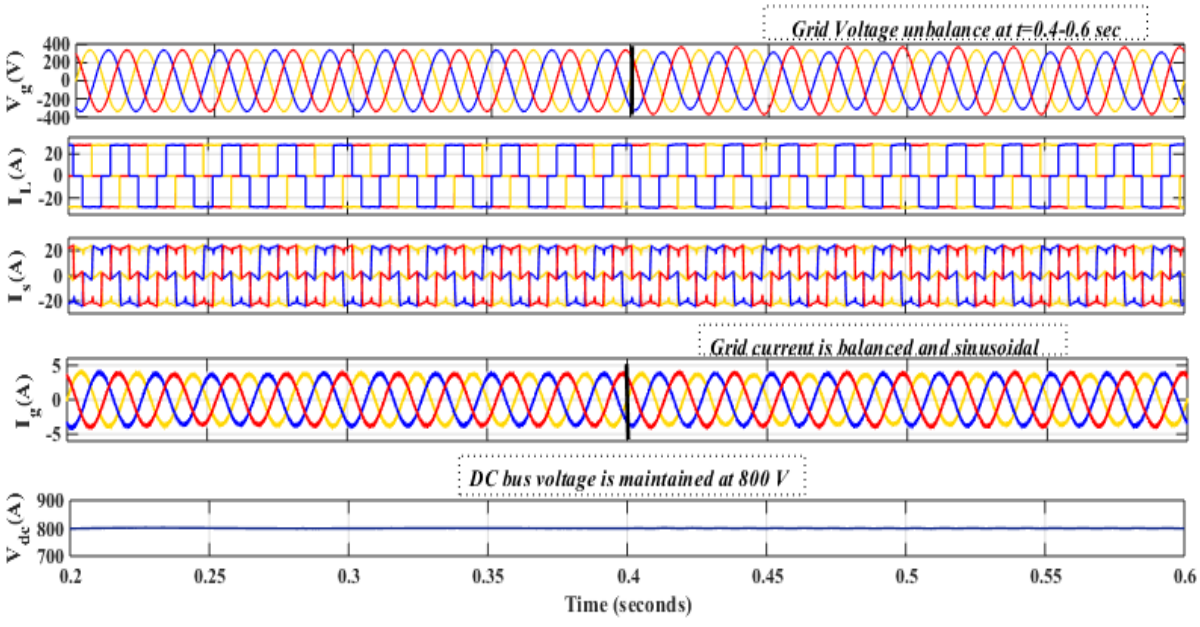


**Fig. 6.21. System performance with non-linear load under unbalanced grid**

Figure 6.21 shows the simulation results of the system for unbalanced grid condition. From t= 0.4 to t= 0.6sec, grid unbalancing is created by increasing the voltage of phase 'b' to 370 V and

reducing the voltage of phase 'c' to 315 V. The grid current under grid unbalanced condition is found to be balanced and sinusoidal. The $V_{dc}$ is maintained at 800V.

### (d) Grid voltage sag and swell voltage condition

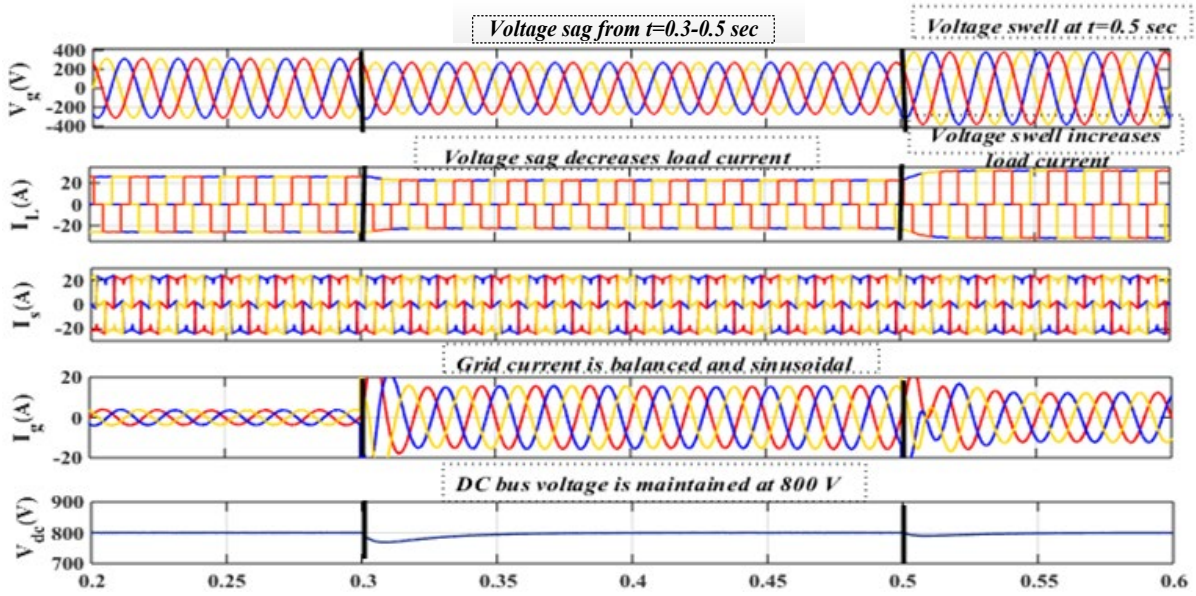


**Fig. 6.22. System performance with non-linear load under grid voltage swell and sag**

Figure 6.22 shows the simulation results of the system for grid voltage sag and swell. Voltage sag from t= 0.3 to 0.5 sec and swell from t= 0.5 to 0.6 sec is given in grid voltage. Voltage sag of 270 V at t= 0.3 to 0.5sec, decreases the current across the load. Alike, the voltage swell of 378 V at t= 0.5 sec, increases current across the load. Under this dynamic condition, the grid current was found to be balanced and sinusoidal. The $V_{dc}$ is maintained at 800V.

## 6.4.4. Comparison of Proposed Control Algorithms with Other Control Algorithms

### 6.4.4.1. Total Harmonics Distortion (THD)

In this section, the proposed control algorithms viz. Smooth LMS, IZALMS and $RL_0$-VSSCMPN have been compared with other control schemes viz. SRFT, unit template and LMS in terms of total harmonic distortion of grid current as shown in figure 6.23 for the non-linear load considered. The obtained THD of proposed control algorithms and all other control schemes are presented below in table no. 6.1. The load THD is 29.53% while the grid current THD in all the algorithms is well within the IEEE standards. The proposed $RL_0$-VSSCMPN algorithm shows the least THD.

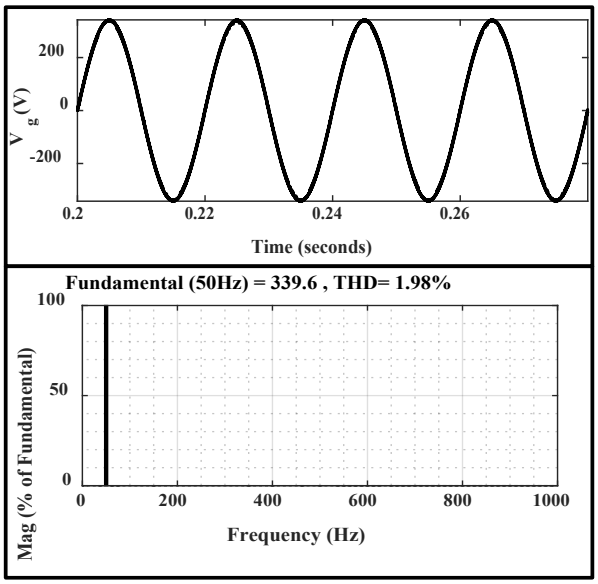


(a) Grid Voltage

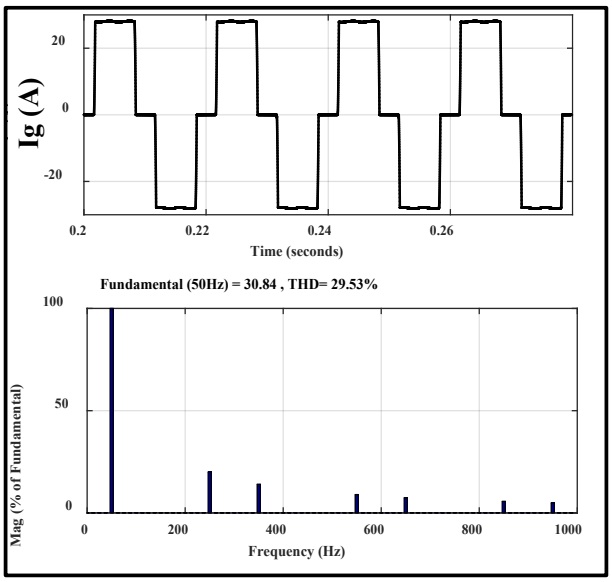


(b) Load Current

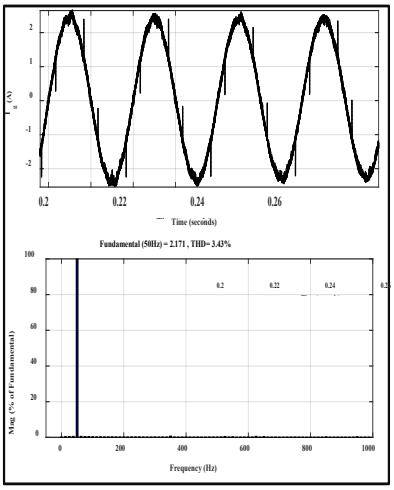

(c) Grid Current (SRFT)

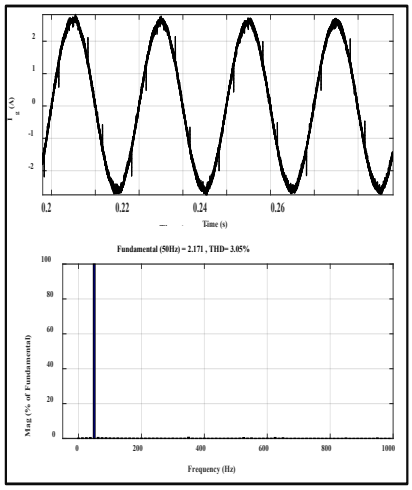

(d) Grid Current (Unit Template)

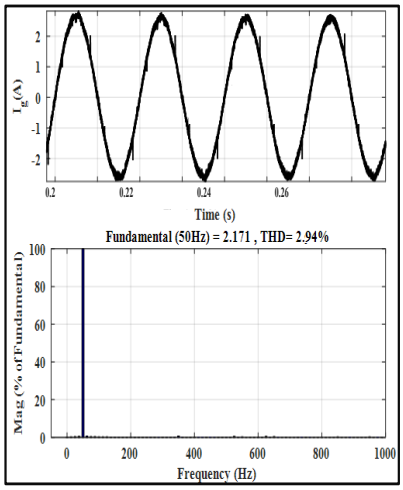


(e) Grid Current (LMS)

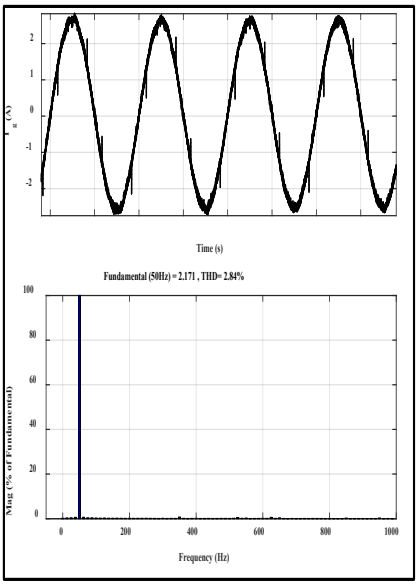

(f) Grid Current (Smooth LMS)

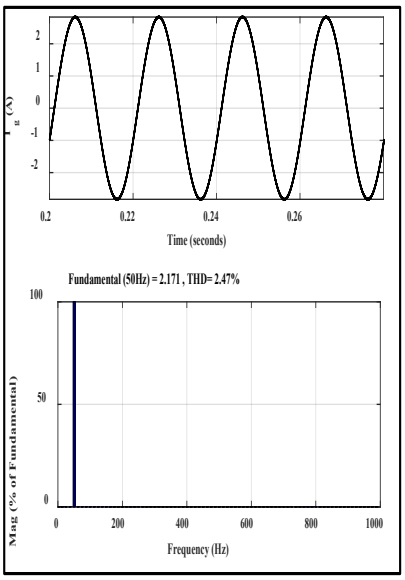


(g) Grid Current (IZALMS)

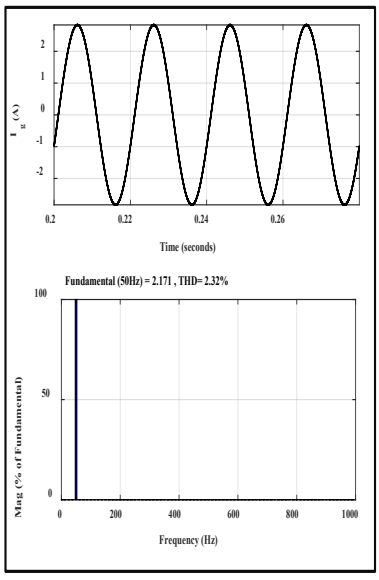


(h) Grid Current ($RL_0$-VSSCMPN)

**Fig. 6.23. Comparison of proposed control schemes with other control algorithms in terms of THD**

**Table No. 6.1. THD of proposed control algorithms and all other control algorithms**

| Control Algorithm | SRFT | Unit Template | LMS | Smooth LMS | IZALMS | RL$_0$-VSSCMPN |
|---|---|---|---|---|---|---|
| THD (%) | 3.43 | 3.05 | 2.94 | 2.84 | 2.47 | 2.32 |

### 6.4.4.2. Weight convergence and dc-offset rejection capability

In this section, the proposed control algorithms viz. Smooth LMS, IZALMS and RL$_0$-VSSCMPN have been compared with LMS based adaptive control algorithm in terms of weight convergence and dc-offset rejection capability. An offset of 2.5A is given in load current as shown in figure 6.24 (a). From the obtained results as shown in figure 6.24 (b), it can be seen that RL$_0$-VSSCMPN control scheme has less steady state oscillation along with fast convergence speed when dc-offset is given in comparison to LMS, Smooth LMS and IZALMS.

It can also be seen that proposed RL$_0$-VSSCMPN control algorithm completely rejects the dc-offset from load current when compared to LMS, Smooth LMS and IZALMS.

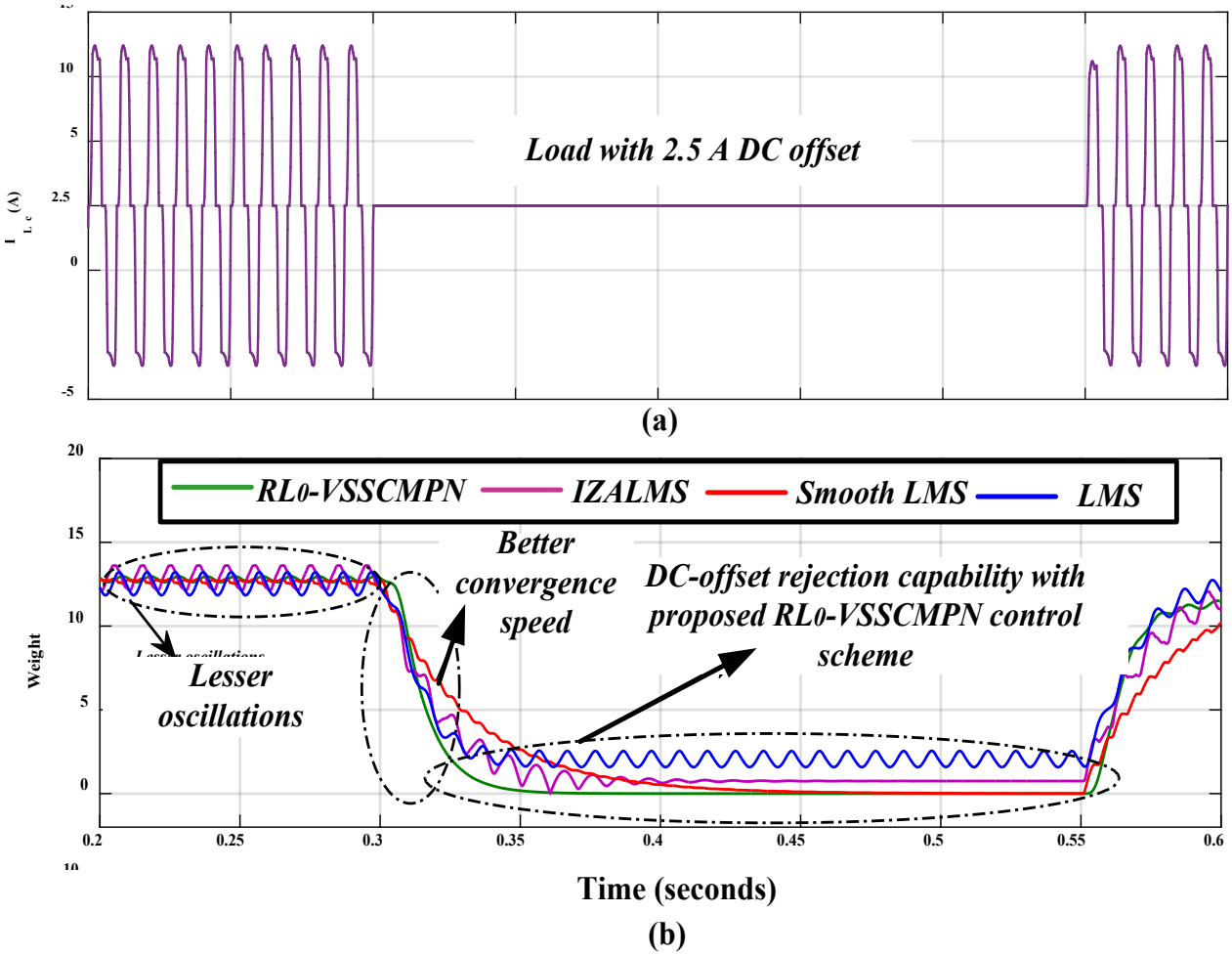


**Fig. 6.24. Comparison of proposed RL$_0$-VSSCMPN control scheme with LMS, Smooth LMS and IZALMS**

## 6.5. HARDWARE IMPLEMENTATION AND PARAMETER SELECTION

The proposed smooth LMS, IZALMS and RL$_0$-VSSCMPN based adaptive control algorithms are tested on the hardware prototype acting as DSTATCOM as shown in figure 6.25. Prototype hardware system consists of VSI that is tied in parallel to the grid at the point of common coupling. The numbering given in figure 6.25 indicates (1) Three phase 415V, 50Hz A.C. supply acting as grid after stepping down to 110 V (2) Interfacing Inductors (3) Load (non-linear) (4) Three-phase Resistive load (5) Three-phase Inductive load (6) Power Analyzer (7) Three-phase voltage source inverter (8) DC supply (9) DSO (10) dSPACE 1202 (MicroLab box) (11) Control desktop (12) Three phase auto transformer used to step down supply voltage to 110 V (13) Sensor circuit.

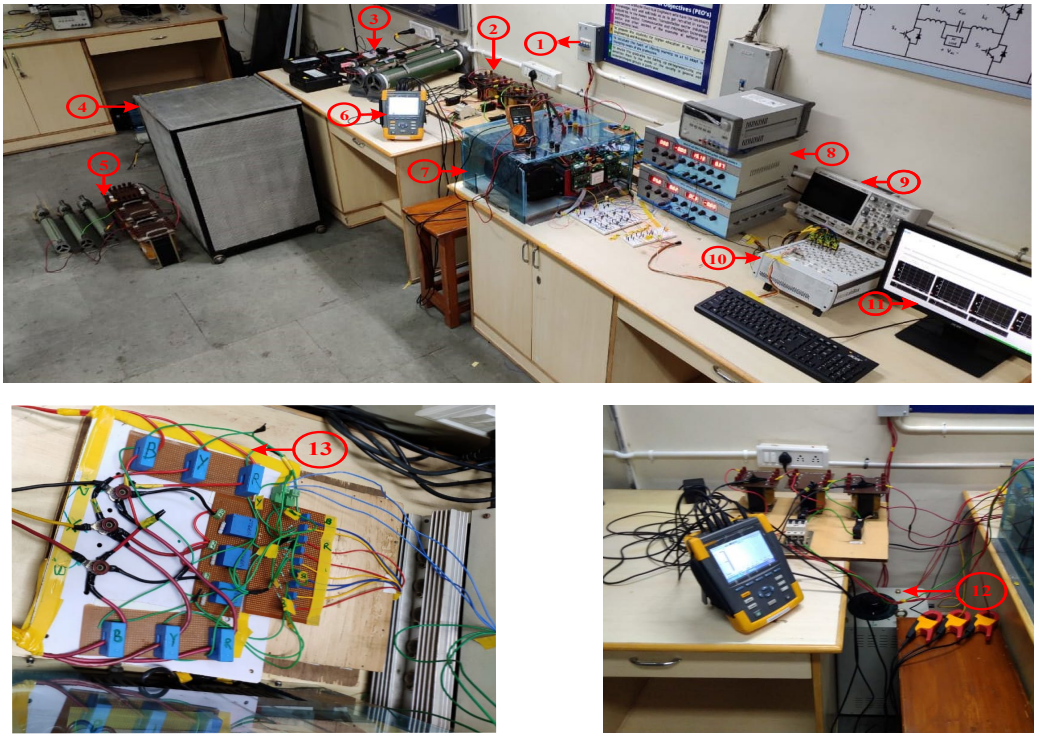


**Fig. 6.25. Hardware setup**

The parameters selection is explained below.

### 6.5.1 Choice of DC-link voltage ($V_{dc}$)

In order to achieve proper operation of the VSI, the minimum dc-link voltage of $V_{dc}$ should be greater than twice the peak phase voltage on the ac side of the VSI and can be calculated as given by equation (6.49) [124].

$$V_{dc} = \frac{2*\sqrt{2}*V_{LL}}{\sqrt{3}} \tag{6.49}$$

where, $V_{LL}$ is line to line voltage = 110 V. The calculated value of the $V_{dc}$ is 180 V, selected value of $V_{dc}$ is = 200 V.

### 6.5.2 Sizing of DC-Link capacitor ($C_{dc}$)

The dc-link capacitor shown in figure 6.1 is designed to ensure a stable dc-link voltage with minimum voltage ripple. The value of dc-link capacitor value can be calculated using equation (6.50) [126]:

$$C_{dc} = \frac{6.k.I_{ph}.V_{ph}.h.t}{(V_{dc1}^2 - V_{dc2}^2)} \quad (6.50)$$

Where, $V_{ph}$ is phase voltage = 63.5 V, $I_{ph}$ is phase current of inverter = 4A, $k$ is constant = 0.1, $h$ is overload factor = 1.2, t is time by which dc voltage recovers to its standard voltage = 0.015 sec, $V_{dc1}$ is reference voltage = 200V, $V_{dc2}$ is minimum dc-link voltage = 195 V. The calculated value of dc-link capacitor $C_{dc}$ = 1.38 mF.

### 6.5.3 Interfacing Inductors ($L_f$)

Interfacing inductor is designed to minimise the ripple in ac side output current of VSI. The basic equation governing dynamics between VSI and PCC is given by equation (6.51) [127]:

$$L_f \frac{di_c}{dt} = V_f - V_s \quad (6.51)$$

Where, $V_f$ is the value of the PWM voltage at the inverter-pole point (mid-point of inverter leg) and $V_s$ is the instantaneous PCC voltage of the corresponding phase. The ripple in current through interfacing inductor will be maximum when $V_s$ is at its peak equal to $V_{sm}$. Therefore, to account for a 10% voltage drop across the interfacing inductors, it can be considered that $V_f$ = 1.1 $V_{sm}$.. Therefore, substituting this value in equation (6.51), equation (6.52) can be obtained.

$$L_f \frac{di_c}{dt} = 1.1\, V_{sm} - V_{sm} = 0.1\, V_{sm} \quad (6.52)$$

where $V_{sm}$ is peak value of phase voltage = 63.5 V, $d_{ic}$ is the ripple in inductor current = 0.2 A, $dt$ is the switching time interval = 0.1ms. The calculated value of $L_f$ = 3.175 mH. A higher value of inductor $L_F$= 5 mH is selected.

The hardware prototype specifications are given in appendix E.

## 6.6. RESULTS AND DISCUSSIONS (EXPERIMENTAL REALIZATION)

### 6.6.1. Smooth LMS Control Algorithm

#### 6.6.1.1. System performance with linear load under load variation

Performance of smooth LMS control algorithm for VSI control under linear load (0.29 kVA, 0.85 lagging p.f.) is shown in figure 6.26 (a) and (b). Waveforms of phase 'a' of grid voltage ($V_g$), grid current ($I_g$), load current ($I_L$) and source i.e. inverter current ($I_s$) before and after

compensation are shown in the figure 6.26 (a). It can be seen that; grid current is maintained sinusoidal and is in phase with voltage after compensation. At the instant marked in figure 6.26 (b), additional load of 0.32kVA UPF has been added to the existing system. It can be seen from the results that; magnitude of grid current increases to meet the increased load demand but the system p.f. is maintained near to unity.

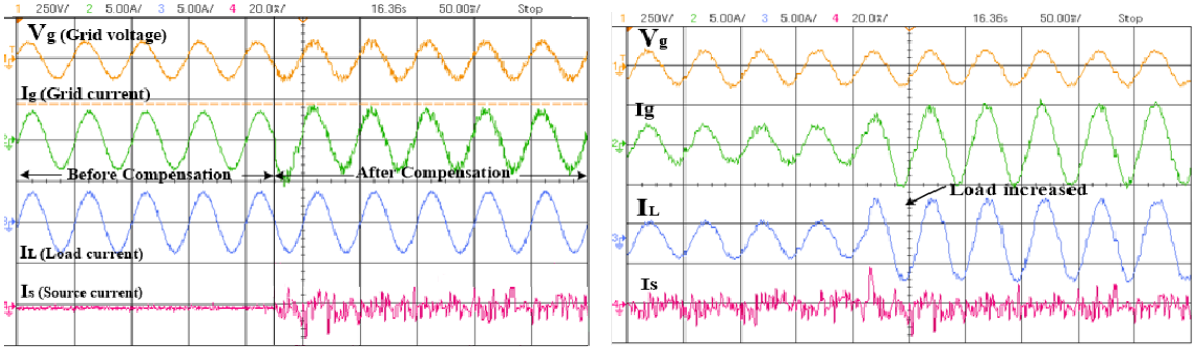


**(a)** **(b)**

**Fig. 6.26. System performance with (a) Steady linear load (b) variable linear load condition**

Figure 6.27 (a) depicts the corresponding demand of load and it can be seen that before compensation grid supplies both real and reactive load demand. After compensation, as seen from figure 6.27 (b), now inverter supplies the reactive power demand of the load. Hence, approximately zero reactive power is taken from grid which improves the grid power factor from 0.85 to 0.98. Figure 6.27(c) shows that, reactive demand of load is fulfilled by inverter alone and increased active load demand is supplied by grid only.

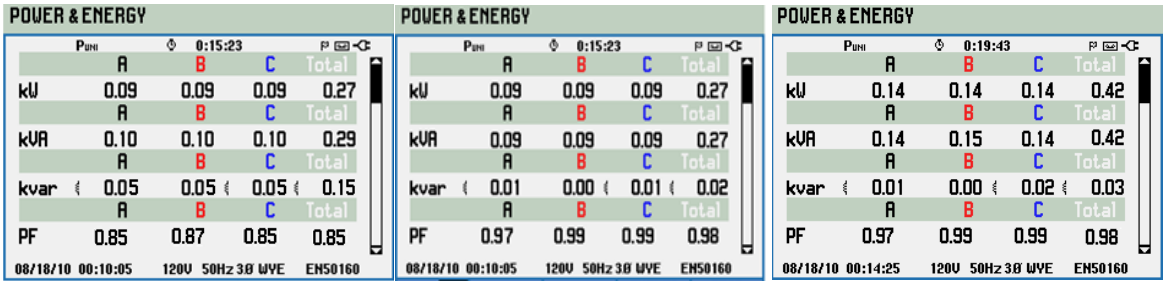


**(a)** **(b)** **(c)**

**Fig. 6.27. Grid Power (a) Before Compensation and (b)After Compensation (c) increased load**

### 6.6.1.2. System performance with non-linear load

### (a) Non-Linear Load variation

Performance of smooth LMS control algorithm for VSI control under non-linear load (3-ϕ bridge rectifier, R=50Ω, L=20mH) is shown in figure 6.28. Waveforms of phase 'a' of grid voltage ($V_g$), grid current ($I_g$), load current ($I_L$) and source i.e. inverter current ($I_s$) before

and after compensation are shown. Grid current is observed to be sinusoidal and in phase with voltage under non-linear load also.

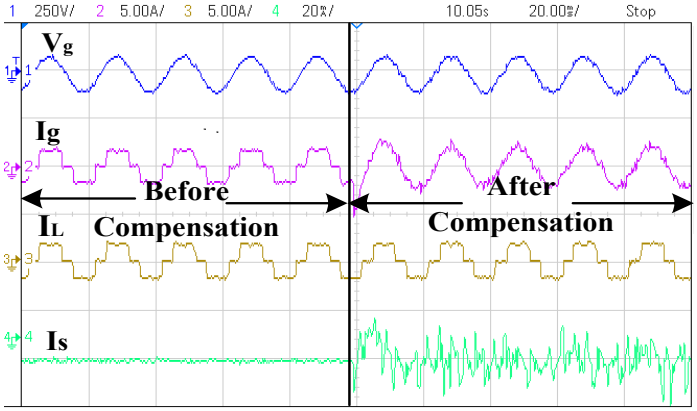


**Fig. 6.28. System performance with non-linear load**

In figure 6.29, robustness of the proposed controller has been examined under varying non-linear load. At the instant marked, three-phase bridge rectifier non-linear load has been changed from (R=50Ω, L=20mH) to (R=30Ω, L=20mH). The grid current is still sinusoidal. Furthermore, it can be seen that grid current magnitude is increased to meet the increased load demand.

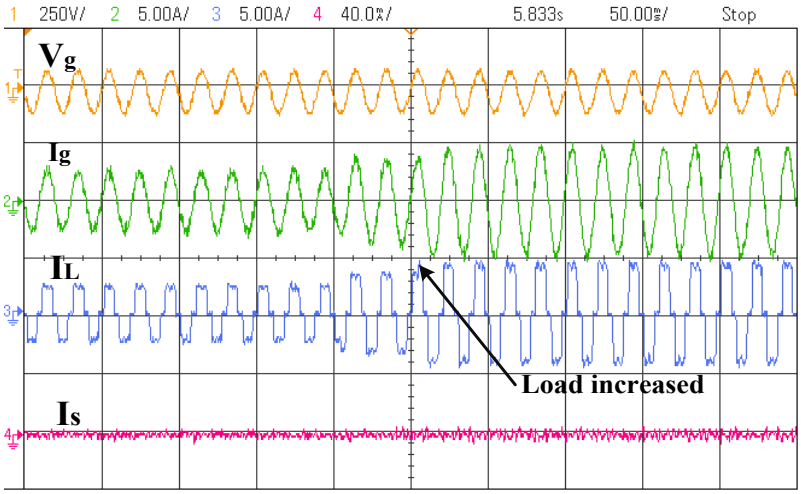


**Fig. 6.29. System performance with variable non-linear load condition**

### (b) Grid unbalancing

Performance of smooth LMS control algorithm for VSI control with non-linear load under unbalanced grid voltage condition is shown. Unbalancing of 21% in phase 'a' is given in grid voltage and corresponding grid and load current are shown in figure 6.30. With the proposed algorithm, it can be seen that under even unbalanced grid condition, grid current is sinusoidal.

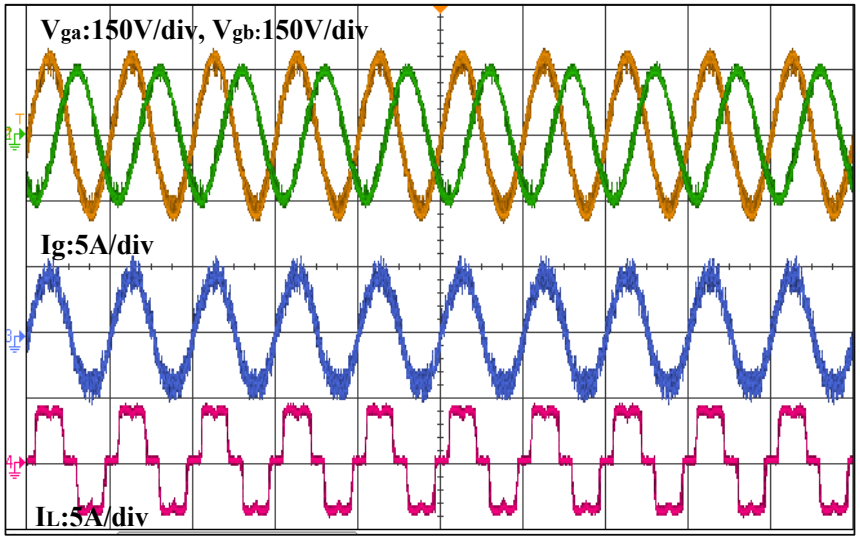


**Fig. 6.30. System performance with unbalanced grid voltage condition**

### (c) Grid voltage sag and swell

Performance of smooth LMS control algorithm for VSI control with non-linear load under grid voltage sag of 15% and grid voltage swell of 15% in the system is given as shown in figure 6.31. Voltage sag at instant indicated, decreases the voltage across the load current and similarly, voltage swell at instant indicated, increases the voltage across the load current. The grid current is still observed to be sinusoidal in both the condition.

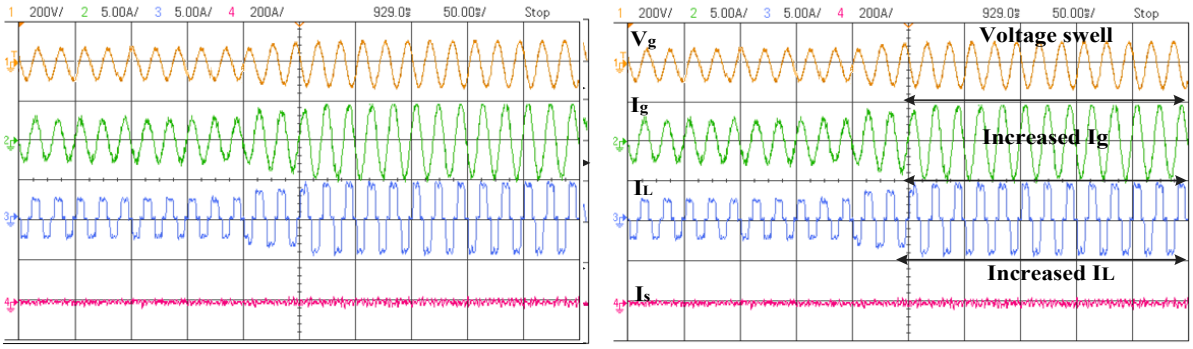


**Fig. 6.31. System performance with voltage sag and swell in grid voltage**

## 6.6.2. Improved Zero Attracting LMS Control Algorithm

### 6.6.2.1. System performance with linear load under load variation

Performance of IZALMS control algorithm for VSI control under linear load (0.34 kVA, 0.93 lagging p.f.) is shown in figure 6.32 (a) and (b). Waveforms of phase 'a' of grid voltage ($V_g$), grid current ($I_g$), load current ($I_L$) and source i.e. inverter current ($I_s$) before and after compensation are shown in the figure 6.32 (a). It can be seen from the results that; grid current is found to be sinusoidal is in phase with voltage after compensation. At the instant

marked in figure 6.32 (b), additional load of 0.30 kVA UPF has been added to the existing system. It can be seen from the results that; magnitude of grid current increases to meet the increased load demand.

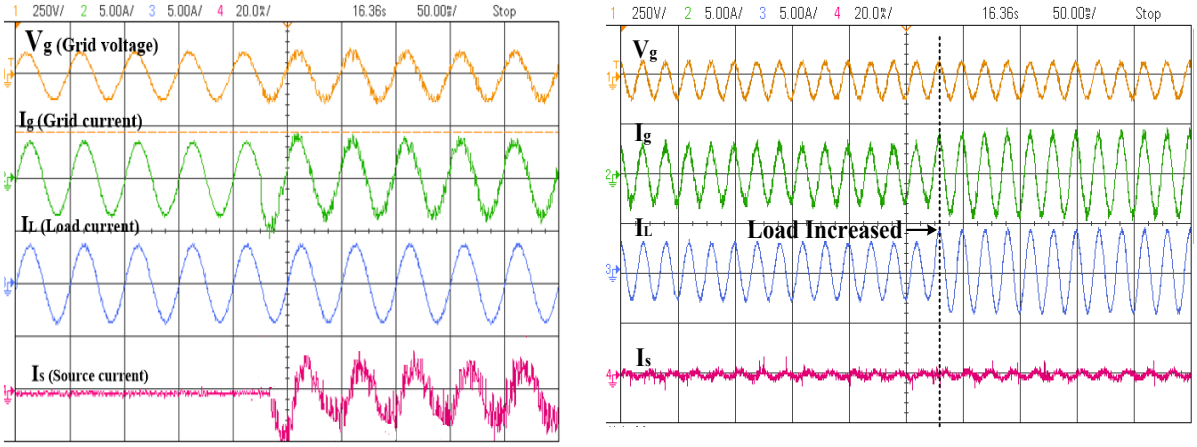


(a) (b)

**Fig. 6.32. System performance with (a) Steady linear load (b) variable linear load condition**

Figure 6.33 (a) depicts the corresponding demand of load and it can be seen that before compensation grid supplies both real and reactive load demand. After compensation as seen from figure 6.33 (b) that now inverter supplies the reactive power demand of the load. Hence, approximately zero reactive power is taken from grid which improves the grid power factor 0.93 to 0.98.

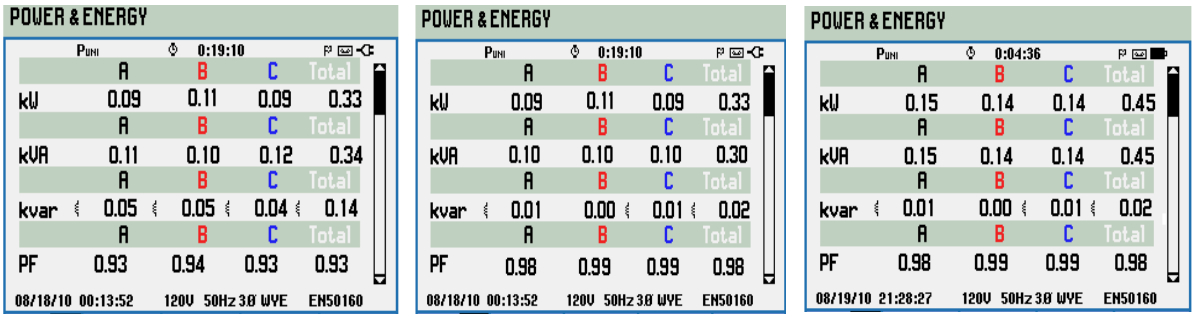


(a) (b) (c)

**Fig. 6.33. Grid Power (a) Before Compensation and (b)After Compensation (c) increased load**

### 6.6.2.2. System performance with non-linear load

Performance of IZALMS control algorithm for VSI control under non-linear load (3-ϕ bridge rectifier, R=50Ω, L=20mH) is shown in figure 6.34. Waveforms of phase 'a' of grid voltage ($V_g$), grid current ($I_g$), load current ($I_L$) and source i.e. inverter current ($I_s$) before and after compensation are shown. Grid current are observed to be sinusoidal under non-linear load also.

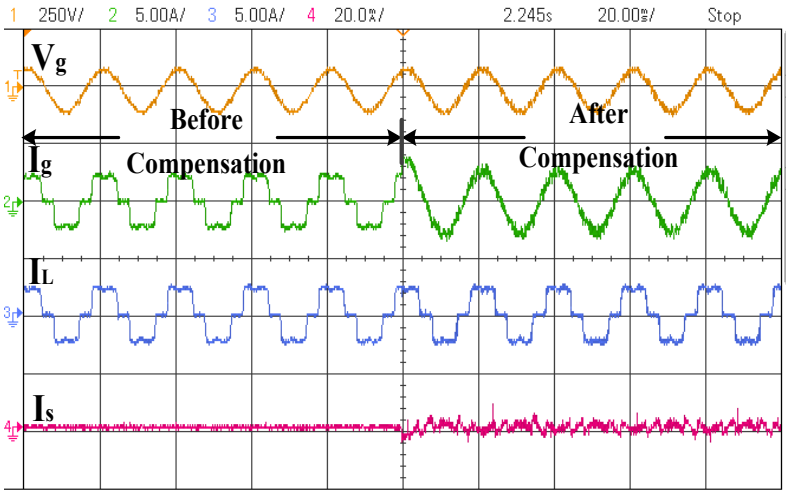


**Fig. 6.34. System performance with non-linear load**

### (a) Non-Linear Load variation

In figure 6.35, robustness of the proposed controller has been examined under varying non-linear load. At the instant marked, a three-phase bridge rectifier non-linear load has been changed from (R=50Ω, L=20mH) to (R=30Ω, L=20mH). The grid current is still sinusoidal. Furthermore, it can be seen that grid current magnitude is increased to meet the increased load demand.

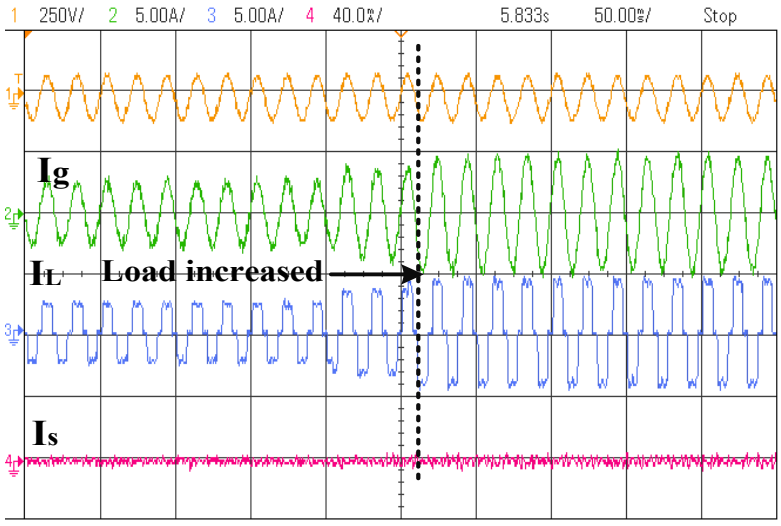


**Fig. 6.35. System performance with variable non-linear load condition**

### (b) Grid unbalancing

Performance of IZALMS control algorithm for VSI control with non-linear load under unbalanced grid voltage condition is shown. Unbalancing of 21% in phase 'a' is given in grid voltage and its corresponding grid and load current are shown in figure 6.36. With the proposed algorithm, it can be seen that under unbalanced grid condition, grid current is sinusoidal.

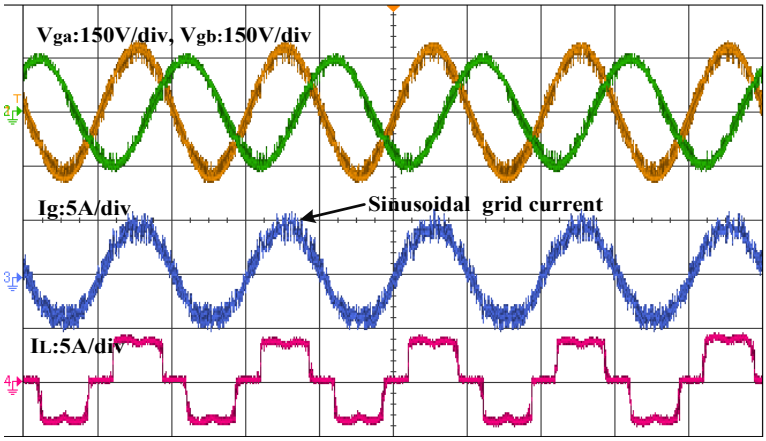


**Fig. 6.36. System performance with unbalanced grid voltage condition**

### (c) Grid voltage sag and swell

Performance of IZALMS control algorithm for VSI control with non-linear load under grid voltage sag of 15% and grid voltage swell of 15% in the system is given as shown in figure 6.37. Voltage sag at instant indicated, decreases the voltage across the load current and similarly, voltage swell at instant indicated, increases the voltage across the load current. The grid current is still observed to be sinusoidal in both the condition.

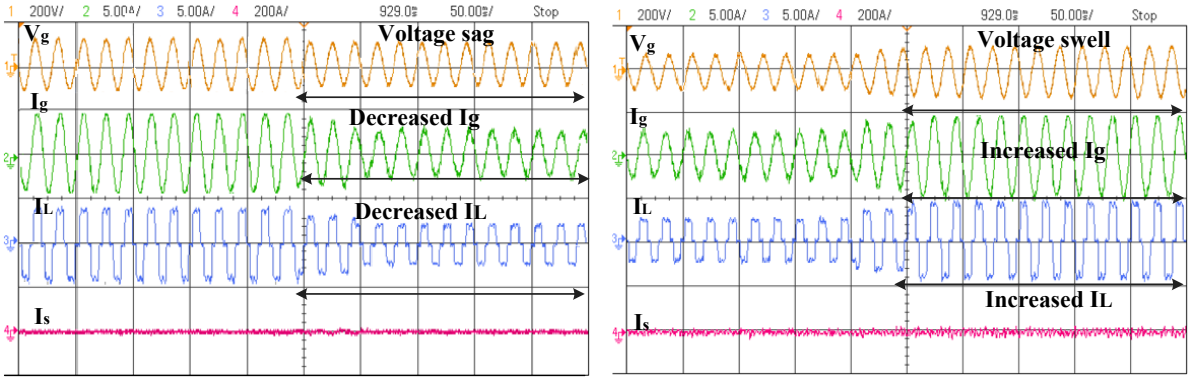


**Fig. 6.37. System performance with voltage sag and swell in grid voltage**

### 6.6.3. $RL_0$-VSSCMPN Control Algorithm

#### 6.6.3.1. System performance with linear load under load variation

Performance of $RL_0$-VSSCMPN control algorithm for VSI control under linear load (0.34 kVA, 0.93 lagging p.f.) is shown in figure 6.38 (a) and (b). Waveforms of phase 'a' of grid voltage ($V_g$), grid current ($I_g$), load current ($I_L$) and source i.e. inverter current ($I_s$) before and after compensation are shown in the figure 6.38 (a). It can be seen from the results that; grid current is found to be sinusoidal is in phase with voltage after compensation. At the instant marked in figure 6.38 (b), additional load of 0.30 kVA UPF has been added to the existing

system. It can be seen from the results that; magnitude of grid current increases to meet the increased load demand.

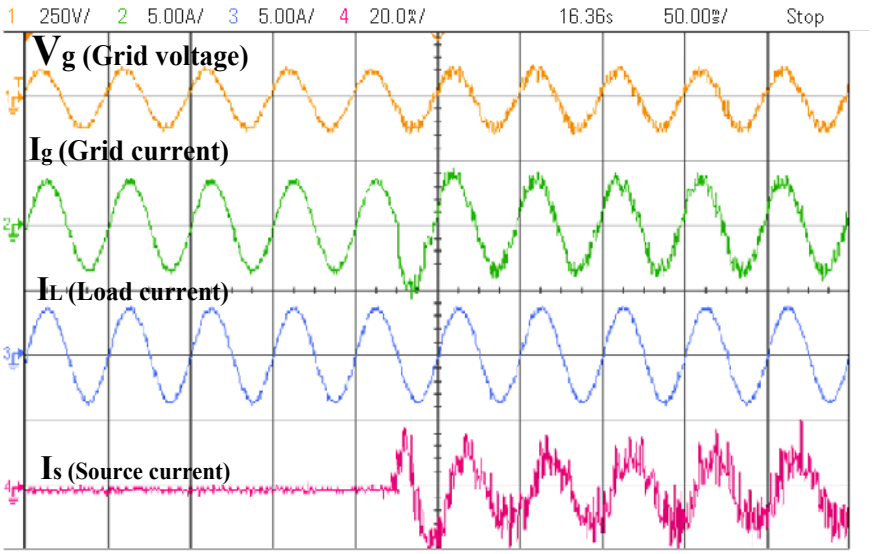


**Fig. 6.38. System performance with linear load**

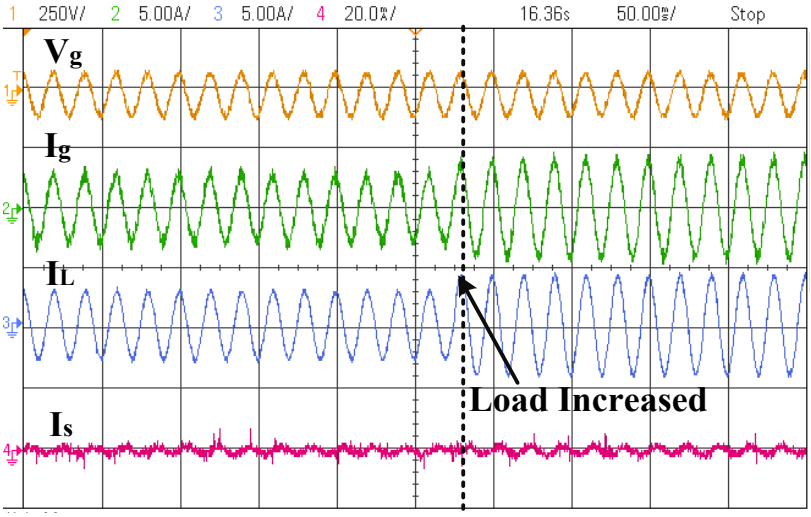


**(a)**

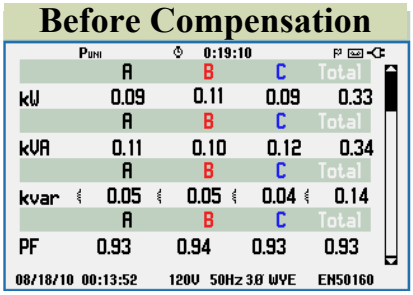


**(b)**

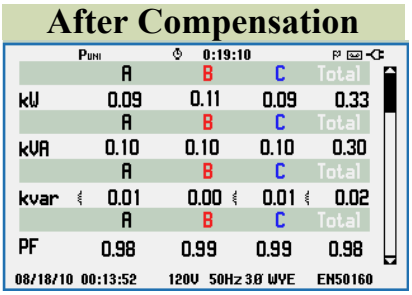


**(c)**

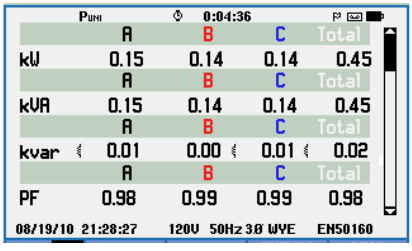


**(d)**

**Fig. 6.39 (a) System performance with varying linear load and Grid Power (b) Before Compensation and (c) After Compensation (d) increased load**

Figure 6.39 (b) depicts the corresponding demand of load and it can be seen that before compensation grid supplies both real and reactive load demand. After compensation, as seen from figure 6.39 (c), now inverter supplies the reactive power demand of the load. Hence, approximately zero reactive power is taken from grid which improves the grid power factor from 0.93 to 0.98. Figure 6.39 (d) shows that, reactive demand of load is fulfilled by inverter alone and increased active load demand is supplied by grid only.

### 6.6.3.2. System performance with non-linear load

#### (a) Non-Linear Load variation

Performance of $RL_0$-VSSCMPN control algorithm for VSI control under non-linear load (3-ϕ bridge rectifier, R=50Ω, L=20mH) is shown in figure 6.40. Waveforms of phase 'a' of grid voltage ($V_g$), grid current ($I_g$), load current ($I_L$) and source i.e. inverter current ($I_s$) before and after compensation are shown. Grid current are observed to be sinusoidal under non-linear load also.

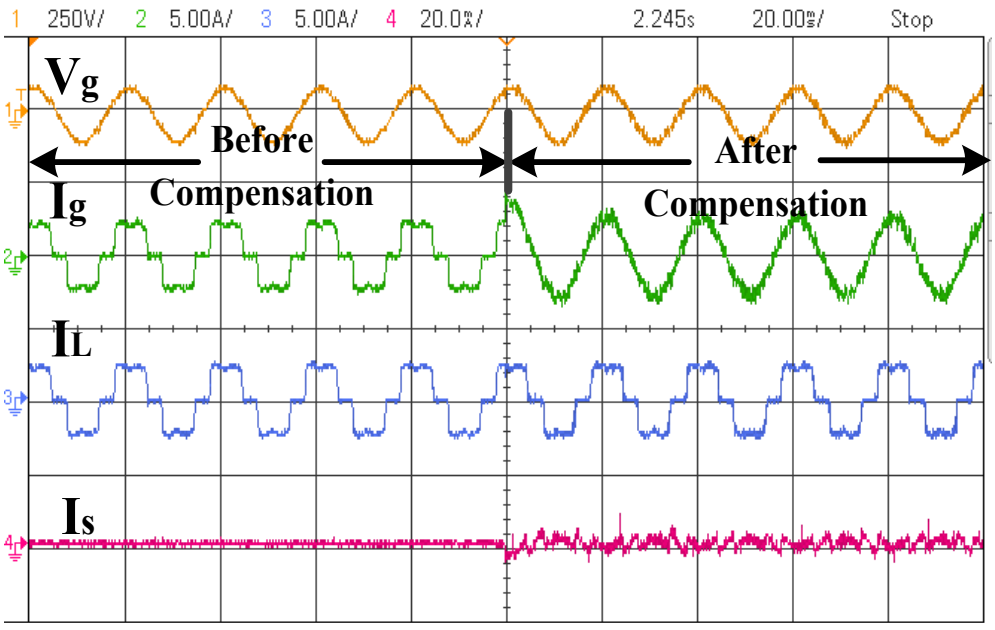


**Fig. 6.40. System performance with non-linear load**

In figure 6.41, robustness of the proposed controller has been examined under varying non-linear load. At the instant marked, a three-phase bridge rectifier non-linear load has been changed from (R=50Ω, L=20mH) to (R=30Ω, L=20mH). The grid current is still sinusoidal. Furthermore, it can be seen that grid current magnitude is increased to meet the increased load demand.

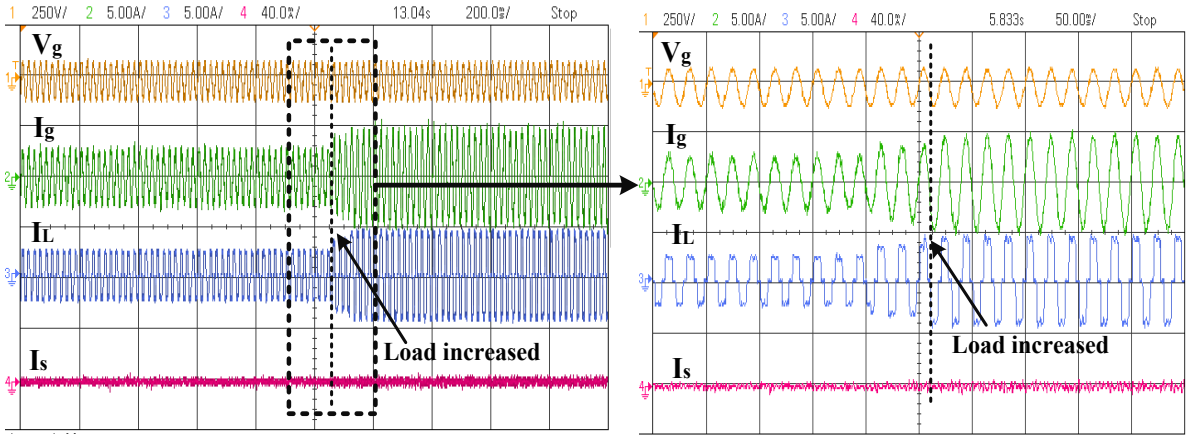


(a) (b)

**Fig. 6.41 System performance with varying non- linear load**

### (b) Grid unbalancing

Performance of RL$_0$-VSSCMPN control algorithm for VSI control with non-linear load under unbalanced grid voltage condition is shown. Unbalancing of 21% in phase 'a' is given in grid voltage and its corresponding grid and load current are shown in figure 6.42. With the proposed algorithm, it can be seen that under unbalanced grid condition, grid current is sinusoidal.

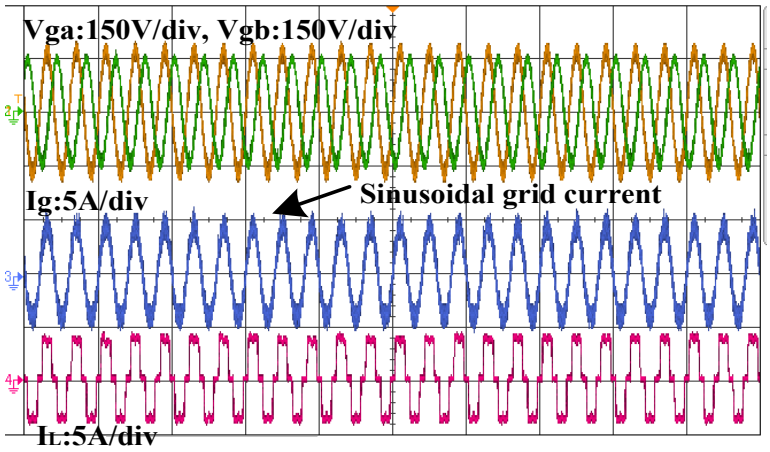


**Fig. 6.42. System performance with unbalanced grid voltages**

### (c) Grid voltage sag and swell

Performance of RL$_0$-VSSCMPN control algorithm for VSI control with non-linear load under grid voltage sag of 15% and grid voltage swell of 15% in the system is given as shown in figure 6.43. Voltage sag at instant indicated, decreases the voltage across the load current and similarly, voltage swell at instant indicated, increases the voltage across the load current. The grid current is still observed to be sinusoidal in both the condition.

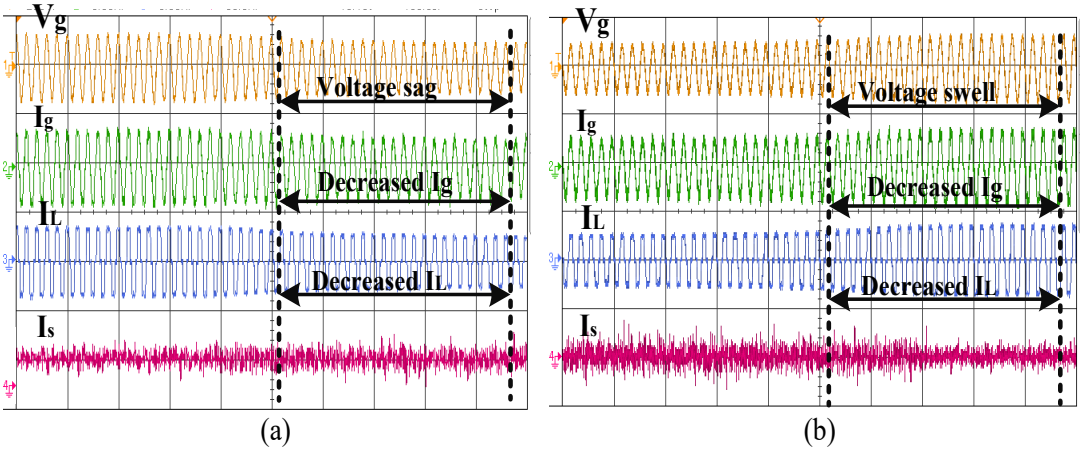


**Fig. 6.43 System performance with grid voltage sag and voltage swell**

### 6.6.4. Comparison of Proposed Control Algorithms with Other Control Algorithms

#### 6.6.4.1. Total Harmonics Distortion (THD)

In this section, the proposed control algorithms viz. Smooth LMS, IZALMS and RL$_0$-VSSCMPN has been compared in terms of total harmonic distortion as shown in figure 6.44 for the non-linear load considered. The load THD is 27.7 % while the grid current THD in all the algorithms is well within the IEEE standards. The THD of proposed RL$_0$-VSSCMPN algorithm shows the least THD of 3.3%.

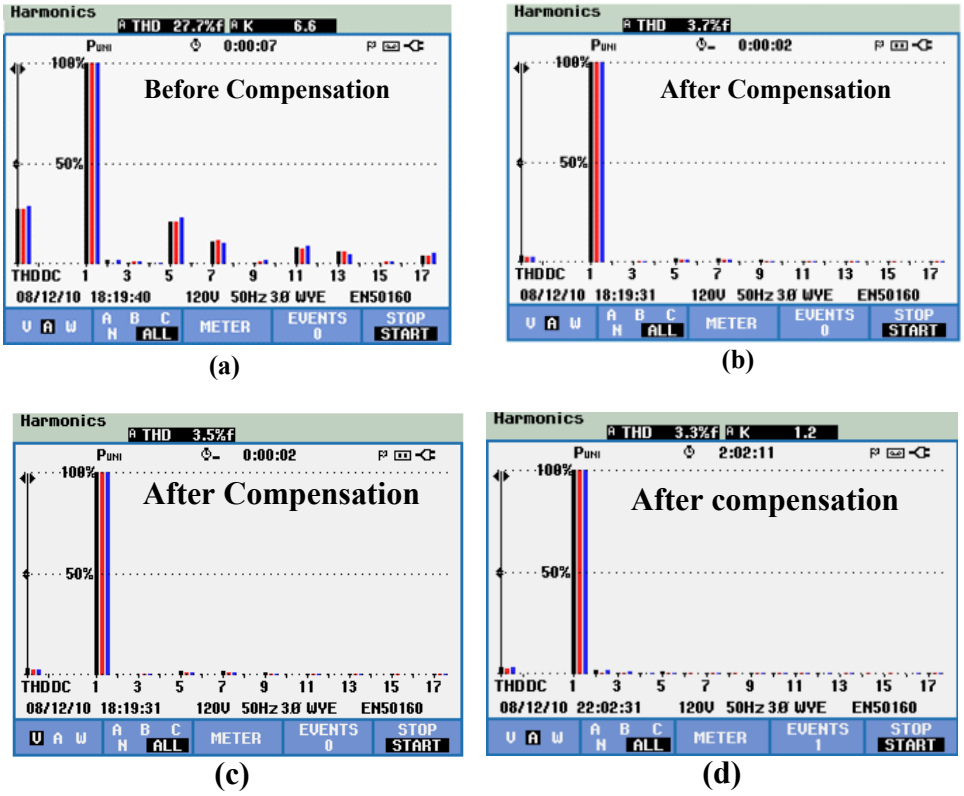


**Fig. 6.44. THD analysis under non-linear load: (a) Load Current (b) Grid Current (Smooth LMS) (c) Grid Current (IZALMS) (d) Grid Current (RL$_0$-VSSCMPN)**

### 6.6.4.2. Weight convergence

In this section, the proposed control algorithms viz. Smooth LMS, IZALMS and RL$_0$-VSSCMPN have been compared with LMS based adaptive control algorithm in terms of weight convergence. Waveforms of grid voltage, grid current, load current and weight component are shown in figure 6.45. Here load of phase 'a' has been disconnected and reconnected at the marked instants as shown in figure 6.45. It can be seen that under initial transient condition, during load disconnection, the proposed RL$_0$-VSSCMPN has faster settling time and less perturbations as compared to LMS, Smooth LMS and IZALMS.

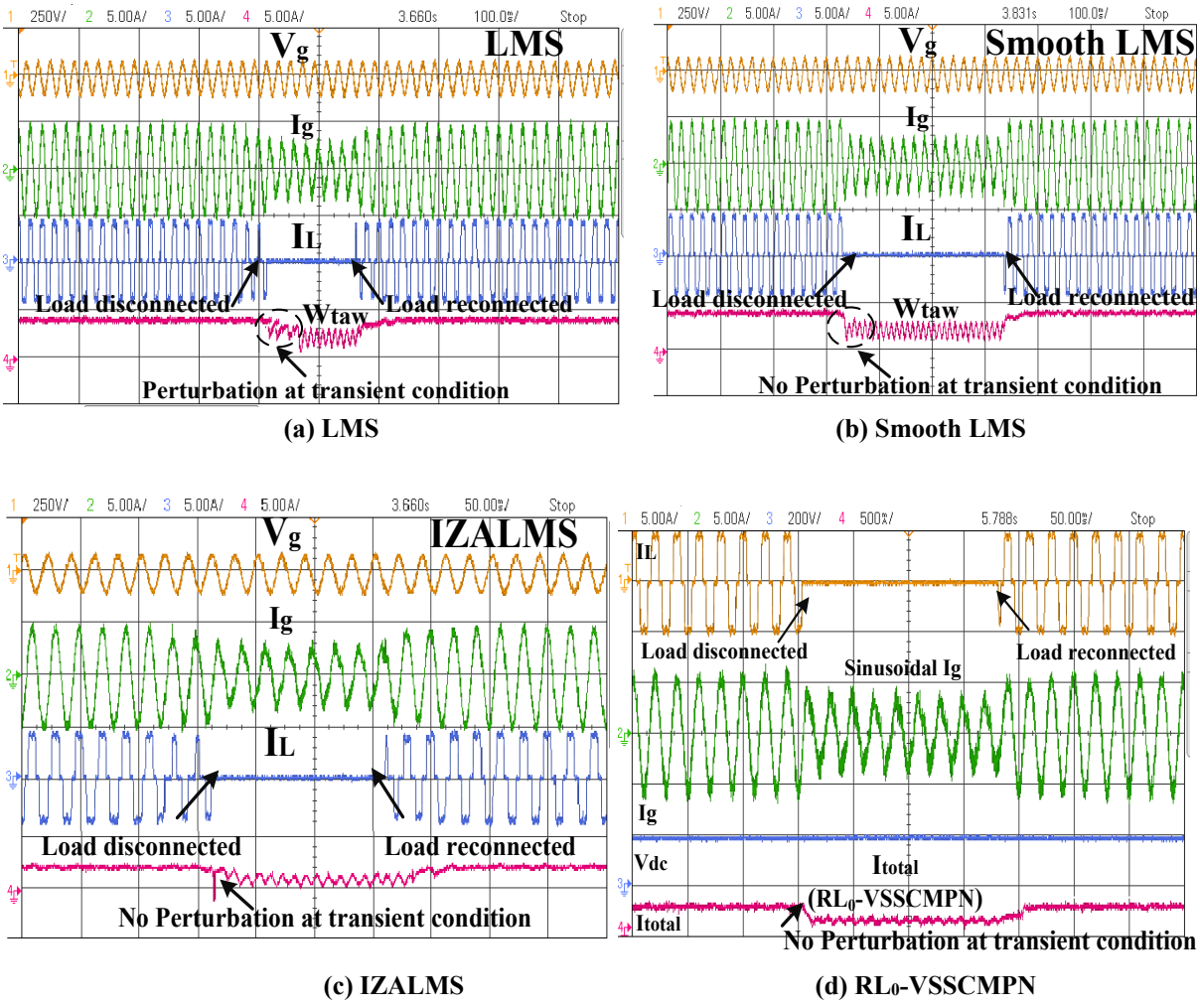


(a) LMS (b) Smooth LMS

(c) IZALMS (d) RL$_0$-VSSCMPN

**Fig. 6.45. Smooth LMS, IZALMS and RL$_0$-VSSCMPN comparison with LMS control algorithm in terms of weight convergence**

## 6.7. CONCLUDING REMARKS

In this chapter, the interfacing control algorithms viz. Smooth LMS, IZALMS and RL$_0$-VSSCMPN for two-stage, three-phase grid interfaced SPV system are proposed and

implemented. The simulation studies for the considered system have been carried out using these developed algorithms and wide range of simulation results under different operating conditions have been shown to prove the feasibility of the control approaches. The performance of the proposed algorithms has been found satisfactory under all test conditions. It has been observed that developed control algorithm maintains power balance, has reduced THD, compensates reactive power, has dc-offset rejection capability. Further, the performance of developed control algorithms is evaluated on hardware prototype. The THD of grid currents is observed to be less than 5% (within IEEE-519 standard) even with nonlinear loads. A comparative study in terms of THD and weight convergence has also been presented to validate the superiority of the proposed algorithms.

# CHAPTER-VII
# CONCLUSIONS AND SCOPE FOR FURTHER WORK

## INTRODUCTION

The continuously increasing energy demand and environmental concerns can be satiated by renewable energy sources. As per the present development, solar photovoltaic generating system is one of the most important green sources of energy. Battery energy storage system is an integral part of PV based standalone microgrid. During the night, or during a period of low solar irradiance, such as a cloudy or rainy day, when the output of PV system is low, batteries are used to supply power to the loads. SPV based generating system necessitate power electronics components. Further, solid state device-based loads have made our life easier but they also draw harmonics from the utility grid and raise power quality issues like poor power factor, unbalancing etc.

The main objective of this research is to model, design and control of SPV based system in stand alone and grid connected mode for improved performance. The characterization studies viz. sensitivity and reliability analysis are carried out to validate the design of the system.

In stand-alone PV system, the solar PV array is connected to load via dc-dc converter (boost). MPPT algorithm control the switching of the dc-dc converter to track the maximum power that can be obtained from the PV array under uniform and partial shading scenarios. Intelligent MPPT control algorithms are used to track the maximum power under PSC. These algorithms were able to track global peak out of many local peaks. Using intelligent control algorithm, the performance of the system is also improved.

Battery energy storage systems are used as another energy source in stand-alone PV system to compensate the changes in PV output due to change in environmental conditions. But, when two different power sources are coupled at the generation point, the dc link control at CCP becomes an issue. So, control algorithms were developed in order to maintain voltage across dc link under variable input and output condition. PV system supplies power to the load and is also used to charge the battery after the load demand is met. Discharge characteristics of battery has been shown for the different discharge current ratings. The proposed control algorithm has been analysed on MATLAB/Simulink toolbox for considered conditions.

The effective working and utilization of PV inverter depends on its control algorithm. Novel LMS based adaptive interfacing control algorithms are proposed for PV inverter. These control

algorithms provide multi-functionalities to the interfacing inverter such as feeding active and reactive demand of the load, dc offset rejection, harmonics curtailment etc. The performance of proposed algorithms for solar PV based microgrid have been analyzed for linear as well nonlinear loads for both input and output side variations using MATLAB Simulink toolbox and hardware prototype.

## 7.2. MAIN CONCLUSIONS

The following are the significant findings of the presented research work:

- In the present work, design and modelling of stand-alone PV system and double stage three phase for grid interfaced solar PV based microgrid along with its characterization studies viz. sensitivity and reliability analysis have been carried out. The sensitivity functions of the PV cell and boost converter for different PV array configurations (S, P, SP, TCT, BL, HC) have been developed. The results of the sensitivity analysis demonstrate that the PV cell output is more sensitive to the intensity of irradiation, whereas the converter output is more sensitive to the inductor value and switching frequency. Reliability of SPV based microgrid and its various components has been calculated using pareto analysis, reliability block diagram, fault tree analysis and markov's model. Pareto analysis was used to determine the component with the highest failure rate. Reliability block diagram computes the reliability of stand-alone PV system and grid interfaced solar PV based microgrid with BESS for different PV array configurations. The fault tree has been developed for the proposed system. System failure is represented at the top of an event and subsequent down events which make the happening of top event have been shown. The down events are indicated with their failure rate. Furthermore, markov model for individual component as well as for the complete SPV based microgrid has been developed. It has been observed that grid interfaced SPV based microgrid with BESS is more reliable than stand-alone SPV based microgrid for SP/BL/HC PV array configuration.

- In solar PV system, the SPV output varies due to varying environmental conditions and due to partial shading of PV arrays, which reduces the efficiency of system. In order to extract the maximum power and to minimize the losses caused due to partial shading, maximum power point techniques viz. Novel intelligent based AFLC and asymmetrical interval type 2 FLC are proposed. Also, different PV array configurations viz. series, series-parallel, total cross tied are used to increase the efficiency and reduce the losses of the system. MATLAB/Simulation results show the efficacy of the proposed algorithms for various PV

configurations studied under steady-state as well as dynamic conditions. Further, a comparative study of the proposed algorithms with conventional ANFIS based control algorithm is carried out in terms of tracked GMPP, shading losses, fill factor and mismatch losses.

- For rural areas that are not connected to the power grid, standalone operation of a PV system is the best alternative. But due to diurnal cycle of the earth and weather condition, solar energy in not constant and sometimes it may lead to the insufficient PV generation to meet the power demand of the varying local load. For reliable operation of solar PV system, battery energy storage system needs to be connected in parallel with PV system as a backup source. Further, power variations in the system are caused by changes in load demand and generation, resulting in dc-link voltage variations. This variation of dc link voltage at common coupling point is seen in ac voltage and is detrimental for system performance. Hence, it is essential to control the dc-link voltage irrespective of variations occurred. To work upon this, novel nonlinear autoregressive-moving average-L2 has been proposed to control the dc-link voltage in stand-alone PV system with BESS. MATLAB/Simulink results show the efficacy of the proposed algorithm under input/output variation conditions. The proposed control algorithm has been compared with conventional PI controller in terms of dc link voltage.

- Power converter i.e., inverter control is essential in bidirectional power flow in a grid-connected microgrid. In addition to supplying energy to the load at the appropriate voltage and frequency, the inverter should have additional functionality such as active filtering and load balancing which maintains power quality and voltage profile of the grid. Novel PV inverter algorithms, Smooth LMS, IZALMS, reweighted $L_0$ norm with variable step size CMPN based adaptive control algorithms are proposed for inverter control in a grid-tied solar PV based microgrid. MATLAB/Simulation results show the efficacy of the proposed algorithms under steady-state as well as transient input/output operating conditions viz. load and grid unbalancing, grid voltage sag and swell condition etc. For nonlinear loads, the THD of grid currents is less than 5% (as specified by IEEE-519). Further, a comparative study of the proposed algorithms with conventional SRF theory and unit template-based control algorithm is carried out confirming the improved performance of proposed algorithms. The proposed control algorithms were also tested on hardware setup acting as DSTATCOM developed in laboratory. The THD of grid current is again observed to be within 5% with proposed control algorithms on hardware prototype.

## 7.3. SUGGESTIONS FOR FURTHER WORK

There are several important aspects which need to be investigated further, but could not be covered in this research work.

- The present work focuses on the design and control of solar PV based microgrid under healthy grid condition. The performance of the proposed system can be evaluated considering the fault conditions also.
- MPPT control algorithms in the present work are simulated for solar PV system with different PV array configurations. The performance of the implemented algorithms for varying environmental situations may be verified experimentally with different PV array configurations.
- The present work on stand-alone PV system with BESS can be extended to grid tied solar PV system with BESS and proposed control algorithms in the present work can be tested on real time systems.
- Due to laboratory limitation, the PV inverter control algorithms were tested on DSTATCOM. The proposed control algorithms in the present work may be tested on grid tied real time system to verify efficacy of the implemented algorithms.

# REFERENCES


[1] H. B. Massawe, "Grid Connected Photovoltaic Systems with Smart Grid functionality," *IET Electric Power Applications*, Vol. 13, no.6, June, pp. 37–39, 2013.

[2] S. Luthra, S. Kumar, R. Kharb, M. F. Ansari, and S. L. Shimmi, "Adoption of smart grid technologies: An analysis of interactions among barriers," *Renew. Sustain. Energy Rev.*, vol. 33, pp. 554–565, 2014.

[3] M. Obi and R. Bass, "Trends and challenges of grid-connected photovoltaic systems - A review," *Renew. Sustain. Energy Rev.*, vol. 58, pp. 1082–1094, 2016.

[4] H. E. K. Baitie and T. Selmi, "Review of smart grid systems' requirements," *2015 Tenth International Conference on Ecological Vehicles and Renewable Energies (EVER)* , pp. 1-6, doi: 10.1109/EVER.2015.7113004, 2015.

[5] R. Hudson and G. Heilscher, "PV grid integration - System management issues and utility concerns," *Energy Procedia*, vol. 25, pp. 82–92, 2012.

[6] E. Romero-Cadaval, G. Spagnuolo, L. G. Franquelo, C. A. Ramos-Paja, T. Suntio, and W. M. Xiao, "Grid-connected photovoltaic generation plants: Components and operation," *IEEE Ind. Electron. Mag.*, vol. 7, no. 3, pp. 6–20, 2013.

[7] P. Paniyil, V. Powar, R. Singh , B. Hennigan, P. Lule, M. Allison, J Kimsey, A. Carambia, D. Patel, D.Carrillo, Z. Shriber, T. Bazer, J. Farnum, K. Jadhav and D. Pumputis, "Photovoltaics- And battery-based power network as sustainable source of electric power," *Energies*, vol. 13, no. 19, pp. 1–22, 2020.

[8] A. Mohanty, M. Viswavandya, D. K. Mishra, P. K. Ray, and S. Pragyan, "Modelling & Simulation of a PV Based Micro Grid for Enhanced Stability," *Energy Procedia*, vol. 109, pp. 94–101, 2017.

[9] M. Gaayathri and K. Ranjith Kumar, "Modelling And Simulation of PV-BES based Microgrid System Operating In Standalone Mode," *IOP Conf. Ser. Mater. Sci. Eng.*, vol. Vol. 1084, pp. 1-8, 2021.

[10] X. Xiong and Y. Yang, "A photovoltaic-based DC microgrid system: Analysis, design and experimental results," *Electronics*, vol. 9, no. 6, pp. 1–17, 2020.

[11] E. Figueres, G. Garcerá, J. Sandia, F. González-Espín, and J. C. Rubio, "Sensitivity study of the dynamics of three-phase photovoltaic inverters with an LCL grid filter," *IEEE Trans. Ind. Electron.*, vol. 56, no. 3, pp. 706–717, 2009.

[12] Q. Li-Nan, Z. Ling-Zhi, S. Tao, and L. Jing, "Identification of photovoltaic power system based on sensitivity analysis," *Asia-Pacific Power Energy Eng. Conf. APPEEC*,

pp. 1–5, 2013.

[13] X. G. Zhu, Z. H. Fu, X. M. Long, and Xin-Li, "Sensitivity analysis and more accurate solution of photovoltaic solar cell parameters," *Sol. Energy*, vol. 85, no. 2, pp. 393–403, 2011.

[14] M. A. Azghandi, S. M. Barakati, and B. Wu, "Dynamic Modeling and Control of Grid-Connected Photovoltaic Systems based on Amplitude-Phase Transformation", *Iranian Jou. of Elec.and Electronic Engg*, vol. 14, no. 4, pp. 342–352, 2018.

[15] R. Yan and T. K. Saha, "Voltage variation sensitivity analysis for unbalanced distribution networks due to photovoltaic power fluctuations," *IEEE Trans. Power Syst.*, vol. 27, no. 2, pp. 1078–1089, 2012.

[16] C. Rodriguez and G. A. J. Amaratunga, "Dynamic stability of grid-connected photovoltaic systems," *IEEE Power Eng. Soc. Gen. Meet.*, vol. 2, pp. 2193–2199, 2004.

[17] D. Oliva, E. Cuevas, and G. Pajares, "Parameter identification of solar cells using artificial bee colony optimization," *Energy*, vol. 72, pp. 93–102, 2014.

[18] P. P. Dash and M. Kazerani, "Sensitivity analysis of a current-source inverter-based three-phase grid-connected photovoltaic system," *IEEE Electr. Power Energy Conf. EPEC*, pp. 1-8, doi: 10.1109/EPEC.2016.7771676, 2016.

[19] Y. Xue, M. Manjrekar, C. Lin, M. Tamayo, and J. N. Jiang, "Voltage stability and sensitivity analysis of grid-connected photovoltaic systems," *IEEE Power Energy Soc. Gen. Meet.*, pp. 1–7, doi: 10.1109/PES.2011.6039649, 2011.

[20] L. Guo, Z. Meng, Y. Sun, and L. Wang, "Parameter identification and sensitivity analysis of solar cell models with cat swarm optimization algorithm," *Energy Convers. Manag.*, vol. 108, pp. 520–528, 2016.

[21] L. Shu, J. Zheng, X. Shen, H. Yin, and J. Li, "Parameters' sensitivity analysis of grid-connected photovoltaic power generation model under different kinds of disturbances," *Proc. - 2012 IEEE Symp. Electr. Electron. Eng. EEESYM 2012*, pp. 658–661, 2012.

[22] H. Andrei, T. Ivanovici, E. Diaconu, M. R. Ghita, O. Marin, and P. C. Andrei, "Analysis and experimental verification of the sensitivity of PV cell model parameters," *2012 Int. Conf. Synth. Model. Anal. Simul. Methods Appl. to Circuit Des. SMACD 2012*, pp. 129–132, 2012.

[23] T. F. Elshatter and M. T. Elhagry, "Sensitivity analysis of the photovoltaic model parameters," *Midwest Symp. Circuits Syst.*, vol. 2, pp. 914–917, 1999.

[24] J. Chureemart and P. Churueang, "Sensitivity analysis and its applications in power system improvements," *5th Int. Conf. Electr. Eng. Comput. Telecommun. Inf. Technol.*

*ECTI-CON*, vol. 2, pp. 945–948, 2008.

[25] W. M. Rohouma, I. M. Molokhia, and A. H. Esuri, “Comparative study of different PV modules configuration reliability,” *Desalination*, vol. 209, no. 3, pp. 122–128, 2007.

[26] C. Singh and A. Lago-Gonzalez, “Reliability Modeling of Generation Systems Including Unconventional Energy Sources,” *IEEE Power Eng. Rev.*, vol. PAS-104, no. 5, pp. 1049-1056, 1985.

[27] L. H. Stember, W. R. Huss, and M. S. Bridgman, “A Methodology for Photovoltaic System Reliability & Economic Analysis,” *IEEE Trans. Reliab.*, vol. R-31, no. 3, pp. 296–303, 1982.

[28] S. V. Dhople and A. D. Domínguez-García, “Estimation of photovoltaic system reliability and performance metrics,” *IEEE Trans. Power Syst.*, vol. 27, no. 1, pp. 554–563, 2012.

[29] A. Khosroshahi, M. Abapour, and M. Sabahi, “Reliability evaluation of conventional and interleaved DC-DC boost converters,” *IEEE Trans. Power Electron.*, vol. 30, no. 10, pp. 5821–5828, 2015.

[30] N. Gupta, R. Garg, P. Kumar, "Sensitivity and reliability models of a PV system connected to grid" *Renewable and Sustainable Energy Reviews*, vol. 69, pp. 188-196, 2017.

[31] S. Baschel, E. Koubli, J. Roy, and R. Gottschalg, “Impact of component reliability on large scale photovoltaic systems’ Performance,” Energies, vol. 11, no. 6, pp. 1579- 1595, 2018.

[32] M. Aten, G. Towers, C. Whitley, P. Wheeler, J. Clare, and K. Bradley, “Reliability comparison of matrix and other converter topologies,” *IEEE Trans. Aerosp. Electron. Syst.*, vol. 42, no. 3, pp. 867–873, 2006.

[33] G. Song, H. Chen, and B. Guo, “A layered fault tree model for reliability evaluation of smart grids,” *Energies*, vol. 7, no. 8, pp. 4835–4857, 2014.

[34] S. Yang, A. Bryant, P. Mawby, D. Xiang, L. Ran, and P. Tavner, “An industry-based survey of reliability in power electronic converters,” *IEEE Trans. Ind. Appl.*, vol. 47, no. 3, pp. 1441–1451, 2011.

[35] F. Chan and H. Calleja, “Reliability estimation of three single-phase topologies in grid-connected PV systems,” *IEEE Trans. Ind. Electron.*, vol. 58, no. 7, pp. 2683–2689, 2011.

[36] M. R. Sagayaraj and S. P. Anita, A Merceline, “Markov Models in System Reliability with Applications,” *Int. J. Innov. Res. Dev.*, vol. 3, no. 11, pp. 328–336, 2014.

[37] F. Chan and H. Calleja, “Design strategy to optimize the reliability of grid-connected

PV systems," *IEEE Trans. Ind. Electron.*, vol. 56, no. 11, pp. 4465–4472, 2009.

[38] F. Obeidat and R. Shuttleworth, "Reliability prediction of PV inverters based on MIL-HDBK-217F N2," *2015 IEEE 42nd Photovolt. Spec. Conf. PVSC*, 2015.

[39] E. Chiodo and D. Lauria, "Some Basic Properties of the Failure Rate of Redundant Reliability Systems in Industrial Electronics Applications," *IEEE Trans. Ind. Electron.*, vol. 62, no. 8, pp. 5055–5062, 2015.

[40] E. E. Kostandyan and K. Ma, "Reliability estimation with uncertainties consideration for high power IGBTs in 2.3 MW wind turbine converter system," *Microelectron. Reliab.*, vol. 52, no. 9–10, pp. 2403–2408, 2012.

[41] R. N. Bharti, R. Kumar, and M. Professor, "Modeling and Simulation of Maximum Power Point Tracking for Solar PV System using Perturb and Observe Algorithm," *Int. J. Eng. Res. Technol.*, vol. 3, no. 7, pp. 675–681, 2014.

[42] S. Singh and L. Mathew, "Design and Simulation of Intelligent Control MPPT Technique for PV Module Using MATLAB/ SIMSCAPE," *Int. J. Adv. Res. Electr. Electron. Instrum. Eng. ISO Certif. Organ.*, vol. 3297, no. 9, pp. 2320–3765, 2007.

[43] C. L. Liu, J. H. Chen, Y. H. Liu, and Z. Z. Yang, "An asymmetrical fuzzy-logic-control-based MPPT algorithm for photovoltaic systems," *Energies*, vol. 7, no. 4, pp. 2177–2193, 2014.

44] R. Reshma Gopi, S. Sreejith, "Converter topologies in photovoltaic applications – A review," *Renewable and Sustainable Energy Reviews*, vol. 94, pp. 1-14, 2018.

[45] H. Mahamudul, H. Metselaar, and S. Mekhilef, "Effective photovoltaic system design by applying MPPT algorithm and phase change material," *7th IET Int. Conf. Power Electron. Mach. Drives, PEMD 2014*, pp. 1–6, 2014.

[46] S. Jain and V. Agarwal, "A single-stage grid connected inverter topology for solar PV systems with maximum power point tracking," *IEEE Trans. Power Electron.*, vol. 22, no. 5, pp. 1928–1940, 2007.

[47] J. J. Nedumgatt, K. B. Jayakrishnan, S. Umashankar, D. Vijayakumar, and D. P. Kothari, "Perturb and observe MPPT algorithm for solar PV systems-modeling and simulation," *Proc. - 2011 Annu. IEEE India Conf. Eng. Sustain. Solut. INDICON-2011*, vol. 19, no. 1, 2011.

[48] R. B. A. Koad, A. F. Zobaa, and A. El-Shahat, "A Novel MPPT Algorithm Based on Particle Swarm Optimization for Photovoltaic Systems," *IEEE Trans. Sustain. Energy*, vol. 8, no. 2, pp. 468–476, 2017.

[49] Y. Yang and F. P. Zhao, "Adaptive perturb and observe MPPT technique for grid-

connected photovoltaic inverters," *Procedia Eng.*, vol. 23, pp. 468–473, 2011.

[50] A. Morales-Acevedo, J. L. Diaz-Bernabe, and R. Garrido-Moctezuma, "Improved MPPT adaptive incremental conductance algorithm," *IECON Proc. (Industrial Electron. Conf.*, pp. 5540–5545, 2014.

[51] D. Sera, T. Kerekes, R. Teodorescu, and F. Blaabjerg, "Improved MPPT algorithms for rapidly changing environmental conditions," *EPE-PEMC 2006 12th Int. Power Electron. Motion Control Conf. Proc.*, pp. 1614–1619, 2007.

[52] S. Jain and V. Agarwal, "A new algorithm for rapid tracking of approximate maximum power point in photovoltaic systems," *IEEE Power Electron. Lett.*, vol. 2, no. 1, pp. 16–19, 2004.

[53] E. Koutroulis, K. Kalaitzakis, and N. C. Voulgaris, "Development of a microcontroller-based, photovoltaic maximum power point tracking control system," *Power Electron. IEEE Trans.*, vol. 16, no. 1, pp. 46–54, 2001.

[54] M. A. Elgendy, B. Zahawi, and D. J. Atkinson, "Evaluation of incremental conductance MPPT algorithm at low perturbation rates," *7th IET Int. Conf. Power Electron. Mach. Drives*, 2014.

[55] R. K. Kharb, S. L. Shimi, S. Chatterji, and M. F. Ansari, "Modeling of solar PV module and maximum power point tracking using ANFIS," *Renew. Sustain. Energy Rev.*, vol. 33, pp. 602–612, 2014.

[56] P. Srinivasa Rao, G. Saravana Ilango, and C. Nagamani, "Maximum power from PV arrays using a fixed configuration under different shading conditions," *IEEE J. Photovoltaics*, vol. 4, no. 2, pp. 679–686, 2014.

[57] L. Qin and X. Lu, "Matlab/Simulink-Based Research on Maximum Power Point Tracking of Photovoltaic Generation," *Phys. Procedia*, vol. 24, pp. 10–18, 2012.

[58] T. Esram and P. L. Chapman, "Comparison of Photovoltaic Array Maximum Power Point Tracking Techniques," *IEEE Trans. Energy Convers.*, vol. 22, no. 2, pp. 439–449, 2007.

[59] S. Lyden and M. E. Haque, "Maximum Power Point Tracking techniques for photovoltaic systems: A comprehensive review and comparative analysis," *Renew. Sustain. Energy Rev.*, vol. 52, pp. 1504–1518, 2015.

[60] T. K. Soon and S. Mekhilef, "A fast-converging MPPT technique for photovoltaic system under fast-varying solar irradiation and load resistance," *IEEE Trans. Ind. Informatics*, vol. 11, no. 1, pp. 176–186, 2015.

[61] K. Sundareswaran, V. Vigneshkumar, and S. Palani, "Development of a hybrid genetic

algorithm/perturb and observe algorithm for maximum power point tracking in photovoltaic systems under non-uniform insolation," *IET Renew. Power Gener.*, vol. 9, no. 7, pp. 757–765, 2015.

[62] P. Mohanty, G. Bhuvaneswari, R. Balasubramanian, and N. K. Dhaliwal, "MATLAB based modeling to study the performance of different MPPT techniques used for solar PV system under various operating conditions," *Renew. Sustain. Energy Rev.*, vol. 38, pp. 581–593, 2014.

[63] G. N. Psarros, E. I. Batzelis, and S. A. Papathanassiou, "Partial Shading Analysis of Multistring PV Arrays and Derivation of Simplified MPP Expressions," *IEEE Trans. Sustain. Energy*, vol. 6, no. 2, pp. 499–508, 2015.

[64] M. A. Ghasemi, H. Mohammadian Forushani, and M. Parniani, "Partial shading detection and smooth maximum power point tracking of PV arrays under PSC," *IEEE Trans. Power Electron.*, vol. 31, no. 9, pp. 6281–6292, 2016.

[65] Y. Hu, W. Cao, J. Wu, B. Ji, and D. Holliday, "Thermography-based virtual MPPT scheme for improving PV energy efficiency under partial shading conditions," *IEEE Trans. Power Electron.*, vol. 29, no. 11, pp. 5667–5672, 2014.

[66] Y. Wang, X. Lin, Y. Kim, N. Chang, and M. Pedram, "Architecture and control algorithms for combating partial shading in photovoltaic systems," *IEEE Trans. Comput. Des. Integr. Circuits Syst.*, vol. 33, no. 6, pp. 917–930, 2014.

[67] J. R. Louis, S. Shanmugham, K. Gunasekar, N. R. Atla, and K. Murugesan, "Effective utilisation and efficient maximum ower extraction in partially shaded photovoltaic systems using minimumdistance-average-based clustering algorithm," *IET Renew. Power Gener.*, vol. 10, no. 3, pp. 319–326, 2016.

[68] F. Salema and M. A. Awadallah, "Detection and assessment of partial shading in photovoltaic arrays," *Journal of Electrical Systems and Information Technology*, vol. 3, pp. 23–32, 2016.

[69] N. A. Ahmed and M. Miyatake, "A novel maximum power point tracking for photovoltaic applications under partially shaded insolation conditions," *Electr. Power Syst. Res.*, vol. 78, no. 5, pp. 777–784, 2008.

[70] J. Ahmed and Z. Salam, "An improved method to predict the position of maximum power point during partial shading for PV arrays," *IEEE Trans. Ind. Informatics*, vol. 11, no. 6, pp. 1378–1387, 2015.

[71] A. M. I. Aldaoudeyeh, "Photovoltaic-battery scheme to enhance PV array characteristics in partial shading conditions," *IET Renew. Power Gener.*, vol. 10, no. 1, pp. 108–115,

2016.

[72] R. Hariharan, M. Chakkarapani, G. Saravana Ilango, and C. Nagamani, "A Method to Detect Photovoltaic Array Faults and Partial Shading in PV Systems," *IEEE J. Photovoltaics*, vol. 6, no. 5, pp. 1278–1285, 2016.

[73] J. Shi, W. Zhang, Y. Zhang, F. Xue, and T. Yang, "MPPT for PV systems based on a dormant PSO algorithm," *Electr. Power Syst. Res.*, vol. 123, pp. 100–107, 2015.

[74] M. Seyedmahmoudian, R. Rahmani, S. Mekhilef, A. Maung Than Oo, A. Stojcevski, T. Soon,and A. S. Ghandhari "Simulation and Hardware Implementation of New Maximum Power Point Tracking Technique for Partially Shaded PV System Using Hybrid DEPSO Method," *IEEE Trans. Sustain. Energy*, vol. 6, no. 3, pp. 850–862, 2015.

[75] S. E. Boukebbous and D. Kerdoun, "Study, modeling and simulation of photovoltaic panels under uniform and nonuniform illumination conditions," *Rev. des Energies Renouvelables*, vol. 18, no. 2, pp. 257–268, 2015.

[76] A. A. Elserougi, M. S. Diab, A. M. Massoud, A. S. Abdel-Khalik, and S. Ahmed, "A switched PV approach for extracted maximum power enhancement of PV arrays during partial shading," *IEEE Trans. Sustain. Energy*, vol. 6, no. 3, pp. 767–772, 2015.

[77] O. Bingöl and B. Özkaya, "Analysis and comparison of different PV array configurations under partial shading conditions," *Sol. Energy*, vol. 160, pp. 336–343, 2018.

[78] F. Belhachat and C. Larbes, "Modeling, analysis and comparison of solar photovoltaic array configurations under partial shading conditions," *Sol. Energy*, vol. 120, pp. 399–418, 2015.

[79] R. Ramaprabha, "Selection of an Optimum Configuration of Solar PV Array under Partial Shaded Condition Using Particle Swarm Optimization," *Int. J. Electr. Comput. Eng.*, vol. 8, no. 1, pp. 89–96, 2014.

[80] R. Ramaprabha and B. L. Mathur, "A comprehensive review and analysis of solar photovoltaic array configurations under partial shaded conditions," *Int. J. Photoenergy*, vol. 2012, pp. 1-16, 2011.

[81] M. Jazayeri, S. Uysal, and K. Jazayeri, "A comparative study on different photovoltaic array topologies under partial shading conditions," *IEEE PES T&D Conf. Expo.*, pp. 1–5, 2014.

[82] K. Sundareswaran, P. Sankar, P. S. R. Nayak, S. P. Simon, and S. Palani, "Enhanced energy output from a PV system under partial shaded conditions through artificial bee colony," *IEEE Trans. Sustain. Energy*, vol. 6, no. 1, pp. 198–209, 2015.

[83] I. R. Balasubramanian, S. I. Ganesan, and N. Chilakapati, "Impact of partial shading on the output power of PV systems under partial shading conditions," *IET Power Electron.*, vol. 7, no. 3, pp. 657–666, 2014.

[84] C. Manickam, G. P. Raman, G. R. Raman, S. I. Ganesan, and N. Chilakapati, "Efficient global maximum power point tracking technique for a partially shaded photovoltaic string," *IET Power Electron.*, vol. 9, no. 14, pp. 2637–2644, 2016.

[85] S. J. Chiang, K. T. Chang, and C. Y. Yen, "Residential photovoltaic energy storage system," *IEEE Trans. Ind. Electron.*, vol. 45, no. 3, pp. 385–394, 1998.

[86] T. Feehally, A. .J Forsyth, R. Todd, M. P. Foster, D. Gladwin, D. A. Stone, D, Strickland, "Battery energy storage systems for the electricity grid: UK research facilities," *IET Conf. Publ.*, vol. 2016, no. CP684, 2016.

[87] S. R. Sivarasu, E. Chandira Sekaran, and P. Karthik, "Development of renewable energy based microgrid project implementations for residential consumers in India: Scope, challenges and possibilities," *Renew. Sustain. Energy Rev.*, vol. 50, pp. 256–269, 2015.

[88] V. Narayanan, S. Kewat, and B. Singh, "Solar PV-BES Based Microgrid System with Multifunctional VSC," *IEEE Trans. Ind. Appl.*, vol. 56, no. 3, pp. 2957–2967, 2020.

[89] A. Gundogdu and R. Celikel, "NARMA-L2 controller for stepper motor used in single link manipulator with low-speed-resonance damping," *Engg. Sci.and Technology, an International Journal,* vol. 24, Iss. 2,pp. 360-371, 2021.

[90] N. Beniwal, I. Hussain, and B. Singh, "Control and operation of a solar PV-battery- grid-tied system in fixed and variable power mode," *IET Generation, Transmission & Distribution*, vol. 12, Iss. 11, pp. 2633–2641, 2018.

[91] Y. Al-Dunainawia, M. F. Abboda and A. Jizany, "A new MIMO ANFIS-PSO based NARMA-L2 controller for nonlinear dynamic systems," *Engineering Applications of Artificial Intelligence*, vol. 62, pp. 265-275, 2017.

[92] I. A. Pragash, J. Booma, and A. J. D. Rega, "An integrated control for standalone PV system with battery," *Int. Conf. Circuit, Power Comput. Technol.*, pp. 1–7, 2016.

[93] C. N. Bhende, "Voltage Control of Stand-Alone Photovoltaic- Diesel Generator-Battery ′ System," *IECON - 40th Annu. Conf. IEEE Ind. Electron. Soc.*, pp. 2292–2297, 2014.

[94] S. Barcellona, D. De Simone, and L. Piegari, "Simple control strategy for a PV-battery system," *7th International Conference on Renewable Power Generation*, vol. 2019, Iss. 18, pp. 4809–4812, 2019.

[95] S. Jha, I. Hussain, B. Singh, and S. Mishra, "Optimal operation of PV-DG-battery based microgrid with power quality conditioner," *IET Renw Power Gen.*, vol. 13, no. 3, pp.

418–426, 2019.

[96] R. Dharavath and I. Jacob Raglend, “Intelligent Controller Based Solar Photovoltaic with Battery Storage System for Conditioning the Electrical Power,” *Adv. Intell. Syst. Comput.*, vol. 1048, no. 2, pp. 43–54, 2020.

[97] N. Gira and A. K. Dahiya, “Solar PV-BES in distribution system with novel technique for DC voltage regulation,” *Eng. Sci. Technol. an Int. J.*, vol. 23, no. 5, pp. 1058–1067, 2020.

[98] A. Kami and L. Luo, “Energy balance based DC-link voltage control of grid tied battery connected multistage bidirectional PV inverter system,” *2nd Int. Conf. Power Renew. Energy, ICPRE*, pp. 1017–1022, 2018.

[99] A. Saidi and B. Chellali, “Simulation and Control of Solar Wind Hybrid Renewable Power System,” *6th Int. Conf. Syst. Control*, pp. 51–56, 2017.

[100] S. Mumtaz and L. Khan, “Indirect adaptive neurofuzzy Hermite wavelet based control of PV in a grid-connected hybrid power system,” *Turkish J. Electr. Eng. Comput. Sci.*, vol. 25, no. 5, pp. 4341–4353, 2017.

[101] R. Karthikeyan, “Stand-alone Photovoltaic / Wind Energy Hybrid Generation System with MPPT for Rural Applications,” *Fourth International Conference on Computing, Communications and Networking Technologies (ICCCNT)*, pp. 1–6, 2013.

[102] X. Li, Y. Li, X. Han, and D. Hui, “Energy Procedia Application of Fuzzy Wavelet Transform to Smooth Wind / PV Hybrid Power System Output with Battery Energy Storage System,” *Energy Procedia*, vol. 12, pp. 994–1001, 2011.

[103] A. Mohammadzadeh and S. Rathinasamy, “Energy management in photovoltaic battery hybrid systems: A novel type-2 fuzzy control,” *Int. J. Hydrogen Energy*, vol. 45, no. 41, pp. 20970–20982, 2020.

[104] S. I. Rasel, R. N. Ali, M. S. U. Chowdhury, and M. M. Hasan, “Design & simulation of grid connected Photovoltaic system using Simulink,” *Proc. 3rd Int. Conf. Adv. Electr. Eng. ICAEE*, pp. 238–242, 2016.

[105] B. Singh, K. Al-haddad and A. Chandra, “Power Quality Improvement,” *IEEE Transactions on Industrial Electronics*, vol. 46, no. 5, pp. 960–971, 1999.

[106] H. Abdel-Gawad and V. K. Sood, “Overview of connection topologies for grid-connected PV systems,” *Can. Conf. Electr. Comput. Eng.*, pp. 1–8, 2014.

[107] O. Phochai, W. Ongsakul, and J. Mitra, “Voltage control strategies for grid-connected solar PV systems,” *Proc. 2014 Int. Conf. Util. Exhib. Green Energy Sustain. Dev. ICUE*, pp. 19–21, 2014.

[108] M. E. Ropp and S. Gonzalez, “Development of a MATLAB/simulink model of a single-phase grid-connected photovoltaic system,” *IEEE Trans. Energy Convers.*, vol. 24, no. 1, pp. 195–202, 2009.

[109] M. Joshi and P. G. A. Vaidya, “3-Modeling and Simulation of Single Phase Grid Connected Solar Photovoltaic System,” *2014 Annual IEEE India Conference (INDICON), 2014,* pp. 1-6, doi: 10.1109/INDICON.2014.7030623.

[110] R. Avtar, “Simulation and Modelling of Photovoltaic,”*Energy Reports*, Vol.4, pp. 701-712, 2018.

[111] L. Bruno and G. Campanhol, “Single-Stage Three-Phase Grid-Tied PV System With Universal Filtering Capability Applied to DG Systems and AC Microgrids,” *IEEE Transactions on Power Electronics*, vol. 32, no. 12, pp. 9131-9142, 2017.

[112] A. A. Hassan, F. H. Fahmy, A. Nafeh, M. El-Sayed, “Modeling and Simulation of a Single Phase Grid Connected Photovoltaic System,” *Wseas Trans. Syst.*, vol. 5, no. 1, pp. 16-25, 2010.

[113] B. Singh, C. Jain, and S. Goel, “ILST control algorithm of single-stage dual purpose grid connected solar PV system,” *IEEE Trans. Power Electron.*, vol. 29, no. 10, pp. 5347–5357, 2014.

[114] Y. Jung, G.Yu, J.Choi, and J.Choi, “High-frequency DC link inverter for grid-connected photovoltaic system,” *Conf. Rec. IEEE Photovolt. Spec. Conf.*, pp. 1410–1413, 2002.

[115] C. N. Rowe, T. J. Summers, R. E. Betz, and D. Cornforth, “A comparison of instantaneous and fryze power calculations on P-F and Q-V droop in microgrids,” *AUPEC 2010 - 20th Australas. Univ. Power Eng. Conf. “Power Qual.,”* pp. 5–9, 2010.

[116] B. Singh and S. Kumar, “Modified power balance theory for control of DSTATCOM,” *2010 Jt. Int. Conf. Power Electron. Drives Energy Syst. Power India*, pp. 1–8, 2010.

[117] S. M. Hsu, “Discussion of ‘A New Approach to Load Balancing and Power Factor Correction in Power Distribution System,’” *IEEE Trans. Power Deliv.*, vol. 15, no. 4, pp. 1325–1326, 2000.

[118] E. Society, "IEEE Recommended Practice and Requirements for Harmonic Control in Electric Power Systems," in IEEE Std 519 , pp. 1-29, doi: 10.1109/IEEESTD.2014.68264592014,.

[119] B. Singh and J. Solanki, \A Comparison of Control Algorithms for DSTATCOM," *IEEE Transactions on Industrial Electronics,* vol. 56, no. 7, pp. 2738-2745, 2009.

[120] Y. E. Wu and C. L. Shen, “Implementation of a DC power system with PV grid-connection and active power filtering,” *2nd Int. Symp. Power Electron. Distrib. Gener.*

*Syst. PEDG 2010*, pp. 116–121, 2010.

[121] A. Panda, M. K. Pathak, and S. P. Srivastava, "A single phase photovoltaic inverter control for grid connected system," *Sadhana - Acad. Proc. Eng. Sci.*, vol. 41, no. 1, pp. 15–30, 2016.

[122] P. García, C. A. García, L. M. Fernández, F. Llorens, and F. Jurado, "ANFIS-Based control of a grid-connected hybrid system integrating renewable energies, hydrogen and batteries," *IEEE Trans. Ind. Informatics*, vol. 10, no. 2, pp. 1107–1117, 2014.

[123] N. Altin and I. Sefa, "DSPACE based adaptive neuro-fuzzy controller of grid interactive inverter," *Energy Convers. Manag.*, vol. 56, pp. 130–139, 2012.

[124] N. Gupta and R. Garg, "Tuning of asymmetrical fuzzy logic control algorithm for SPV system connected to grid," *Int. J. Hydrogen Energy*, vol. 42, no. 26, pp. 16375–16385, 2017.

[125] M. Mangaraj and A. K. Panda, "Modelling and simulation of KHLMS algorithm-based DSTATCOM," *IET Power Electron.*, vol. 12, no. 9, pp. 2304–2311, 2019.

[126] A. K. Singh, I. Hussain, and B. Singh, "Double-Stage Three-Phase Grid-Integrated Solar PV System With Fast Zero Attracting Normalized Least Mean Fourth Based Adaptive Control," *IEEE Trans. Ind. Electron.*, vol. 65, no. 5, pp. 3921–3931, 2018.

[127] N. Beniwal, I. Hussain, and B. Singh, "PNLMS based adaptive control algorithm for solar PV grid tied system," *11th Int. Conf. Ind. Inf. Syst. ICIIS 2016 - Conf. Proc.*, vol. 2018–Janua, pp. 661–665, 2018.

[128] N. Beniwal, I. Hussain, and B. Singh, "Second-order volterra-filter-based control of a solar PV-DSTATCOM system to achieve lyapunov's stability," *IEEE Trans. Ind. Appl.*, vol. 55, no. 1, pp. 670–679, 2019.

[129] S. Kewat and B. Singh, "Improved Reweighted Zero-Attracting Quaternion-Valued LMS Algorithm for Islanded Distributed Generation System at IM Load," *IEEE Trans. on Indust. Electron.*, vol. 67, no. 5, pp. 3705–3716, 2020.

[130] Y. He and H. Zhang, "Design of adaptive filter based on Matlab and Simulink," *Commun. Comput. Inf. Sci.*, vol. 175 CCIS, no. PART 1, pp. 292–297, 2011.

[131] N. Beniwal, I. Hussain, and B. Singh, "Implementation of the DSTATCOM with an i-PNLMS-Based Control Algorithm under Abnormal Grid Conditions," *IEEE Trans. Ind. Appl.*, vol. 54, no. 6, pp. 5640–5648, 2018.

[132] M. Singh and A. Chandra, "Application of adaptive network-based fuzzy inference system for sensorless control of PMSG-based wind turbine with nonlinear-load-compensation capabilities," *IEEE Trans. Power Electron.*, vol. 26, no. 1, pp. 165–175,

2011.

[133] B. Singh, S. R. Arya, A. Chandra, and K. Al-Haddad, “Implementation of adaptive filter in distribution static compensator,” *IEEE Trans. Ind. Appl.*, vol. 50, no. 5, pp. 3026–3036, 2014.

[134] B. Singh and S. R. Arya, “Adaptive theory-based improved linear sinusoidal tracer control algorithm for DSTATCOM,” *IEEE Trans. Power Electron.*, vol. 28, no. 8, pp. 3768–3778, 2013.

[135] S. R. Arya and B. Singh, “Performance of DSTATCOM using leaky LMS control algorithm,” *IEEE J. Emerg. Sel. Top. Power Electron.*, vol. 1, no. 2, pp. 104–113, 2013.

[136] P. Mitra and G. K. Venayagamoorthy, “An adaptive control strategy for DSTATCOM applications in an electric ship power system,” *IEEE Trans. Power Electron.*, vol. 25, no. 1, pp. 95–104, 2010.

[137] T. Aboulnasr and K. Mayyas,"A Robust Variable Step-Size LMS-typeAlgorithm: Analysis and Simulations," *IEEE Transactions on Signal Processing*, vol. 45, no. 3, pp. 631-639, 1997.

[138] R. L. De Araujo Ribeiro, C. C. De Azevedo, and R. M. I. De Sousa, “A robust adaptive control strategy of active power filters for power-factor correction, harmonic compensation, and balancing of nonlinear loads,” *IEEE Trans. Power Electron.*, vol. 27, no. 2, pp. 718–730, 2012.

[139] R. Serizel, M. Moonen, B. Van Dijk, and J. Wouters, “Low-rank approximation based multichannel wiener filter algorithms for noise reduction with application in cochlear implants,” *IEEE Trans. Audio, Speech Lang. Process.*, vol. 22, no. 4, pp. 785–799, 2014.

[140] J. Chen, J. Benesty, Y. Huang, and S. Doclo, “New insights into the noise reduction Wiener filter,” *IEEE Trans. Audio, Speech Lang. Process.*, vol. 14, no. 4, pp. 1218–1233, 2006.

[141] M. Mangaraj, T. Penthia, and A. K. Panda, “Implementation of sparse LMS control algorithm in DSTATCOM,” *2016 Natl. Power Syst. Conf. NPSC 2016*, pp. 1–6, 2017.

[142] S. Pradhan, I. Hussain, B. Singh, and B. K. Panigrahi, “Modified VSS-LMS-based adaptive control for improving the performance of a single-stage PV-integrated grid system,” *IET Sci., Measurement & Tech.*, vol. 11, pp. 388–399, 2017.

[143] A. Arora and A. Singh, “Design and analysis of functional link artificial neural network controller for shunt compensation,” *IET Gener. Transm. Distrib.*, vol. 13, no. 11, pp. 2208–2215, 2019.

[144] H. Bellia, R. Youcef, and M. Fatima, “A detailed modeling of photovoltaic module using

MATLAB," *NRIAG J. Astron. Geophys.*, vol. 3, no. 1, pp. 53–61, 2014.

[145] R. B. Bollipo, S. Mikkili, and P. K. Bonthagorla, "Hybrid, optimal, intelligent and classical PV MPPT techniques: A review," *CSEE J. Power Energy Syst.*, vol. 7, no. 1, pp. 9–33, 2021.

[146] T. Logeswaran and A. SenthilKumar, "A review of maximum power point tracking algorithms for photovoltaic systems under uniform and non-uniform irradiances," *Energy Procedia*, vol. 54, pp. 228–235, 2014.

[147] S. Salman, X. Ai, and Z. Wu, "Design of a P-&-O algorithm based MPPT charge controller for a stand-alone 200W PV system," *Prot. Control Mod. Power Syst.*, vol. 3, no. 1, 2018.

[148] B. Pakkiraiah, G. D. Sukumar, B. Pakkiraiah, and G. D. Sukumar, "Research Survey on Various MPPT Performance Issues to Improve the Solar PV System Efficiency," *J. Sol. Energy*, vol. 2016, pp. 1–20, 2016.

[149] F. Chan and H. Calleja, "Reliability estimation of three single-phase topologies in grid-connected PV systems," *IEEE Trans. Ind. Electron.*, vol. 58, no. 7, pp. 2683–2689, 2011.

[150] A. Ahadi, H. Hayati, and S. M. Miryousefi Aval, "Reliability evaluation of future photovoltaic systems with smart operation strategy," *Front. Energy*, vol. 10, no. 2, pp. 125–135, 2016.

[151] W. Jianing and Y. Shaoze, "Reliability analysis of the solar array based on fault tree analysis," *J. Phys. Conf. Ser.*, vol. 305, no. 1, 2011.

[152] S. R. Ratna and R. Ravi, "Securing jammed network using reliability behavior value through neuro-fuzzy analysis," *Sadhana - Acad. Proc. Eng. Sci.*, vol. 40, no. 4, pp. 1139–1153, 2015.

[153] Y. Z. Li, R. Luan, and J. C. Niu, "Forecast of power generation for grid-connected photovoltaic system based on grey model and Markov chain," *3rd IEEE Conf. Ind. Electron. Appl. ICIEA*, pp. 1729–1733, 2008.

[154] N. Gokmen, E. Karatepe, B. Celik, and S. Silvestre, "Simple diagnostic approach for determining of faulted PV modules in string based PV arrays," *Sol. Energy*, vol. 86, no. 11, pp. 3364–3377, 2012.

[155] J. Solórzano and M. A. Egido, "Automatic fault diagnosis in PV systems with distributed MPPT," *Energy Convers. Manag.*, vol. 76, pp. 925–934, 2013.

[156] A. Dolara, G. C. Lazaroiu, S. Leva, and G. Manzolini, "Experimental investigation of partial shading scenarios on PV (photovoltaic) modules," *Energy*, vol. 55, pp. 466–475, 2013.

[157] M. Tadj, K. Benmouiza, A. Cheknane, and S. Silvestre, “Improving the performance of PV systems by faults detection using GISTEL approach,” *Energy Convers. Manag.*, vol. 80, pp. 298–304, 2014.

[158] J. A. Jiang *et al.*, “On a hybrid MPPT control scheme to improve energy harvesting performance of traditional two-stage inverters used in photovoltaic systems,” *Renew. Sustain. Energy Rev.*, vol. 69, pp. 1113–1128, 2017.

[159] F. Salem and M. A. Awadallah, “Detection and assessment of partial shading in photovoltaic arrays,” *J. Electr. Syst. Inf. Technol.*, vol. 3, no. 1, pp. 23–32, 2016.

[160] O. Bingöl and B. Özkaya, “Analysis and comparison of different PV array configurations under partial shading conditions,” *Sol. Energy*, vol. 160, no. July 2017, pp. 336–343, 2018.

[161] W. Mara and M. Piotrowicz, “Calculation of Dynamic MPP-Tracking Efficiency of PV-Inverter Using Recorded Irradiance,” *Proc. 20th Int. Conf. Mix. Des. Integr. Circuits Syst. - Mix. 2013*, pp. 431–434, 2013.

[162] K. S. Narendra, And S. Mukhopadhyay, " Adaptive Control Using Neural Networks and Approximate Models" *IEEE Transactions on Neural Networks*, Vol. 8, No. 3, May 1997.

[163] A. A. A. Radwan and Y. A. R. I. Mohamed, “Power Synchronization Control for Grid-Connected Current-Source Inverter-Based Photovoltaic Systems,” *IEEE Trans. Energy Convers.*, vol. 31, no. 3, pp. 1023–1036, 2016.

[164] Z. A. Ghani, M. A. Hannan, and A. Mohamed, “Investigation of three-phase grid-connected inverter for photovoltaic application,” *Prz. Elektrotechniczny*, vol. 88, no. 7 A, pp. 8–13, 2012.

[165] P. P. Dash and M. Kazerani, “Dynamic modeling and performance analysis of a grid-connected current-source inverter-based photovoltaic system,” *IEEE Trans. Sustain. Energy*, vol. 2, no. 4, pp. 443–450, 2011.

[166] N. A. Rahim and S. Mekhilef, “Implementation of three-phase grid connected inverter for photovoltaic solar power generation system,” *PowerCon Int. Conf. Power Syst. Technol. Proc.* , vol. 1, pp. 570–573, 2002.

[167] R. Mechouma, B. Azoui, and M. Chaabane, “Three-phase grid connected inverter for photovoltaic systems, a review,” *2012 1st Int. Conf. Renew. Energies Veh. Technol. REVET 2012*, pp. 37–42, 2012.

[168] J. B. Evans, P. Xue, and B. Liu, "Analysis and Implementation of Variable Step Size Adaptive Algorithms," *IEEE Transactions on Signal Processing*, vol. 41, no. 8, pp.

2517-535, 1993.

[169] N. Beniwal, I. Hussain, B. Singh, A. Chandra, and K. Al-Haddad, "Adaptive control scheme for three-phase four wire grid tied SPV system with DSTATCOM capabilities," *2016 Natl. Power Syst. Conf. NPSC 2016*, pp. 1–6, 2017.

[170] A. Feuer, "Performance analysis of the smothed least mean square (SLMS) algorithm," *Signal Process.*, vol. 11, pp. 265–276, 1986.

[171] J. Chen, C. Richard, Y. Song, D. Brie, Transient performance analysis of zero-attracting LMS, *IEEE Signal Process. Lett.,* vol. 23, pp. 1786–1790, 2016.

[172] N. Beniwal, I. Hussain, and B. Singh, "Hybrid VSS–LMS–LMF based adaptive control of SPV-DSTATCOM system under distorted grid conditions," *IET Renew. Power Gener.*, vol. 12, no. 3, pp. 311–322, 2018.

[173] A. Ranjan, Seema, and B. Singh, "Reweighted L1 Norm penalized Least Mean Square Fourth Algorithm based Solar Grid Interfaced System for Alleviating Power Quality Problems," *IEEE Int. Conf. Power Electron. Smart Grid Renew. Energy*, vol. 56, no. 5, pp. 5352–5362, 2020.

[174] K. Tiwari, Seema, and B. Singh, "CMPN Adaptive Control Algorithm for Double Stage PV-Grid Connected System,"*IEEE Int. Conf. Power Electron. Smart Grid Renew. Energy*, pp. 2–7, 2020.

# APPENDIX-A

## Manufacturer datasheet of PV module

SW-02-5005US 07-2012

**Sunmodule**™

SW 230 mono / Version 2.0

### PERFORMANCE UNDER STANDARD TEST CONDITIONS (STC)*

| | | SW 230 |
|---|---|---|
| Maximum power | $P_{max}$ | 230 Wp |
| Open circuit voltage | $V_{oc}$ | 37.4 V |
| Maximum power point voltage | $V_{mpp}$ | 30.0 V |
| Short circuit current | $I_{sc}$ | 8.16 A |
| Maximum power point current | $I_{mpp}$ | 7.68 A |

*STC: 1000W/m², 25°C, AM 1.5

### PERFORMANCE AT 800 W/m², NOCT, AM 1.5

| | | SW 230 |
|---|---|---|
| Maximum power | $P_{max}$ | 166.9 Wp |
| Open circuit voltage | $V_{oc}$ | 33.9 V |
| Maximum power point voltage | $V_{mpp}$ | 27.2 V |
| Short circuit current | $I_{sc}$ | 6.58 A |
| Maximum power point current | $I_{mpp}$ | 6.14 A |

Minor reduction in efficiency under partial load conditions at 25°C: at 200W/m², 95% (+/-3%) of the STC efficiency (1000 W/m²) is achieved.

### THERMAL CHARACTERISTICS

| | |
|---|---|
| NOCT | 46 °C |
| TC $I_{sc}$ | 0.004 %/K |
| TC $V_{oc}$ | -0.30 %/K |
| TC $P_{mpp}$ | -0.45 %/K |
| Operating temperature | -40°C to 85°C |

### COMPONENT MATERIALS

| | |
|---|---|
| Cells per module | 60 |
| Cell type | Mono crystalline |
| Cell dimensions | 6.14 in x 6.14 in (156 mm x 156 mm) |
| Front | tempered glass (EN 12150) |
| Frame | Clear anodized aluminum |
| Weight | 46.7 lbs (21.2 kg) |

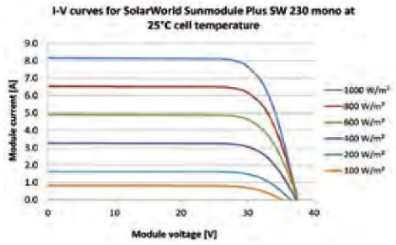


### SYSTEM INTEGRATION PARAMETERS

| | | |
|---|---|---|
| Maximum system voltage SC II | | 1000 V |
| Max. system voltage USA NEC | | 600 V |
| Maximum reverse current | | 16 A |
| Number of bypass diodes | | 3 |
| UL Design Loads* | Two rail system | 113 psf downward<br>64 psf upward |
| UL Design Loads* | Three rail system | 170 psf downward<br>64 psf upward |
| IEC Design Loads* | Two rail system | 113 psf downward<br>50 psf upward |

*Please refer to the Sunmodule installation instructions for the details associated with these load cases.

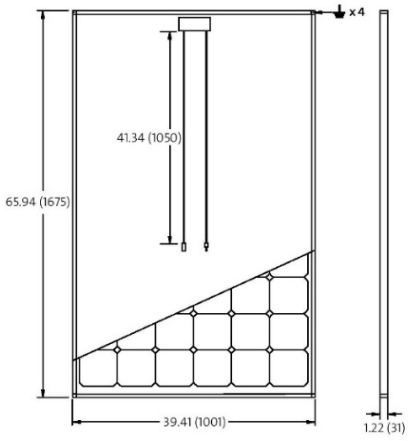


### ADDITIONAL DATA

| | |
|---|---|
| Power tolerance[2] | -0 Wp / +5 Wp |
| J-Box | IP65 |
| Connector | MC4 |
| Module efficiency | 13.72 % |
| Fire rating (UL 790) | Class C |

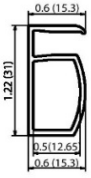


**VERSION 2.0 FRAME**
- Compatible with "Top-Down" mounting methods
- Grounding Locations: 4 corners of the frame

1) Sunmodules dedicated for the United States and Canada are tested to UL 1703 Standard and listed by a third party laboratory. The laboratory may vary by product and region. Check with your SolarWorld representative to confirm which laboratory has a listing for the product.
2) Measuring tolerance traceable to TUV Rheinland: +/- 2% (TUV Power Controlled).
3) All units provided are imperial. SI units provided in parentheses.

SolarWorld AG reserves the right to make specification changes without notice.

# APPENDIX-B

## (a) Parameters for simulation of Stand-alone PV system

| | Parameters | Attributes |
|---|---|---|
| **PV module** | Power | 1.28 kW |
| **SW-80** | Array Short circuit current | 22 A |
| | Array Open circuit voltage | 86.8 V |
| | Array current at MPP | 18.08 A |
| | Array voltage at MPP | 70.8 V |
| **Boost Converter** | Duty Ratio | 0.5- 0.7 |
| | Inductor | 1.1 mH |
| | Capacitor | 500 μF |
| | Switching frequency | 10 kHz |

## (b) Parameters for simulation of grid-tied SPV system

| | Parameters | Attributes |
|---|---|---|
| **PV Sunmodule** | Power | 11.78 kW |
| **SW-213** | Array Short circuit current | 23.52 A |
| | Array Open circuit voltage | 726 V |
| | Array current at MPP | 22.05 A |
| | Array voltage at MPP | 580 V |
| **Boost Converter** | Duty Ratio | 0.5- 0.6 |
| | Inductor | 5 mH |
| | Capacitor | 2.2 μF |
| | Switching frequency | 10 kHz |
| **Inverter** | Switching frequency | 10 kHz |
| | DC link voltage | 800 V |
| | DC link capacitor | 3 μF |
| | Interfacing Inductance | 5 mH |
| | Line-to-line voltage, Line-to-neutral voltage | 415 V, 220 V |
| **Grid** | Grid frequency | 50 Hz |

| | | |
|---|---|---|
| | Line-to-line voltage, Line-to-neutral voltage | 415 V, 220 V |
| | Grid Resistance ($R_s$) Inductance ($L_s$) | 0.11Ω, 0.35 mH |
| **Load** | Linear Load | 14.14 kVA, 0.71 lagging p.f |
| | Non-Linear Load | Three phase bridge rectifier with RL Load, R= 20 Ω, L=100mH |
| **PI Gains** | DC PI gain $K_{pd}$, $K_{id}$ | 0.5, 0.1 |
| | AC PI gain $K_{pa}$ , $K_{ia}$ | 0.11,0.11 |

**(c) Parameters for simulation of Stand-alone PV system with BESS**

| | **Parameters** | **Attributes** |
|---|---|---|
| **PV module** | Power | 4.7 kW |
| | Array Short circuit current | 8.01 A |
| | Array Open circuit voltage | 812 V |
| | Array current at MPP | 7.1 A |
| | Array voltage at MPP | 661 V |
| **Boost Converter** | Duty Ratio | 0.5- 0.6 |
| | Inductor | 1.1 mH |
| | Capacitor | 2μF |
| | Switching frequency | 10 kHz |
| | DC link voltage | 650 V |

# APPENDIX-C

## (a) Data for sensitivity analysis of solar cell

| Components | Value |
|---|---|
| PV Module power | 65 W |
| Rated Voltage, Current | 18 V, 3.6 A |
| Open-Circuit Voltage | 21.7 V |
| Series Cells, Diode Ideality Factor | 72 |
| Reference insolation, Temperature | 0.96 |
| Series and Parallel Resistance | 0.56 Ω, 70Ω |
| Energy Gap | 0.70 |
| Reference insolation, | 1000W/$m^2$ |
| Temperature | 298 K |

## (b) Data for sensitivity analysis of boost converter

| Components | Value |
|---|---|
| Inductor | 3.07-9.89 mH |
| Capacitor | 1.25-2.73 μF |
| Duty Ratio | 0.5-0.7 |
| Switching Frequency | 20 kHz |

# APPENDIX-D

**Data for reliability analysis**

| Components | Reliability Value |
|---|---|
| PV Module | 0.99 |
| Boost converter | 0.96 |
| Battery | 0.90 |
| Battery Charger | 0.95 |
| Capacitor | 0.99 |
| Inverter | 0.83 |
| Switch | 0.97 |
| Synchronizer | 0.91 |
| Grid | 0.99 |
| Load | 0.90 |

# APPENDIX-E

**Parameters of developed hardware prototype**

| | Parameters | Attributes |
|---|---|---|
| **Three phase AC mains** | Grid frequency | 50 Hz |
| | Line-to-line voltage | 110 V |
| **Inverter** | DC link voltage | 200 V |
| | Interfacing Inductance | 5 mH |
| | Line-to-line voltage | 110 V |
| **Load** | Linear Load | 0.29 kVA, 0.85 lagging p.f |
| | Non-Linear Load | Three phase bridge rectifier with RL load, R= 50Ω, L= 20mH |
| | Grid Resistance ($R_s$) Inductance ($L_s$) | 0.11Ω, 0.35 mH |
| **PI Gains** | DC PI gain $K_{pd}$, $K_{id}$ | 0.5,0.01 |
| | AC PI gain $K_{pa}$ , $K_{ia}$ | 0.11,0.11 |

# LIST OF PUBLICATIONS

**Journal Papers**

1. P. Verma, R. Garg, and P. Mahajan, "Smooth LMS-based adaptive control of SPV system tied to grid for enhanced power quality," IET Power Elec., Vol. 13, Iss. 15, pp. 3456-3466, 2020. doi: 10.1049/iet-pel.2020.0134. Indexing: Science Citation Index Expanded (SCIE), Impact Factor: 2.839.

2. P. Verma, R. Garg, P. Mahajan, "Asymmetrical interval type-2 fuzzy logic control based MPPT tuning for PV system under partial shading condition" ISA Transactions, Vol. 100, 2020, pp. 251–263. Indexing: Science Citation Index Expanded (SCIE), Impact Factor: 5.468.

3. P. Verma, R. Garg, P. Mahajan, "Asymmetrical Fuzzy Logic Control based MPPT algorithm for Stand-alone PV System Under Partially Shaded Conditions" International Journal of Science & technology, Vol. 27, Iss. 6, pp. 3162-3174, 2020. DOI: 10.24200/SCI.2019.51737.2338. Indexing: Science Citation Index Expanded (SCIE), Impact Factor: 0.718

4. P. Verma, R. Garg, P. Mahajan, "Reliability assessment of Grid interfaced PV based Microgrid for different PV array configurations" accepted in International Journal of Information Technology (Springer).

**Proceedings Papers- International**

5. P. Verma, P. Mahajan, R. Garg, "Comparison of intelligent and conventional MPPT algorithms for photovoltaic system under partially shahded conditions" Recent Developments in Control, Automation & Power Engineering (RDCAPE), pp. 505-510, Noida, India, 2017.

6. P. Verma, P. Mahajan, R. Garg, "DC Link Voltage Control of Stand-Alone PV Tied with Battery Energy Storage System" 20th International Conference on Intelligent Systems Design and Applications (ISDA 2020) held December 12-15, 2020, pp. 1–11, 2021.https://doi.org/10.1007/978-3-030-71187-0_86.

7. P. Verma, P. Mahajan, R. Garg, "Sensitivity Analysis of solar PV system for different PV array configurations" accepted in 16th International Conference on ICInPro 2021 (Springer).

**Book Chapter**

8. P. Verma, R. Garg, P. Mahajan, "Grid integration of Renewable Energy systems: Power electronics topologies for grid integration, Advanced control techniques of grid connected PV inverters" accepted in Renewable Energy Systems: Modelling, Optimization, and Applications (RESMOA 2021).

**Submitted Paper**

9. P. Verma, R. Garg, P. Mahajan, "Design and Implementation of Improved Zero Attracting LMS adaptive filter for power quality refinement of PV system interfaced to grid" revision R2 submitted in Arabian Journal for Science And Engineering (SCIE) since 31 July 2021.